UNIVERSITÄT BAYREUTH

SILICON AND OXYGEN VOLUME DIFFUSION IN WADSLEYITE AND IMPLICATIONS TO MANTLE TRANSITION ZONE RHEOLOGY

Dissertation

zur Erlangung des akademischen Grades eines
Doktors der Naturwissenschaften
- Dr. rer. nat. -

in der Bayreuther Graduiertenschule für Mathematik und Naturwissenschaften (BayNAT)
der Universität Bayreuth

vorgelegt von:

Dmitry Druzhbin

aus Nowosibirsk (Russland)

Bayreuth, 2019

This doctoral thesis was prepared at the Department of Bayerisches Geoinstitut, University of Bayreuth from November 2014 until October 2019 supervised by Prof. Dr. Tomoo Katsura.

This is a full reprint of the thesis submitted to obtain the academic degree of Doctor of Natural Sciences (Dr. rer. nat.) and approved by the Bayreuth Graduate School of Mathematical and Natural Sciences (BayNAT) of the University of Bayreuth.

Date of submission: 18.10.2019

Date of defense (disputation): 17.12.19

Acting dean: Prof. Dr. Markus Lippitz

Doctoral Committee:

Prof. Dr. Tomoo Katsura (reviewer)

Prof. Dr. Daniel Frost (reviewer)

Prof. Dr. Leonid Dubrovinsky (chairman)

Prof. Dr. Gregor Golabek

Acknowledgements

I would like to thank the people at the Bayerisches Geoinstitut for helping me during my Ph.D. time in Bayreuth. Great thanks to my supervisors Prof. Dr. D. Frost and Prof. Dr. S. Chakraborty, especially, to my main supervisor Prof. Dr. Tomoo Katsura for his support and patience over these years. I also would like to thank H. Fei for his help and guidance in diffusion experiments.

Many thanks to Tiziana Boffa-Ballaran for her help with X-ray diffractometers; many thanks to Svyatoslav Shcheka and Esther Posner for their help and advice with multi-anvil experiments; thanks to Prof. Dr. H. Keppler for introducing me an FTIR spectrometer. I would like to thank gratefully R. Dohmen at Ruhr-University of Bochum (Germany) for his help with a thin-film depositions and numerical simulations; I would like to appreciate NanoSIMS team at Institute of Geology and Geophysics (Chinese Academy of Science, Beijing), especially, Prof. Dr. Yangting Lin and J. Zhang.

I thank the sample preparation team: A. Rother, H. Schulze, and, especially, R. Njul. Without their work, this thesis would not have existed. Thanks to S. Übelhack, H. Fischer and S. Linhardt. Thanks to the secretariat: P. Buchert, J. Potzel, L. Kison-Herzing and A. Dinius for their help with reimbursement forms and other paperwork. Special thanks to André Zametzer and Lisa Eberhard for the help on the “Zusammenfassung”.

Finally, I would like to thank all my friends from BGI for their support, particular, during the last two years of my Ph.D. And, of course, I thank my family for their faith in me.

Contents

Summary

Silicon is the slowest diffusing species in the majority of mantle minerals, and therefore provide the rate-limiting step for plastic deformation at high temperatures (Costa & Chakraborty, 2008; Dohmen, 2002; H. Fei et al., 2012; H. Fei, Wiedenbeck, Yamazaki, & Katsura, 2013; Shimojuku et al., 2009). Wadsleyite is one of the most abundant minerals in Earth's mantle upper transition zone (MTZ) and the main constituent mineral of subducting slabs in this region.

Robust evaluation of the effect of H_2O content on diffusion properties in wadsleyite has not been considered (Shimojuku, Kubo, Ohtani, Nakamura, & Okazaki, 2010; Shimojuku et al., 2009; Shimojuku, Kubo, Ohtani, & Yurimoto, 2004). As observed for olivine in silicon diffusion experiments (H. Fei et al., 2012) water has a less significant effect on its rheological properties than proposed based on deformation experiments (G. Hirth & Kohlstedt, 2003). However, this may not be the case for wadsleyite since it has a different structure and defect chemistry. Furthermore, previous experiments have showen that wadsleyite can accommodate a significant amount of water (1 – 3 wt.%) (Jacobsen, Demouchy, Frost, Ballaran, & Kung, 2005; Kohlstedt, Keppler, & Rubie, 1996) in comparison to olivine (Bali, Bolfan-Casanova, & Koga, 2008; Smyth & Jacobsen, 2006).

So far there is no study of anisotropy of silicon and oxygen self-diffusion in wadsleyite. Its orthorhombic structure raises the possibility that diffusion rates may be anisotropic (Holl, Smyth, Jacobsen, & Frost, 2008).

In this project, I focused on measuring the volume diffusion coefficients of silicon and oxygen in Mg_2SiO_4 wadsleyite single crystals as a function of temperature, and water content, and investigated the upper MTZ rheology based on silicon and oxygen diffusivities.

Silicon volume diffusion activation enthalpy was obtained from $\Delta H_{Si}^{V} = 150(80)$ to $\Delta H_{Si}^{V} = 220(80)$ kJ/mol, with average $\Delta H_{Si}^{V} = 170(90)$ kJ/mol. This activation enthalpy is a half of that obtained by Shimojuku et al., 2010 of 342(143) kJ/mol using polycrystalline samples. A possible explanation of this disagreement may be two orders of magnitude difference in the water content in the samples between this study and Shimojuku et al., 2010.

The present study shows, that Si is the slowest atomic species in wadsleyite along a mantle geotherm at water contents lower than 1500 wt. ppm. Si diffusivity is strongly water content dependent and anisotropic. The water dependence of Si volume self-diffusivity along the *a*-direction is $D_{Si}^{V}(100) \propto C_{H_2O}^{0.6}$, *b*-direction: $D_{Si}^{V}(010) \propto C_{H_2O}^{1.9(2)}$, and *c*-direction: $D_{Si}^{V}(001) \propto C_{H_2O}^{5.2(5)}$. The water-content exponents obtained in this study in *b*- and *c*- directions are significantly different from that $r = 0.6$ reported by Shimojuku et al., 2010 from polycrystalline samples. The large water content dependence implies that not only Mg-sites are substituted by protons (Smyth, 1987) but the Si-sites are also substitute by protons. Si diffusion in wadsleyite occurs by a vacancy mechanism. Moreover, water exponents suggest that Si-site and O-site vacancies are associated, given that O vacancies produce corridors for Si migration. The large water dependence in the *c*-direction implies Si migration through the Mg-site vacancies in M3 octahedra.

The obtained activation enthalpy for oxygen diffusion ranges from $\Delta H_{O}^{V} = 160(60)$ kJ/mol to $\Delta H_{Si}^{V} = 180(40)$ kJ/mol, which are smaller than those obtained for Fe-bearing wadsleyite by (Shimojuku et al., 2009) with $\Delta H_{O}^{V} = 290(80)$ kJ/mol. The effect of oxygen fugacity on diffusion rates in wadsleyite, however, was not studied so far.

O diffusion in Mg_2SiO_4 wadsleyite is found in this study to be strongly anisotropic and water dependent in *b*- and *c*-directions. The water dependence of O volume self-diffusivity along main crystallographic directions is $D_{O}^{V}(100) \propto C_{H_2O}^{0}$, $D_{O}^{V}(010) \propto C_{H_2O}^{0.5(2)}$, $D_{O}^{V}(001) \propto C_{H_2O}^{3.5(4)}$. At water content higher than 1500 wt.

ppm O diffusivity is the lowest in Mg_2SiO_4 wadsleyite at all MTZ temperatures. O diffusion in wadsleyite occurs by a vacancy mechanism. The large water dependence in the *c*-direction implies O, like Si, migrates through Mg-site vacancies in the M3 octahedra.

The estimated strain rates for Mg_2SiO_4 wadsleyite demonstrate three regions with different water exponents indicated by the superscript: (1) dry wadsleyite with less than 1000 wt. ppm H_2O has $\dot{\varepsilon} \propto C_{H_2O}^{0.7(2)}$ where the water exponent is strongly affected by diffusion along the *a*-direction of the Si atom, (2) intermediate 1000 – 5000 wt. ppm with $\dot{\varepsilon} \propto C_{H_2O}^{0.5(2)}$ and (3) hydrous wadsleyite at more than 5000 wt.ppm H_2O where $\dot{\varepsilon} \propto C_{H_2O}^{3.5(4)}$ is mainly determined by O diffusion along the *c*-direction. Based on Si and O diffusivities in wadsleyite, deformation maps at different water contents and grain sizes were constructed. Additionally, viscosity as a function of temperature for both diffusion and dislocation creep regimes were estimated. According to this study, previous MTZ stress estimations of 1 – 10 MPa (Shimojuku et al., 2009; Vassiliou, Hager, & Raefsky, 1984) together with geophysical observations of its viscosity of $10^{19.5}$ to $10^{21.5}$ Pa·s (Peltier, 1998; Soldati, Boschi, Deschamps, & Giardini, 2009) indicate that the MTZ should be drier then tens wt. ppm H_2O. A hydrous MTZ of 1 wt.% H_2O, however, is proposed at lower stresses from 0.05 to 0.1 MPa, in order to match the observed viscosity range in the MTZ.

Zusammenfassung

Silizium ist das am langsamsten diffundierende Element in Mantelmineralen und ist deshalb limitierend für die plastische Verformung unter hoher Temperatur. (Costa & Chakraborty, 2008; Dohmen, 2002; H. Fei et al., 2012; H. Fei, Wiedenbeck, Yamazaki, & Katsura, 2013; Shimojuku et al., 2009). Wadsleyit ist eines der am häufigsten vorkommenden Mineralen in der oberen Übergangszone des Erdmantels und Hauptbestandteil von subduzierenden Platten unter diesen Bedingungen.

Es gibt noch keine umfassende Untersuchung zum Einfluss des H_2O-Gehaltes auf die Diffusionseigenschaften in Wadsleyit statt (Shimojuku, Kubo, Ohtani, Nakamura, & Okazaki, 2010; Shimojuku et al., 2009; Shimojuku, Kubo, Ohtani, & Yurimoto, 2004). Wie bereits bei Olivin in Silizium-Diffusions Experimenten beobachtet (H. Fei et al., 2012), hat Wasser eine weniger starke Auswirkung auf die rheologischen Eigenschaften als bisher in Deformationsexperimenten angenommen wurde (G. Hirth & Kohlstedt, 2003). Möglicherweise verhalt sich Wadsleyit anders aufgrund der unterschiedlichen Struktur und Defektchemie. Desweiteren zeigten bisherige Experimente, dass Wadsleyit eine signifikantere Menge an Wasser aufnehmen kann (1 – 3 wt.%) (Jacobsen, Demouchy, Frost, Ballaran, & Kung, 2005; Kohlstedt, Keppler, & Rubie, 1996) im Vergleich zu Olivin (Bali, Bolfan-Casanova, & Koga, 2008; Smyth & Jacobsen, 2006).

Bislang gibt es noch keine Untersuchung zur Anisotropie von Silizium und Eigendiffusion in Wadsleyite. Dessen orthorhombische Struktur wirft die Frage auf, ob auch die Diffusionsrate anisotrop ist (Holl, Smyth, Jacobsen, & Frost, 2008).

In diesem Projekt lege ich das Hauptaugenmerk auf das Messen der Volumendiffusionskoeffizienten von Silizium und Sauerstoff in Mg_2SiO_4 Wadsleyit-Einkristallen als Funktion von Temperatur und Wassergehalt.

Außerdem untersuche ich die Rheologie der oberen Mantelschicht basierend auf dem Diffusionsvermögen von dieser Elemente.

Die Aktivierungsenthalpie der Volumendiffusion von Silizium ist von $\Delta H_{Si}^{V} = 150(80)$ bis $\Delta H_{Si}^{V} = 220(80)$ kJ/mol, mit Durchschnittlich $\Delta H_{Si}^{V} = 170(90)$ kJ/mol. Diese Aktivierungsenthalpie ist lediglich die Hälfte, der (Shimojuku et al., 2010) 342(143) kJ/mol für polykristalline Proben. Eine mögliche Erklärung für diese Unstimmigkeit mag die unterschiedliche Größenordnung der Differenz im Wassergehalt der Proben zwischen dieser Studie und (Shimojuku et al., 2010) sein.

Die vorliegende Studie zeigt, dass Si dass sich am langsamsten diffundierende Atom entlang eines geothermischen Gradienten in Wadsleyit mit einem Wassergehalt von weniger als 1500 wt. ppm ist. Die Si Diffusionsrate hängt stark vom Wassergehalt ab und ist anisotrop. Die Wasserabhängigkeit der Si Volumen Eigendiffusion entlang a-Richtung ist $D_{Si}^{V}(100) \propto C_{H_2O}^{0.6}$, b-Richtung: $D_{Si}^{V}(010) \propto C_{H_2O}^{1.9(2)}$, and c-Richtung: $D_{Si}^{V}(001) \propto C_{H_2O}^{5.2(5)}$. Die Wassergehaltsexponenten die in dieser Studie von b- und c- Richtungen stammen, sind signifikant unterschiedlich zu denen von $r = 0.6$, wie sie von (Shimojuku et al., 2010) für polykristallinen Proben bestimmt wurden. Die starke Abhängigkeit vom Wassergehalt legt nahe, dass nicht nur Mg-Plätze durch Protonen substituiert werden (Smyth, 1987), sondern auch Si-Plätze. Si Diffusion in Wadsleyit findet mittels eines Leerstellenmechanismus statt. Ferner suggerieren die Wasserexponenten, dass Si- Plätze und O-Plätze assoziiert sind, vorausgesetzt, dass O-Leerstellen Korridore für Si-Migration erzeugen. Starke Wasserabhängigkeit in c-Richtung legt nahe, dass Si durch Mg Leerstellen in M3 Oktaeder migriert.

Die so erhaltene Aktivierungsenthalpie der Volumendiffusion von O reicht von $\Delta H_{O}^{V} = 160(60)$ kJ/mol bis $\Delta H_{Si}^{V} = 180(40)$ kJ/mol, welche sich als kleiner als die im von (Shimojuku et al., 2009) Fe-enthaltenden Wadsleyite herausstellt. Jedoch wurde die Auswirkung der Sauerstoff-Flüchtigkeit auf die Diffusionsrate in Wadsleyite bislang noch nicht untersucht.

Die O Diffusion in Mg_2SiO_4 Wadsleyite ist wie in dieser Studie beschrieben stark anisotrop und Wasserabhängig in b- und c-Richtung. Die Wasserabhängigkeit von O Volumen-Eigendiffusion entlang der Kristallographischen Hauptrichtungen ist $D_{\mathrm{O}}^{\mathrm{V}}(100) \propto \mathrm{C}_{\mathrm{H_2O}}^{0}$, $D_{\mathrm{O}}^{\mathrm{V}}(010) \propto \mathrm{C}_{\mathrm{H_2O}}^{0.5(2)}$, $D_{\mathrm{O}}^{\mathrm{V}}(001) \propto \mathrm{C}_{\mathrm{H_2O}}^{3.5(4)}$. Ab einem Wassergehalt von mehr als 1500 wt. ppm, ist die O Diffusionsrate die langsamste in Mg_2SiO_4 Wadsleyit über den gesamten Temperaturbereich im MTZ. O-Diffusion in Wadsleyit findet mittels eines Leerstellenmechanismus statt. Die starke Wasserabhängigkeit in c-Richtung impliziert, dass O, wie Si, durch Mg-Platzleerstellen durch M3 Oktaeder migriert.

Die erhaltenen Verformungsraten für Mg_2SiO_4 Wadsleyite weisen drei Regionen mit unterschiedlichen Wasserexponenten auf: (1) Trockener Wadsleyit mit weniger als 1000 wt. ppm H_2O mit $\dot{\varepsilon} \propto \mathrm{C}_{\mathrm{H_2O}}^{0.7(2)}$, in der der Wasser Exponent stark von der Diffusion von Si entlang der a-Richtung beeinflusst wird, (2) dazwischen liegende 1000-5000 wt. ppm mit $\dot{\varepsilon} \propto \mathrm{C}_{\mathrm{H_2O}}^{0.5(2)}$ und (3) wasserreicher Wadsleyite mit mehr als 5000 wt. ppm H_2O mit $\dot{\varepsilon} \propto \mathrm{C}_{\mathrm{H_2O}}^{3.5(4)}$, der hauptsächlich durch die Diffusion von O entlang der c-Richtung bestimmt ist. Basierend auf der Diffusion von Si und O in Wadsleyite wurden Deformationskarten für unterschiedliche Wasseranteile und Korngrößen erstellt. Zusätzlich ist die Viskosität als eine Funktion der Temperatur sowohl bei Diffusions-, als auch bei Deformationskriechen bestimmt worden. Dieser Studie nach sollten bisherige Stressschätzungen in der MTZ mit 1-10 MPa (Shimojuku et al., 2009; Vassiliou, Hager, & Raefsky, 1984) in Verbindung mit geophysikalisch beobachteten Viskositäten von $10^{19.5}$ bis $10^{21.5}$ Pa·s (Peltier, 1998; Soldati, Boschi, Deschamps, & Giardini, 2009) ergeben dass die MTZ mit zehn wt. ppm trocken ist. Einer wasserreiche MTZ mit 1 wt.% H_2O sollte, jedoch, eine niedriger in Stressreichweite von 0.05 bis 0.1 MPa aufweisen um den beobachteten Viskositätsbereich in der MTZ zu erhalten.

1. Introduction to diffusion in minerals

1.1. General definition of diffusion

Diffusion is a process of particles spreading in material through random motion. The concept of diffusion came from physics of heat transfer, molecular diffusion and Brownian motion. Concretely, *atomic diffusion* is a process whereby the thermally activated random movement of atoms results in the net transport of atoms driven by a concentration gradient (from high concentration regions to low concentration regions) (**Fig.1.1**). As mentioned in the next, diffusion within a crystal lattice is only possible with the existence of lattice *point defects*, which is critical difference from diffusion in liquids and gases.

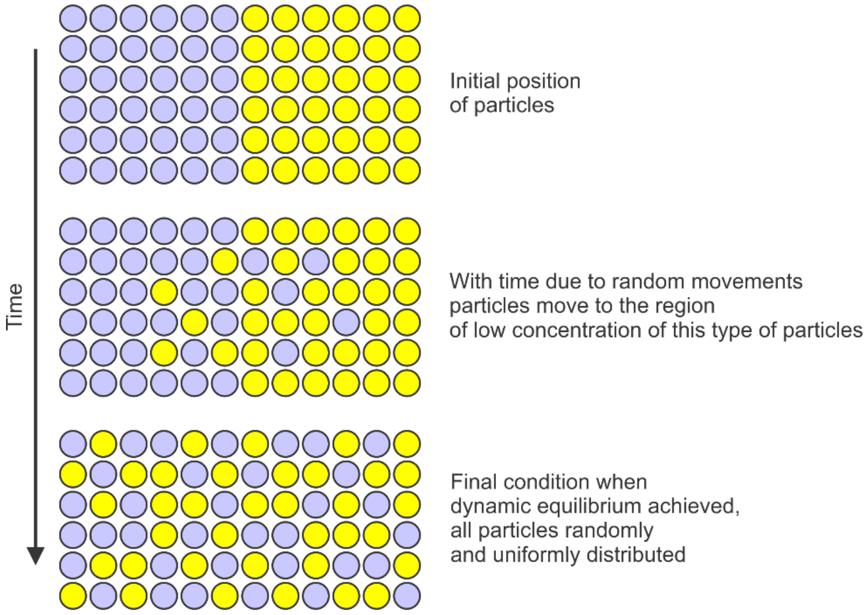

Fig. 1.1. Example of a diffusion process due to a concentration gradient. Colors of spheres indicate types of atoms.

1.2. Point defects and defect notation

The lattice of a real crystal is always imperfect since a site in the crystal lattice can have an irregular structural element so-called point defect. There are three possible point defects listed below (**Fig. 1.2**). An unoccupied regular lattice site is referred to as *vacancy*, an introduced atom (or ion) into the unoccupied space between regular lattice site is an *interstitial* atom (or ion), a regular lattice site occupied by a foreign particle is called a *substitutional* point defect.

Based on their origins, defects can be also classified as *thermal* (intrinsic) – formed by thermal activation in a closed system (e.g. vacancies, interstitial atoms), and *chemical* (extrinsic), which is formed as a result of interaction with the environment that is only in open systems (e.g. impurity atoms).

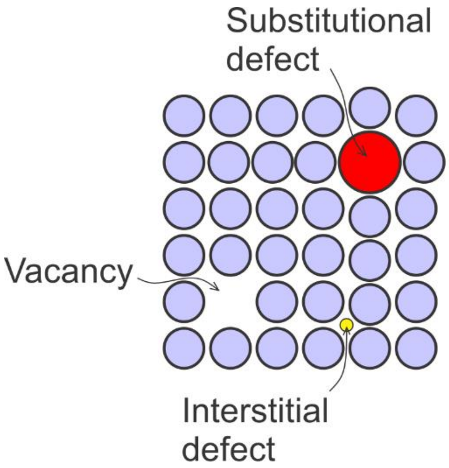

Fig. 1.2. Three kinds of point defects in crystalline solids.

Defects represent regions with an increase of energy in the crystal. Thus, the total Gibbs energy of a crystal can be presented as a deviation from the energy of an ideal crystal:

$$G(P,T) = G^0(P,T) + n \cdot G_{\mathrm{f}} - T \cdot S_{conf} \tag{1.1}$$

where $G^0(P,T)$ is the Gibbs free energy of an ideal crystal, n is the number of defects in the crystal, G_{f} is the free energy of a defect formation and S_{conf} is the configurational entropy of the crystal which is related to the possible number of configurations of defects distribution in the crystal lattice. The *defect concentration* at thermodynamic equilibrium is found with the free energy minimization and constrains the Boltzmann factor as in the formula:

$$C = \frac{n}{N} = const \cdot \exp\left(-\frac{G_\mathrm{f}}{kT} \right) \tag{1.2}$$

where N as the number of possible lattice sites, n is the number of point defects and k is the Boltzmann constant (Schmalzried, 1995).

The Kröger-Vink notation is a very useful sum of conventions to describe a point defect and its reactions for ionic crystals in terms of its electric charge and lattice position (Kröger & Vink, 1956). Namely, it shows the chemical species of the defects, the site that these defects occupy and their effective charges. The notation follows the scheme: $\mathrm{X_Y^Z}$ with X indicating the atomic species that occupy lattice site Y, and Z denotes the effective charge ($^\bullet$ is for the effective positive charge, $'$ is for the effective negative charge, neutrality is denoted by ×). Thus, for example, $\mathrm{O_i''}$ is an oxygen ion with a double negative charge on an interstitial site, $\mathrm{V_O^{\bullet\bullet}}$ is an oxygen vacancy (or vacancy on the oxygen site) with a double positive charge, e' and $h^\bullet$ are electron and electron hole respectively. Defects that bound to each other via electrostatic attraction or elastically through distortion of the surrounding lattice can group together forming *clustered defects*. For example $[\mathrm{V_{Na}'}, \mathrm{V_{Cl}^\bullet}]^\times$ designates a clustered pair of Na and Cl vacancies. Defect reactions or equations must consider three balances: the material balance (atomic species), the charge balance and the site balance. For example, Frenkel disorder reaction $\mathrm{V_i^\times} + \mathrm{A_A^\times} = \mathrm{A_i^\bullet} + \mathrm{V_A'}$, where an ion A is displaced from its original lattice site to an interstitial site, creating a vacancy at the original site and an interstitial defect.

1.3. Types of diffusion

Based on a prevalence of a certain point defect there are three main diffusion mechanisms (**Fig. 1.3**). During the *vacancy diffusion mechanism* an elementary atom jump is an elementary vacancy step in the opposite direction. Literally, an atom exchanges its position with a vacancy. This mechanism is by far the most general among all diffusion mechanisms. For diffusion of small impurity atoms, the *interstitial diffusion mechanism* occurs when an interstitial impurity atom jumps to another interstitial position. In the case of an interstitial atom moves onto a regular lattice site by substituting the particle that was originally there, the *interstitialcy diffusion mechanism* takes place.

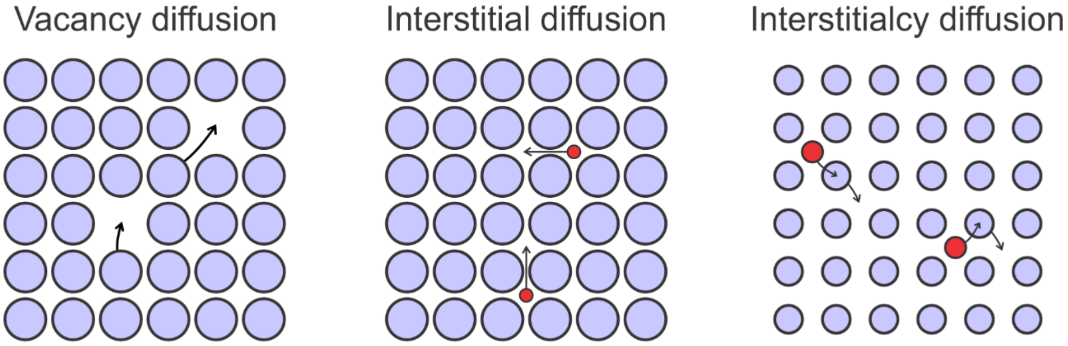

Fig. 1.3. Diffusion mechanisms. Colors and size of spheres indicate types of atoms.

Considering variations of diffusing species and diffusion medium, diffusion can be classified into various types. *Volume diffusion* (or lattice diffusion) emerges in the interior of a single phase such as the diffusion of silicon and oxygen in an olivine single crystal. Depending on the diffusion medium, volume diffusion can be either isotropic or anisotropic. In an *isotropic* medium (glasses or melts), diffusion properties are identical in all directions. Unlike isotropic, an *anisotropic* medium (non-isometric minerals) has dependence of diffusivity on crystallographic directions. *Surface diffusion* occurs when intrinsic particles of the crystal or adsorbed foreign particles move along crystal surfaces, usually at much higher rate than a volume diffusion. In a particular case, *grain-boundary diffusion* emerges along interfaces, including boundaries between two different minerals or grains of the same mineral. *Diffusion along dislocations* (pipe diffusion) also can be taken as another type of diffusion. A highly distorted crystal structure in the interface or dislocations leads to a high concentration of defects, and thereafter to exceeding of the grain-boundary or pipe diffusion compare to the volume diffusion in a crystal.

Self-diffusion, tracer and chemical diffusions are classifications of diffusion type, considering differences in the diffusion species. Diffusion of exactly the same chemical species can be assigned as *self-diffusion*. Such self-diffusion cannot be measured. However, isotopes of a given species have an identical electron distribution and therefore very similar chemical bonding. Their motion through the matrix does not cause any changes in energy and there is no interaction between them. Consequently, when there is a gradient in the concentration of one isotope and no chemical or electrical potential gradient, diffusion of isotopes can be assigned as self-diffusion. Diffusion of a component with a low concentration is a *tracer diffusion* as long as there are no major concentration gradients. *Chemical diffusion* occurs in the presence of concentration or chemical potential gradient. It controls the diffusion of two different chemical species and motion of one affects that of another because of chemical interactions.

1.4. Mathematical description

Analogically to Fourier's law of heat conduction, the phenomenological law describing diffusion was proposed by the German physiologist Adolf Fick in 1855 and is referred to *Fick's first law* (Fick, 1995). It states that the atomic flux is linearly proportional to the concentration gradient:

$$J = -D\frac{\partial C}{\partial x} \tag{1.3}$$

where J is the flux of atoms, C is the concentration of atoms, D is the *diffusion coefficient*. This is a definition of the diffusion coefficient (or *diffusivity*), which connects vectors of the flux and concentration gradient. The dimension of D is m^2/s in SI units, its magnitude indicates the "rate" of diffusion, and if diffusion is mentioned without any special qualification it refers to volume diffusion.

From Fick's first law and the law of mass conservation:

$$\frac{\partial C}{\partial t} = -\frac{\partial J}{\partial x} \tag{1.4}$$

Fick's second law can be deduced:

$$\frac{\partial C}{\partial t} = -D\frac{\partial^2 C}{\partial x^2} \tag{1.5}$$

Together with boundary and initial conditions, this equation determines the concentration C change with time caused by diffusion.

If the diffusion coefficient is concentration dependent, instead of **Eq. 1.5** one must use:

$$\frac{\partial C}{\partial t} = -\frac{\partial}{\partial x}\left(D\frac{\partial C}{\partial x}\right) \tag{1.6}$$

As another approach, it is useful to consider that particles execute a random walk with equal length steps, with the same probability uncorrelated jumps in all directions (so-called *Brownian motion*) (Mehrer, 2007). Then D is a measure of their mobility or the jump frequency. In order to obtain this result, let us consider the individual path R of a one diffusing particle (atom or ion) in a crystal after a sequence of n jumps with a length r. According to **Fig. 1.4** this path is the sum of all jumps:

$$R = \sum_{i=1}^{n} r_i \tag{1.7}$$

And an average over an ensemble of such particles, after squaring **Eq. 1.7** gives:

$$\langle R^2 \rangle = \sum_{i=1}^{n} \langle {r_i}^2 \rangle + 2\sum_{i=1}^{n-1}\sum_{j=i+1}^{n} \langle r_i r_j \rangle \tag{1.8}$$

As far as all jump directions are equally probable and independent of all prior jumps, the term containing the double sum is equal to zero, and for a random, uncorrelated path we obtain:

$$\langle {R^2}_{random} \rangle = \sum_{i=1}^{n} \langle {r_i}^2 \rangle \tag{1.9}$$

Since we consider a motion of particle in a crystal, **Eq. 1.9** can be reduced to:

$$\langle {R^2}_{random} \rangle = \langle n \rangle r^2 \tag{1.9}$$

where the average number of jumps of a particle $\langle n \rangle$ is useful to introduce via the jump frequency (or jump rate) Γ of an atom or ion as follows:

$$\langle n \rangle = \Gamma \cdot Zt \tag{1.10}$$

where Z is denoted to a coordination number.

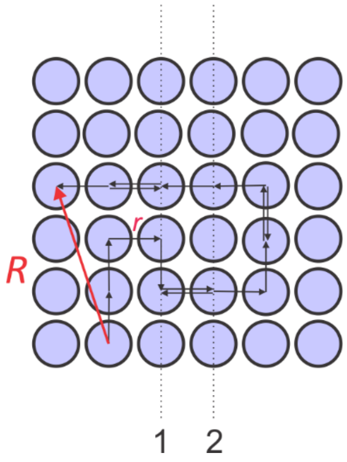

Fig. 1.4. Schematic representation of a jump sequence of a particle in a lattice

Here, jump frequency means the average number of times moving from one site to its neighboring one. According to **Fig. 1.4** flux of particles jumping from plane number 1 to the neighboring plane number 2 is given using jump frequency Γ by:

$$J = \frac{1}{2}\Gamma(N_1 - N_2) \tag{1.11}$$

where N_1 and N_2 are numbers of diffusing particles per unit area in plane 1 and 2, respectively. In terms of concentrations per unit volume C **Eq. 1.11** transforms to:

$$J = \frac{1}{2}\Gamma \cdot r \cdot (C_1 - C_2) \tag{1.12}$$

Since change in concentration is equal to:

$$(C_1 - C_2) = -r\frac{\partial C}{\partial x} \tag{1.13}$$

one can get the following equation:

$$J = -\frac{1}{2}\Gamma \cdot r^2 \frac{\partial C}{\partial x} \tag{1.14}$$

From **Eq. 1.3** and **Eq. 1.14** we obtain:

$$D = \frac{1}{2}\Gamma \cdot r^2 \tag{1.15}$$

Combination of **Eqs. 1.9**, **1.10** and **1.15** gives:

$$\langle R^2{}_{random} \rangle = \Gamma \cdot Zt \cdot r^2 = Z \cdot 2Dt \tag{1.16}$$

As a result, it can be deduced from **Eq. 1.16** that the *diffusion length* x, which is equal to the average path of diffusion particle, is proportional to the square root of diffusion duration:

$$x \propto \sqrt{2Dt} \tag{1.17}$$

In the vacancy diffusion mechanism, however, the probability that an atom will exchange sites with the same vacancy, that it has exchanged places before can be high (so-called “reverse” jump). Thus the probability that the atom will move in any other direction with the help of another vacancy is lower. Consequently, diffusion via this mechanism does no longer fulfill criterion of uncorrelated jumps, and particles do not execute a strictly random walk. In this case more jumps are required to achieve a given distance R. Therefore diffusion coefficient can be expressed as follows (Herring & Bardeen, 1951):

$$D_{non-random} = fD_{random} \tag{1.18}$$

where *correlation factor* f should be applied such as:

$$f = \lim_{n\to\infty} \frac{\langle R^2 \rangle}{\langle R^2{}_{random} \rangle} = 1 + 2 \lim_{n\to\infty} \frac{\sum_{i=1}^{n-1} \sum_{j=i+1}^{n} \langle r_i r_j \rangle}{\sum_{i=1}^{n} \langle r_i{}^2 \rangle} \tag{1.19}$$

1.5. Diffusion anisotropy

The formulas above are correct only in the case of homogeneous isotropic crystals. Strictly speaking, diffusion coefficient is the second-rank tensor, because diffusion in a non-isometric crystal, which unit cell is not a cubic shape, may vary with the transport direction (Y. Zhang, 2010). In such crystals, diffusion coefficients along three crystallographic axes are necessary to describe the diffusion fully. In the crystals with an orthorhombic unit cell, for example, the diffusion coefficient can be written as the following tensor (by choosing the x, y and z axis along the crystallographic directions a, b and c):

$$D = \begin{pmatrix} D_a & 0 & 0 \\ 0 & D_b & 0 \\ 0 & 0 & D_c \end{pmatrix} \tag{1.20}$$

And diffusivity along any other direction is $D = D_a cos^2\theta_a + D_b cos^2\theta_b + D_c cos^2\theta_c$, where θ_a, θ_b and θ_c are the angles between the diffusion direction and crystallographic axes a, b and c respectively. For crystals with triclinic, monoclinic and orthorhombic symmetry all three principal diffusivities are different: $D_a \neq D_b \neq D_c$. For uniaxial materials, such as trigonal, tetragonal, and hexagonal crystals: $D_a = D_b \neq D_c$.

1.6. Temperature and pressure dependence of a diffusivity

The fact that D is driven by atomic exchange with point defects suggests that atomic diffusion is a thermally activated process. Hence, one can express temperature dependence of diffusivity by means of the Arrhenius-type formula, and its activation energy ΔE may be decomposed into ΔE_v and ΔE_i, which are the energies of a point-defect formation and an atom – defect exchange, respectively:

$$D = D_0 \cdot \exp\left(-\frac{\Delta E_v + \Delta E_i}{RT}\right) = D_0 \cdot \exp\left(-\frac{\Delta E}{RT}\right) \tag{1.21}$$

In addition, one should note that D has a response on a pressure P change. Change in the free energy of vacancy formation is given by:

$$\Delta G_v = \Delta E + P\Delta V_v - T\Delta S_v \tag{1.22}$$

where ΔV_v is a change in volume by vacancy formation. Then pressure dependence can be formulated by:

$$D = D_0 \cdot \exp\left(-\frac{\Delta G_v}{RT}\right) = D_0 \cdot \exp\left(\frac{\Delta S_v}{RT}\right) \cdot \exp\left(-\frac{\Delta E + P\Delta V_v}{RT}\right) \tag{1.23}$$

2. Earth structure

By studying earthquakes worldwide, seismic wave velocity changes can be recorded. These changes occur when seismic waves pass through the Earth's interior with different properties (e.g., density). If at some depth velocity changes abruptly and waves reflect then this depth is called a seismic discontinuity. Based on observed seismic discontinuities we can subdivide Earth into distinct layers (**Fig. 2.1**). The major layers are the *crust*, the *mantle* and the *core*. The mantle is subdivided into the *upper mantle*, *transition zone* and the *lower mantle*. The core itself has outer and inner cores.

Based on mechanical properties, the Earth’s upper mantle can be divided into the lithospheric mantle and asthenosphere. *Lithospheric mantle* is the part of the lithosphere which includes also the Earth’s crust. Lithospheric mantle is uppermost hard and brittle layer of mantle. The thickness of the oceanic lithosphere (oceanic crust and uppermost mantle under it) is ~65-100 km (Forsyth, 1975; Gaherty, Kato, & Jordan, 1999). For the continental lithosphere, Gung, Panning, & Romanowicz, 2003 suggested a 200-300 km thickness. The *asthenosphere* is the plastic layer of the mantle that underlies the lithosphere.

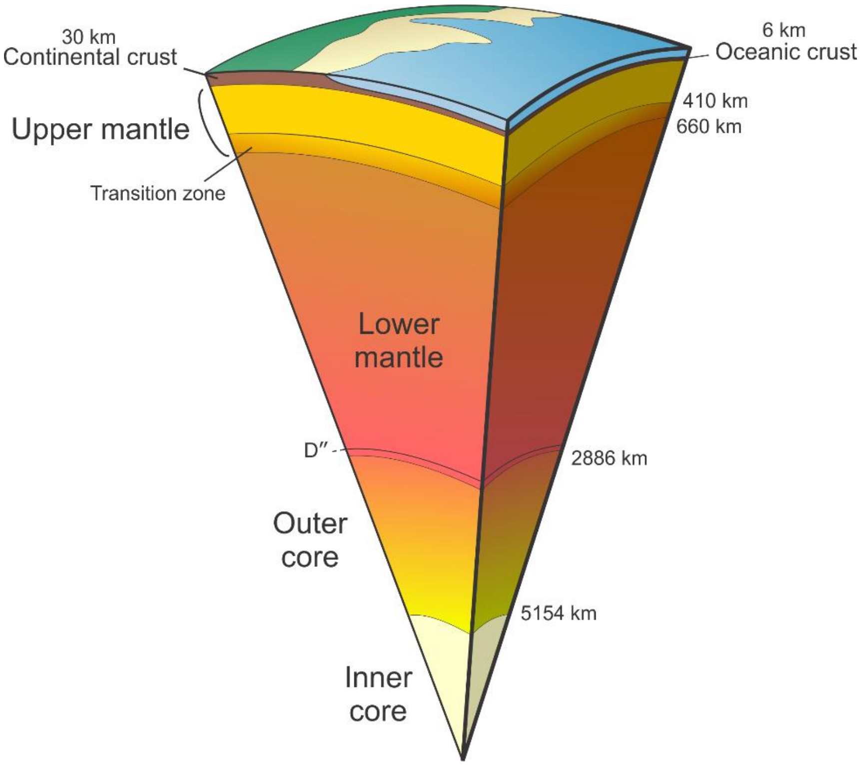

Fig. 2.1. The main components of the Earth interior. Transition zone has a ~525 km discontinuity related to the phase transition from Olivine to Wadsleyite.

2.1. $(Mg,Fe)_2SiO_4$ polymorphs in the earth's mantle

In 1962 Ringwood proposed a mineralogical model of the mantle in which the $(Mg,Fe)_2SiO_4$ polymorphs *olivine*, *wadsleyite* and *ringwoodite* are the main minerals of the Earth’s upper mantle and transition zone (Ringwood, 1962). Namely, at depths to 410 km olivine takes around 60% in volume, and coexists with garnet, ortho- and clinopyroxenes. Its Mg and Fe end members are forsterite (Mg_2SiO_4) and fayalite (Fe_2SiO_4). The seismic discontinuities at 410 and 525 km depths are assigned to the olivine to wadsleyite and wadsleyite to ringwoodite polymorphic transformations. Then, ringwoodite dissociates to bridgmanite and ferropericlase at the 660-km depth where the lower mantle begins.

2.2. Wadsleyite stability field

Wadsleyite (β-$(Mg,Fe)_2SiO_4$) is a high-pressure polymorph of olivine (α-$(Mg,Fe)_2SiO_4$). It has been synthesized for the first time by (Ringwood & Major, 1966) and discovered in a Peace River meteorite (Price, 1983). It will be the major mineral of the upper mantle transition zone between 410 to 525 km depths. The phase relations of all three olivine polymorphs have been experimentally investigated in a variety of studies (Y. Fei & Bertka, 1999; Frost & Dolejš, 2007; Inoue, Ueda, Tanimoto, Yamada, & Irifune, 2010; Katsura & Ito, 1989b; Katsura et al., 2004; Morishima et al., 1994; Ringwood & Major, 1970). **Fig. 2.2** shows a phase diagram of Mg_2SiO_4 at high pressures and temperatures based on Fei & Bertka (1999).

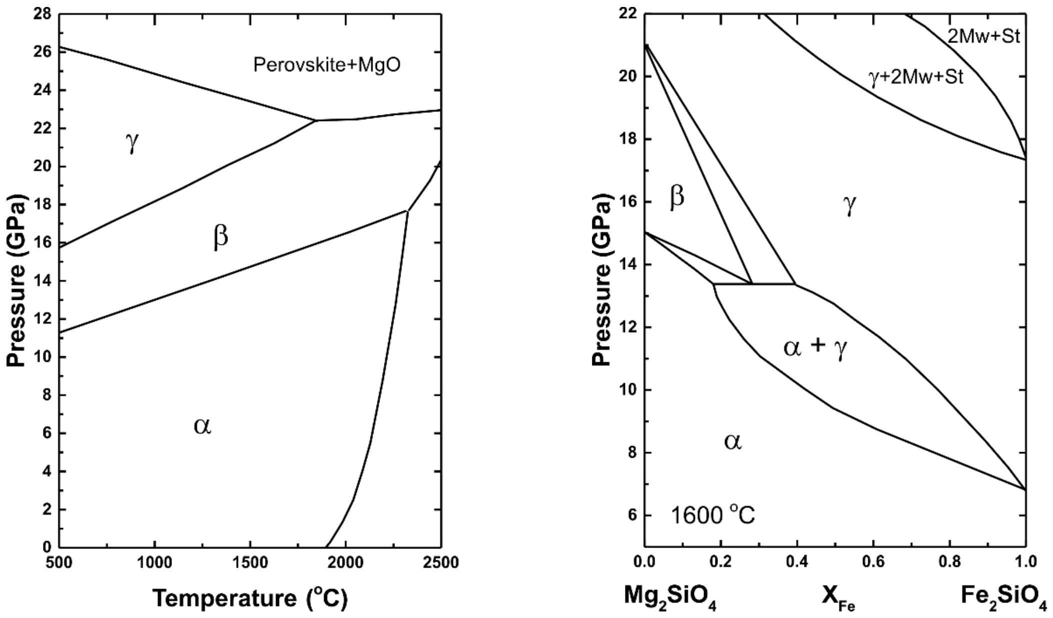

Fig. 2.2. Phase diagrams of the Mg_2SiO_4 (left) and Mg_2SiO_4-Fe_2SiO_4 (right) systems at high pressure and temperature based on (Y. Fei & Bertka, 1999). Mw and St is denoted to (Mg,Fe)O and SiO_2 correspondingly.

The $(Mg,Fe)_2SiO_4$ solid solutions have been investigated at different temperatures (Inoue et al., 2010; Katsura & Ito, 1989a) showing that the wadsleyite stability field does not extend into the Fe-rich region where olivine directly transforms to ringwoodite (γ-$(Mg,Fe)_2SiO_4$) (**Fig. 2.2**). Under hydrous conditions, the pressure of the olivine-wadsleyite transition becomes lower, and the wadsleyite-ringwoodite boundary shifts to higher pressures (Frost & Dolejš, 2007; Inoue et al., 2010). Thus, the incorporation of water expands the wadsleyite stability field.

2.3. $(Mg,Fe)_2SiO_4$ wadsleyite polymorphs structures

Olivine (α-$(Mg,Fe)_2SiO_4$) is a member of the olivine group of orthosilicate minerals with layered structure. Each is presented by isolated tetrahedra of SiO_4 connected to each other via polyhedra occupied by Mg^{2+} and Fe^{2+} divalent cations (**Fig. 2.3 a**). It has the orthorhombic symmetry with the P*bnm* space group. Cell parameters at ambient conditions are a = 4.7535, b = 10.1943, c = 5.9807 Å with a unit cell volume of V = 289.80 Å^3 (Hazen, 1976).

Ringwoodite (γ-$(Mg,Fe)_2SiO_4$) is the major phase in the mantle transition zone at depths of 525 to 670 km. It crystalizes in the spinel structure with the cubic symmetry and *Fd-3m* space group. The ringwoodite structure is made of two types of layers: one is formed by $(Mg,Fe)O_6$ octahedra and SiO_4 tetrahedra (OT layer), the second is made only by $(Mg,Fe)O_6$ octahedra (O layer). The cell parameter at ambient conditions are a = 8.113 Å^3 with a unit cell volume of V = 534.00 Å^3.

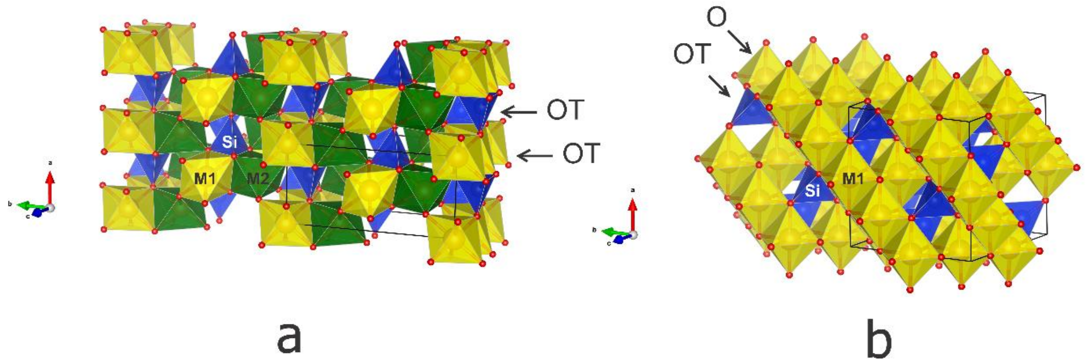

Fig. 2.3. Crystal structures of olivine (**a**) and ringwoodite (**b**). The unit cells are marked by the black frames. The SiO_4 tetrahedra (T) are shown in blue. The MgO_6 octahedra (O) are colored as yellow (M1) and green (M2). The O atoms are shown in red color.

2.4. Wadsleyite structure

Wadsleyite belongs to the spinelloid group of minerals because of its spinel-like structure with three octahedral (M1, M2 and M3) sites, occupied by Mg^{2+} and Fe^{2+} divalent cations, and one tetrahedral site occupied by Si, where oxygen anions form cubic-close-packed arrays (**Fig. 2.4**). The structure can be considered to consist of two kinds of layers: one is formed by $(Mg,Fe)O_6$ octahedra and SiO_4 tetrahedra (OT layer), and the other is formed only by $(Mg,Fe)O_6$ octahedra (O layer).

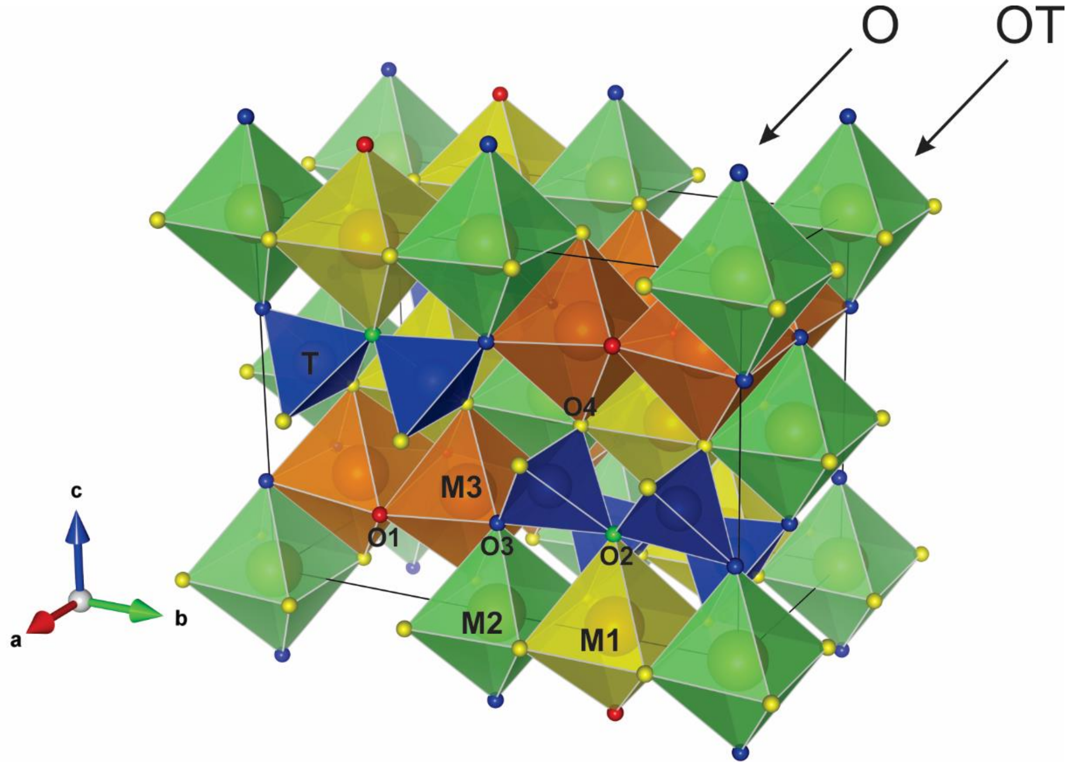

Fig. 2.4. Iron-free wadsleyite crystal structure. The unit cell is marked as a black frame. Silicon-oxygen tetrahedra (T) are shown in blue. MgO_6 octahedra (M1, M2, M3) and oxygen atoms (O1, O2, O3, O4) are shown in colors corresponding to their positions in the crystal structure.

The O anions in the O2 sites connect two SiO_4 octahedra to form Si_2O_7 dimers, whereas the O anions in the O1 sites are not bonded to Si. Non-Si-bonded O anions have a potential to be protonated to incorporate significant amounts of water. Anhydrous wadsleyite has an orthorhombic symmetry with the *Imma* space group. Its unit cell parameters of the Mg end member are $a =$

$5.7008(5), b = 11.4407(12), c = 8.2582(7)$ Å with a cell volume $V = 538.61$ Å^3 (Holl et al., 2008) under ambient conditions. However, there is a report that very hydrated iron-bearing wadsleyite has the monoclinic symmetry with the $I2/a$ space group and a ß angle of 90.4° (Smyth J. Kawamoto, 1997). This distortion was also reported for iron-free wadsleyite (Holl et al., 2008; Kudoh & Inoue, 1999), and modelled by (Ye, Smyth, & Frost, 2011).

2.5. Defects in wadsleyite

Based on the structural elements in wadsleyite, which are Me (Mg or Fe metal ions), Si and O, the major species and defects can be presented as follows: $\mathrm{Me}_{\mathrm{Me}}^{\times}$, $\mathrm{Si}_{\mathrm{Si}}^{\times}$, $\mathrm{O}_{\mathrm{O}}^{\times}$, $\mathrm{V}_{\mathrm{Me}}^{\prime\prime}$, $\mathrm{V}_{\mathrm{Si}}^{\prime\prime\prime\prime}$, $\mathrm{V}_{\mathrm{O}}^{\bullet\bullet}$ and $\mathrm{Me}_{\mathrm{i}}^{\bullet\bullet}$, $\mathrm{Si}_{\mathrm{i}}^{\bullet\bullet\bullet\bullet}$, $\mathrm{O}_{\mathrm{i}}^{\prime\prime}$.

Additionally dissolved water in wadsleyite creates point defects related to hydrogen in the crystal structure. Like in other nominally anhydrous minerals (and wadsleyite is one of them) following the charge balance requirements there are several possible types of hydrogen incorporation in wadsleyite (Karato, 2008):

- Molecular water at an interstitial site:

$$\mathrm{H_2O(fluid)} \leftrightarrow \mathrm{(H_2O)_i} \tag{2.1}$$

- One or two protons at Me-site vacancies:

$$\mathrm{H_2O(fluid)} + \mathrm{Me}_{\mathrm{Me}}^{\times} \leftrightarrow \mathrm{(2H)}_{\mathrm{Me}}^{\times} + \mathrm{MeO} \tag{2.2}$$

$$\mathrm{H_2O(fluid)} + \mathrm{Me}_{\mathrm{Me}}^{\times} \leftrightarrow \mathrm{H}_{\mathrm{Me}}^{\prime} + \mathrm{(OH)}_{\mathrm{O}}^{\bullet} + \mathrm{MeO} \tag{2.3}$$

- Protons at Si-site vacancies and oxygen at O-site:

$$\mathrm{2H_2O(fluid)} + \mathrm{Si}_{\mathrm{Si}}^{\times} \leftrightarrow \mathrm{(4H)}_{\mathrm{Si}}^{\times} + \mathrm{SiO_2} \tag{2.4}$$

$$\mathrm{(OH)}_{\mathrm{O}}^{\bullet} + \mathrm{V}_{\mathrm{Si}}^{\times} \leftrightarrow \mathrm{H}_{\mathrm{Si}}^{\prime\prime\prime} + \mathrm{SiO_2} \tag{2.5}$$

$$2\mathrm{(OH)}_{\mathrm{O}}^{\bullet} + \mathrm{V}_{\mathrm{Si}}^{\times} \leftrightarrow \mathrm{(2H)}_{\mathrm{Si}}^{\prime\prime} + \mathrm{SiO_2} \tag{2.6}$$

$$3\mathrm{(OH)}_{\mathrm{O}}^{\bullet} + \mathrm{V}_{\mathrm{Si}}^{\times} \leftrightarrow \mathrm{(3H)}_{\mathrm{Si}}^{\prime} + \mathrm{SiO_2} \tag{2.7}$$

$$4\mathrm{(OH)}_{\mathrm{O}}^{\bullet} + \mathrm{V}_{\mathrm{Si}}^{\times} \leftrightarrow \mathrm{(4H)}_{\mathrm{Si}}^{\times} + \mathrm{SiO_2} \tag{2.8}$$

- Silicon atom at interstitial position:

$$\mathrm{Si}_{\mathrm{Si}}^{\times} \leftrightarrow \mathrm{V}_{\mathrm{Si}}^{''''} + \mathrm{Si}_{\mathrm{i}}^{\bullet\bullet\bullet\bullet} \tag{2.9}$$

- Two protons at a regular O-site and an interstitial oxygen:

$$\mathrm{H_2O(fluid)} \;+\; 2\mathrm{O}_{\mathrm{O}}^{\times} \leftrightarrow (2\mathrm{OH})_{\mathrm{O}}^{\bullet} + \mathrm{O}_{\mathrm{i}}^{''} \tag{2.10}$$

- Two protons at an interstitial oxygen:

$$\mathrm{H_2O(fluid)} \;+\; \mathrm{O}_{\mathrm{i}}^{''} + \mathrm{V}_{\mathrm{O}}^{\bullet\bullet} \leftrightarrow (2\mathrm{OH})_{\mathrm{i}}^{'} + \mathrm{V}_{\mathrm{O}}^{\bullet\bullet} \tag{2.11}$$

According to Eq. 2.3, 2.5 – 2.7 it is also possible for wadsleyite to have defects that are partially hydrogen-occupied vacancies such as if only one proton goes to the Me-site vacancy or if less than four protons go to the Si-site vacancy. Using equations for reactions 2.1 – 2.11 and different charge neutrality conditions we can evaluate values of the water fugacity exponents (**Table 2.1**) at which the concentration of each of these defects depends on water content (detailed derivations are presented in (Kohlstedt, 2006)).

Table 2.1. *Water content exponents for defect concentrations in wadsleyite at different charge neutrality conditions, expressed by* $[\boldsymbol{x}] \propto \boldsymbol{C}^{\boldsymbol{r}}_{\mathbf{H_2O}}$.

Charge neutrality	**Defects in wadsleyite**						
	$\mathrm{Mg}_{\mathrm{Mg}}^{\bullet}$	$\mathrm{V}_{\mathrm{Mg}}^{''}$	$\mathrm{H}_{\mathrm{Mg}}^{'}$	$2\mathrm{H}_{\mathrm{Mg}}^{\times}$	$(\mathrm{OH})_{\mathrm{O}}^{\bullet}$	$\mathrm{V}_{\mathrm{O}}^{\bullet\bullet}$	$\mathbf{O}_{\mathrm{i}}^{''}$
$[(\mathrm{OH})_{\mathrm{O}}^{\bullet}] = [\mathrm{V}_{\mathrm{Mg}}^{''}]$	-1/6	1/3	2/3	1	1/3	-1/3	1/3
$[(\mathrm{OH})_{\mathrm{O}}^{\bullet}] = [\mathrm{H}_{\mathrm{Mg}}^{'}]$	0	0	1/2	1	1/2	0	0
$[\mathrm{Mg}_{\mathrm{Mg}}^{\bullet}] = [\mathrm{V}_{\mathrm{Mg}}^{''}]$	0	0	1/2	1	1/2	0	0
$[\mathrm{Mg}_{\mathrm{Mg}}^{\bullet}] = [\mathrm{H}_{\mathrm{Mg}}^{'}]$	1/4	-1/2	1/4	1	3/4	1/2	-1/2
	Defects in wadsleyite						
	$\mathrm{V}_{\mathrm{Si}}^{''''}$	$\mathrm{Si}_{\mathrm{i}}^{\bullet\bullet\bullet\bullet}$	$\mathrm{H}_{\mathrm{Si}}^{'''}$	$2\mathrm{H}_{\mathrm{Si}}^{''}$	$3\mathrm{H}_{\mathrm{Si}}^{'}$	$4\mathrm{H}_{\mathrm{Si}}^{\times}$	
$[(\mathrm{OH})_{\mathrm{O}}^{\bullet}] = [\mathrm{V}_{\mathrm{Mg}}^{''}]$	2/3	-2/3	1	4/3	5/3	2	
$[(\mathrm{OH})_{\mathrm{O}}^{\bullet}] = [\mathrm{H}_{\mathrm{Mg}}^{'}]$	0	0	1/2	1	3/2	2	
$[\mathrm{Mg}_{\mathrm{Mg}}^{\bullet}] = [\mathrm{V}_{\mathrm{Mg}}^{''}]$	0	0	1/2	1	3/2	2	
$[\mathrm{Mg}_{\mathrm{Mg}}^{\bullet}] = [\mathrm{H}_{\mathrm{Mg}}^{'}]$	-1	1/3	-1/4	1/2	5/4	2	

So far it is still not clearly known what hydrogen-related defects are dominant in wadsleyite. Predictions (Smyth, 1987) and infrared spectroscopy studies (Deon et al., 2010; Jacobsen et al., 2005) suggest that water is mostly incorporated as $(\mathrm{OH})^{\bullet}_{\mathrm{O}}$ at the oxygen positions of M3 octahedron that are not-bonded to Si. However, the observed water dependency of Si-self diffusion in polycrystalline wadsleyite (Shimojuku et al., 2010) implies the existence of a considerable amount of Si-related defects created due to water incorporation. Changes in the defect chemistry and their concentration at different fugacities were studied by (Nishihara, Shinmei, & Karato, 2008) using infrared spectroscopy. Concentration of OH was found to be both $f_{\mathrm{H_2O}}$ and $f_{\mathrm{O_2}}$ sensitive. Assuming that with water incorporation hydrogen fully occupies the vacancy at Me-site, then $[(2\mathrm{H})^{\times}_{\mathrm{Me}}] \propto {f_{\mathrm{H_2O}}}^{1/2} {f_{\mathrm{O_2}}}^{1/12}$ under the charge neutrality condition of $[\mathrm{Fe}'_{\mathrm{Me}}] = 2[\mathrm{V}''_{\mathrm{Me}}]$.

2.6. Wadsleyite crystals synthesis

Many studies and types of experiments require single crystals of sufficient size and quality. Atomic volume diffusion experiments are not an exception and impose some restrictions on crystal size. Minimal size of wadsleyite crystals when volume diffusion experiments can be performed is 0.4 - 0.5 mm.

Previously, large crystals of wadsleyite were obtained by solid-state recrystallization using a Kawai-type multi-anvil apparatus (Kawazoe, Buchen, & Marquardt, 2015; Sawamoto, 1986) and by a method of recrystallization in carbonate solutions under a temperature gradient (Shatskiy et al., 2009).

In the experiments of (Shatskiy et al., 2009) a starting material of forsterite powder was used with different carbonate solutions at 15.5 – 16.5 GPa and 1670 – 1970 K. Resulting wadsleyite crystals exceeded 1 mm and coexisted with quenched melt. The crystals contained numerous melt inclusions and cracks, and only some portion of crystals of 0.7 mm in size were transparent and free from inclusions.

Solid-state recrystallization experiments of (Sawamoto, 1986) used a mixture of forsterite and fayalite as a starting material and resulted in Fe-bearing wadsleyite crystals of 0.5 mm size with a variation of $\mathrm{Mg/(Mg + Fe)}$ in different crystals. Pressure and temperature conditions corresponded to near wadsleyite-ringwoodite phase boundary (19 – 21.5 GPa, 1940 – 2670 K). Successful synthesis of ~1 mm Fe-bearing wadsleyite crystals using San-Carlos olivine as a starting material at conditions of 16 GPa and 1870 K was performed by (Kawazoe, Buchen, and Marquardt 2015). Resulting crystals had no inclusions and were chemically homogeneous.

3. Rheology

Rheology (from the Greek *rheos*, meaning “stream” or “flow”) denotes the deformation and flow of matter. Rheological properties of mantle materials influence dynamics in the Earth’s interior as well as the dynamics of lithospheric plates (Karato & Wu, 1993), and mantle flow is related to the origin of volcanic and seismic activities on the Earth. Therefore, understanding mantle rheology is important (Karato, 2010). However, the determination of rheological properties is always challenging, because deformation involves many types of microscopic mechanisms with different pressure and temperature dependencies.

3.1. Deformation

Deformation refers to a change in the shape of a body. It can be classified into several general types. Instantaneous and recoverable deformation is called *elastic* deformation. Thereafter, recoverable but time dependent deformation is called *anelastic* deformation. Non-recoverable deformation is called viscous or *plastic deformation*.

Two most important terms for deformation are stress, and strain. *Stress* is the force per unit area acting on a given plane along a certain direction. Stress is a second rank tensor. It can be presented as a sum of diagonal tensor of *isotropic stresses* (or hydrostatic stresses) and non-diagonal tensor of *deviatoric stresses*:

$$\sigma = \begin{bmatrix} \sigma_{11} & \sigma_{12} & \sigma_{13} \\ \sigma_{21} & \sigma_{22} & \sigma_{23} \\ \sigma_{31} & \sigma_{32} & \sigma_{33} \end{bmatrix} = \begin{bmatrix} \sigma_h & 0 & 0 \\ 0 & \sigma_h & 0 \\ 0 & 0 & \sigma_h \end{bmatrix} + \begin{bmatrix} \sigma_{11} - \sigma_h & \sigma_{12} & \sigma_{13} \\ \sigma_{21} & \sigma_{22} - \sigma_h & \sigma_{23} \\ \sigma_{31} & \sigma_{32} & \sigma_{33} - \sigma_h \end{bmatrix} \tag{3.1}$$

where

$$\sigma_h = \frac{\sigma_{11} + \sigma_{22} + \sigma_{33}}{3} \tag{3.2}$$

Isotropic stress tensor components do not cause plastic flow, but volume change. Deviatoric stresses tensor, in turn, cause distortion and plastic deformation (Karato, 2008).

Deformation is characterized by a displacement gradient, d_{ij}:

$$d_{ij} = \frac{\partial u_i}{\partial x_j} = \frac{1}{2}\left(\frac{\partial u_i}{\partial x_j} + \frac{\partial u_j}{\partial x_i}\right) + \frac{1}{2}\left(\frac{\partial u_i}{\partial x_j} - \frac{\partial u_j}{\partial x_i}\right) \tag{3.3}$$

where u_i is the displacement and x_j is the spatial coordinate.

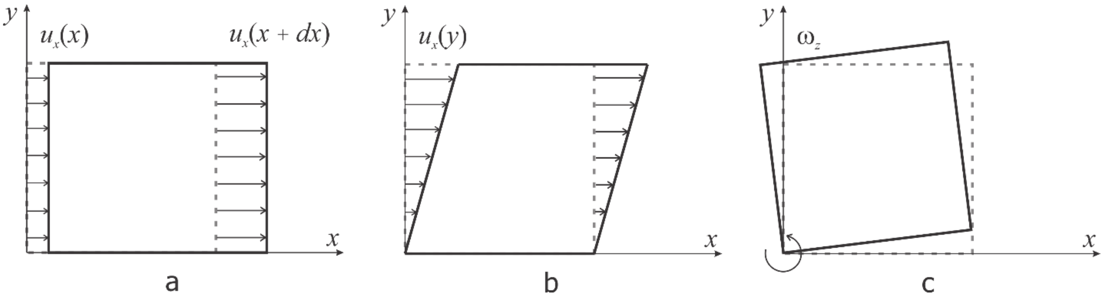

Fig. 3.1. Schematic of types of simple deformations: (**a**) normal strain, (**b**) simple shear, (**c**) rotation. Dotted line corresponds to the initial shape.

The first term in the right part of the **Eq. 3.3** is a strain tensor:

$$\varepsilon_{ij} = \frac{1}{2}\left(\frac{\partial u_i}{\partial x_j} + \frac{\partial u_j}{\partial x_i}\right) \tag{3.4}$$

The diagonal components of ε_{ij} tensor are *normal strain* components and represents the change in length (**Fig. 3.1 a**). Non-diagonal strain tensor elements correspond to *shear strain* (**Fig. 3.1 b**).

The second component on the right side of **Eq. 3.3** is an antisymmetric tensor:

$$\omega_{ij} = \frac{1}{2}\left(\frac{\partial u_i}{\partial x_j} - \frac{\partial u_j}{\partial x_i}\right) \qquad (3.5)$$

This tensor indicates the rotation of a body with the axis normal to the ith and jth directions (**Fig. 3.1 c**).

3.2. Deformation experiments

Stress/strain rate relations can be experimentally determined by measuring the sample dimension before and after an experiment where measurable deviatoric stresses are applied.

There is a range of experimental techniques that have been used to generate deviatoric stress in plastic deformation studies. The simplest way is *dead weight loading*, in which load is applied by a mass being placed on top of a sample (Kohlstedt & Goetze, 1974). The stress can be evaluated by measuring a mass of load m and a cross-section area of loading A, thus, $\sigma = mg/A$, where g is a gravity acceleration (Karato, 2008). This method allows a very accurate stresses to be applied, but its use is limited to a low applied pressure range (~ 3 GPa).

A method developed by (Paterson, 1970) uses a load cell placed in a chamber filled with a noble gas to generate high pressure, so called a *gas-medium apparatus*. The resolution of stress measurements is nearly the same as that at room pressure. The magnitude of the applied stress is near that within the Earth's interior and slow strain rates can be achieved. However, a major limitation of this technique is the limited pressure (0.5 GPa) that can be applied in comparison with that in the Earth's mantle.

On the other hand, the Griggs apparatus (Griggs, 1967) was developed from the piston-cylinder apparatus and provides the capability to deform rocks to ~3 GPa (Borch & Green, 1987, 1989). It uses a hydraulic ram to compress a sample surrounded by a soft material, and a second piston is applied onto the sample through the hole at the center of the hydraulic ram to generate a deviatoric stress. Generated pressure is, however, still insufficient to investigate the rheological properties of the Earth's mantle.

In order to conduct deformation experiments above a few GPa, a deformation-DIA (D-DIA) apparatus was designed (Wang, Durham, Getting, & Weidner, 2003). An advantage of this apparatus is the ability to generate pressure up to ~20 GPa (Kawazoe et al., 2010, 2011). Based on the multi-anvil apparatus, the D-DIA uses six tungsten carbide anvils to compress a cubic sample assembly. Deviatoric stress can be applied by moving two anvils forward or backward at a desired rate relatively to the other four. However, available stress and strain rate obtained in this apparatus are at least 2-4 orders of magnitude higher than that in the Earth's interior (Karato, 2010). Misleading results due to the extremely high density of defects caused by very high stresses could lead to unreliable rheological properties of the Earth's materials.

Deviatoric stress can also be generated by squeezing a sample in a multi-anvil apparatus (Karato & Rubie, 1997) or in a diamond anvil cell (DAC) (Mao et al., 2008). In these cases, both stress and strain rate tend to be very high and not well characterized. Moreover, the DAC method has a highly inhomogeneous temperature distribution. The rotational Drickamer apparatus (RDA) can generate a high pressure by using tapered anvils. It has, however, very poor resolution of strain measurement by X-ray stress measurement, and sample temperature cannot be measured using a thermocouple.

3.3. Self-diffusion and rheological properties

Because of the limitations of deformation experiments, an independent way to study mantle rheology is necessary. There are two typical models that describe rock and mineral deformation: diffusion creep and dislocation creep (Coble, 1963; H. J. Frost & Ashby, 1982; Herring, 1950; Weertman et al., 1999). All these models shows a connection of self-diffusion of the slowest atomic species and a plastic deformation in the mantle.

3.3.1. Diffusion creep

After a sufficient time migration of vacancies caused by diffusion of the slowest atomic species in the crystal will lead them to reach its surface, where they disappear. Under differential stresses, vacancies move toward the site where stresses are the greatest (Raj & Ashby, 1971) and atoms move to the side where stresses are the lowest. Such a change in mass distribution produces a change of crystal's shape (**Fig. 3.2**).

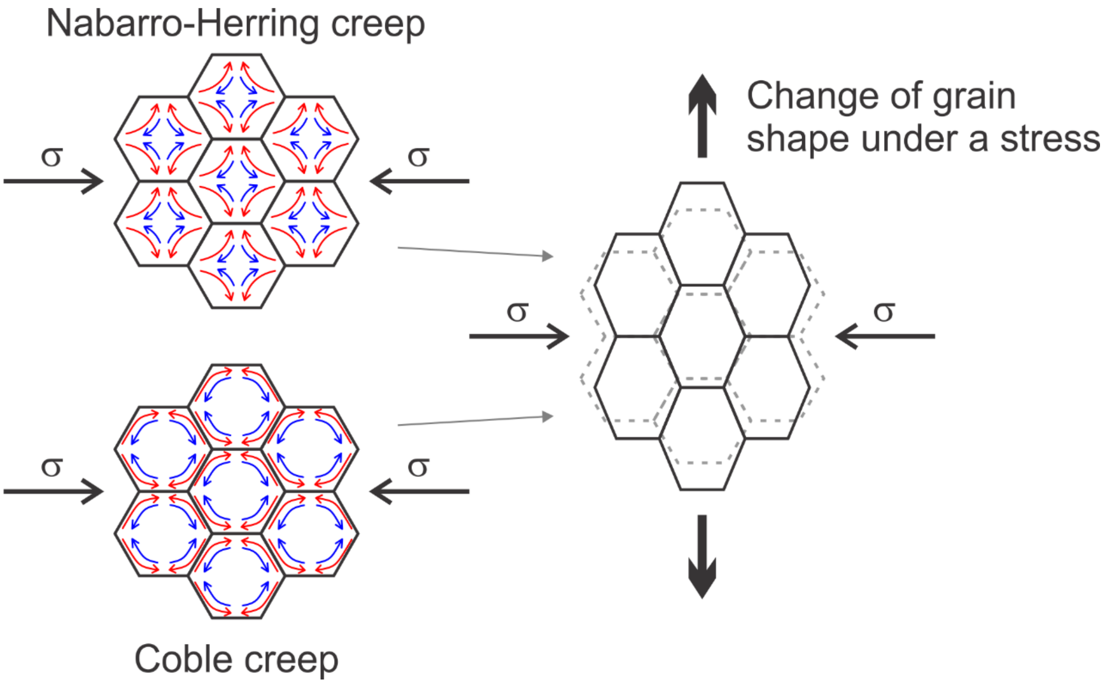

Fig. 3.2. A conceptual drawing showing the process of diffusional creep. Grains are shortened in the horizontal direction from the original size (dotted line) under a stress σ. Red arrows indicate migration of atoms, blue arrows denote to movement of vacancies.

When diffusion of atoms and, thus vacancies too, occurs within a crystal, *Nabarro-Herring creep* takes place. If diffusion occurs on grain boundaries, *Coble creep* takes place.

Nabarro and Herring proposed their model for creep of polycrystalline solids at high-temperature (close to melting temperature T_{melt}) when volume diffusion is dominant (Herring, 1950; Nabarro, 1948). The vacancy concentration in a crystal (or one grain in terms of a polycrystalline material), C_0, can be written as:

$$C_0 = A \cdot exp\left(\frac{-G_f}{RT}\right) \tag{3.6}$$

where G_f is the free energy of vacancy formation, R is the gas constant, and A is a constant. By applying a stress of σ, the vacancy formation energy will be changed by $\pm\sigma\Omega$. Thus, their concentration changes to

$$C_{\text{def}}(\sigma) = C_0 \cdot exp\left(\frac{\pm\sigma\Omega}{RT}\right) \tag{3.7}$$

where σ is the stress, and Ω is the atomic volume. The vacancy movement in the scale of the grain size causes their fluxes. From Fick's law, the flux of vacancies can be written as:

$$J_v = \alpha \cdot D_v \cdot \frac{\partial C_{def}}{\partial x} = \alpha \cdot D_v \cdot C_0 \cdot \frac{\exp(\sigma\Omega/\mathrm{RT}) - \exp\,(-\sigma\Omega/\mathrm{RT})}{d} \tag{3.8}$$

where D_v is the diffusion coefficient of vacancies, d is the grain size, and α is a geometry factor. The low stresses and high temperatures lead to $\sigma\Omega \ll \mathrm{RT}$, and therefore,

$$J_v = \alpha \cdot \frac{2D_v \cdot C_0}{d} \cdot \frac{\sigma\Omega}{RT} \tag{3.9}$$

Mass transport involves both vacancies and atoms, so these formulas must be use for atoms as well but with an opposite sign:

$$J_a = -\alpha \cdot \frac{2D_a \cdot C_0}{d} \cdot \frac{\sigma\Omega}{RT} \tag{3.10}$$

Since diffusion of atoms is the hopping from its normal site to its neighbor vacancy site, we have $J_v = J_a = J$. Then the volume that arrives on the crystal surface per time during migration of vacancies through the area A:

$$\frac{\partial V}{\partial t} = J \cdot A \tag{3.11}$$

Now we can derive how a crystal changes its shape with time due to fluxes given by **Eqs. (3.8)** and **(3.9)**. If the grain facet is d^2, then Eq. 3.4 gives the strain rate as:

$$\dot{\varepsilon} = \frac{\partial \varepsilon}{\partial t} = \frac{1}{d} \cdot \frac{\partial d}{\partial t} = \frac{1}{d^3} \cdot \frac{\partial d \cdot d^2}{\partial t} = \frac{1}{d^3} \cdot \frac{\partial V}{\partial t} \tag{3.12}$$

$$\dot{\varepsilon}_{NH} = \frac{1}{d^3} \cdot J \cdot A = \frac{1}{d^3} \cdot J \cdot d^2 \tag{3.13}$$

$$\dot{\varepsilon}_{NH} = \alpha \cdot \frac{2D_v \cdot C_0}{d^2} \cdot \frac{\sigma\Omega}{RT} = \alpha_{NH} \cdot \frac{D_v}{d^2} \cdot \frac{\sigma\Omega}{RT} \tag{3.14}$$

The relationships above lead to inverse proportionality between strain rate and grain size squared, $\dot{\varepsilon}_{NH} \propto 1/d^2$, indicating that smaller grains deform faster.

Coble refined a previous model by including the influence of diffusive mass transport along grain-boundaries (Coble, 1963). In this case, the diffusion coefficient D_v used in the previous model is replaced by

$$D^{\mathrm{eff}} = D_v + \frac{\pi\delta}{d} D_{gb} \tag{3.15}$$

where D_{gb} represents the diffusion coefficient at the grain boundary and δ is the effective grain boundary thickness. By replacing D_v by D^{eff} and changing indices in **Eq. 3.14** we have a strain rate for the Coble creep mechanism:

$$\dot{\varepsilon}_C = \alpha_C \cdot \frac{D^{\mathrm{eff}}}{d^2} \cdot \frac{\sigma\Omega}{RT} \tag{3.16}$$

If the grain boundary diffusion is much faster or grain size is very small, especially at low temperatures ($T \ll T_{\mathrm{melt}}$), then $(\pi\delta/d)D_{gb} \gg D_v$ and we have:

$$\dot{\varepsilon}_C = \alpha \cdot \pi \cdot \frac{\delta D_{gb}}{d^3} \cdot \frac{\sigma\Omega}{RT} \tag{3.17}$$

Like in a previous mechanisms, strain rate is grain size dependent, though its grain size dependency is larger $\dot{\varepsilon}_C \propto 1/d^3$. Therefore, the diffusion creep can be calculated from the volume or grain boundary diffusion of the slowest diffusing species.

3.3.2. Dislocation creep

Plastic deformation caused by motion of dislocations through the crystal lattice is called *dislocation creep* (**Fig. 3.3**).

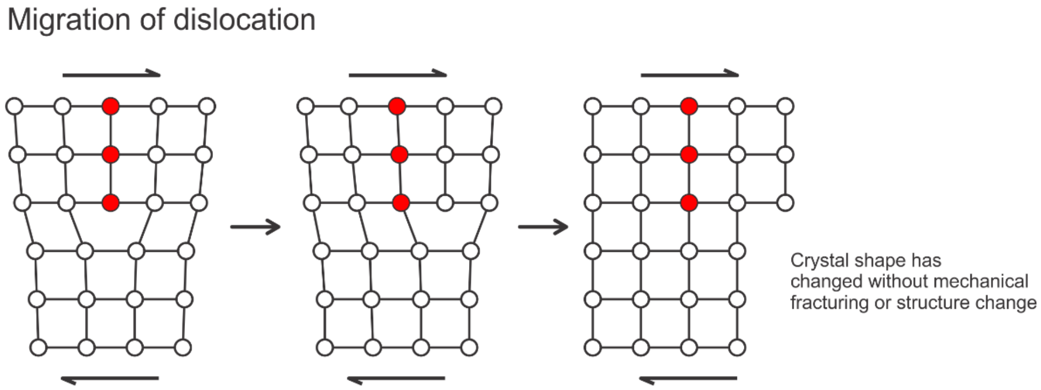

Fig. 3.3. Dislocation creep, controlled by the dislocation migration in the lattice.

The rate of deformation due to dislocation motion is proportional to dislocation density and velocity:

$$\dot{\varepsilon} = b\rho v \tag{3.18}$$

This is the Orowan Equation, where b is a Burgers vector of dislocations, ρ is the dislocation density, and the average dislocation velocity $v = \left(l_g/l_c\right)v_c$ with the glide distance l_g and the climb distance l_c, v_c is the climb velocity (Weertman, 1955). Density can be given in terms of differential stress, σ, and shear modulus, G (Weertman et al., 1999):

$$\rho = \left(\frac{\sigma}{Gb}\right)^2 \tag{3.19}$$

Climb velocity of the dislocation can be given by (J. P. Hirth & Lothe, 1982):

$$v_c = 2\pi \frac{\sigma V_m}{RT} \frac{D}{b} \frac{1}{\ln\left(R_o/r_c\right)} \tag{3.20}$$

where D is the diffusivity of the slowest atomic species, R_o is the average spacing between dislocations, and r_c is the radius of a dislocation core (generally taken to be $r_c \approx b$). By combining **Eqs. (3.18) – (3.20)** we obtain (Weertman et al., 1999):

$$\dot{\varepsilon} = 2\pi \frac{GV_m}{RT} \left(\frac{\sigma}{G}\right)^3 \frac{D}{b^2} \frac{1}{ln(G/\sigma)} \frac{l_g}{l_c} \tag{3.21}$$

Although it is possible to consider other models to describe dislocation creep, according to (Kohlstedt, 2006), however, the Weertman model yields strain rates comparable to the measured creep data in olivine. Assuming that the model is applicable to wadsleyite, we will use it for our further estimation of the strain rate.

3.3.3. Viscosity

When material flows under a given strain rate, stresses proportional to the strain rate are generated. This relation is expressed as the following equation (Karato, 2008):

$$\sigma_{ij} = 2 \sum_{k,l} \eta_{ijkl} \dot{\varepsilon}_{kl} \tag{3.22}$$

Viscosity in **Eq. 3.22** is defined as a fourth-rank tensor η_{ijkl}. In case of isotropic materials the plastic properties are characterized by a single scalar parameter of shear viscosity η. Usually this parameter referred to as simply viscosity. The SI unit of viscosity is the unit of stress multiplied by time, which is Pa·s (kg/m·s).

Materials with linear relationship between stress and strain are under Newtonian viscous behavior where viscosity is a constant (**Fig 3.4 a**) (Batchelor, 2000; Van Der Pluijm & Marshak, 2004). For a non-linear relationship between stress and strain $\dot{\varepsilon} \propto \sigma^n$ ($n > 1$) in materials non-Newtonian term is applied. In that case viscosity is a function of stress and strain (having in mind that it can also be written in terms of tensor):

$$\eta_{\text{eff}} \propto \sigma / \dot{\varepsilon} \tag{3.23}$$

This viscosity is referred to an effective viscosity since it changes with changing stress and strain rate.

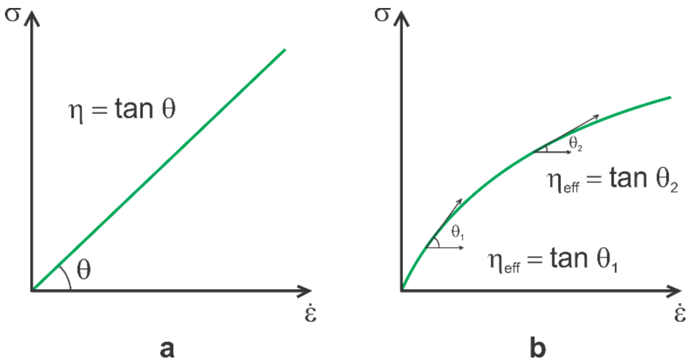

Fig. 3.4. Linear or Newtonian (a) and non-linear or non-Newtonian (b) behaviors. The viscosity is defined by the slope of the stress/strain rate relationship.

In the case of rocks in the Earth's interior, they first elastically respond to applied stresses, then continue to respond in a viscous way. However, if time-accumulated strain due to the viscous response is much larger than the elastic strain, the elastic response can be neglected. Therefore, within the large amount of time specific for geologic processes we can approximate the behavior of the Earth's mantle rocks as a viscous medium. This assumption was first suggested by (Maxwell, 1867).

The diffusion coefficient is related to the viscosity η via the Stokes-Einstein equation. Stokes-Einstein equation was first derived by Einstein in his Ph.D thesis for the diffusion coefficient of a spherical particle with a radius r undergoing Brownian motion in a stationary fluid (Einstein, 1905):

$$D = \frac{kT}{6\pi\eta r} \tag{3.24}$$

By assuming the density, the volume and mass fraction of ions in mantle minerals according to (McKenzie, 1967) from **Eq. 3.24** we have:

$$\eta = 10kT\frac{r^2}{mD} \tag{3.25}$$

where m and r are the mass and radius of the diffusing ion.

In another way viscosity is related to the diffusion via the strain rate. Under assumption that a material behaves in a Newtonian fashion and deforms by both volume and grain-boundary diffusion we can use **Eq. 3.16** and **Eq. 3.23** (Raj & Ashby, 1971):

$$\eta = \alpha \frac{RT \cdot d^2}{\Omega \cdot D_{\mathrm{eff}}} \tag{3.26}$$

3.4. Rheology of wadsleyite

Plastic deformations experiments on presynthesized wadsleyite samples performed at 14–19 GPa and 300–2273 K have made it possible identify through TEM observations the following slip systems (Thurel, Cordier, Frost, & Karato, 2003; Thurel, Douin, & Cordier, 2003): [100](010), [100](001), [100]{011}, [100]{021}, 1/2⟨111⟩{101}, [010](001), [010]{101} and ⟨101⟩(010). Slip system [001](010) was distinguished (Demouchy et al., 2011; Kawazoe et al., 2013) as dominantly activated at 16-18 GPa and 1700 – 1900 K governing the plasticity of wadsleyite. As a result of a stress relaxation test it was reported that water content can change the crystallographic preferred orientation in wadsleyite (Demouchy et al., 2011). In particular, with increasing water content the density of [100] axes parallel to the shear direction decreases, and the density of [001] axes increases. Systems 1/2⟨111⟩{101} and [100](010) were found (Thurel, Douin, et al., 2003) to be the easiest slip systems under 13 GPa and 1600 K. Information on the potential activity of slip systems was also obtained from modeled Peierls stresses in wadsleyite (Metsue, et al., 2010). Calculations showed the easiest one is not the [001](010) but 1/2⟨111⟩{101} and [100](010) is on the second place. The easiest slip systems are shown in **Fig. 3.5**.

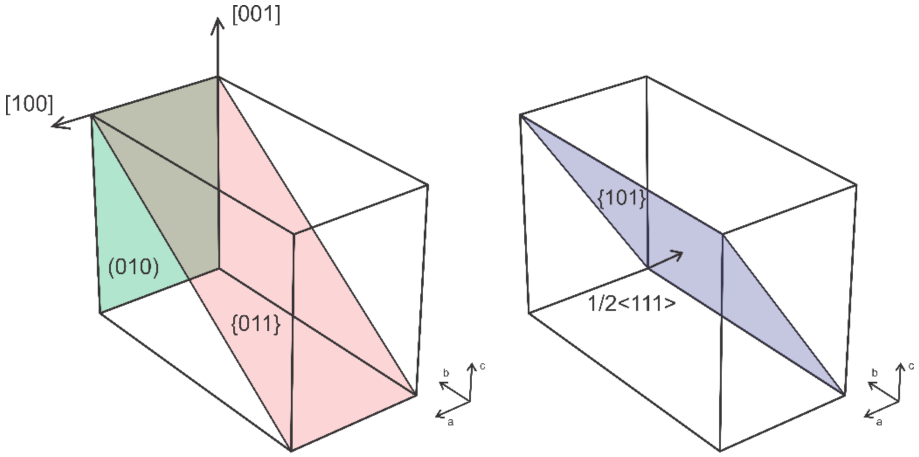

Fig. 3.5. Easy slip systems in wadsleyite at high pressure and temperature.

Resent deformation experiments have enabled the strain rate in wadsleyite to be determined. Creep strength measurements on hydrous wadsleyite were performed with the deformation-DIA apparatus and synchrotron radiation (Kawazoe et al., 2011) and resulted in a power creep relationship:

$$\dot{\varepsilon} = 10^{-11.9} C_{H2O}^{2.7} \sigma^{3.0} \exp\left(-\frac{211\ \mathrm{kJ/mol}}{RT}\right) \qquad (3.4)$$

where C_{H2O} is a water content in wt.ppm (230 – 1100 wt ppm H_2O), σ is a stress. High stresses of 100 – 540 MPa applied during these experiments results in high strain-rates of 10^{-6} – 10^{-3} s^{-1}, however the typical geological strain-rates are 10^{-12} – 10^{-16} s^{-1}. Another problem is that under laboratory conditions all deformation mechanisms could operate, and dominance of one is very sensitive to precise conditions of the experiment. In contrast, under geological conditions these three mechanisms operate independently and the dominant mechanisms of deformation could be identified for a given parameter space.

An alternative approach is based on using seismological observations. Seismic waves passed through the Earth's interior, and carry information on elastic and anelastic properties of the Earth. Wadsleyite produces detectable seismic anisotropy among major minerals in the mantle TZ (Karato, 2008; Mainprice, 2007). The source of anisotropy in the mantle is usually assumed to be the lattice preferred orientation of intrinsically anisotropic wadsleyite under strain in the mantle (Karato, 1998; Kawazoe et al., 2013; Montagner, 1998). Consequently the presence of seismic anisotropy can be taken as evidence for deformation by dislocation creep.

On the other hand, atomic diffusion can control deformation. There are several models describing rheological parameters that are based on the diffusion rate of the slowest atomic species (Coble, 1963; H. J. Frost & Ashby, 1982; Herring, 1950; Weertman et al., 1999). Recent silicon diffusion experiments in polycrystalline wadsleyite (Shimojuku et al., 2010, 2004) suggested grain size and stress of wadsleyite under mantle TZ conditions to be a few mm and 1 – 10 MPa correspondingly. Their grain-size/stress deformation mechanism maps constructed based on $(Mg,Fe)_2SiO_4$ polycrystalline wadsleyite diffusion data confirmed that dislocation creep dominates in the mantle TZ and diffusion mechanism in cold slabs with grain sizes less than 10 – 100 µm. However, these diffusion results were water content independent. It is known that wadsleyite can incorporates significant amounts of water, which can affect its rheological parameters.

Relative viscosity was estimated from postglacial rebound data and gravity data (Peltier, 1998; Soldati et al., 2009) to be $\eta = 10^{19.5}$ Pa·s. Modeling of mantle TZ and subducting slabs allow to estimate their viscosities to be from $\eta = 10^{20}$ - 10^{21} Pa·s and $\eta = 10^{23} - 10^{24}$ Pa·s for a subducting slab in TZ. Dislocation recovery experiments resulted in $\eta \sim 10^{19.5} - 10^{19}$ Pa·s for wadsleyite at water content of 1 – 2 wt.% (H. Fei et al., 2017).

Variation of a cold subducted slab's behavior is captured by seismic tomography images. As slabs sink into the mantle transition zone from region to region, some of them flatten to form stagnant slabs, others penetrate into the lower mantle (Fukao, Widiyantoro, & Obayashi, 2001; Grand, 2002; Van der Hilst, Widiyantoro, & Engdahl, 1997; Van der Hist, Engdahl, Spakman, & Nolet, 1991; Widiyantoro, Kennett, & van der Hilst, 1999; Zhao, 2004). For instance subducted slabs are highly deformed in the western Pacific (e.g., (Fukao, Obayashi, Inoue, & Nenbai, 1992; Fukao, Obayashi, & Nakakuki, 2009)) above 660 km depth leaving no clear image of further decent in the lower mantle.

4. Diffusion experiments

Experiments to measure a diffusion coefficient can be divided in two stages: introduction of the diffusing species into the sample and then determination of the magnitude of diffusion.

4.1. Designs of diffusion experiments

Normally, designs of all diffusion experiments are based on reproducing the specified boundary conditions of existing solutions of non-steady Fick's second law (**Eq. 1.5)**. For diffusion experiments in minerals the sources of a diffusing species may be a surrounding solution or a gas phase, a thin film coated on the sample's surface or a fine-grained powder surrounding the sample. There are two widely adopted setups, which are referred to as a diffusion couple and thin-film setups.

The *diffusion couple* setup is made of two materials with different compositions placed together, so that the initial composition profile is step-like. Starting from this profile, the component diffuses across the interface between them by keeping the sample at sufficiently high temperature for a certain duration, so that the compositional profile asymptotically approaches a uniform compositional distribution. This procedure is referred to as *diffusion annealing*. The annealing duration and temperature conditions are chosen so that a transitional diffusion profile can be observed by an adopted analytical method.

The *thin-film* setup consists of a thin layer of a small amount of diffusant that is covered on the sample surface. This layer has a thickness from one atom to hundreds of nanometers and is enriched in a stable isotope or it has a different composition designed to create a controlled chemical gradient. A thin film of a diffusion source can be deposited on a polished single crystal or polycrystalline sample. A thin-film setup is close to a diffusion couple design, but differs because the reservoir is finite. However, it is commonly used for a slow diffusion species when the thicknesses of a thin-film can be neglected in solving the diffusion equation (Dohmen, Becker, Meißner, Etzel, & Chakraborty, 2002) and, therefore this method was adopted in this study.

4.2. Thin-film deposition

For the thin-film setup a geometrically and chemically uniform film is required. Many techniques for a thin-film production have been used before (Smith, 1995), such as chemical vapor deposition (CVD) and molecular beam epitaxy (MBE), which produce defined pure films of very precise chemistry. These processes are, however, expensive and time consuming. Thermal vapor deposition (TVD) (Ganguly, Ito, & Zhang, 2007; Y. Zhang, 2010) and radio frequency sputtering (Dimanov & Jaoul, 1998; Gardés et al., 2006) are relatively fast techniques, however, thin films produced by these techniques usually have very different compositions from their sources, and it is very difficult to produce thin films with exactly the desired compositions. In addition, since only a small fraction of the evaporated material condenses on the substrate, the source materials, which have expensive isotope tracers in many studies, tend to be wasted. Although the majority of methods produce very thin films about a few tens of angstroms, they are too thin for measurements of longer diffusion profiles. In the case of TVD, diffusion already takes place to some degree during deposition, because the substrate, on which deposition is to be made, also heats up.

The Pulsed Laser Deposition (PLD) can avoid most of these problems with the other thin-film production techniques. The principle is simple and presented in **Fig. 4.1 a**. The method is based on a physical vapor deposition process in a vacuum chamber. A high-energy laser beam with a short wave-length (Nd:YAG or Excimer laser) hits the surface of the material to be deposited (target). This target can be either a single crystal or polycrystalline material pressed to pellets with a desired composition for the thin film. The laser beam converts the target material to a plasma plume perpendicular to the target surface. The substrate is placed a few centimeters away from the target in the path of the plasma beam. In a series of laser pulses, a controlled amount of the material nominally identical in composition to the target lays on the substrate.

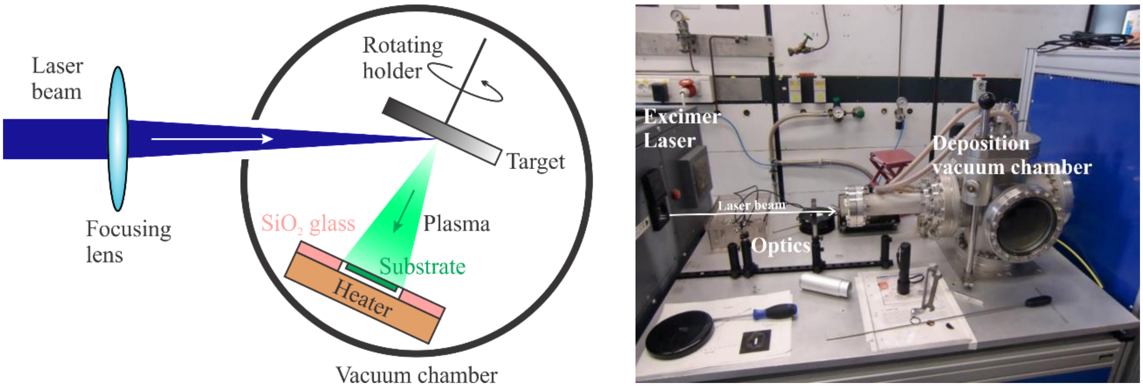

a b

Fig. 4.1. (**a**) Schematic illustration of the principle of thin film creating by pulsed laser deposition. (**b**) Overview of the PLD facility in Bochum.

A number of process parameters such as the wavelength and the energy flux of the laser pulse must be optimized. The system in the Institut für Geologie, Mineralogie und Geophysik, Ruhr-Universität Bochum is specially designed to deposit thin films of numerous mineralogical compositions, ranging from simple oxides such as TiO_2 and ZrO_2 (Dohmen, 2008; Dohmen, Marschall, & Ludwig, 2009) to various complex silicates, including olivine, pyroxenes, and garnet (Dohmen, 2002; H. Fei et al., 2012, 2013; Milke, Dohmen, Becker, & Wirth, 2007) as well as aluminous spinel (Vogt, 2008). The setup in Bochum (**Fig. 4.1 b**) uses an excimer laser (Lambda Physik LPX305i) that can be operated at three different wavelengths (193, 248, and 351 nm) with pulse energies usually with hundreds of mJ. The actual energy flux at the target can be controlled by an aperture or focusing lenses. For deposition of most silicates, a wavelength of 193 nm was found to be optimal. The system requires high vacuum conditions (10^{-5} Pa), to introduce an additional gas flow for a possible control over the stoichiometry of the film. The substrate placed on a ceramic crucible, whose design can provide several samples to be coated at one time, is loaded on a SiC heater and fixed by a quartz glass at a distance of 20-50 mm from the target. The heater is capable to heat up the substrate to 1000 ℃ in a few minutes. The target is able to rotate about one axis, such that the laser is scanned over the surface of the target during ablation, preventing early target erosion.

The calibration of deposition rates is needed for each target and setup conditions to obtain desired thickness of thin films. A silicon wafer is used for this purpose in a short time deposition (5-10 minutes). After the test deposition, the wafer has a specific color that depends on the difference in the optical path length. By comparison with the Michel Levy color chart used for polarization microscopy, the retardation can be inferred from the color. Then the thickness of the layer can be calculated by the ratio $g/2n_{\mathrm{film}}$, where g is the retardation, n_{film} is the thin film reflectivity.

Initially deposited thin films are expected to be amorphous. Therefore, for most diffusion studies, preliminary recrystallization is required (H. Fei et al., 2012, 2013). Heating before deposition can be used to “prepare” the substrate by evaporating adsorbed components, particularly water.

4.3. Analytical methods

Analytical methods used in diffusion studies have been previously reviewed by (Cherniak et al., 2010). A wide range of diffusivity (from 10^{-9} to 10^{-24} m^2/s) can be measured by direct profiling methods, where the concentration of diffusant is determined as a function of depth. For short diffusion distances, Rutherford Backscattering Spectroscopy (RBS), Nuclear Reaction Analysis (NRA) and Elastic Recoil Detection (ERD) can be applied as well as Secondary Ion Mass Spectrometry (SIMS) in a depth profiling method. For long diffusion profiles, measurements by step-scanning are used: the electron microprobe (EPM), SIMS and infrared spectroscopy (IR).

4.3.1. Secondary Ion Mass Spectrometry (SIMS)

SIMS is a very powerful analytical method capable for analysis of almost all elements and isotopes ratios. Its spatial resolution in step-scanning mode is about 10 µm and <20 nm in depth profiling method. In SIMS and NanoSIMS, a solid surface is bombarded by a *primary beam* of ions with energies typically of several kilo-electron volts (keV) (**Fig. 4.2**).

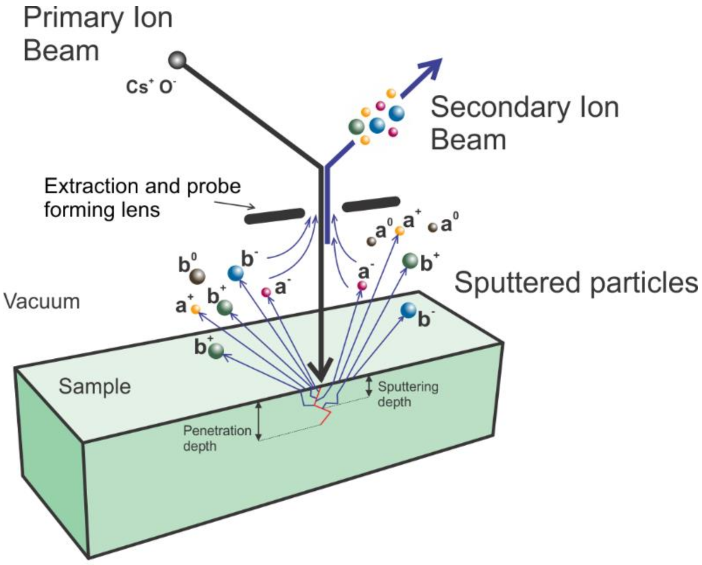

Fig. 4.2. The physical principle of NanoSIMS. Secondary particles (a, b) are neutral, positively, and negatively charged. Formed by electro-magnetic lenses secondary ion beam consists of positive and negative ions. In NanoSIMS extraction and probe forming lens location enable simultaneously focusing the primary beam, and formatting the secondary ion beam. In ordinary SIMS these beams are separated.

The choice of primary ion species (e.g., Cs^+ or $^{16}O^-$) is based mainly on the species of the analysed secondary ions. Each ion hitting the surface triggers many collisions in the sample. It causes particles from depths close to a sample surface (2 – 20 nm) to be “sputtered”. A part of the sputtered particles is ionized in the process of ejection. These ions are referred to as “secondary” ions. These ions are, then, physically separated by special electro-magnetic optics and form a secondary ion beam. Then secondary ions of different mass-to-charge ratio are physically separated by the Lorentz force as they pass through a magnetic field arranged perpendicular to the velocity vector of the secondary ions and counted.

NanoSIMS uses a co-linear optics (**Fig. 4.2** and **Fig. 4.3**) capable of simultaneously focusing the primary ions, and collecting almost all the secondary ions. In this system, the primary beam hits the sample surface with normal incidence. With a coaxial configuration of NanoSIMS, much smaller spot sizes and higher collection efficiency can be achieved than ordinary SIMS. This is the most important fundamental property of the NanoSIMS. Shadowing effects from topography (when some slopes of the surface face away from the incident beam) on the sample surface, which can reduce the useful yield, are also minimized with this geometry. The multicollection chamber such as that in the NanoSIMS 50L CAMECA installed in the Institute of Geology and Geophysics, Chinese Academy of Science, at Beijing (**Fig. 4.4**), can have up to seven ion detectors simultaneously performing ion detection of species.

However, high spatial resolution demands low primary beam current (pA) and subsequently the number of secondary ions produced are consequently low. Additionally, the charge of primary and secondary ions must be opposite.

The depth-profiling mode is used when the diffusion length is less than a few micrometers. In this regime, the primary beam hits the sample surface to make a square shape crater with a side dimension of tens of nanometers (NanoSIMS) to 250 µm. Atoms or ions from deeper and deeper parts in the sample are collected to measure the change in chemistry with depth. A successive crater-depth measurement must be performed to calibrate the rate of sputtering.

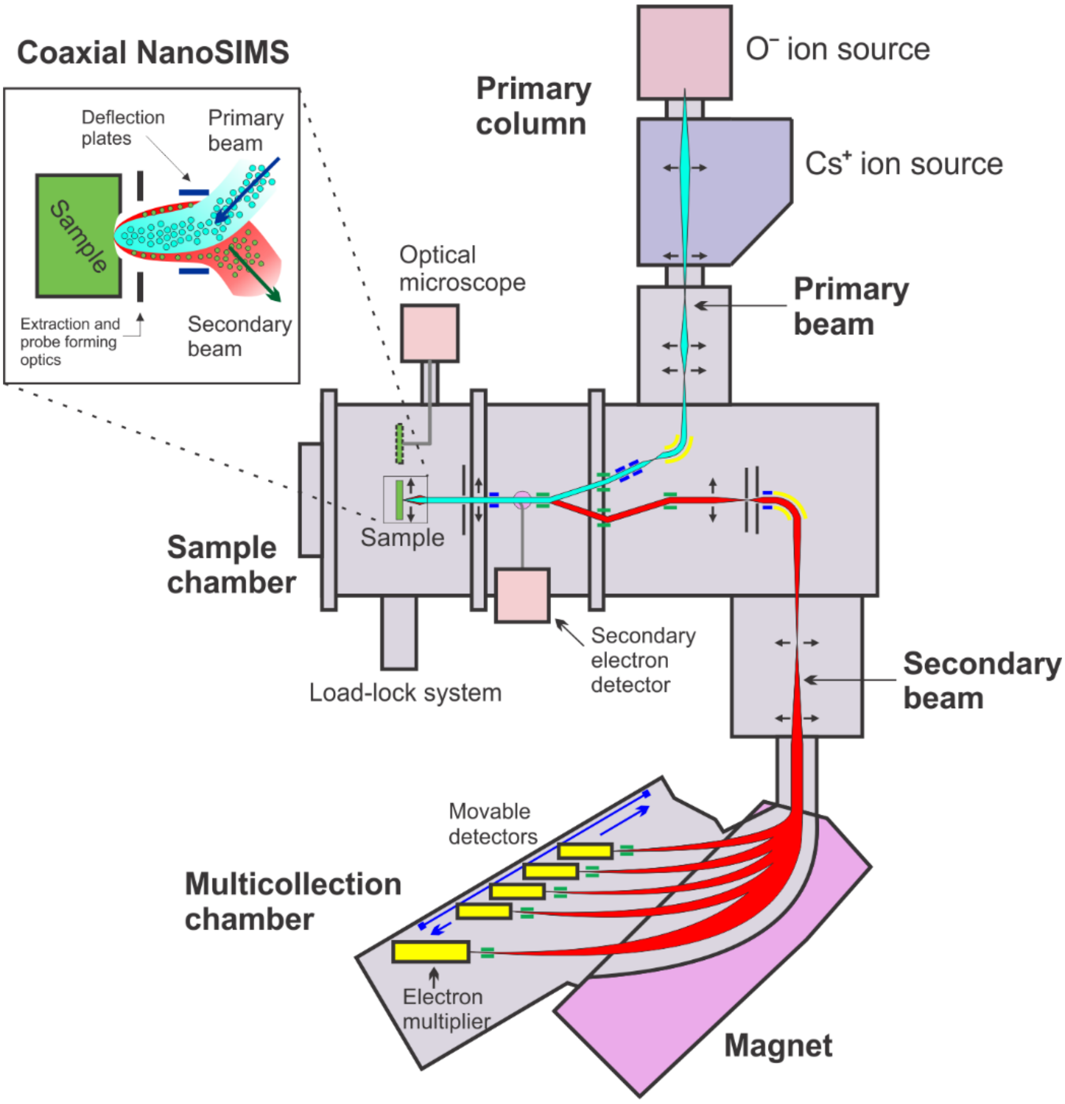

Fig. 4.3. Schematic of the NanoSIMS 50L from CAMECA with the major components (simplified from (Hoppe, Cohen, & Meibom, 2013)) and coaxial probe forming principle.

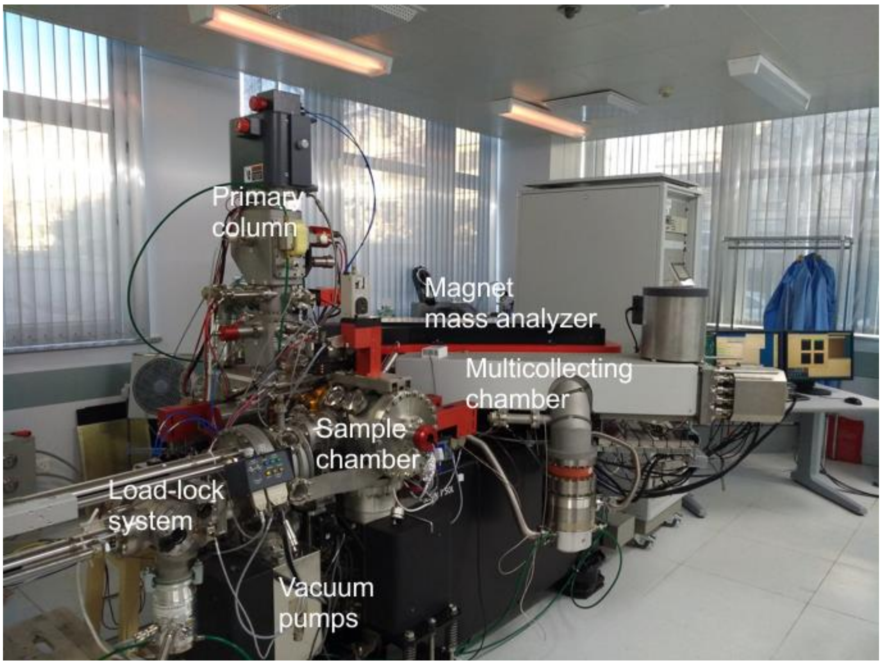

Fig. 4.4. NanoSIMS 50L from CAMECA installed in Institute of Geology and Geophysics, Chinese Academy of Science, Beijing, P.R. China.

4.4. Diffusion coefficient determination

In order to obtain a diffusion coefficient, resulted diffusion profiles are fitted to an analytical solution of the **Eq. (1.5)** under given initial and boundary conditions. There are a large number of analytical solutions for many different initial and boundaries conditions.

The configuration of the *diffusion couple* gives one of the simplest mathematical solutions. Let us consider two materials that are in contact at an interface. The materials are semi-infinite, initially uniform but with different initial concentrations of isotopes. The initial concentration of a given species is $C = C_1$ for $x < h$ and $C = C_0$ for $x > h$, where h is the interface position. During a diffusion process, atoms flow across the interface and homogenize the couple. The solution of the **Eq. 1.4** for such boundary conditions is:

$$C(x,t) = \frac{C_0 + C_1}{2} - \frac{C_1 - C_0}{2} \cdot \operatorname{erf}\left(\frac{x-h}{\sqrt{4Dt}}\right) \qquad (4.1)$$

where erf is the notation of the so-called error function:

$$\mathrm{erf}(x) = \frac{2}{\sqrt{\pi}} \int_0^x \exp(-z^2)\,\mathrm{d}z \tag{4.2}$$

Another strategy is to solve the diffusion equation numerically using a *finite-difference scheme* (Crank, 1975). Numerical approaches are not limited and can resolve cases that are more complex, e.g., the diffusion coefficient depends on the diffusant concentration, and the boundary conditions at the surface are functions of time. In order to perform this calculation technical software such as Mathematica, Matlab, Mathcad or even an Excel spreadsheet can be used.

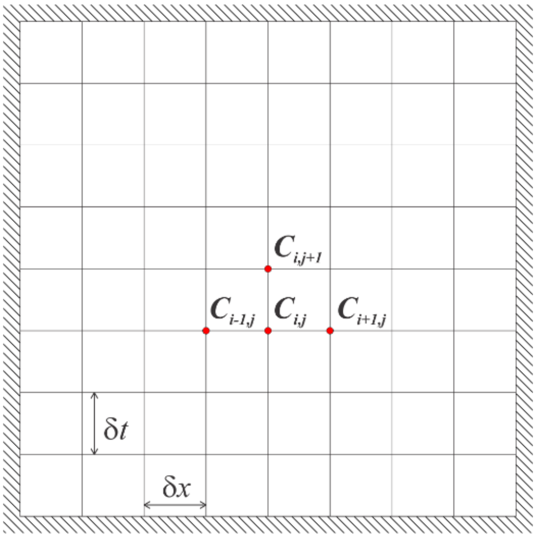

Fig. 4.5. Grid of time and space intervals, and corresponding concentrations, used for numerical calculations (Crank, 1975).

To obtain a unique solution by numerical methods initial and boundary conditions must be specified. Then, the diffusion space and time should be discretized by a set of mesh points of equal small intervals of space δx and time δt (**Fig. 4.5**). The coordinates of each grid point will be ($i\delta x$, $j\delta t$). Let the value of the concentration at this point be denoted by $C_{i,j}$. The Fick's second low equation turns in to a simple algebraic equation by replacing the derivatives by finite difference approximations:

$$\frac{C_{i,j+1} - C_{i,j}}{\delta t} = D\left(\frac{C_{i+1,j} - 2C_{i,j} + C_{i-1,j}}{\delta x^2}\right) \tag{4.3}$$

This approach is known as the *Forward Euler Scheme*. In this finite-difference scheme, the concentration at any $(i\delta x,\ j\delta t)$ is calculated from knowledge of the concentration at the same and neighboring points for the preceding time δt. The obtained equation can be rewritten in a form that is more common:

$$C_{i,j+1} = C_{i,j} + F(C_{i+1,j} - 2C_{i,j} + C_{i-1,j}) \tag{4.4}$$

with the *Fourier number* $F = D\delta t/\delta x^2$.

Numerical approaches are not limited by the method described above. There is also a Backward Euler Scheme, a Crank-Nicolson scheme and so on (Crank, 1975). They are more efficient in terms of computer resources, but require algorithms that are more complex.

4.5. Possible uncertainties

The error in a diffusion coefficient can depend on those of the individual analyses and the complexities of the specific diffusion couple (Zhang et al., 2010). Error in the crater depth measurement is one of the primary sources. The effective depth resolution can be lower than the nominal resolution due to high surface roughness, non-uniform film deposition an grain growth. For depth-profiles analysis by SIMS, (Hofmann, 1994) presented the approach where a measured profile can be fitted by convolving a real depth profile by

$$C'(x) = \int_{-\infty}^{+\infty} C(x') \cdot g(x - x')dx' \tag{4.5}$$

where $C'(x)$ is the measured concentration, $C(x)$ is the real concentration, and a resolution function:

$$g(x - x') = \frac{1}{\sigma\sqrt{2\pi}} \cdot exp\left(\frac{(x - x')^2}{2\sigma^2}\right) \tag{4.6}$$

with σ is a value determined by simulation of the measured profile or from a steep profile with a zero diffusion time. A simple estimation of deviation of real diffusion coefficient D from a determined coefficient D_C was suggested by (Ganguly, Cheng, & Chakraborty, 1998) as follows:

$$\frac{D}{D_C} = 1 - 8 \cdot \left(\frac{\sigma}{L}\right)^2 \tag{4.7}$$

where L is the length of the diffusion profile. The convolution effect would be bigger in case of short diffusion profiles and small diffusion coefficients.

The convolution caused by surface roughness was made by (H. Fei et al., 2012, 2013) by replacing $4Dt$ in the analytical solution by $4Dt + {L_0}^2$. Where L_0 is the nominal profile length in zero-time diffusion profile. A few diffusion experiments using samples with a variety of surface roughness resulted in the positive linear correlation between L_0 and surface roughness σ (**Fig. 4.6**) that were used for convolution.

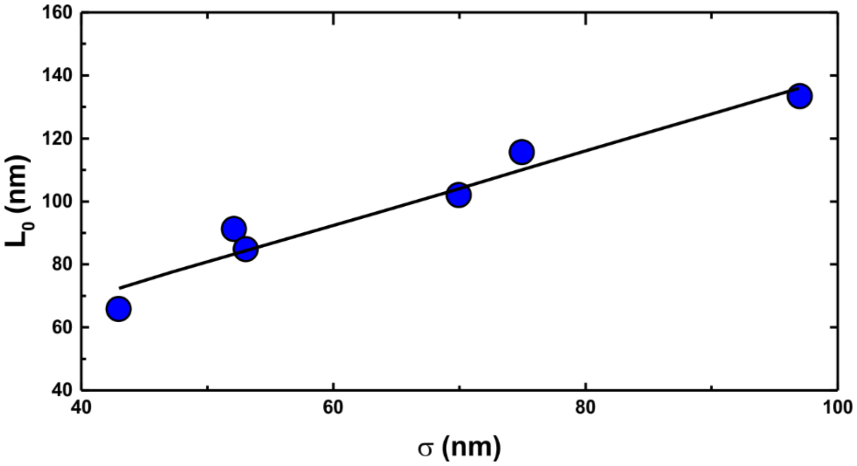

Fig. 4.6. Nominal diffusion length in zero-time diffusion experiments and surface roughness correlation (modified from (H. Fei et al., 2012)).

5. Water in wadsleyite

5.1. FTIR spectroscopy for H_2O measurements

Fourier Transform Infrared (FTIR) spectroscopy is a convenient technique to not only measure water contents in rocks and minerals but also specify the site information of hydroxyl groups (Bell, Rossman, Maldener, Endisch, & Rauch, 2003).

The common components of FTIR spectrometers are a light source, interferometer, sample compartment, detector, amplifier, Analog/Digital convertor, and computer. The core of the spectrometer is the interferometer whose design is usually based on the Michelson interferometer (Michelson, 1891) (**Fig. 5.1**).

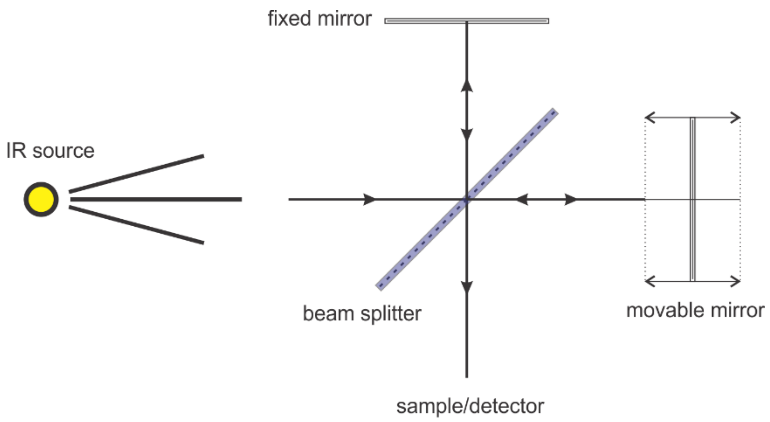

Fig. 5.1. Schematic diagram of the optical layout of a Michelson interferometer. Fixed and movable mirrors are able to get reflected beams from an IR source at a beam splitter. The splitter has an optical retardation. Partially reflected at the splitter beam passes through a sample holder and focuses on a detector.

In order to obtain an infrared spectrum of a sample, a spectrometer examines the transmitted light of an infrared beam (polarized or un-polarized) that paths through the sample. Once the infrared spectrum is measured, it is transformed into an FTIR spectrum via a mathematical operation known as Fourier transform (based on an idea that each spectrum can be presented as a sum of cosine and sine functions) (Griffiths, De Haseth, & Winefordner, 2006).

The transmittance (T) is defined by the intensity ratio of the transmitted (I) and of the incident beam (I_0). Each molecule or molecular group absorbs photons of certain energies (or wavelength, since the photon energy $E = hc/\lambda$). Then the transmittance of is a function of a wavenumber $k = 1/\lambda$:

$$T(k) = \frac{I(k)}{I_0(k)} \tag{5.1}$$

The obtained spectrum for the quantitative analysis are presented by the absorbance (A) of the sample as a function of wavenumber k. The concentration of the detected OH groups can be extracted in general from the absorption FTIR spectrum by assuming its proportionality to the absorbance. The absorbance is given by the base 10 negative logarithm of $T(k)$. Then, according to the Bouguer–Lambert–Beer law (or simply Beer's law):

$$A(k) = -log_{10}T(k) = \varepsilon(k)bc \tag{5.2}$$

where $A_i(k)$ is an absorbance at wavenumber k, b is a sample thickness, $\varepsilon(k)$ is the molar absorption coefficient, c is a concentration.

By combining the absorbance and sample thickness that can be measured, coefficient $\varepsilon(v)$ is calibrated for each mineral using an independent method (SIMS, nuclear reaction analysis). Based on the absolute values of hydrogen content measured by the other method, a variety of calibrations has been constructed (Deon et al., 2010; Koch-Müller & Rhede, 2010; Libowitzky & Rossman, 1997; Paterson, 1982).

Paterson calibration, which was obtained on glasses and quartz, has been used to determine the water content in wadsleyite from un-polarized FTIR spectrum. It is an equation of the water concentration C_{OH}:

$$C_{OH}(wt.ppm) = \frac{X_i}{150\xi}\int \frac{k(v)}{(3780 - v)}dv \tag{5.3}$$

where X_i is the extinction coefficient (2590 wt. ppm for Mg_2SiO_4 wadsleyite (Bolfan-Casanova et al., 2000), $k(v)$ is the absorbance at wavenumber v, ξ is the orientation factor (equal to 1/3 for unpolarized and 1 for polarized spectra).

Another calibration was suggested by (Libowitzky & Rossman, 1997) based on stoichiometric hydrous silicates and oxide minerals. Its general equation is:

$$C_{OH}(wt.\%) = A \cdot \frac{1.8}{b \cdot d \cdot 246.6 \cdot (3753 - \sum v_i A_i / \sum A_i)} \tag{5.4}$$

where A is a total absorbance, v_i and A_i are a wavenumber and absorbance of the band i correspondingly, b is a sample thickness, d is the density (3.47 g/cm^3 for Mg_2SiO_4 wadsleyite).

However, calibration for the OH quantification in nominally anhydrous minerals such as wadsleyite can lead to underestimation of the water content (Thomas et al., 2009). In the *Deon calibration* the relations between the absorption coefficient and water content were recalibrated, and the coefficient ε of 73000 L/mol(H_2O)/cm^{-2} was suggested (Deon et al., 2010).

5.2. Studies of OH in wadsleyite

Wadsleyite belongs to the family of nominally anhydrous minerals in which water is found in general as a hydroxyl point defect charge balanced with a cation site vacancy. Several possible structural positions of protons have been reported. First, as mentioned above, is the protonation of an oxygen at the O1 position, which is not-bonded with Si (Smyth, 1987, 1994). Another candidate for protonation is O2 oxygen between two SiO_4 tetrahedra (Downs, 1989). Neutron powder diffraction (NPD) for wadsleyite with 1.6 wt.% H_2O reveals hydrogen sites along O1···O4 and O1···O3 octahedral edges of M3 (Sano-Furukawa et al., 2011) and single crystal neutron diffraction for anhydrous wadsleyite showed no other sites except one along O1···O4 octahedral edges of M3 (Purevjav, Okuchi, Tomioka, Wang, & Hoffmann, 2016). Studies based on methods less sensitive to hydrogen (due to its low electron density) such as single crystal x-ray diffraction have reported about the same hydrogen sites as obtained by NPD (Deon et al., 2010; Holl et al., 2008). A wide range of possible hydrogen siteshave been infered from spectroscopic studies. Additionally to those already mentioned, some bands on infrared spectra were assigned to the O4···O4 on the tetrahedral edge of Si_2O_7 group and O1···O1 along edge of the M3 octahedra (Jacobsen et al., 2005).

By theoretical predictions, if the O1 were fully hydrated, wadsleyite would contain up to 3.3 wt.% H_2O (Smyth, 1987). An experimental study reported it contains up to 2.4 wt.% of water in iron-bearing samples (Kohlstedt et al., 1996). Fe-free wadsleyite (Demouchy, Deloule, Frost, & Keppler, 2005; Jacobsen et al., 2005) shows lower water content, maybe due to the additional Mg vacancies produced by ferric iron in iron bearing wadsleyite (Bolfan-Casanova, 2005; Hirschmann, Aubaud, & Withers, 2005). Temperature dependence of water content of iron-free wadsleyite was observed (Demouchy et al., 2005), namely from 2.2 wt.% at 900 °C to 0.9 wt.% at 1400 °C, though it has not been obtained in iron-bearing wadsleyite (Demouchy et al., 2005; Hirschmann et al., 2005; Litasov & Shatskiy, 2011). Additionally, wadsleyite showed a different water cantent (Jacobsen et al., 2005; Shatskiy et al., 2009) along unit cell directions, water content along the c-direction is at least 1.1 times higher than along the b-direction and 2.0 times higher along the a-direction.

One might suggest from a diamond inclusion of ringwoodite studied by (Pearson et al., 2014) with up to 1.4 wt.% of H_2O that wadsleyite and the whole mantle TZ could be hydrous. Recently obtained data on dislocation mobility in ringwoodite suggested based on relative estimation of a mantle transition zone viscosity that wadsleyite and ringwoodite should contain 1 – 2 wt.% of H_2O (H. Fei et al., 2017) supporting the idea of a globally hydrous mantle TZ.

Different picture to hydrous TZ could be constructed from the physical parameters measured for the mantle TZ. Electrical conductivity data (Huang, Xu, & Karato, 2005; Yoshino, Manthilake, Matsuzaki, & Katsura, 2008) yields for wadsleyite and ringwoodite water contents ~ 0.1 - 0.2 wt.% H2O for the mantle in the north Pacific. Another study (Chang & Ferreira, 2019) based on global tomography images of the mantle transition zone near subducted slabs in the western Pacific suggested dry transition zone for this regions (~ 0.02 wt.ppm).

6. Diffusion studies of wadsleyite

6.1. Fe-Mg cation interdiffusion

The first data on Fe-Mg diffusion rates in wadsleyite were obtained from samples with a compositional range of iron from 0.18 to 0.1 (Chakraborty et al., 1999). In that study only two experimental data points were obtained for wadsleyite at constant pressure of 15 GPa and at 1100 ($3(1) \times 10^{-15}$ m^2/s), 1200 ^oC ($7(1) \times 10^{-15}$ m^2/s) in a gold capsule at estimated oxygen fugacities of 10^{-8} to 10^{-9} bars. This result gave an estimate of the activation energy of 145 kJ/mol (no error was given).

Further investigation of Fe-Mg and Mg-Ni diffusion were performed using a polycrystalline sample of $(Mg,Fe,Ni)_2SiO_4$ wadsleyite at 13 GPa and 1200 ^oC (Farber, Williams, & Ryerson, 2000). Through the usa of Ni capsules it was assumed that the oxygen fugacity was maintained at the Ni-NiO buffer. The starting material for diffusion annealing was olivine with ~ 1.5 wt. ppm of water, thus there was a phase transition to wadsleyite during the experiments, in which water was estimated to be several tens of wt. ppm. The diffusion coefficient was determined to be $5(3) \times 10^{-14}$ m^2/s.

Subsequent studies of Fe-Mg interdiffusion were carried out using the diffusion couple method at pressures 16 and 17 GPa and temperatures of 1230 – 1530 °C with different initial X_{Mg} = Mg/(Mg + Fe) ratios (Kubo, Shimojuku, & Ohtani, 2004). The Ni-NiO oxygen-fugacity buffer was chosen in all runs and NaCl powder was used as a surrounding material both during synthesis of the starting material and diffusion annealing experiments, thus it was impossible to maintain same water content in case of a high-water content sample. For samples with 50 – 90 wt. ppm H_2O coefficients were determined to be $1.24 \times 10^{-9} \cdot \exp(-172\ (\mathrm{kJ/mol})/\mathrm{RT})$ m^2/s for X_{Mg} = 0.95 and $1.77 \times 10^{-9} \cdot \exp(-143\ (\mathrm{kJ/mol})/\mathrm{RT})$ m^2/s for X_{Mg} = 0.90.

All studies together with additional experimental data points with H_2O contents of 35 wt. ppm obtained at the Ni-NiO fugacity buffer were summarized and analyzed by (Holzapfel, Chakraborty, Rubie, & Frost, 2009). Activation energy was constrained to ~ 230 kJ/mol by data obtained at 15 GPa. The relatively high activation volume of 13.9(1.5)×10^{-6} m^3/mol was found to describe all available data. In combination all results under dry conditions (several tens wt. ppm) and Ni-NiO oxygen fugacity were fitted best to the Arrhenius formula as a function of pressure, temperature and composition:

$$D_{Fe-Mg}(\mathrm{m}^2/\mathrm{s}) = 1.24 \times 10^{-6} \cdot \exp[11.8 \cdot (0.86 - X_{\mathrm{Mg}})] \cdot \exp\left(\frac{-[229 + (P - 15) \times 13.9]\frac{\mathrm{kJ}}{\mathrm{mol}}}{RT}\right) \quad (6.1)$$

where X_{Mg} is a composition of Mg, R is a gas constant, T is a temperature in K, P is a pressure in GPa (**Fig. 6.1**).

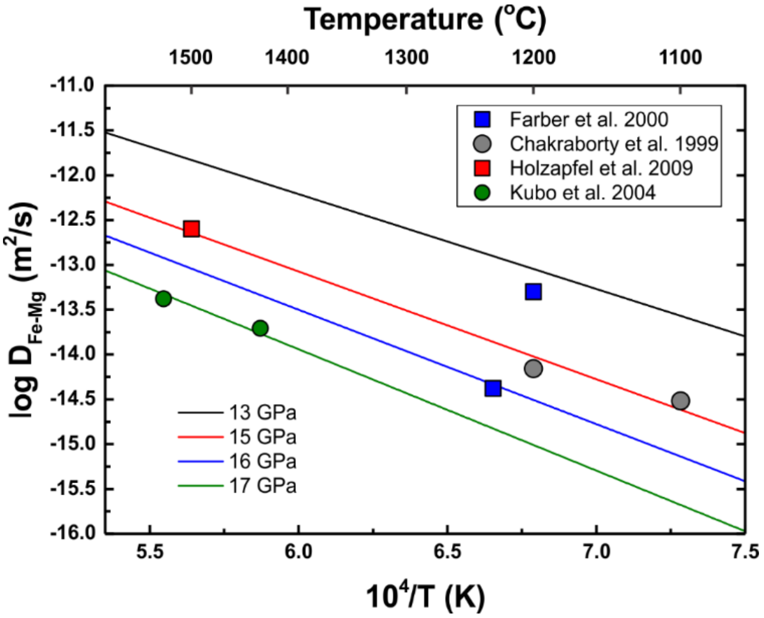

Fig. 6.1. Diffusion rates of Mg-Fe in $(Mg,Fe)_2SiO_4$ wadsleyite at different pressures from previous studies.

Mg-Fe and Mg diffusion data in wadsleyite as a function of temperature taken from previous studies are presented in **Fig. 6.2** in comparison with Mg-Fe and Mg diffusion data in other mantle phases. Mg-Fe diffusion in wadsleyite is comparable with Mg diffusion in ringwoodite (~ -13.5 log units m^2/s) at 1600 °C (Farber et al., 2000; B. Zhang, Yoshino, & Zhao, 2019). Diffusion of Mg-Fe in the mantle TZ increases at least two orders of magnitude when olivine transforms to wadsleyite (Chakraborty, 1997; Chakraborty, Farver, Yund, & Rubie, 1994; Dohmen & Chakraborty, 2007) and then drops 6 orders of magnitude to very low values in the lower mantle after transformation to bridgmanite (Xu et al., 2011). The difference in water content might be the reason for the significant difference in activation energies for dry (1.5 wt. ppm) ringwoodite of (Farber et al., 2000) with 247 kJ/mol and wet (3000 wt. ppm) ringwoodite of (B. Zhang et al., 2019) with 140(5) kJ/mol. Since both wet and dry ringwoodite samples in Zhang et al., 2019 were fitted simultaneously no energy difference was obtained between them. However, they managed to evaluate the exponent of water dependency of $D_{\mathrm{Fe-Mg}} \propto C_{\mathrm{H_2O}}^{0.25}$. Activation energy for dry wadsleyite Fe-Mg diffusion (229 kJ/mol) was found to be close to that of dry ringwoodite (247 kJ/mol) and olivine (275(25) kJ/mol).

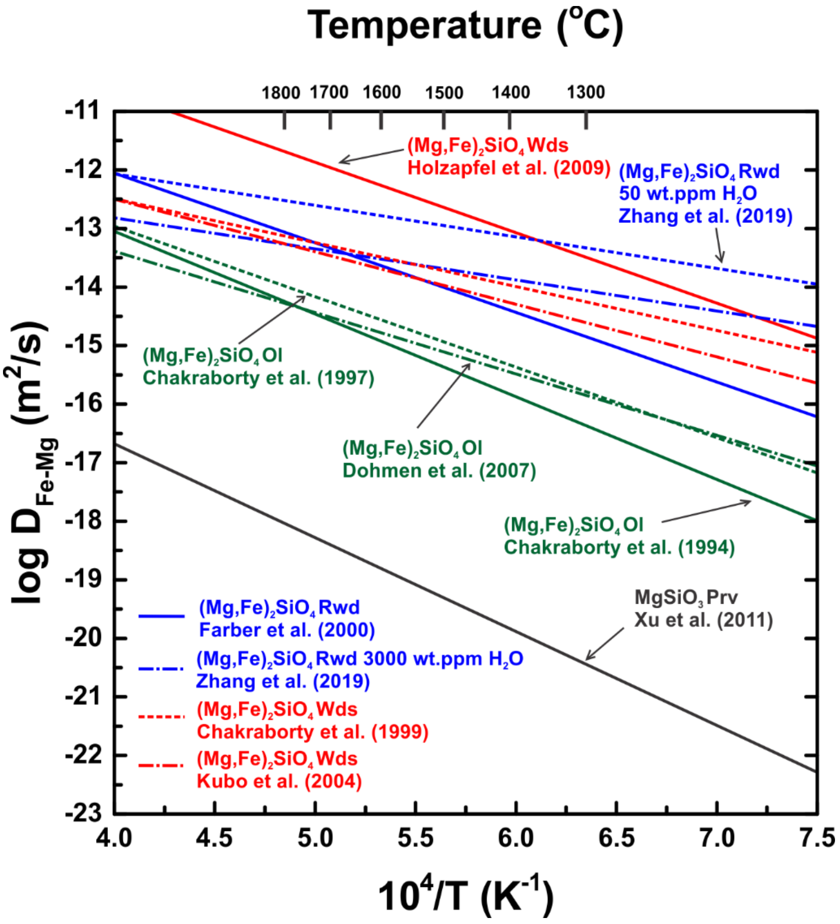

Fig. 6.2. Diffusion rates of Mg-Fe in (Mg,Fe)$_2$SiO$_4$ wadsleyite in comparison with other mantle phases from previous studies.

6.2. Si and O diffusion

There are a couple of studies of diffusion of silicon and oxygen of Fe-free and Fe-bearing wadsleyite (Shimojuku et al., 2010, 2009, 2004). Diffusion couples were provided as a polycrystalline wadsleyite (5 – 12 µm grain size), one side polished and then covered by an isotope enriched layer with a composition of $^{29}\mathrm{SiO_2}$ or $(\mathrm{Mg,Fe})_2{}^{29}\mathrm{Si}^{18}\mathrm{O}_4$ (in case of iron-bearing sample). $^{29}\mathrm{Si}$ enriched thin-film coating was performed by pulsed laser deposition. The oxygen fugacity was controlled by using of a Ni capsule with a NiO powder on top of it. Secondary ion mass spectroscopy was used in all studies to obtain diffusion profiles with depth. These profiles consisted of volume and grain-boundary diffusion parts, which were fitted separately for determination of these diffusion rates (**Fig. 6.3**). For the volume diffusion part, a solution of the thin film diffusion model was used (Crank, 1975), for the grain boundary part they used the equation of (Le Claire, 1963).

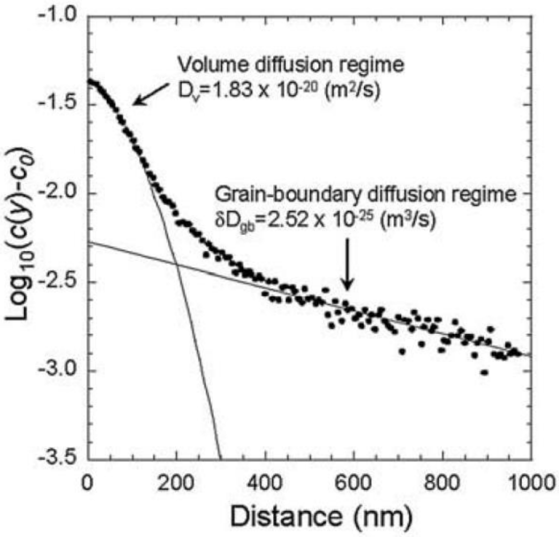

Fig. 6.3. Volume and grain-boundary diffusion profiles of wadsleyite (taken from (Shimojuku et al., 2009)).

Initially Fe-free wadsleyite showed silicon volume diffusion rates as well as the grain boundary diffusion at “wet” conditions (water content of 14 – 507 wt. ppm), at 18 GPa and 1430 – 1630 °C. These values were recalculated in the next study (Shimojuku et al., 2010) by applying convolution of diffusion profiles in order to minimize the effect of high surface roughness (Dohmen, Becker, & Chakraborty, 2007) and compared with data obtained at nominally dry conditions (20 – 60 wt. ppm). Obtained values of both the volume and grain-boundary diffusion coefficients were fitted by Arrhenius equation for an activation enthalpy estimation (**Fig. 6.4**). Diffusion rates of silicon in "wet" samples are around half an order of magnitude higher those in "dry" samples. These result suggest that the incorporation of water also should accompany the creation of point defects related to Si sites, however more detailed information was not able to be obtained.

It should be noted that the fitting of diffusion profiles are problematic, namely both diffusion types are not well separated by this fitting. Furthermore, estimation of water content for "wet" samples showed significant water loss during experiments (around one order of magnitude).

The subject of another study (Shimojuku et al., 2009) was a comparison of iron-free and –bearing wadsleyite. In this study, the diffusion rate was obtained for oxygen as well as for silicon. Due to recrystallization of deposited thin films, the resulting roughness of the sample's surface was high (50 – 300 nm) after diffusion annealing. Since that could lead to possible elongation of diffusion profiles and, thus, to artificially faster diffusion rates, the obtained profiles were convoluted according to **Eq. 4.5**. Water contents in all samples were a few tens of wt. ppm and the changes of water contents during annealing experiments were not significant (from 80 to 10 wt. ppm). Convoluted profiles were fitted to obtain the diffusion coefficients in the same way as (Shimojuku et al., 2004). The Si diffusivity in $(\mathrm{Mg}_{0.9},\mathrm{Fe}_{0.1})_2{}^{29}\mathrm{Si}^{18}\mathrm{O}_4$ is comparable for both volume and grain-boundary diffusion in comparison with that in iron-free wadsleyite with similar water contents. The Arrhenius equation fitting of data from Fe-bearing wadsleyite gave activation enthalpies higher (409(103) kJ/mol) than that for Fe-free samples (261(121) – 342(143) kJ/mol) (**Fig. 6.4**)

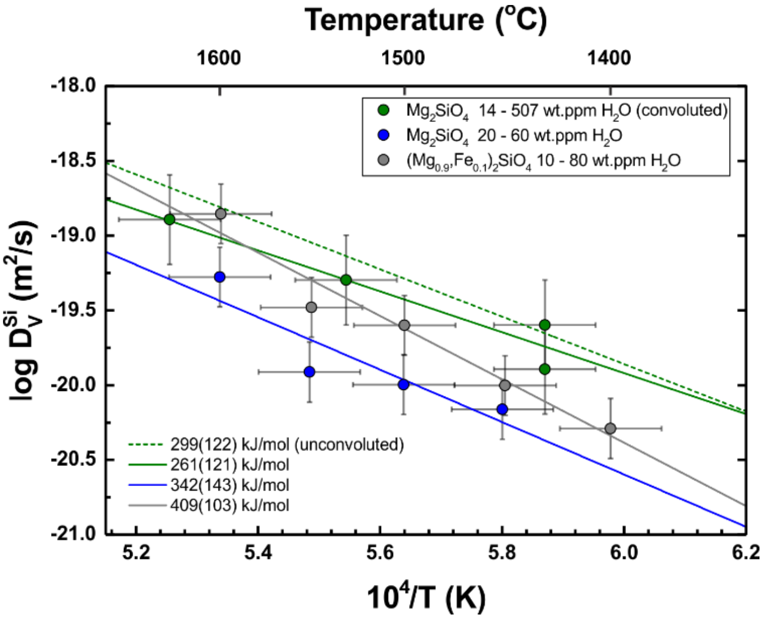

Volume diffusion

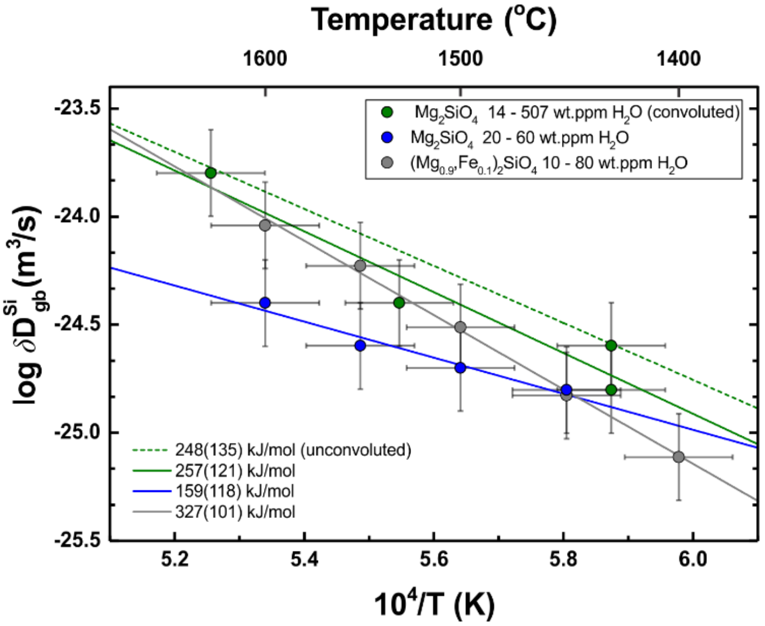

Grain-boundary diffusion

Fig. 6.4. Silicon volume and grain boundary diffusion in wadsleyite at different temperatures. Data is taken from Shimojuku et al. (2004, 2009 and 2010).

Simultaneously with Si diffusion in (Mg,Fe)$_2$SiO$_4$ wadsleyite O diffusion rates were obtained (Shimojuku et al., 2009) both for volume and grain-boundary diffusion. As presented in **Fig. 6.4** and **Fig. 6.5** oxygen diffusion is almost one order of magnitude faster than silicon diffusion in wadsleyite at water contents of 10 – 80 wt.ppm and at temperatures less than about 1800 °C. Both O and Si diffusion rates are around 6 orders of magnitude lower than previously obtained data for Mg-Fe interdiffusion (Holzapfel et al., 2009). All this suggests that Si controls the rate of diffusion creep and climb-controlled dislocation creep in wadsleyite at least at this temperature, pressure and water content. The activation enthalpy for O diffusion was found to be smaller than that for silicon diffusion, precisely H_{wd} = 291(79) – 367(83) kJ/mol.

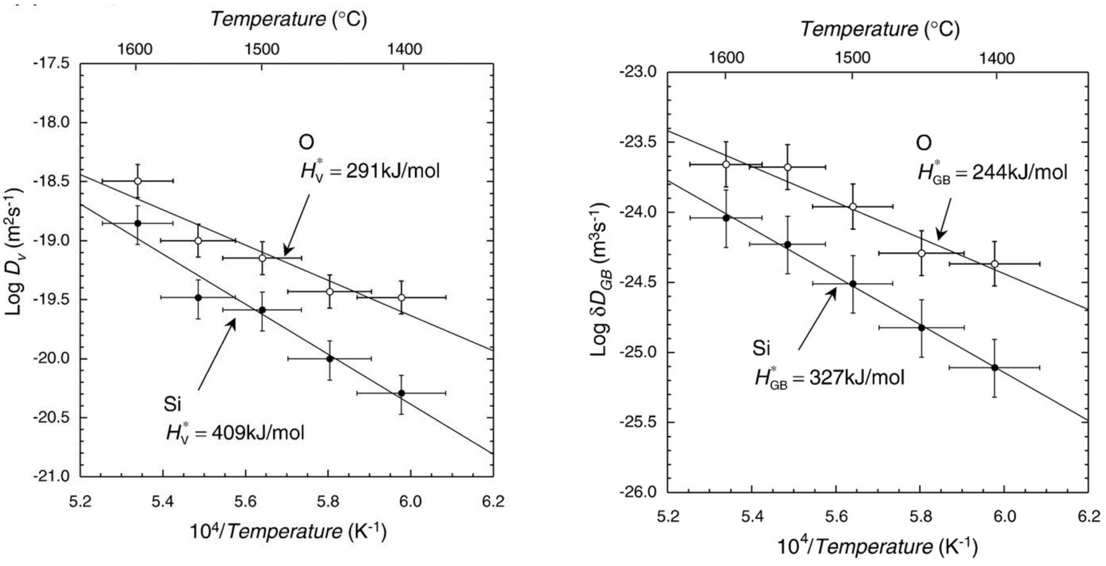

Fig. 6.5. Oxygen and Silicon volume and grain boundary diffusion in $(Mg,Fe)_2SiO_4$ wadsleyite at different temperatures. Data is taken from (Shimojuku et al., 2009).

Considering the volume and grain-boundary diffusion differences in wadsleyite, in **fig. 6.4** and **Fig. 6.5** it is clear that grain-boundary diffusion is about 1-3 orders of magnitude lower than the silicon lattice diffusion coefficient under the same temperature.

Fig. 6.6 shows Si and O volume diffusion rates of wadsleyite (Shimojuku et al., 2010, 2009, 2004) with its other polymorphs (olivine and ringwoodite) (Dohmen, 2002; H. Fei et al., 2012) and $MgSiO_3$ silicate perovskite (Dobson, Dohmen, & Wiedenbeck, 2008; Xu et al., 2011). Si and O diffusion in wadsleyite are about at least orders of magnitude faster than those in olivine, also Si and O diffusion rates in wadsleyite are about one order of magnitude faster than those in ringwoodite at 520 km depth. Half an order faster Si and O diffusion in perovskite suggests enhancement of diffusivity at 660 km depth.

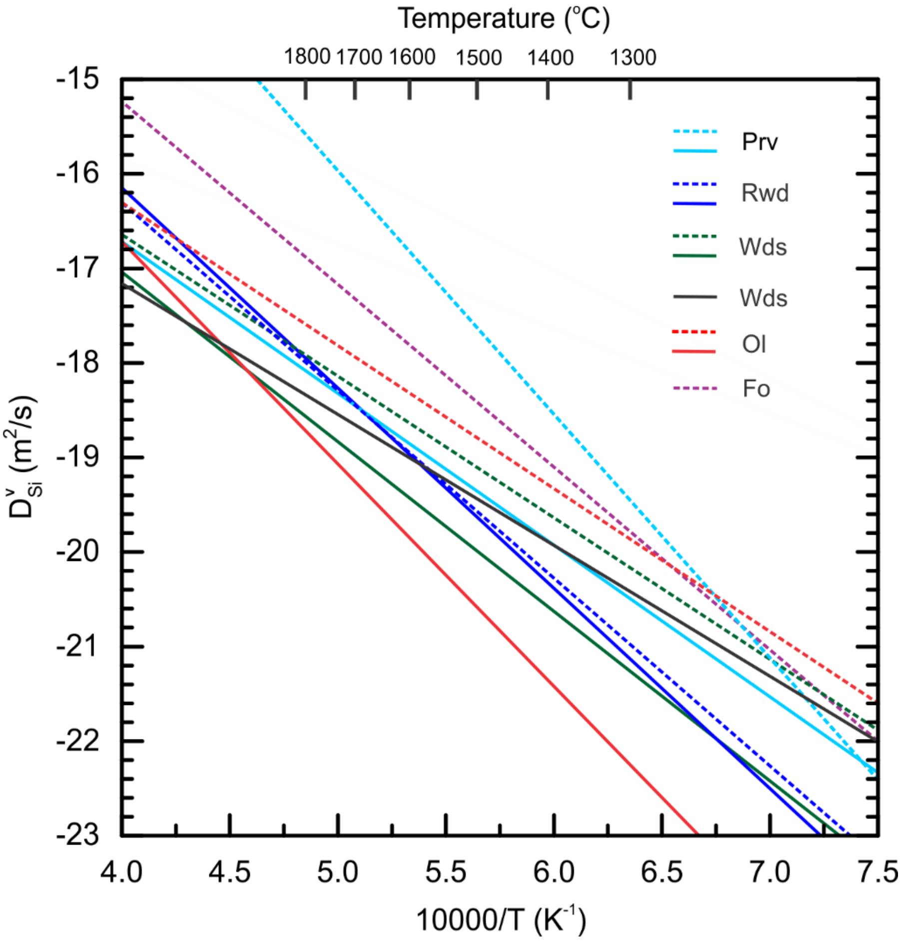

Fig. 6.6. Si (solid lines) and O (dashed lines) volume diffusion rates as a function of temperature taken from literature. Silicon and oxygen diffusion ($\Delta H_{Si} = 409(103)$ and $\Delta H_O = 291(79)$ kJ/mol) in Fe-bearing wds is taken from (Shimojuku et al., 2009). Silicon diffusion rates in Fe-free wds ($\Delta H_{Si} = 261(112) - 299(122)$ kJ/mol) is taken from (Shimojuku et al., 2010, 2004) – black line. Olivine data is taken from (Dohmen, 2002) where $\Delta H_{Si} = 529(41)$ and $\Delta H_O = 338(14)$ kJ/mol. Rwd data is taken from (Shimojuku et al., 2009) with $\Delta H_{Si} = 483(84)$ and $\Delta H_O = 367(83)$ kJ/mol. Perovskite (Prv) is taken from (Xu et al., 2011) for Si diffusion ($\Delta H_{Si} = 308(58)$ kJ/mol) and O diffusion ($\Delta H_O = 501(80)$ kJ/mol). Forsterite data for Si diffusion is taken from (H. Fei et al., 2014) with $\Delta H_O = 370(60)$ kJ/mol.

Compare lattice Si diffusion activation enthalpies (Shimojuku et al., 2010, 2009, 2004) between different most abundant mantle minerals one might say that they are relatively lower than that for Fe-bearing samples of ringwoodite

ΔH_{Si}(Rwd) = 483(94) kJ/mol (Shimojuku et al., 2009) and olivine ΔH_{Si}(Ol) = 450 – 530 kJ/mol (Costa & Chakraborty, 2008; Dohmen, 2002). On the other hand they are comparable with those for olivine ΔH_{Si}(Ol) = 290(15) kJ/mol (Houlier, Cheraghmakani, & Jaoul, 1990) or pure forsterite ΔH_{Si}(Fo) = 375 kJ/mol (Jaoul, Poumellec, Froidevaux, & Havette, 1981). Previously obtained activation enthalpies for a dry perovskite are 308(58) – 347(73) kJ/mol (Dobson et al., 2008; Xu et al., 2011). Lower activation enthalpy suggests lower energy required for defect formation, thus concentration of silicon related defects (vacancies for example) in wadsleyite is probably much higher than that in olivine or ringwoodite where activation enthalpy is closer to one of olivine.

A small effect of water on Si diffusivity in olivine was observed by (H. Fei et al., 2013). Namely, $D_{Si} \propto (C_{H2O})^{0.32\pm0.07}$ for water contents up to 800 wt.ppm in iron-free forsterite at 8 GPa and 1600 - 1800 K. This exponent is lower than 1.2 proposed by deformational studies (G. Hirth & Kohlstedt, 2003). Unlike for silicon atoms, oxygen diffusion had no discernible water dependency (H. Fei et al., 2014).

The various olivine diffusion studies also did not provided any observation of a significant diffusion anisotropy for oxygen and silicon (Costa & Chakraborty, 2008; Dohmen, 2002; H. Fei et al., 2012; Jaoul et al., 1981). No significant diffusion anisotropy was found also in perovskite (Xu et al., 2011). The polycrystalline nature of the previously studied samples of wadsleyite and ringwoodite (Shimojuku et al., 2010, 2009, 2004) does not allow any conclusions about presence of a diffusion anisotropy in these minerals to be made.

7. Experimental methods

Diffusion experiments in wadsleyite are in general two-stage (three-stage in case of additional dehydration experiments) processes with the crystal synthesis as the first set of experiments, and actual diffusion annealing experiments in the second stage. Samples pass through a preparation process before diffusion annealing including polishing, orienting and isotopic layer deposition. **Fig. 7.1** shows a general procedure in a diffusion experiment in wadsleyite.

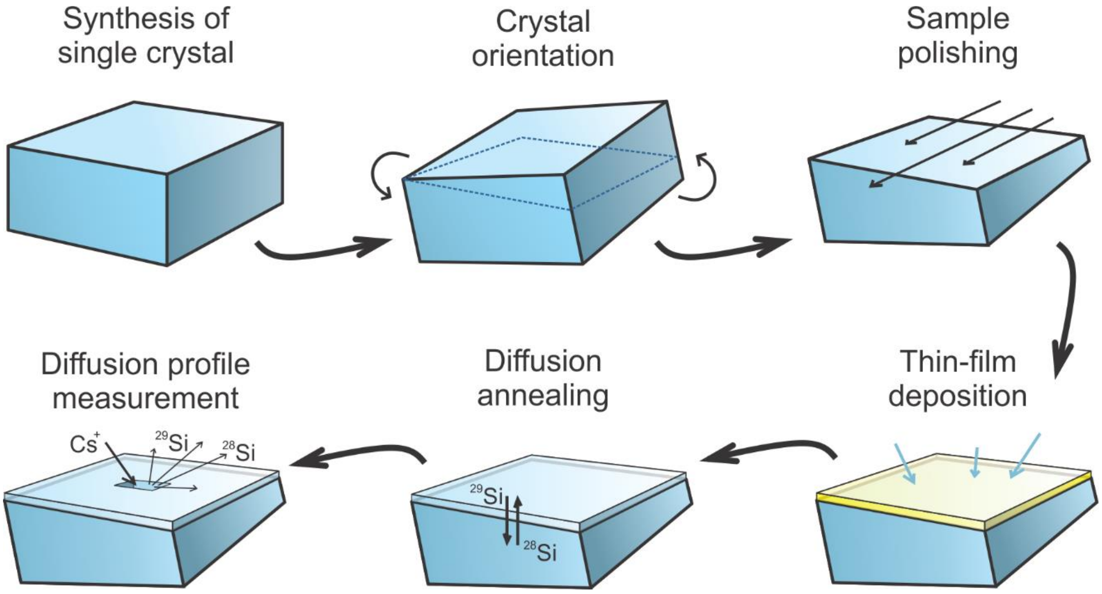

Fig. 7.1. General experimental procedure for silicon diffusion measurements in wadsleyite single crystal. Change of thin-film color denoted to its crystallization from amorphous to the sample's crystal structure.

7.1. Synthesis of single crystal

Volume diffusion experiments require single crystals of several hundred microns size. In order to obtain such crystals of wadsleyite, high-pressure and high-temperature synthesis experiments were conducted using a large volume multi-anvil apparatus (5000-tonf Zwick press at Bayreuth University) in this study (**Fig. 7.2**).

Although, (Shatskiy et al., 2009) mentioned that single-crystal growth by solid-state crystallization is impractical, (Kawazoe et al., 2015) synthesized large wadsleyite crystals with $(Mg,Fe)_2SiO_4$ composition simply by annealing in the solid state at high temperatures. I succeeded in obtaining large enough crystals for our experiments by this method within a few attempts. To optimize pressure and temperature conditions we performed a series of experiments at different pressures and temperatures (see S**ection 8.1**, **Table 8.1**).

Fig. 7.2. 5000-tonf Zwick press at Bayreuth University used in all diffusion experiments carried out for this study.

The priority was obtaining crystals as big as possible within a smaller number of runs. In order to increase the number of successful runs, we tested three types of starting materials using the assembly shown in **Fig. 7.3**; synthesized forsterite powder, thoroughly grinded synthetic forsterite crystal, and a combination of these two with polycrystalline forsterite. The starting material was loaded into a platinum capsule, which was sealed at both ends by bending the capsule edges and then arc-welding to minimize the water loss in some runs.

In each run, a capsule was placed in a MgO cylinder in a stepped $LaCrO_3$ heater with a ZrO_2 thermal insulator. The pressure medium was an $MgO + 5\% \ Cr_2O_3$ octahedron with an edge length of 18 mm (standard 18/8 cell assembly at the Bayerisches Geoinstitut). The synthesis temperature was measured using W97%Re3% - W75%Re25% thermocouple with a junction placed at the end of the capsule.

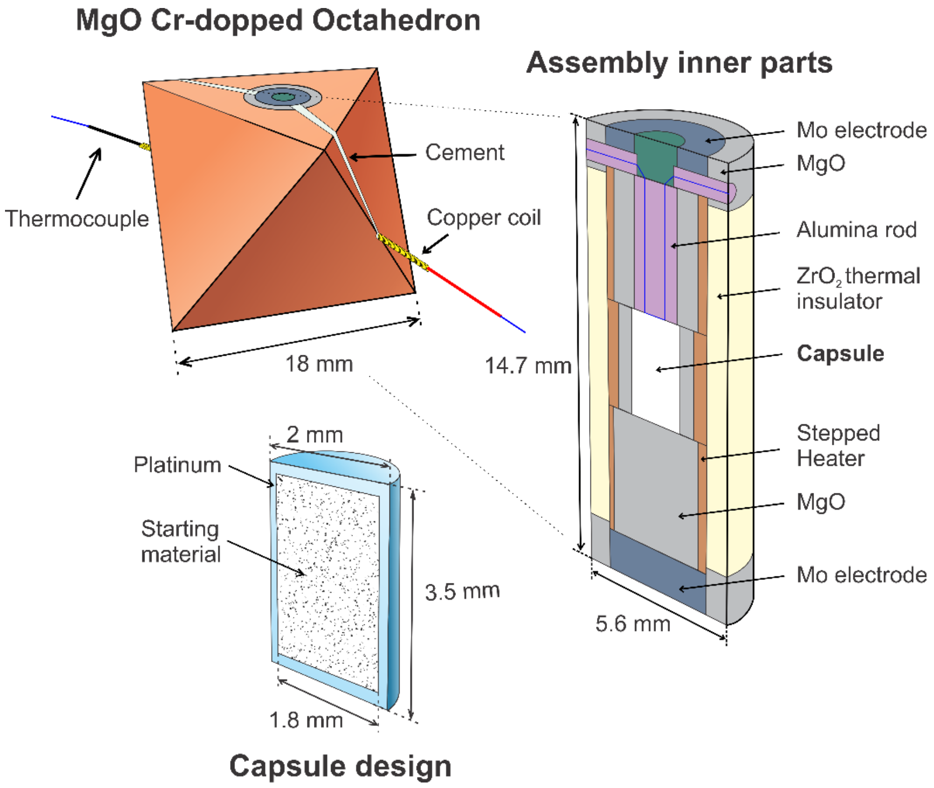

Fig. 7.3. Details of assembly for high PT synthesis experiments (standard 18/8 cell assembly at the Bayerisches Geoinstitut) with cross-sections of a capsule and assembly inner parts.

The pressure calibration made by (Keppler & Frost, 2005) was used for pressure estimation. Compression to the target pressure took 5 – 6 hours. After that, the sample was heated up to the target temperature of around 100 °C/min, and kept at this temperature, which was automatically maintained for 3 hours. Then the sample was quenched by switching off the heating power. Subsequent decompression to ambient pressure took 15 hours to prevent mechanical damage.

7.2. FTIR analysis

We performed H_2O content measurements for samples after synthesis using the Fourier-transform infrared (FT-IR) technique. OH recalculated as H_2O is referred to as the water content since no molecular water is present in nominally anhydrous minerals.

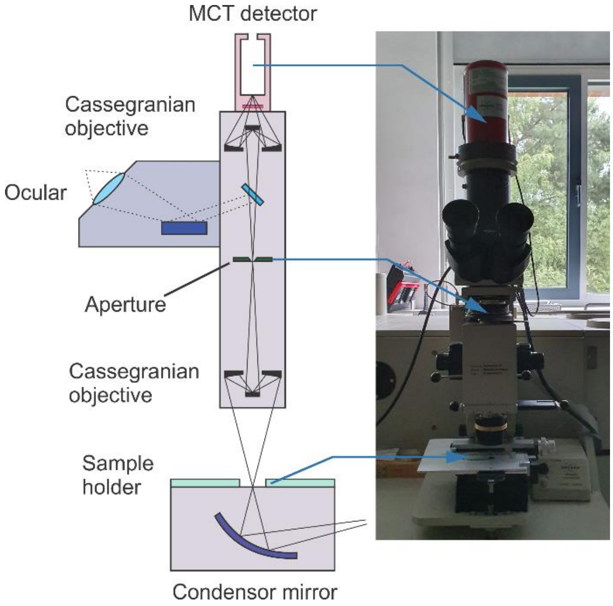

Fig. 7.4. Image and schematic of the Bruker IR microscope used for FTIR sample analysis. (Redraw from (Bolfan-Casanova, 2000))

The water content was measured by the Bruker IFS 120 HR Fourier-transform infrared spectrometer (Siesler, Ozaki, Kawata, & Heise, 2008) coupled with a Bruker IR microscope (**Fig. 7.4**). CaF_2 beam-splitter and a high sensitivity, narrow-band MCT (mercury-cadmium-telluride) detector cooled by liquid nitrogen were used. Analyses were made at room temperature and pressure. Several samples from each sample were mounted in epoxy resin and polished from both sides to a thickness of 100(3) μm. Three unpolarized FTIR spectra on each crystal were collected for each synthesis run with an aperture size of 30 to 1.5 μm and wavenumber resolution of $1 - 2$ cm^{-1}. After a baseline correction and thickness normalization to 1 cm, the water contents in the crystals were calculated using the calibration given by (Paterson, 1982). Integration was performed over the wavenumber range 2800 to 3800 cm^{-1}.

Previous diffusion studies found significant H loss during diffusion experiments. To ensure no water loss during our annealing experiments, polarized FT-IR spectra were collected after diffusion profiles were obtained. Since measurement was performed with the incident light along the diffusion direction calculated water content are results from spectra with the electric vector parallel to the other directions perpendicular to the diffusion one. Wadsleyite has a different water distribution along crystallografic orientations and therefore it was necessary to evaluate water content along the diffusion direction as well. For this purpose, we used ratio of H_2O content from different crystallographic orientation in wadsleyite obtained by (Jacobsen et al., 2005) as a reference assuming that the magnitude of anisotropy in this study is identical to those of our samples.

7.3. Dehydration experiments

The lowest H_2O content obtained in “wet experiments” was around 500 wt. ppm. It cannot be referred to as a “dry” sample. In order to get samples with a much lower water content, an additional treatment was performed to dehydrate the wadsleyite crystals.

For dehydration, several crystals from the same synthesis run were put in a CsCl buffer in a welded gold capsule. The assembly design and HP-HT experimental technique was the same as used for the synthesis experiments described in the Synthesis section above except for the pressure and temperature conditions which were 19 – 20 GPa and 1400 – 1600 ℃ correspondingly. The duration of each dehydration experiment varied from 1 to 5 hours.

7.4. Sample preparation and thin film deposition

Experimental results can have errors caused by resolution of analytical instruments and surface roughness of samples. The diffusion rate of silicon in wadsleyite is so slow that it only produces diffusion lengths of around a few hundred nanometers, and hence a surface roughness of 50 nm or higher is a significant source of the depth resolution error. Considering this, samples were carefully polished and numerous annealing methods were tested to obtain a smooth surface.

7.4.1. Crystal orientation

The procedure of orientating wadsleyite crystals consisted of five steps. **(1)** In the first step, appropriate size (> 0.5 mm) crystals without cracks and visible inclusions were chosen. **(2)** After that, each crystal was mounted on a glass needle and fixed with super glue to avoid them possible falling off during further procedures. **(3)** Next, I found their orientation with respect to diffractometer angles, which is called an orientation matrix. In order to do that, each crystal were placed into the x-ray beam produced by a Mo x-ray tube in a four-circle single-crystal Oxford diffractometer to obtain fast single-crystal diffraction. With the software CrysAlis^{Pro} I analyzed the diffraction pattern and found the unit cell parameters and the orientation matrix **(4)** Subsequent orientation parallel to one of the crystallographic axes was performed with a Bruker diffractometer equipped with a highly precise 2D point detector. During this step, according to the obtained orientation matrix I found the maximum intensity of x-ray peaks diffracted from the desired crystallographic plane. Then I precisely determine the angle relative to the horizont this peak was found and simply rotate sample to this angle. After that crystal is oriented that desired crystallographic plane is parallel to the floor. **(5)** In the last step, oriented crystals were fixed by ultraviolet glue, detached from the needle and then embed in epoxy resin for polishing.

After polishing, the procedure described in detail in the next section, the sample's orientation was checked by SEM with an EBSD detector. The example of CPO (crystallographic preferred orientation) of some oriented samples presented in a **Fig. 7.5** shows results of accurate orientation.

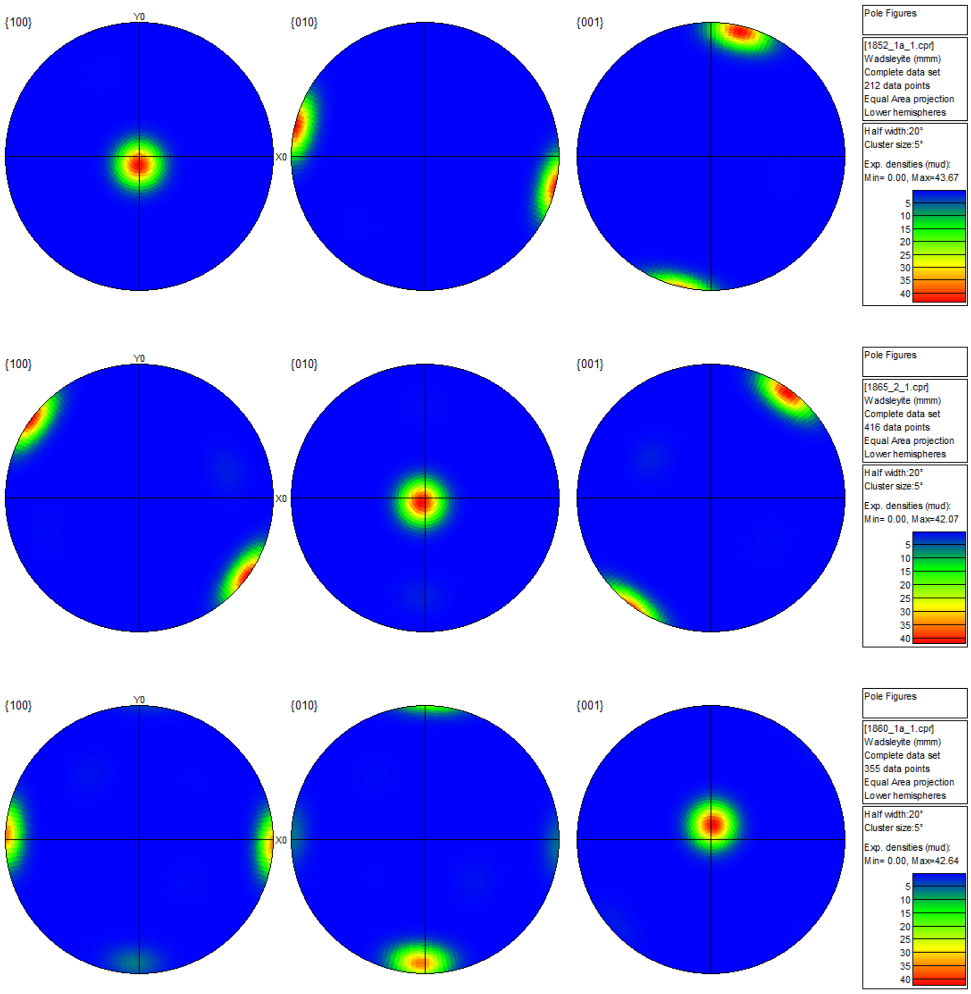

Fig. 7.5. Pole figure plots of samples oriented in *a*- (Z1852_1a), *b*- (Z1865_2) or *c*- (Z1860_1a) direction.

7.4.2. Sample polishing and roughness measurement

The oriented crystals were polished on the plane, in whose normal direction a diffusion profile will be obtained. The roughness of the polished plane was analyzed using a 3D-Nanofocus confocal microscope at University of Bayreuth (**Fig. 7.6**). It consists of a confocal measurement head, which is motor-driven in the vertical direction. The sample is placed on a high-precision x-y stage. The stage movement is carried out by the joystick control or by the system computer. The controller unit contains control electronics, power supply and the computer.

The measurement principle is based on scanning of various height levels of the surface. The light beam from an external light source focuses on the surface at a different height that is reached by the movement of an objective. The light beam reflects from the surface and arrives at a detector which forms an image of the surface at a focused height. By vertical movements of the objective lens, the detector records many images at different height levels (~1000 images). Unfocused beams are disabled by a multi-pinhole disk (a rotating disk with many pinholes). A computer combines all these recorded images in a one topographical 2D or 3D image. This image can be analyzed further in a μSoft software produced by the Company 3D-Nanofocus. The possible area of the measurement depends on the applied objective lens. It can be 160x160 nm for x100 magnification lenses, 320x320 for x50 lenses or 800x800 nm for x20 lenses, which can be changed before measurement.

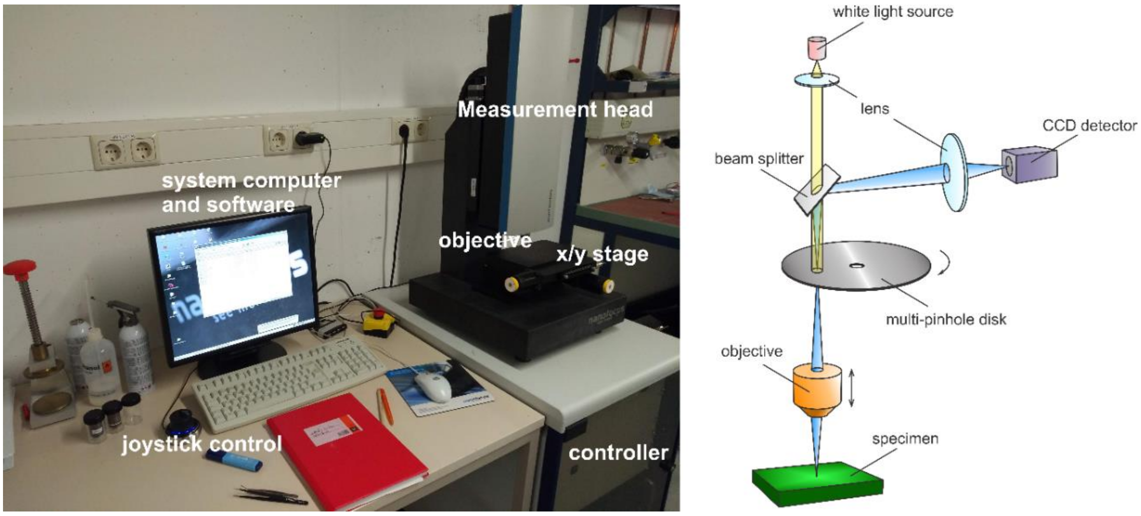

Fig. 7.6. 3D-Nanofocus confocal microscope at the University of Bayreuth, its schematic design and basic principle of work.

The wadsleyite crystals oriented by means of the single-crystal diffractometer were preliminarily polished mechanically using sandpapers and then diamond paste with grain sizes from 6 to 0.25 μm until they were free of visible scratches. An example of mechanically polished surfaces is shown in **Fig. 7.7 a, b**. Since their roughness was not low enough and many micro-scratches were present on the surface, the mechanically polished surfaces were chemically polished using an alkaline colloidal silica solution for 2 – 7 hours until all scratches produced by mechanical polishing were removed. The final roughness was reduced to a few nm (**Fig. 7.7 c**) by this procedure. As shown by (Watson, Cherniak, Thomas, Hanchar, & Wirth, 2016), such polishing does not lead to near-surface structural damage.

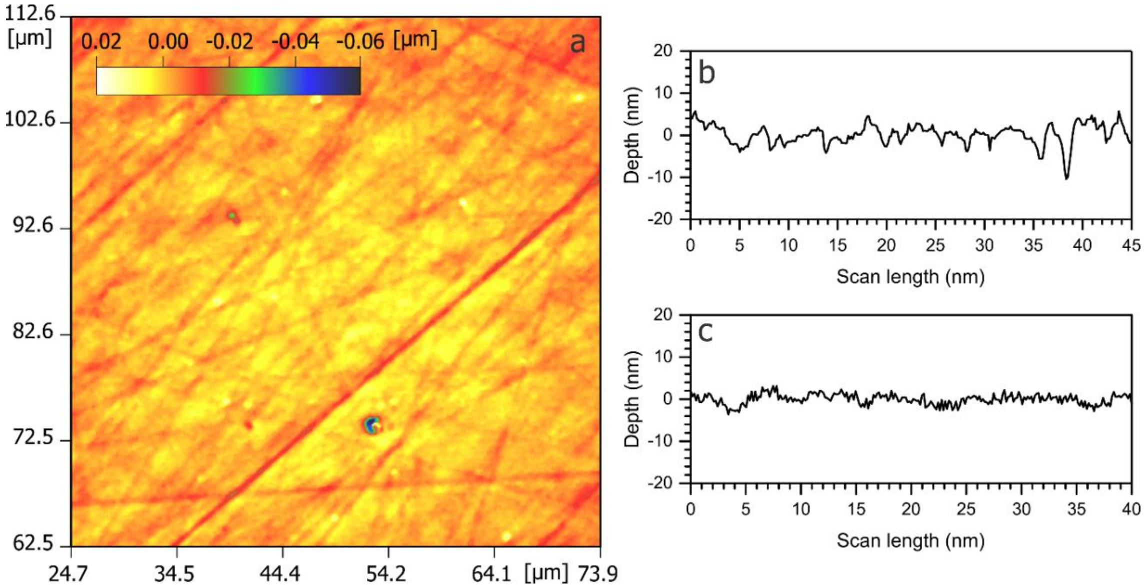

Fig. 7.7. Example of the 2D surface topography of a sample after mechanical polishing (**a**) and its surface profile (**b**). (**c**) is an example of a surface profile after chemical polishing.

7.4.3. Isotopic layer deposition

Following the sample polishing, crystals were removed from epoxy resin by heating samples to 50 – 80 °C. Then they were washed in a distilled water, acetone and ethanol at 40 °C for 10 minutes in each solution. Washed crystals then were put in a special holder, which is a pyrophyllite plate with drilled pits in it, to produce simultaneous deposition on many samples (**Fig. 7.8 a**). The pulsed laser deposition system (PLD) at Ruhr-University, Bochum was used for the deposition. The principle of the PLD system is shown in **Section 4.2**. Prior deposition samples were heated at ~200 °C for a few minutes to remove free water on the sample surface for a better contact between film and substrate. After that, surfaces were deposited with an isotopically enriched film with 500 to 1000 nm thickness. We used a solid solution with $Mg_2{}^{29}Si^{18}O_4$ forsterite composition powder sintered in a pellet as a target material so that we could produce a diffusion couple of ^{29}Si-rich thin film and a crystal with the same composition. The polished surface of crystals after deposition changed color indicating the presence of the coated layer (**Fig. 7.8 b**).

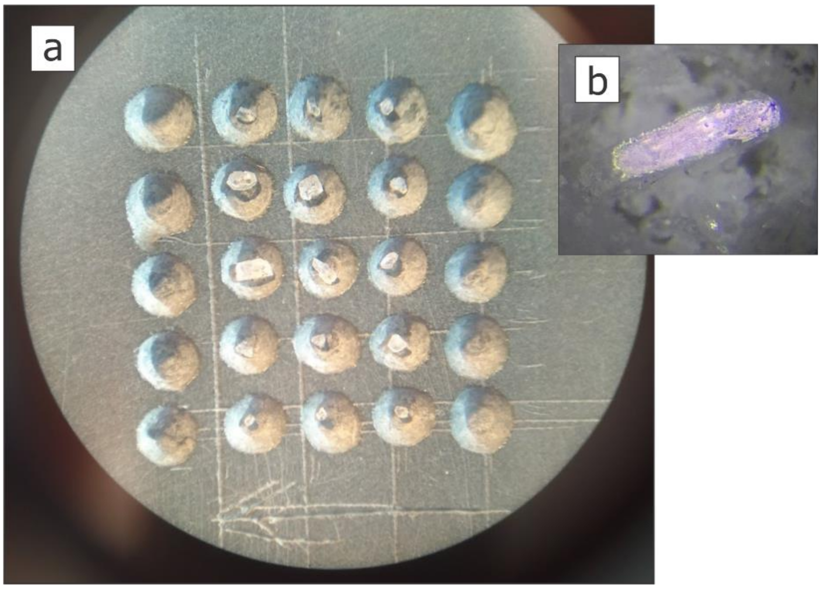

Fig. 7.8. Crystals prepared for deposition on a pyrophyllite holder (**a**). Crystal after deposition (**b**). Surface changed color, indicating presence of deposited thin film.

After that, we analyzed the effect of deposition on surface roughness by the confocal microscope. As shown in **Fig. 7.9 a**, **b** the resulting surface is smooth and its roughness is still within 10 nm. We found that without pre-heating before deposition the surface roughness increased to >50 nm (**Fig. 7.9 c**).

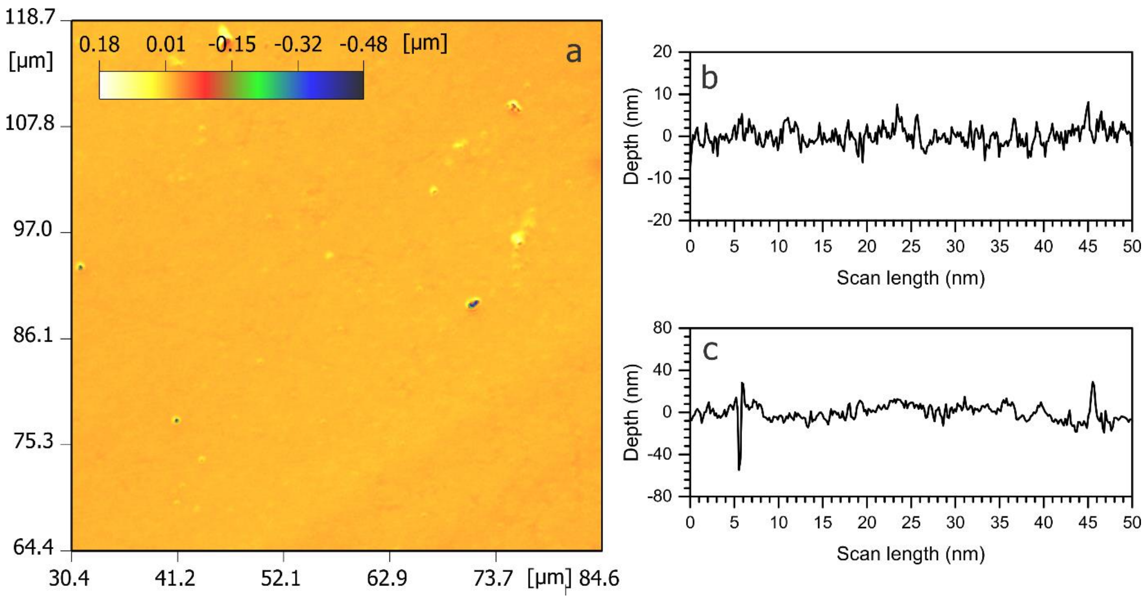

Fig. 7.9. Example of the 2D surface topography of a sample after thin film deposition (**a**) and its surface profile (**b**). (**c**) is an example of a surface profile after deposition without prior heating of a sample.

7.5. Diffusion annealing

The main problems that we encountered were to find a proper material surrounding a crystal to prevent a significant increase of the surface roughness after diffusion annealing. The surrounding material should be soft enough to prevent mechanical damage. It should maintain the water content in the sample and be unreactive with wadsleyite crystals. Among different test setups (**Fig 7.10**) it was found that a mixture of forsterite and enstatite as a surrounding material leads to a reaction between crystals and the surroundings and complete breakage of crystals. CsCl or NaCl as a surrounding material causes corrosion of crystals (even in case sample was covered by gold foil) and significantly decreases the H_2O concentration in the samples. Finally, we used a capsule design shown in **Fig. 7.11**. It was established that the crystal should be placed on a polished (less than 10 nm roughness) single-crystal diamond disk to minimize the sample's surface damage during the annealing experiment. We used Ia-type diamond synthesized by the CVD technique and then (100)-oriented (**Fig. 7.12 a**). The diamond surface was polished by manufacture to a roughness of 5 nm. Each sample was loaded in a gold capsule with outer diameter 2 mm and inner diameter 1.8 mm. Gold powder was used as a surrounding buffer to avoid mechanical breakage of the crystal from at high pressures and to prevent its dehydration during the diffusion.

Fig. 7.10. Schematics of all rejected setups tested in this work for diffusion annealing experiments. Thin-film is marked as a red area. A short list of the main problems I faced by using each setup is given below each design picture.

However, in some runs the thin film completely or partially reacted with the diamond surface during the annealing. A small amount of dry, pure $MgSiO_3$ enstatite powder was placed on a crystal's backside to control the silica activity. Besides low surface roughness and stable water content, this setup allows samples to be easily removed from the assembly after experiments without any damage tp the single crystal.

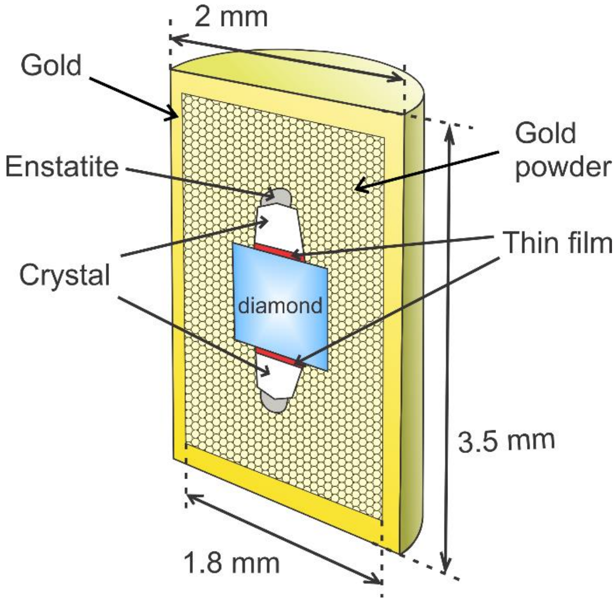

Fig. 7.11. Details of a capsule design for annealing experiments. In some runs we used CsCl pellets instead of a gold powder as a surrounding material and crystals were covered by gold foil for protection.

Annealing experiments were performed using a Kawai-type multi-anvil apparatus (5000-tonf Zwick press at Bayreuth University). Assuming that a pressure variation of 1.5 GPa is negligible for diffusion rates in wadsleyite as is in forsterite (H. Fei et al., 2012) and in order to stay in the wadsleyite stability field, we performed experiments at different pressures for different temperatures: at 1600, 1400 and 1300 ℃ and at 20, 19, and 18.5 GPa, correspondingly. We used the same assembly design (**Fig. 7.3**) that we used in the synthesis experiments (see **Section 7.1**). The annealing durations varied from 10 minutes to 10 hours.

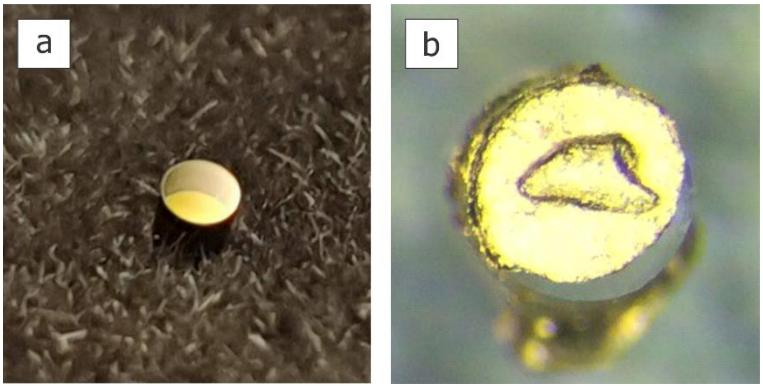

Fig. 7.12. Photo of a diamond used in diffusion annealing experiments (**a**) and photo of a crystal on a diamond, protected by gold foil after annealing in CsCl (**b**).

7.6. SIMS analysis

The wadsleyite crystals recovered after annealing experiments were mounted in discs of epoxy resin (10 mm diameter and 1.5 mm thickness) and covered by a 10 nm gold coat (**Fig. 7.13 a**). Seven epoxy discs can be loaded simultaneously for analysis using a special sample holder in the NanoSIMS (**Fig. 7.13 b**). This enabled us to quickly change analysis spots between samples. In this study, we used a NanoSIMS facility installed at Institute of Geology and Geophysics, Chinese Academy of Science at Beijing. We used a Cs^+ primary beam with different 20 – 160 pA current focused to 10×10 µm raster on the sample surface. Detailed description of the machine and the method is described in the **Section 4.3.1**. Since every NanoSIMS measurement in depth mode is a very time consuming process we used a compromise beam current that further analysis could be performed by using data from a center of a crater that is not effected by the crater's edges. Profiles of obtained craters are shown in **Sections 8.5** and **11.3**.

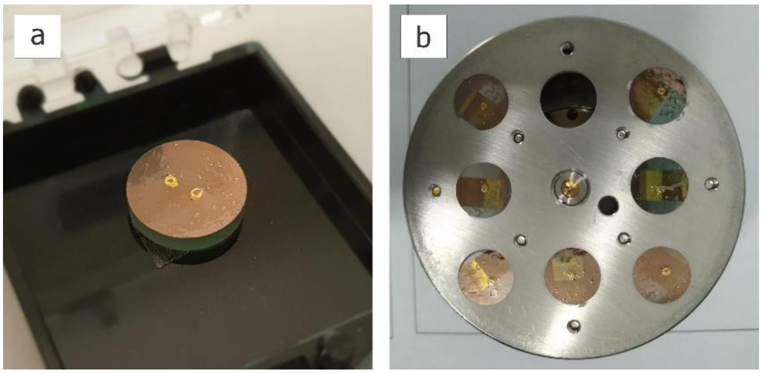

Fig. 7.13. Photo of an epoxy round coated by gold with samples ready for analysis (**a**) and a photo of special sample holder for NanoSIMS analysis (**b**).

Secondary ion intensities of the sputtered crater have been collected as a series of 2D images (**fig. 9.11**). Each image has an area distribution of a number of sputtered ions from the surface of a 10×10 µm area and several nm depth, where the number of particles corresponds to a specific RGB color. They were further analyzed using ImageJ software with an installed plugin for work with a CAMECA SIMS files. Each measurement lasted for several hours and resulted in a stack of several hundreds of these images depending on the beam configuration and diffusion profile length. We stopped each measurement when ^{29}Si intensity is minimal during several tens of collected images. As shown in **Fig. 7.14** obtained images have lower intensities around the edges, which may be due to the presence of a small edge effect.

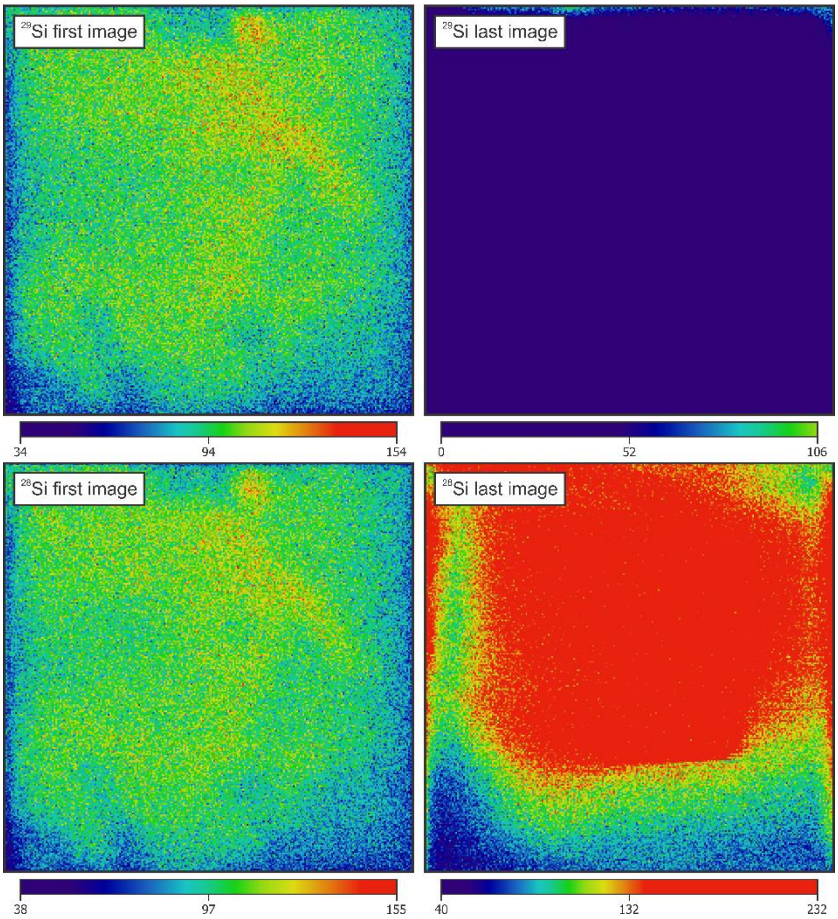

Fig. 7.14. Example of resulted 2D images of secondary ^{29}Si and ^{28}Si ions intensities analyzed in ImageJ software.

7.7. Data fitting and self-diffusion coefficient

The volume diffusion coefficient of Si, $D_{\mathrm{Si}}^{\mathrm{V}}$, and O, $D_{\mathrm{O}}^{\mathrm{V}}$, were obtained mostly by fitting an isotope profile with depth to the following equation:

$$C(x,t) = \frac{C_0 + C_1}{2} - \frac{C_1 - C_0}{2} \cdot \mathrm{erf}\left(\frac{x-h}{\sqrt{4D^{\mathrm{V}}t + L_0^2}}\right) \tag{7.1}$$

where L_0 is the nominal diffusion length at zero time. As shown in **Fig 7.15**, the diffusion length at zero time obtained by run Z1702 is not zero, which should mainly come from the surface roughness and depth resolution of NanoSIMS.

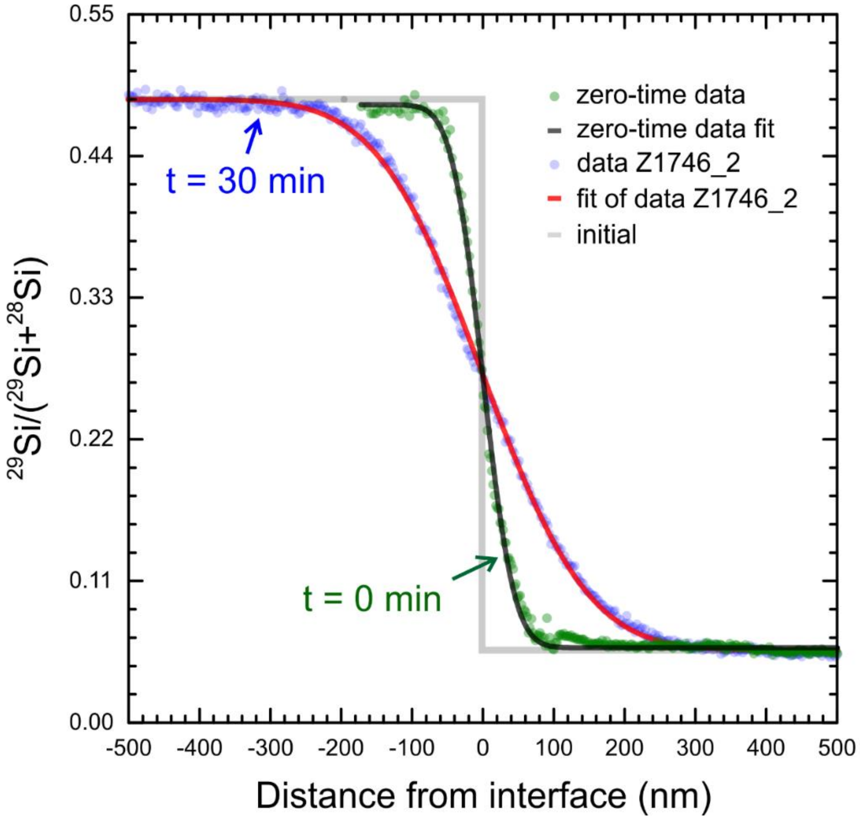

Fig. 7.15. Examples of fitted Si self-diffusion zero (run Z1702) and non-zero (run Z1746) profiles.

Since the number of wadsleyite single crystals that can be used for diffusion experiments is limited, L_0 was obtained only in two zero-runs from samples with different surface roughness by fitting depth profiles to equation:

$$C(x,t) = \frac{C_0 + C_1}{2} - \frac{C_1 - C_0}{2} \cdot \operatorname{erf}\left(\frac{x-h}{\sqrt{L_0^2}}\right) \tag{7.2}$$

The nominal diffusion length L_0 obtained in this study at different sample roughnesses is shown in **Fig. 7.16** together with previous data by (H. Fei et al., 2012) for olivine samples. Since all L_0 can be approximated by the linear function of the surface roughness similar to (H. Fei et al., 2012), this approximation is used in further fittings.

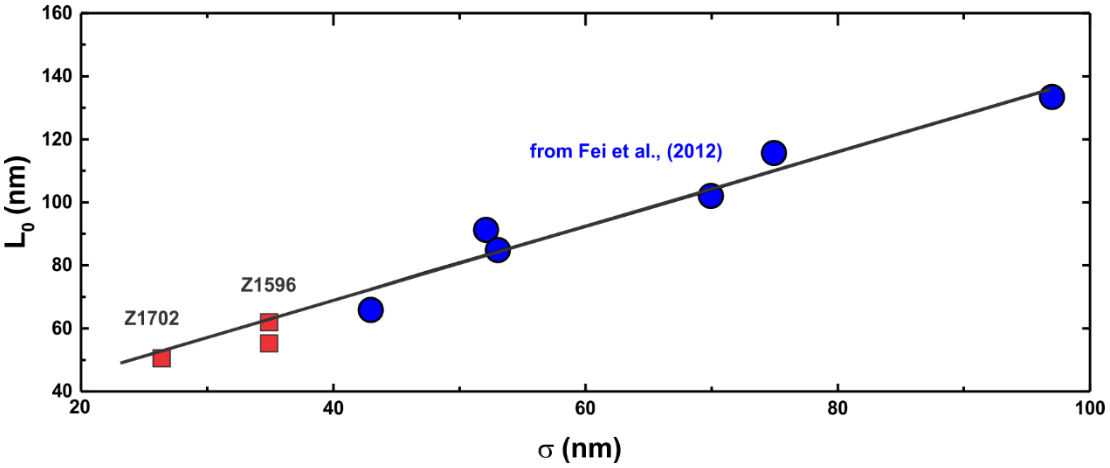

Fig. 7.16. Nominal diffusion length at different surface roughness of studied samples. Red squares are data obtained in this study. Blue rounds are data from (H. Fei et al., 2012), and solid black line is its linear approximation.

In some profiles relatively low isotope ratios were observed near the surface away from the interface between the thin film and single crystal (**Fig. 7.17**).

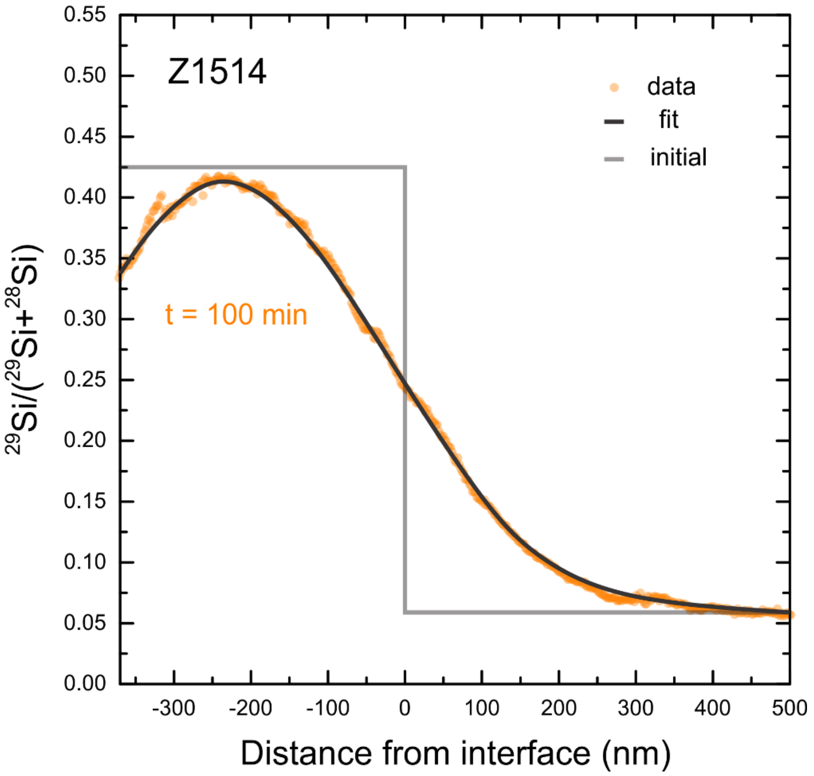

Fig. 7.17. Example of fitted a Si self-diffusion profile (run Z1514) with isotope ratio diminution near the sample surface (orange dots). Solid black line is a numerical simulation of this profile.

This has also been observed in previous studies (Xu et al., 2011; Dohmen et al., 2002). In cases of this near surface diminution, the isotope profile was numerically simulated to evaluate$D_{\mathrm{Si}}^{\mathrm{V}}$. Detailed description of these simulations is shown in **Section 4.4**. The resulting diffusion coefficients for silicon self-diffusion in wadsleyite are summarized in **Table 8.5** (**Section 8.7**).

8. Results

8.1. Synthesis of wadsleyite crystals

Results of wadsleyite single crystals synthesis are summarized in **Table 8.1**. The first four runs (Z1254, Z1296, Z1303 and Z1306) were conducted at pressures of 16.5 to 19 GPa, which were estimated by the pressure-load calibration provided by the BGI multi-anvil laboratory (Keppler & Frost, 2005). Though, these conditions should be in the stability field of wadsleyite (Inoue et al., 2010; Katsura & Ito, 1989b; Katsura et al., 2004, 2003; Shatskiy et al., 2009), obtained samples were forsterite. Since the pressure calibrations were made between room temperature and 1400 ℃, the higher temperature in the present investigation may have lowered the sample pressures. Another possibility is that forsterite may have well annealed during heating, which may have made it very inert.

Wadsleyite formed in experimental runs at a temperature of 1770 ℃ and a pressure of 21 GPa. The first run where wadsleyite crystals were successfully synthesized (Z1309) used forsterite powder as a starting material. Raman spectroscopy and microfocus X-ray diffraction were used for sample identification. The grain sizes were from 300 to 800 µm, which were suitable for the diffusion study. However, this sample contained melt, which may have been produced by water adsorbed on the starting forsterite powder.

Inclusions were found in the majority of the synthesized crystals, probably due to initial contamination of the starting forsterite powder we used. For this reason, grinded synthesized single crystal of forsterite provide by the Japanese company “Oxides” was used as a starting material in later runs, which results in wadsleyite crystals with no inclusions. The same forsterite crystal was used by (H. Fei et al., 2012).

It must be noted, however, that Wadsleyite crystals synthesized from forsterite ground from a single crystal had a wider size distribution, from less than 50 µm to ~1 mm. In one run (Z1478), a single crystal of forsterite was added to the starting material. It did not lead to an increase in size of the resulting wadsleyite crystals. Moreover, the largest crystals have numerous cracks parallel to each other in most runs, which are probably caused upon decompression. Since this leads to crystals spliting into many thin plates (< 100 µm thickness), the majority of them could not be used in further diffusion experiments.

However, many crystals with sizes from 0.4 to 0.6 mm and a few with sizes around 1 mm had no inclusions and cracks (**Fig. 8.1**). Uniform extinction upon sample rotation under cross-polarized light indicated that the crystals were single crystals. Crystals that had no obvious cracks and impurities were used in the further preparation process.

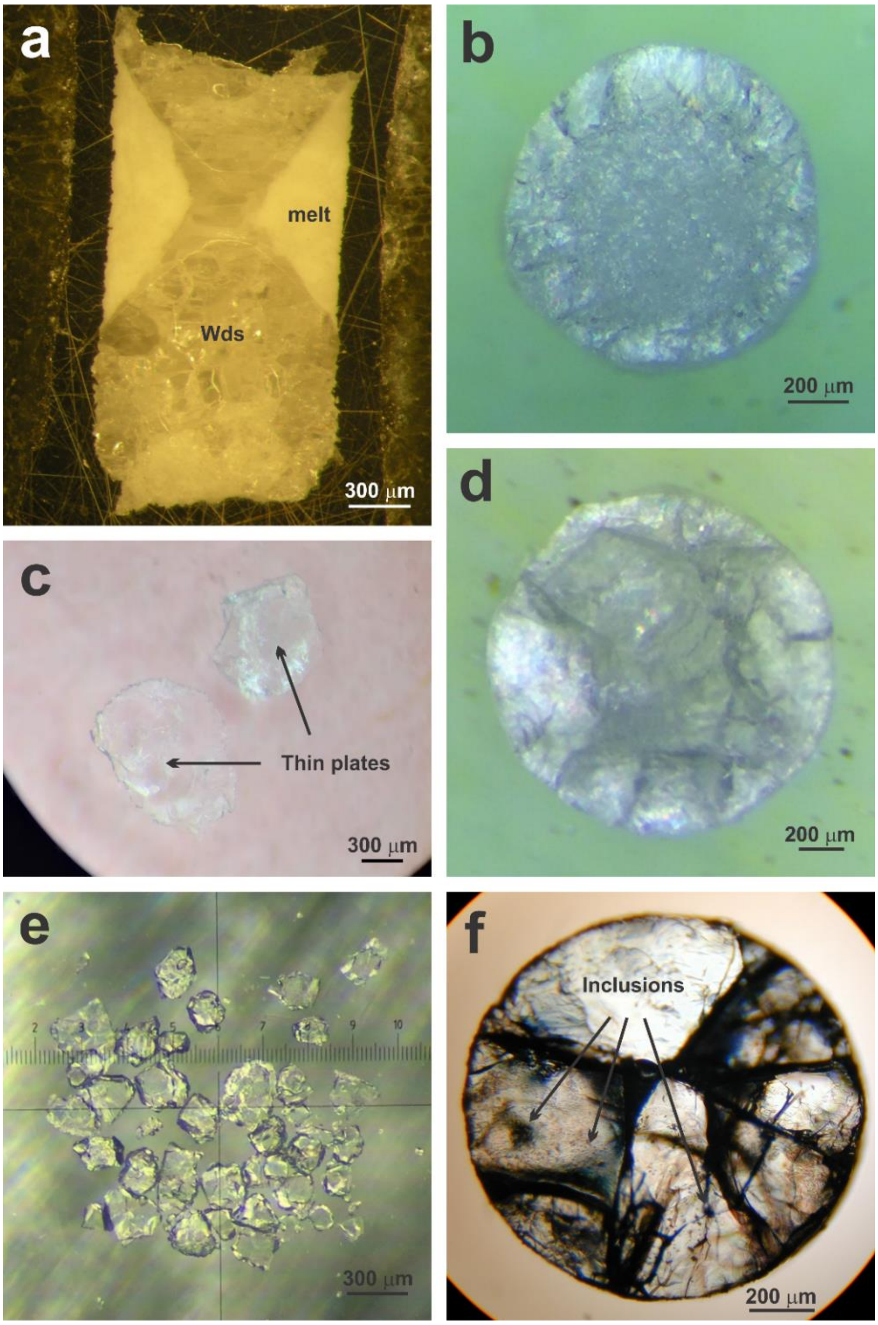

Fig. 8.1. Optical micrographs of Mg_2SiO_4 wadsleyite single crystals. **(a)** Melt and wadsleyite crystals in coexistence (run Z1309). **(b)** Round shape crystal aggregate, which has a few hundred µm crystals on the outside and less than 100 micron in the inner part (run Z1451). **(c)** An example of thin plates of 100 µm thickness left from large crystals after decompression (run Z1870). **(d)** Wadsleyite single crystals larger than 1 mm in the middle part of a round shape crystal aggregate after long heating (run Z1646). **(e)** Crystals with the most common size and shape among all obtained crystals (run Z1328). **(f)** Inclusions found in some (~ 1 mm) crystals (run Z1478).

Table 8.1. *Experimental conditions and results of wadsleyite single crystal growth.*

Run number	P (GPa)	T (℃)	Time (min)	Starting material	Run products	C_{H_2O} (wt. ppm)$^+$		
						Paterson	L&R	Deon
Z1254*	16.5	1700	90	Fo powder	Fo crystals	-	-	-
Z1296*	17	1750	150	Fo powder	Fo crystals	-	-	-
Z1303	18	1750	100	Fo powder	Fo crystals	-	-	-
Z1306	19	1770	90	Fo powder	Fo crystals	-	-	-
Z1309	21	1770	220	Fo powder	Wds crystals 300 – 800 µm + melt	566(30)	563(28)	865(33)
Z1321	21	1770	120	Fo single crystal (grinded)	Wds crystals <50 – 500 µm	-	-	-
Z1338	21	1770	160	Fo single crystal (grinded)	Wds crystals <50 – 500 µm	108(9)	134(7)	194(10)
Z1449	21	1770	240	Fo single crystal (grinded)	Wds crystals 300 – 500 µm	179(14)	166(8)	184(12)
Z1451	21	1770	90	Fo powder	Wds crystals 200 – 400 µm	-	-	-
Z1478	21	1770	180	Fo powder + Fo single crystal	Wds crystals^{in} >1000 µm + melt	926(44)	1088(52)	1505(70)
Z1481*	21	1770	180	Fo single crystal (grinded)	Wds crystals <50 µm	< 30	< 30	< 30
Z1534	21	1770	180	Fo single crystal (grinded)	Wds crystals 300 – 400 µm	125(10)	153(12)	224(11)
Z1539	21	1770	180	Fo powder	Wds crystals^{in} + melt	-	-	-
Z1599	21	1770	150	Fo powder	Wds crystals^{in} + melt	338(27)	233(22)	447(22)
Z1603	21	1770	120	Fo powder	Wds crystals^{in} + melt	1122(26)	1336(66)	1883(70)

$^+$ water contents calculated using calibrations of Paterson (Paterson, 1982), L&R (Libowitzky & Rossman, 1997) and Deon (Deon et al., 2010)

* starting material was preliminary dried in an oven

^{in} indicate presence of inclusions in grown crystals

$^{++}$ experiments where welded capsule was used

Table 8.1 (continued). *Experimental conditions and results of wadsleyite single crystal growth.*

Run number	P (GPa)	T (°C)	Time (min)	Starting material	Run products	C_{H_2O} (wt. ppm)$^+$		
						Paterson	**L&R**	**Deon**
Z1634^{++}	21	1770	120	Fo single crystal (grinded)	Wds crystals 100 – 400 μm	314(15)	394(12)	572(7)
Z1639^{++}	21	1770	180	Fo single crystal (grinded)	Wds crystals 100 – 500 μm	93(5)	113(5)	163(8)
Z1646^{++}	21	1770	210	Fo single crystal (grinded)	Wds crystals 400 – 1000 μm	763(19)	970(20)	1373(22)
Z1649^{++}	21	1770	300	Fo single crystal (grinded)	Wds crystals < 500 μm	805(20)	997(25)	1526(42)
Z1654^{++}	21	1770	140	Fo single crystal (grinded)	Wds crystals < 500 μm	532(27)	648(32)	911(35)
Z1792^{++}	21	1770	180	Fo powder + Fo single crystal	Wds crystals^{in} < 1000 μm	3050(56)	3230(37)	3854(145)
Z1800^{++}	21	1770	150	Fo single crystal	Wds crystals < 1000 μm	1660(24)	1704(34)	2105(40)
Z1868^{++}	21	1770	150	Fo single crystal	Wds crystals < 1000 μm	3402(35)	3602(45)	4020(123)
Z1870^{++}	21	1770	180	Fo single crystal	Wds crystals < 1000 μm	5020(120)	5133(118)	6230(120)

$^+$ water contents calculated using calibrations of Paterson (Paterson, 1982), L&R (Libowitzky & Rossman, 1997) and Deon (Deon et al., 2010)

* starting material was preliminary dried in an oven

^{in} indicate presence of inclusions in grown crystals

$^{++}$ experiments where welded capsule was used

Synthesized crystals had the orthorhombic symmetry with the *Imma* space group. The unit cell parameters of wadsleyite from were $a = 5.692(9), b = 11.400(14), c = 8.272(9)$ Å with a cell volume of $V = 536.760$ Å^3, which was obtained using a crystal from the run Z1478. The average full-width at half-maximum of the final phi scans was 0.3(1)° (**Fig. 10.2. a**) showing the high quality of the crystals. A peak from a desirable crystallographic plane is very sharp and intense. Uniform extinction under polarized light for this crystals excluded crystal twinning or the presence of more than one single crystal (**Fig. 8.2. b**).

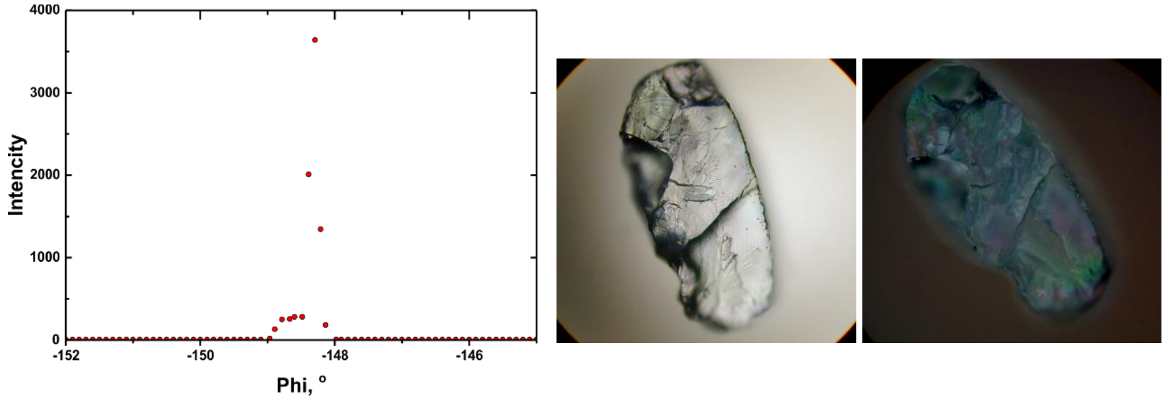

(a) (b)

Fig. 8.2 Final Phi scans of a crystal from run Z1478 (a), its transmitted optic microscope with and without polarized light.

8.2. FT-IR spectra and concentration of H_2O

In this section, we show the FTIR spectra of the crystals obtained by different synthesis runs (**Fig. 8.3**) that were used in the diffusion experiments (**Fig. 8.5**). Detailed spectra are presented in Appendix (**Section 11.1**). We also present here results of water calculations for samples after diffusion annealing. Water contents of the samples after synthesis and diffusion annealing are presented in **Table 10.1** and **Table 8.4**, respectively.

For spectra from synthesized crystals, identified infrared absorption peaks can be separated in to two groups. The main group of most intense peaks consists of triplet of 3358, 3311 and 3260 cm^{-1}. These bands correspond to 3360, 3317, 3264 cm^{-1} peaks in the spectra of (Jacobsen et al., 2005) (**Fig. 8.4**). The second group has peaks at 3613 and 3579 cm^{-1}, which are similar to 3614 and 3581 cm^{-1} by (Jacobsen et al., 2005).

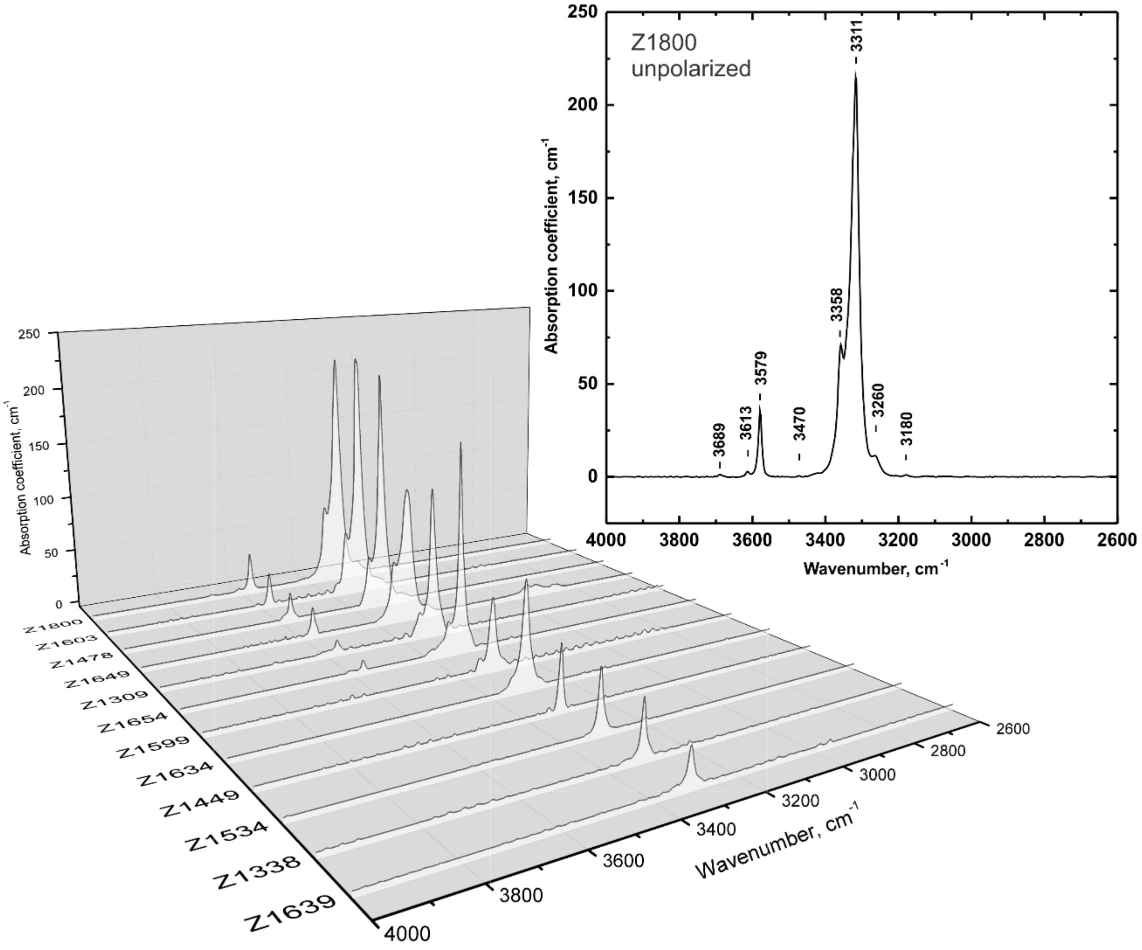

Fig. 8.3. A series of unpolarized FTIR spectra of Mg_2SiO_4 wadsleyite obtained from different synthesis runs (left) and an FTIR spectrum with positions of identified peaks (right).

The peaks that were not included in these groups were found at 3689, 3470, 3180 cm^{-1}. I did not observe any significant difference in peak positions among samples from different synthesis runs. As in previous studies (Demouchy et al., 2005; Deon et al., 2010; Jacobsen et al., 2005) a peaks at 3327 cm^{-1} for low water contents (60-80 wt. ppm) shift to 3317 cm^{-1} with increasing water content (1300 wt. ppm). Positions of identified peaks of all samples are presented in **Section 11.1**. The difference among the spectra is mostly in higher peaks intensities and the appearance of peaks caused by higher water contents. No additional main peak appeared and no significant peak shifts occurred after the diffusion experiments (**Fig. 8.5**).

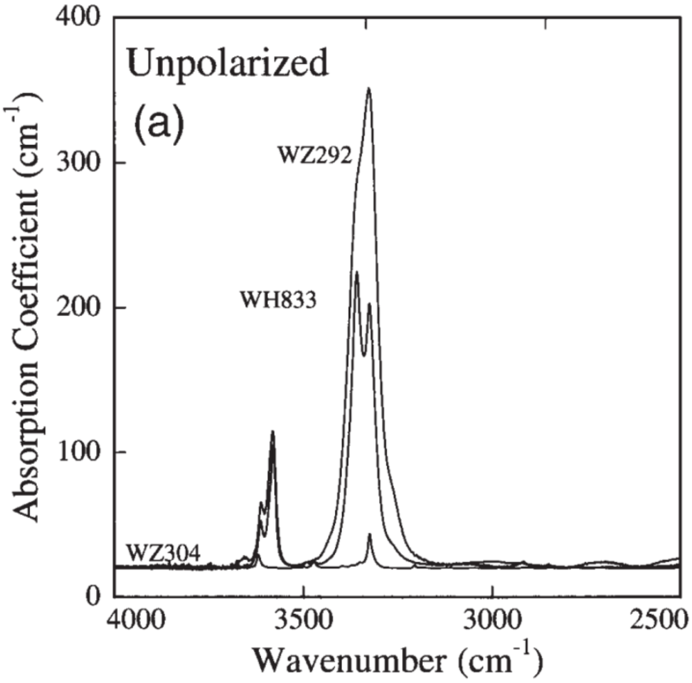

Fig. 8.4. Unpolarized FTIR spectra of iron-free wadsleyite of 150 – 9600 wt. ppm water contents. Picture is taken from (Jacobsen et al., 2005).

However, in some runs two peaks of the main group (~3354 cm^{-1} and ~3323 cm^{-1}) have a tendency to have similar intensities. It could be due to small saturation effects in this samples, though the same was observed in samples containing only a few thousands of wt. ppm H_2O by (Jacobsen et al., 2005), which was not specified as H_2O saturated. The majority of peaks are easily distinguishable and are not oversaturated, thus the obtained spectra were concidered satisfacting for further water estimation. Additionally, some spectra have a peak at ~3406 cm^{-1}.

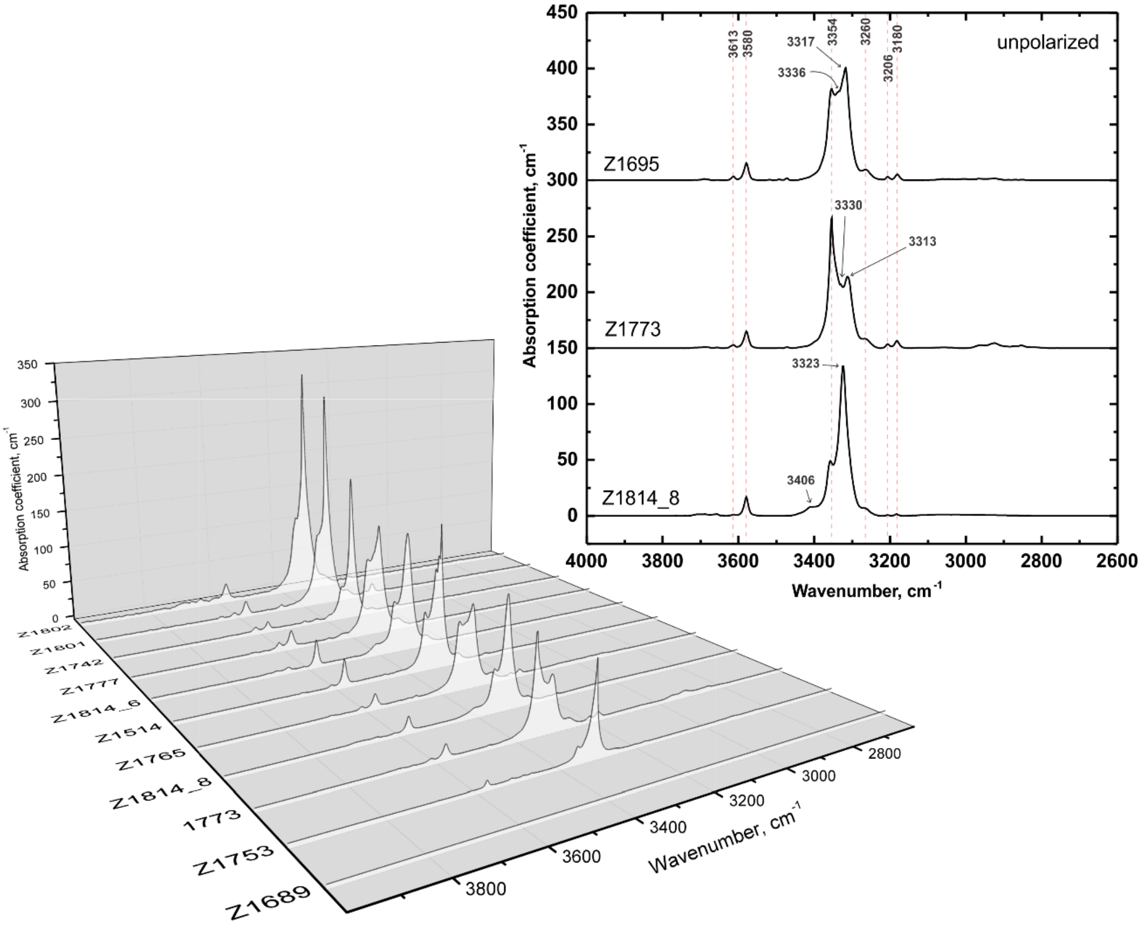

Fig. 8.5. A series of unpolarized FTIR spectra of Mg_2SiO_4 wadsleyite obtained from samples after *diffusion experiments* (left) and FTIR spectra with identified peaks of three observed types of peak positions (right). Positions of peaks that do not change beyween samples are marked by red dotted line.

Water content in the samples were estimated using the calibration by (Paterson, 1982) with comparing with those by (Libowitzky & Rossman, 1997) and (Deon et al., 2010) (**Table 8.1**, **Table 8.2** and **Table 8.3**). In order to be sure that water contents do not change during annealing experiments we measured water contents before and after diffusion annealing for the same samples. Due to special preparations of samples for FTIR, which makes the sample is unusable for the subsequent annealing experiments, only those crystals that had been broken in fragments were used for water estimation before the diffusion annealing. That put large limitations on the number of samples used for this analysis.

Table. 8.2. *Resulted water content after annealing experiments and before annealing (last column).*

Sample number	P (GPa)	T (℃)	Annealing time (min)	$C_{\mathrm{H_2O}}(\mathrm{wt.\,ppm})^{+}$			
				Paterson	**L&R**	**Deon**	**Before (Paterson)**
Z1695_2	20	1600	600	< 30	< 30	< 30	546(55)
Z1753_1	20	1600	10	456(35)	562(43)	802(49)	445(23)
Z1753_2	20	1600	10	456(35)	562(43)	802(49)	445(23)
Z1514_4	20	1600	100	1733(120)	2007(137)	3050(144)	1645(84)
Z1814_61	19	1400	100	2181(63)	2641(106)	3799(130)	-
Z1814_62	19	1400	100	2181(63)	2641(106)	3799(130)	-
Z1886_3	20	1600	600	< 30	< 30	< 30	-
Z1890	20	1600	600	< 30	< 30	< 30	-
Z1895_1	20	1600	240	3100(32)	3754(35)	4818(65)	-
Z1893_1	20	1600	45	3023(97)	3608(113)	4698(133)	-
Z1742_1	20	1600	15	978(14)	1167(78)	1636(69)	-
Z1742_2	20	1600	15	978(14)	1167(78)	1636(69)	-
Z1742_3	20	1600	15	978(14)	1167(78)	1636(69)	-
Z1777_1	20	1600	20	2469(78)	2990(114)	3837(119)	-
Z1777_2	20	1600	20	2469(78)	2990(114)	3837(119)	-
Z1801_1	20	1600	30	3523(155)	4266(120)	5475(144)	-
Z1801_2	20	1600	30	3523(155)	4266(120)	5475(144)	-
Z1827_10d1	19.5	1500	20	1547(99)	1846(104)	2587(110)	1609(112)
Z1827_10d2	19.5	1500	20	1547(99)	1846(104)	2587(110)	1609(112)
Z1826_8d1	19.5	1500	60	3570(67)	4135(120)	6283(119)	-
Z1906_75.4	19	1400	600	3056(135)	3701(78)	5324(147)	-
Z1765_2	20	1600	15	2453(54)	3023(84)	3812(101)	-
Z1765_3	20	1600	15	2453(54)	3023(84)	3812(101)	-
Z1746_1	20	1600	30	2817(210)	3411(214)	4378(246)	-
Z1746_2	20	1600	30	2817(210)	3411(214)	4378(246)	-
Z1773_1	20	1600	15	3095(103)	3585(63)	5177(109)	-
Z1773_2	20	1600	15	3095(103)	3585(63)	5177(109)	-
Z1773_3	20	1600	15	3095(103)	3585(63)	5177(109)	-
Z1757	20	1600	10	4814(234)	5745(173)	8387(220)	-
Z1814_81	19	1400	30	2665(46)	3285(52)	4690(67)	-
Z1802_91	19	1400	60	3523(19)	4080(33)	6137(25)	-
Z1802_92	19	1400	60	3523(19)	4266(33)	5475(25)	-
Z1817_21	18.5	1300	150	3055(78)	3765(70)	4748(113)	-

[+] water contents calculated using calibrations of Paterson (Paterson, 1982), L&R (Libowitzky & Rossman, 1997) and Deon (Deon et al., 2010)

8.3. Dehydration experiments

Results of the dehydration experiments are shown in **Table 8.3**. Resulting water contents in samples varied from less than 30 wt. ppm (no FTIR peaks were found) to 870 wt. ppm (Z1815). The optimal PT conditions and annealing time are hard to predict from the results, but it is clear that a longer duration leads to a lower water content in case of the same initial water content. Observed peak positions (**Fig. 8.6**) match with those observed from samples right after synthesis (**Fig. 8.5**). Detailed peak positions and all spectra are presented in supplementary material.

Table. 8.3. *Resulted water content after dehydration experiments.*

Sample number	**P (GPa)**	**T (℃)**	**Dehydration Time (min)**	**C_{H_2O}(wt. ppm)⁺**			
				Paterson	**L&R**	**Deon**	**Before (Paterson)**
Z1815	19	1400	120	868(20)	1007(23)	1385(31)	3500(43)
Z1852	20	1600	300	<30	<30	<30	982(55)
Z1856-1	20	1600	240	122(4)	148(4)	214(5)	978(23)
Z1856-2	20	1600	240	115(3)	143(4)	207(5)	978(23)
Z1860-1	19.5	1500	240	94(3)	120(4)	176(4)	470(33)
Z1860-2	19.5	1500	240	165(4)	207(5)	302(5)	470(33)
Z1863-1	20	1600	240	500(15)	604(14)	854(20)	2390(17)
Z1863-2	20	1600	240	230(10)	291(12)	424(10)	2210(34)
Z1865	20	1600	100	389(9)	465(11)	658(14)	1000(42)
Z1867	20	1600	100	369(9)	445(10)	628(15)	978(23)
Z1871-1	20	1600	60	275(6)	339(6)	484(11)	520(41)
Z1871-2	20	1600	60	322(8)	390(9)	561(13)	520(41)
Z1875-1	20	1600	260	581(13)	673(13)	930(25)	2330(50)
Z1875-2	20	1600	260	434(10)	518(12)	726(17)	2300(43)

[+] water contents calculated using calibrations of Paterson (Paterson, 1982), L&R (Libowitzky & Rossman, 1997) and Deon (Deon et al., 2010)

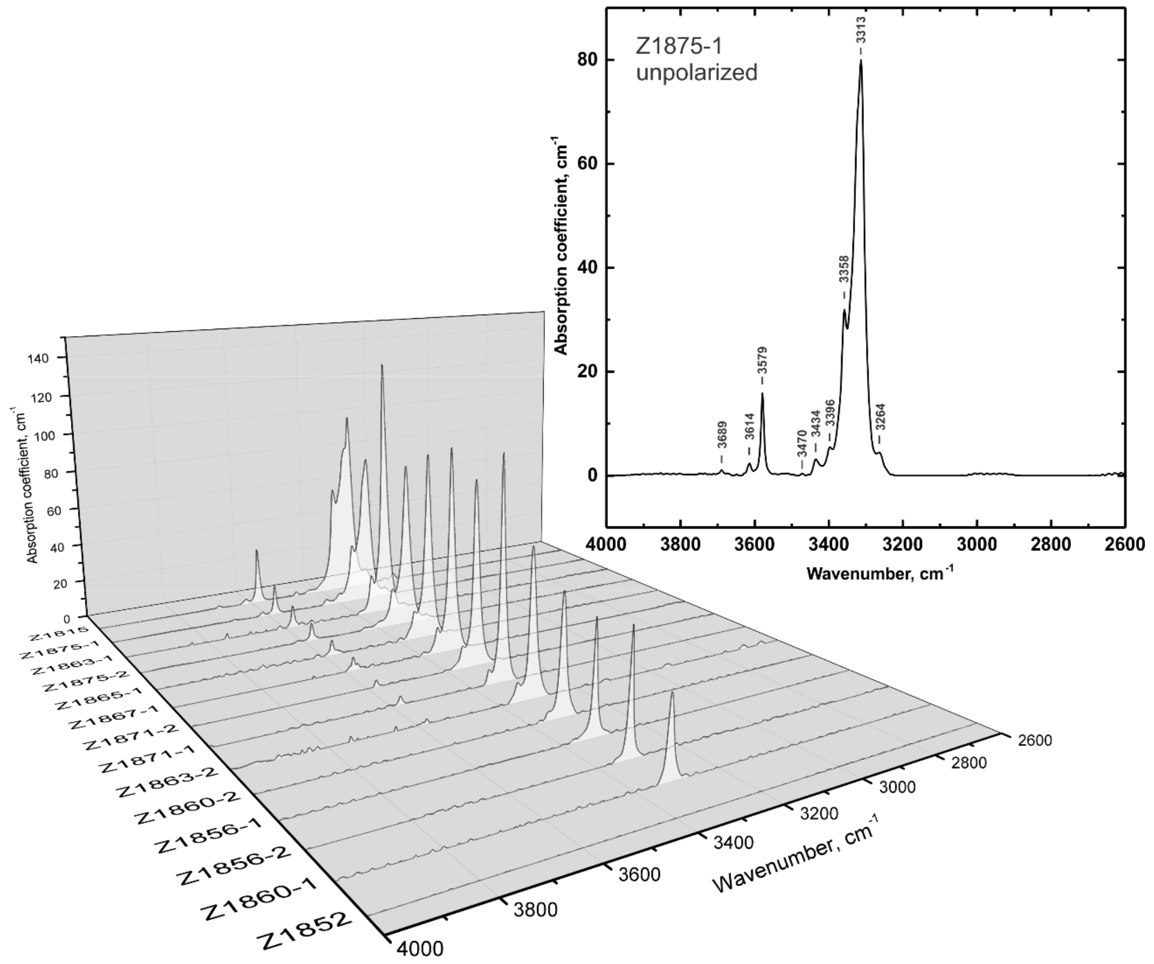

Fig. 8.6. A series of unpolarized FTIR spectra of Mg_2SiO_4 wadsleyite obtained from samples after *dehydration experiments* (left) and an FTIR spectrum with the position of identified peaks (right).

8.4. Results of annealing experiments

Here I describe the most successful setups where wadsleyite crystals did not completely react with the surroundings and were not broken into small fragments (< 200 μm) during annealing experiments.

As shown in **Fig. 8.7 c** wadsleyite undergoes a color change from transparent to a whitish color probably due to a corrosion of the crystal's surface by a reaction with a CsCl. Additionally, the crystal has many cracks after annealing (**Fig. 8.7 b**), but more significant is that the roughness increased to several hundreds of nm or 1 micron in the worst cases (**Fig. 8.8**) in comparison with its roughness before annealing (**Fig. 7.9**). High surface roughness after annealing, water loss

(**Table 8.3**) and reaction with CsCl are reasons that this surrounding material was not used further.

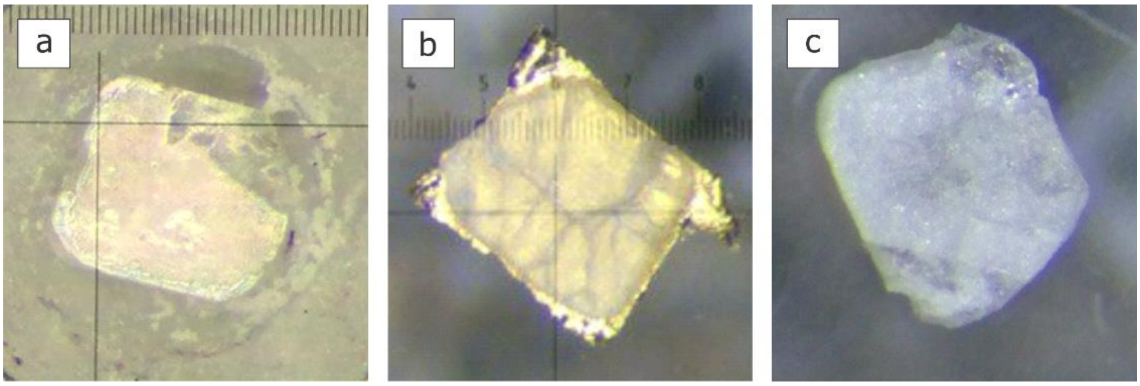

Fig. 8.7. Photo of a crystal in CsCl before an annealing experiment (**a**), photo of this crystal significantly cracked after annealing in CsCl without a diamond (**b**) and the same crystal without gold foil, indicating a very corroded surface after annealing in CsCl (**c**).

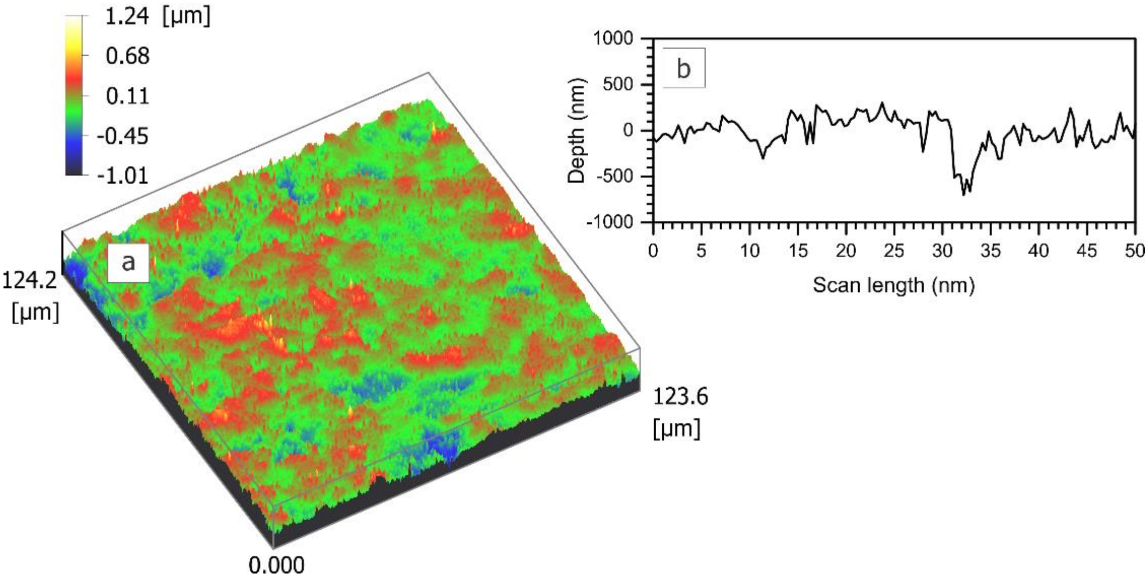

Fig. 8.8. 3D image of the resulting surface topography (**a**) and a surface profile (**b**) of a sample after annealing in surroundings of CsCl without a diamond. Roughness of this surface is 480 nm.

In setups where I used a diamond in contact with a thin film (**Fig. 7.10**, **7.11**) a significant roughness increase was not observed for the majority of samples.

This value was not higher than a few tens on nm in cases where CsCl was used as a surrounding material (**Fig. 8.9**) or < 30 nm when we used gold as a surrounding material (**Fig. 8.10**). Resulting surfaces are in same places around 1 micron lower in height than the rest of the surface (**Fig. 8.9 a**), which is explained by the absence of a thin film in these areas. However, in some runs the complete destruction of surfaces of crystals was observed, so they could not be used for further analysis.

Since it was difficult to avoid gold powder falling between the diamond and crystal, we observed some gold spots on resulting surfaces using a light microscope (**Fig. 8.11**) and in SEM images (**Fig. 8.12**). However, the confocal microscope showed no height change for these spots, indicating that the spots are the same height as the crystal surfaces. For further analysis, those crystals with minimum areas covered by gold spots were chosen. A careful choice of areas without gold spots was made for measurements using the NanoSIMS.

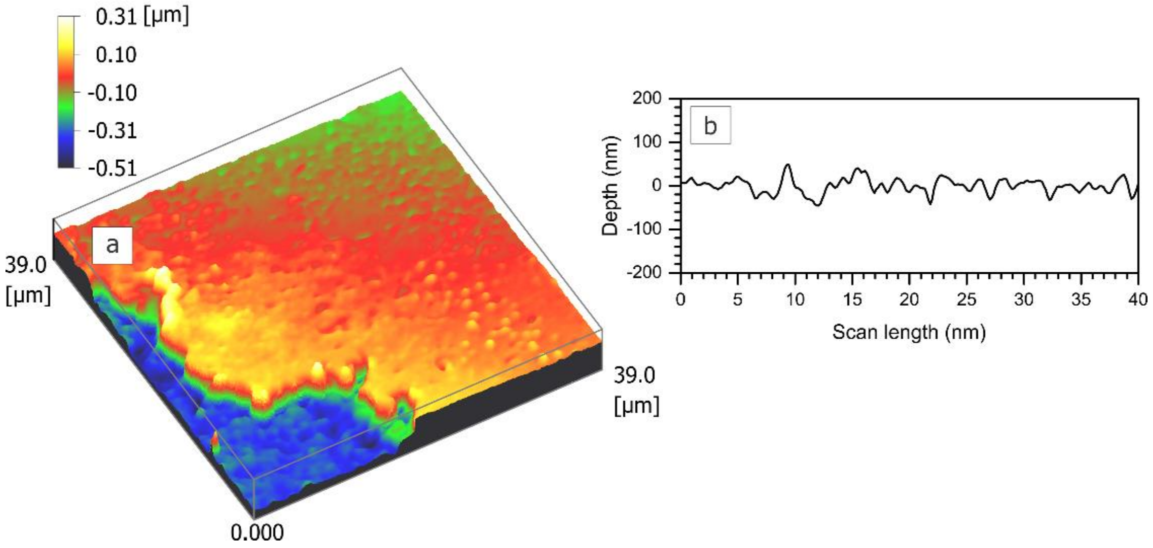

Fig. 8.9. 3D image of the resulting surface topography (**a**) and a surface profile (**b**) of a sample after annealing in surroundings of *CsCl* and with contact with a *diamond*.

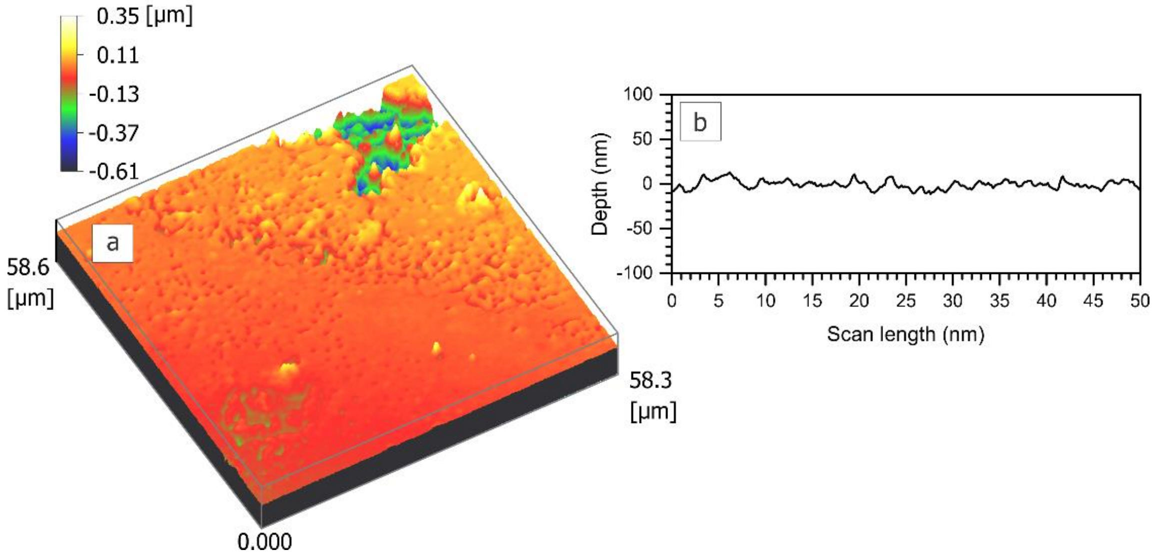

Fig. 8.10. 3D image of the resulting surface topography (**a**) and a surface profile (**b**) of a sample after annealing in surroundings of *gold* and with contact with a *diamond*.

Analysis of a sample (Z1906_67.2) after annealing in gold by a scanning electron microscope (ZEISS Gemini Field Emission SEM) showed the presence of carbon in the thin-film (**Table 8.4**, **Fig. 8.12**) due to diffusion of C from the diamond into wadsleyite. Some areas had a surface height that was lower than average due to the thin-film being torn away (**Fig. 8.12 a**). I also analyzed by SEM one of the samples (Z1899) with a strongly damaged surface (roughness ~ 1 µm). Areas with SiO_2 composition and carbon-rich areas had been observed (**Fig. 8.12 b**, **Table 8.4**). Since the composition of carbon-rich areas is close to $MgCO_3$ I suggest that for these samples a reaction between the diamond and the Mg_2SiO_4 thin film could occur:

$$\mathrm{Mg_2SiO_4 + 2CO_2 = 2MgCO_3 + SiO_2} \tag{8.1}$$

$$\mathrm{2H_2O + C\ (diamond) = CO_2 + 4H_2} \tag{8.2}$$

The reason of why these reactions (**Eqs. 8.1, 8.2**) take place only in a minority of runs is, however, unclear.

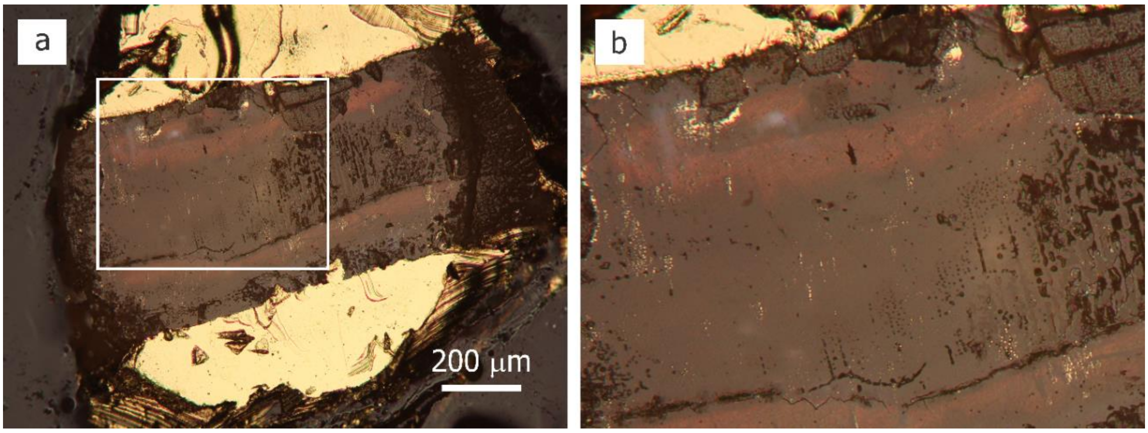

Fig. 8.11. Photos of resulting surfaces after annealing in *gold* with a *diamond*: a crystal embed in gold (**a**) and its magnified image (**b**).

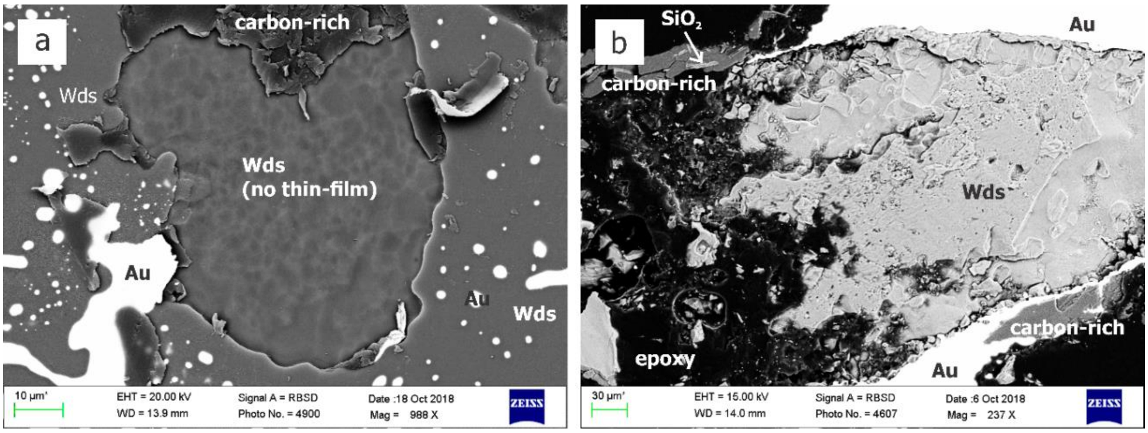

Fig. 8.12. Electron microscope images of resulting surfaces after annealing in *gold* with a *diamond*: an area with partially absent thin-film of run Z1906_67.2 on a crystal surface (**a**) and run Z1899 with a completely damaged surface (**b**).

Table 8.4. *Scanning electron microscope analyses with RBS detector of the samples after diffusion annealing in gold and a diamond.*

Element wt%	**Z1906_67.2** Wadsleyite (thin-film)	**Z1906_67.2** Wadsleyite (no thin-film)	**Z1906_67.2** C-rich area	**Z1906_67.2** Gold
Mg	27.38	33.84	10.13	< detection limit
Si	16.77	20.52	5.60	< detection limit
O	50.74	45.64	64.71	< detection limit
C	5.11	< detection limit	19.56	5.20
Au	< detection limit	< detection limit	< detection limit	91.55
N	< detection limit	< detection limit	< detection limit	3.26

Element wt%	**Z1906_75.4** Wadsleyite	**Z1899*** Wadsleyite	**Z1899*** C-rich area	**Z1899*** SiO_2
Mg	26.71	33.66	29.61	< detection limit
Si	16.32	20.66	< detection limit	46.74
O	51.29	45.68	56.50	53.26
C	5.68	< detection limit	13.89	< detection limit
Au	< detection limit	< detection limit	< detection limit	< detection limit
N	< detection limit	< detection limit	< detection limit	< detection limit

* is denoted to the sample with completely damaged surface

Scanning electron microscope analysis using an RBS detector showed a small dissimilarity in compositions between the thin-films and wadsleyite crystals (**Table 8.4**), i.e. a ratio of Mg/Si (film) = 1.63(1) and Mg/Si (crystal) = 1.65(1). The inaccuracy of this method and the presence of carbon, however, could be the reason for this discrepancy. Since the difference is very small its effect on diffusivity is assumed to be negligible.

8.5. Crater topography

The depth of the craters were determined using a 3D-Nanofocus confocal microscope, the basic work principle of which is shown in a **Section 7.4.2** and **Fig. 7.6**.

Representative topography of a crater obtained by a Cs$^+$ ion beam with high (80 pA) and low (20 pA) current is shown in **Fig. 8.13**. The crater bottom is flat with a roughness less than 10 nm in most runs. Craters have inclined edges, and their bottom areas were thus smaller than the are 10x10 μm at the surface. It was noticed that deeper craters and craters obtained at high beam current had edges that were more inclined from the vertical direction than those at low current.

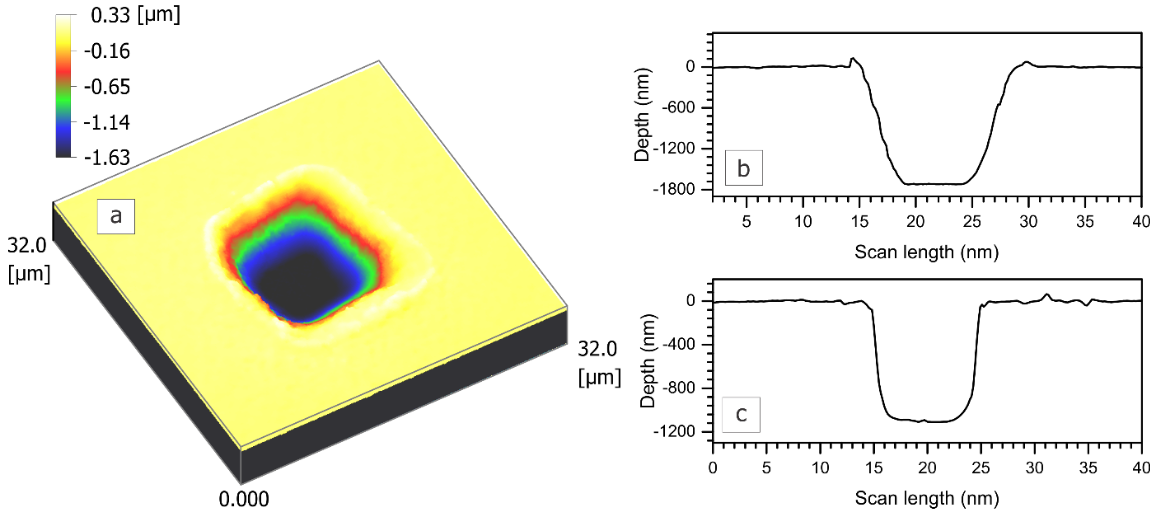

Fig. 8.13. 3D image of a crater topography (**a**) and its surface profile (**b**) after NanoSIMS measurements with a high-current beam (80 pA); (**c**) – profile of a crater made by low-current beam (20 pA).

8.6. Isotopes distribution and diffusion profiles

The NanoSIMS data sets are composed of layers with horizontally 128 × 128 or 256 × 256 pixels (**Fig. 7.14** in **section 7.6**). The ImageJ software enables the isotope ratio for the distribution in the data sets to be analysed. However, each pixel shows a large scattering of isotopes ratio depth profiles. On the other hand, very large areas obtained by combining several 16 × 16 pixel data show asymmetric one-end elongated profiles. Furthermore, areas close to the edges of images can produce artificial data induced by shallow edges of the crater produced by the NanoSIMS machine. A schematic image of an area used in further analysis is presented in **Fig. 8.14.**

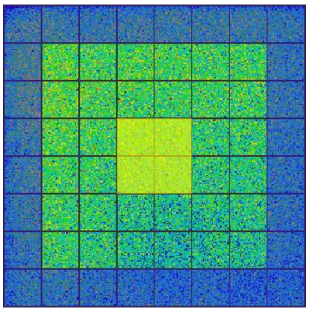

Fig. 8.14. An image of the secondary ion area distribution with 16 × 16 pixels areas chosen for further analysis. *Yellow square* in the center indicates area with a *minimal edge effect*. Blue area has maximum edge effect and was excluded from further analysis.

The NanoSIMS detected $^{29}\mathrm{Si}$ and $^{28}\mathrm{Si}$ individually and simultaneously, whose intensities were converted to $^{29}\mathrm{Si}/(^{29}\mathrm{Si} + {}^{28}\mathrm{Si})$ ratios. Based on the assumption of a constant sputtering rate, the relations of the isotope ratio to the depth were obtained from the depth of the craters. The same conversions were made for $^{18}\mathrm{O}$ and $^{16}\mathrm{O}$ isotopes. Since the isotope data of each pixel were found to be very noisy as mentioned above, we integrated data of 16 × 16 or 32 × 32 pixels, since these integrated pixel sizes lead to minimum noise in the profiles and in sensitivity to the heterogeneity of area distribution (**Fig. 8.15 a**). It is also noted that use of a larger area such as 128 × 128 pixels leads to less reliable D_{Si} determination because of a profile alongation, probably, due to horizontal asymmetrical heterogeneity in the isotope distribution.

For each crater we, obtained 64 profiles for the relations between $^{29}\mathrm{Si}/(^{29}\mathrm{Si} + {}^{28}\mathrm{Si})$ and $^{18}\mathrm{O}/(^{18}\mathrm{O} + {}^{16}\mathrm{O})$ and the crater depth at different locations within a crater. As shown in **Fig. 8.15 b**, profiles close to the crater's edges show significant elongation, which is considered to be an artifact due to the edges. For this reason, I used profiles with no edge effect for further analysis. As it was shown in section 9.5, carbon contamination of a thin film was observed. This could have a large effect on the rate of Si diffusion in wadsleyite. However, measured secondary carbon ions by NanoSIMS, as shown in Fig. 10.15 are placed only at a negligible depth in comparison with a diffusion profile length. Thereby the effect of carbon on D_{Si} was excluded.

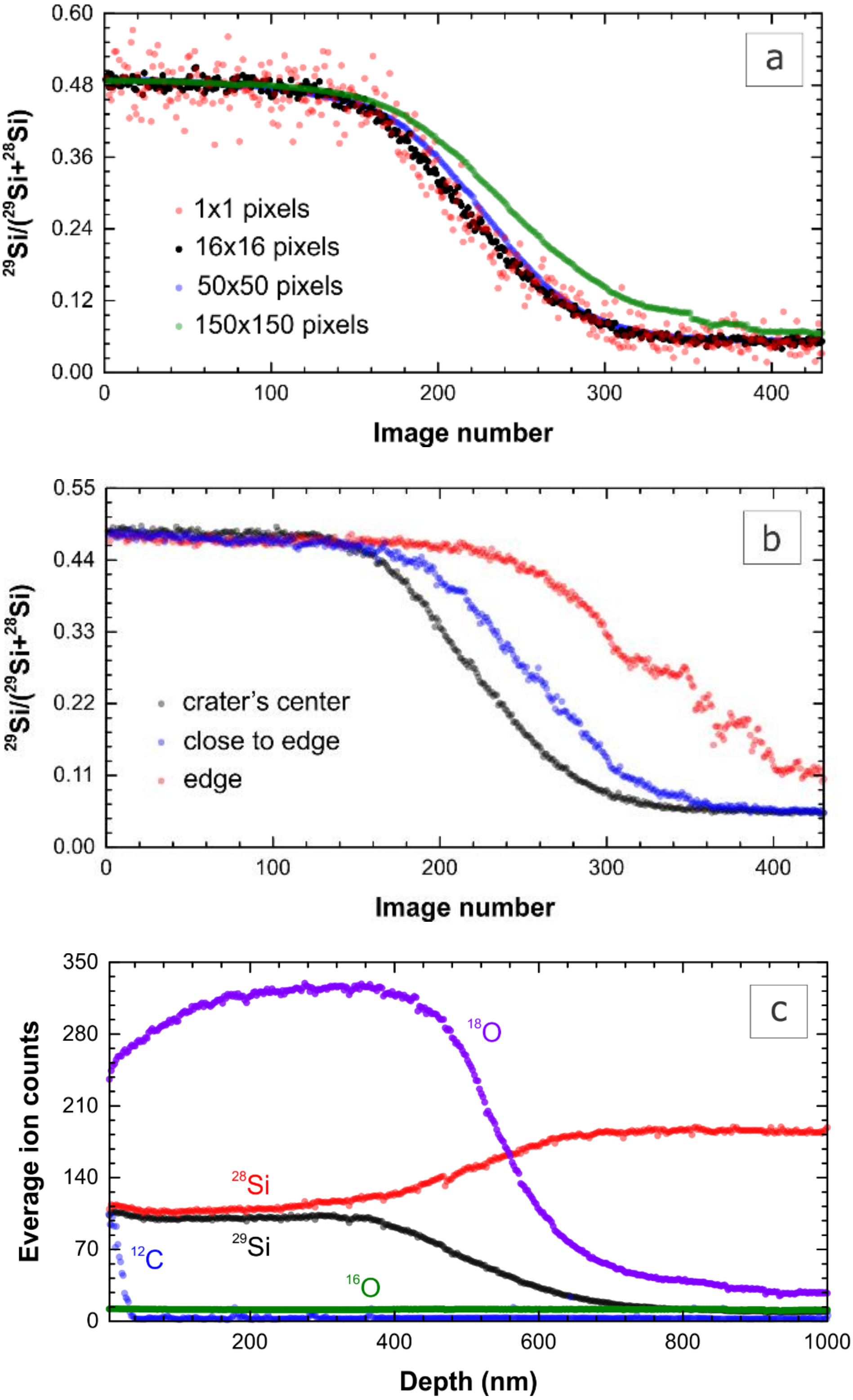

Fig. 8.15. Plots of typical ^{29}Si/(^{29}Si + ^{28}Si) profiles for different area sizes (**a**) and at different positions (**b**). (**c**) plot of secondary Si, O and C ions intensities as a function of depth (run Z1746).

8.7. Si and O volume diffusion coefficients

Fitting procedures and examples of fitted profiles are shown in **Section 7.7**. Here, I present the resulting Si and O diffusivities in Mg_2SiO_4 wadsleyite at different temperatures and water contents (**Table 8.5**).

Table 8.5. *Summary of runs, PT conditions, water contents, annealing durations (time) and obtained diffusion coefficients.*

Analysis run	P (GPa)	T (℃)	orientation	Time (min)	$C_{H_2O}{}^{+}$ (wt.ppm)	D_{Si} (m²/s)	$2\sigma_{Si}$ (m²/s)	D_O (m²/s)	$2\sigma_O$ (m²/s)
Z1695_2	20	1600	[100]	600	< 30	3.90×10^{-19}	0.27×10^{-18}	-	-
Z1753_1	20	1600	[100]	10	456(35)	6.60×10^{-18}	2.30×10^{-18}	3.75×10^{-18}	1.66×10^{-18}
Z1753_2	20	1600	[100]	10	456(35)	7.89×10^{-18}	1.24×10^{-18}	-	-
Z1514_4^{++}	20	1600	[100]	100	1733(120)	3.90×10^{-18}	1.02×10^{-18}	1.45×10^{-18}	1.20×10^{-18}
Z1814_61	19	1400	[100]	100	2181(63)	3.81×10^{-18}	3.40×10^{-18}	9.51×10^{-19}	3.97×10^{-19}
Z1814_62	19	1400	[100]	100	2181(63)	3.47×10^{-18}	5.00×10^{-18}	2.63×10^{-19}	0.24×10^{-19}
Z1886_3	20	1600	[010]	600	< 30	4.06×10^{-18}	0.87×10^{-18}	-	-
Z1890	20	1600	[010]	600	< 30	1.61×10^{-18}	1.35×10^{-18}	-	-
Z1895_1	20	1600	[010]	240	3100(32)	5.55×10^{-17}	3.33×10^{-17}	3.71×10^{-17}	3.23×10^{-17}
Z1893_1	20	1600	[010]	45	3023(97)	4.35×10^{-17}	0.62×10^{-17}	1.39×10^{-17}	1.30×10^{-17}
Z1742_1	20	1600	[010]	15	978(14)	5.48×10^{-18}	1.56×10^{-18}	5.92×10^{-18}	2.94×10^{-18}
Z1742_2	20	1600	[010]	15	978(14)	5.47×10^{-18}	2.76×10^{-18}	8.13×10^{-18}	2.82×10^{-18}
Z1742_3	20	1600	[010]	15	978(14)	5.16×10^{-18}	1.66×10^{-18}	-	-
Z1777_1^{++}	20	1600	[010]	20	2469(78)	2.22×10^{-17}	7.52×10^{-18}	9.45×10^{-18}	3.05×10^{-18}
Z1777_2^{++}	20	1600	[010]	20	2469(78)	2.51×10^{-17}	4.61×10^{-18}	1.10×10^{-17}	5.83×10^{-18}
Z1801_1^{++}	20	1600	[010]	30	3523(155)	7.51×10^{-17}	2.55×10^{-17}	-	-
Z1801_2	20	1600	[010]	30	3523(155)	8.01×10^{-17}	6.83×10^{-18}	1.13×10^{-17}	5.64×10^{-18}
Z1827_10d1	19.5	1500	[010]	20	1547(99)	2.41×10^{-17}	4.12×10^{-18}	4.34×10^{-18}	2.20×10^{-18}
Z1827_10d2	19.5	1500	[010]	20	1547(99)	2.36×10^{-17}	5.51×10^{-18}	6.30×10^{-18}	3.81×10^{-18}
Z1826_8d1	19.5	1500	[010]	60	3570(67)	3.80×10^{-17}	1.01×10^{-17}	-	-
Z1906_75.4	19	1400	[010]	600	3056(135)	1.10×10^{-17}	0.55×10^{-17}	-	-
Z1765_2	20	1600	[001]	15	2453(54)	2.75×10^{-17}	3.10×10^{-18}	6.85×10^{-18}	2.60×10^{-18}
Z1765_3	20	1600	[001]	15	2453(54)	3.14×10^{-17}	4.50×10^{-18}	1.20×10^{-17}	2.80×10^{-18}
Z1746_1	20	1600	[001]	30	2817(210)	3.15×10^{-18}	0.77×10^{-18}	1.23×10^{-18}	0.67×10^{-18}
Z1746_2	20	1600	[001]	30	2817(210)	4.15×10^{-18}	0.52×10^{-18}	1.28×10^{-18}	0.30×10^{-18}
Z1773_1^{++}	20	1600	[001]	15	3095(103)	9.25×10^{-18}	1.40×10^{-18}	2.93×10^{-18}	0.70×10^{-18}
Z1773_2^{++}	20	1600	[001]	15	3095(103)	1.01×10^{-17}	1.50×10^{-18}	4.25×10^{-18}	0.92×10^{-18}
Z1773_3^{++}	20	1600	[001]	15	3095(103)	7.81×10^{-18}	2.00×10^{-18}	3.22×10^{-18}	0.88×10^{-18}
Z1757^{++}	20	1600	[001]	10	4814(234)	8.70×10^{-17}	1.08×10^{-17}	1.25×10^{-17}	3.92×10^{-18}
Z1814_81	19	1400	[001]	30	2665(46)	1.20×10^{-18}	3.00×10^{-19}	1.84×10^{-19}	0.18×10^{-19}
Z1802_91	19	1400	[001]	60	3523(19)	2.50×10^{-17}	3.00×10^{-18}	1.36×10^{-17}	12.3×10^{-18}
Z1802_92	19	1400	[001]	60	3523(19)	1.29×10^{-17}	2.21×10^{-18}	9.05×10^{-18}	3.97×10^{-18}
Z1817_21	18.5	1300	[001]	150	3055(78)	1.10×10^{-18}	2.10×10^{-18}	5.34×10^{-18}	0.32×10^{-18}

$^{+}$ water contents calculated using calibrations of Paterson (Paterson, 1982)
$^{++}$ indicates runs where numerical simulation was used

9. Discussion

9.1. Temperature dependence

9.1.1. Si diffusion

Diffusion coefficients for Si as a function of temperature for the same chosen run conditions (water content, crystallographic orientation) are illustrated in **Fig. 9.1**. The linear relations of log Si volume diffusion to reciprocal temperature dependence can be described by the following equation:

$$D_{\mathrm{Si}} = D_0 \cdot \exp\left(-\frac{\Delta H}{RT}\right) \tag{9.1}$$

where D_0 is the pre-exponential factor, and ΔH is the activation enthalpy. The obtained activation enthalpies range from 147(78) to 219(80) kJ/mol, and that obtained by fitting all data together is 167(89) kJ/mol, which will be used for further discussions.

This activation enthalpy is half of the value obtained by (Shimojuku et al., 2010) using polycrystalline samples. It is also noted that Si self-diffusivity of many other minerals such as olivine and bridgmanite has higher activation enthalpy than that of wadsleyite given in this study (H. Fei et al., 2012; Jaoul et al., 1981; Shimojuku et al., 2009; Xu et al., 2011). One potential reason for the discrepancy with (Shimojuku et al., 2010) is that the high activation enthalpy was produced by higher diffusivity in one data point in (Shimojuku et al., 2010). Although (Shimojuku et al., 2010) obtained the activation enthalpy using four data points at temperatures from 1400 ℃ to 1600℃ as shown in **Fig. 9.2**, the data point at 1600 ℃ is exceptionally higher than the other three points, and the activation enthalpy obtained using these lower-temperature data points is 180(30) kJ/mol, which agrees with that obtained in this study. Though the reason is unclear, more data points at high temperature would give a more reliable value of the activation enthalpy.

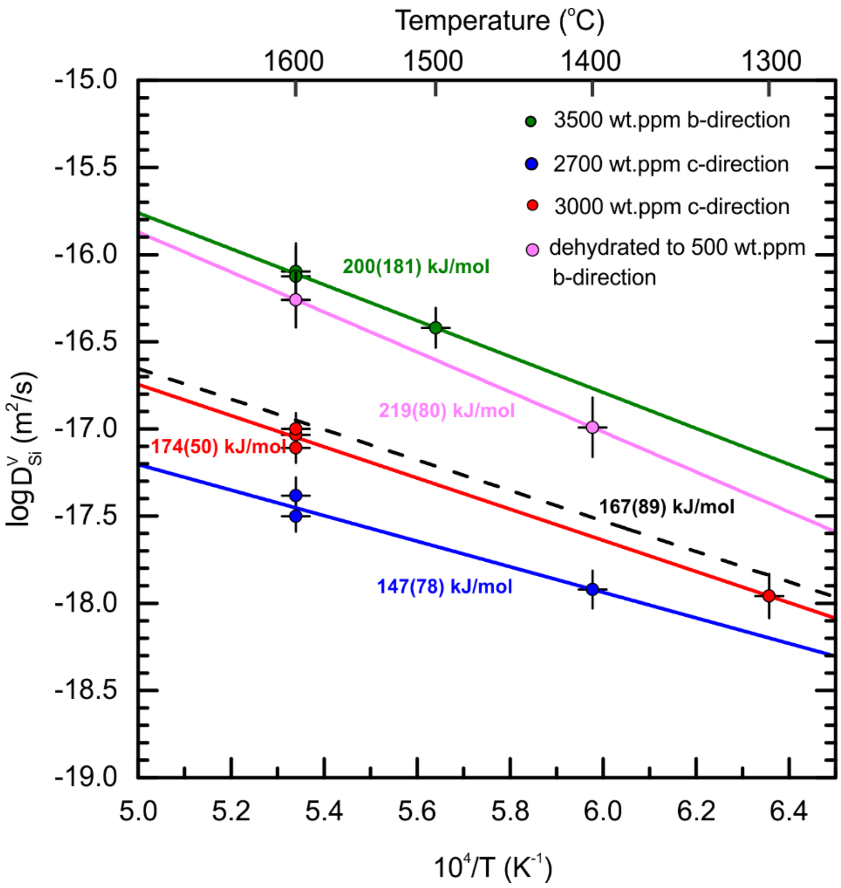

Fig. 9.1. Si volume diffusion coefficients in Mg_2SiO_4 wadsleyite. Solid lines and a corresponding color values represent Arrhenius fitting at different water content and corresponding activation enthalpies. Dashed black line is an Arrhenius fit of all obtained data.

Another possible explanation of the disagreement with (Shimojuku et al., 2010) is the two orders of magnitude difference in the water content in the samples between this study and (Shimojuku et al., 2010). A dominant diffusion mechanism of Si in wadsleyite will be the vacancy mechanisms like other silicates, as suggested by (Chakraborty, 2010; Shimojuku et al., 2010). Then, activation enthalpy should be therefore a result from the sum of the activation enthalpy for vacancy formation and the activation enthalpy for atomic motion (see **section 1.6**, **Eq. 1.21**). Hydrated wadsleyite has more vacancies both on the Mg and Si sites versus "dry" wadsleyite. Thus, it leads to a decreased value of the activation enthalpy for vacancy formation and the total activation enthalpy. It is noticed that, although some samples in (Shimojuku et al., 2010,

2004) contained relatively high H_2O contents to 507 wt. ppm, these samples were dehydrated to 14 wt. ppm of H_2O during the annealing. The activation enthalpy for these samples (261(121) kJ/mol) is lower than for “dry” samples of 20 – 60 wt. ppm H_2O by (Shimojuku et al., 2010) (**Fig. 9.2**).

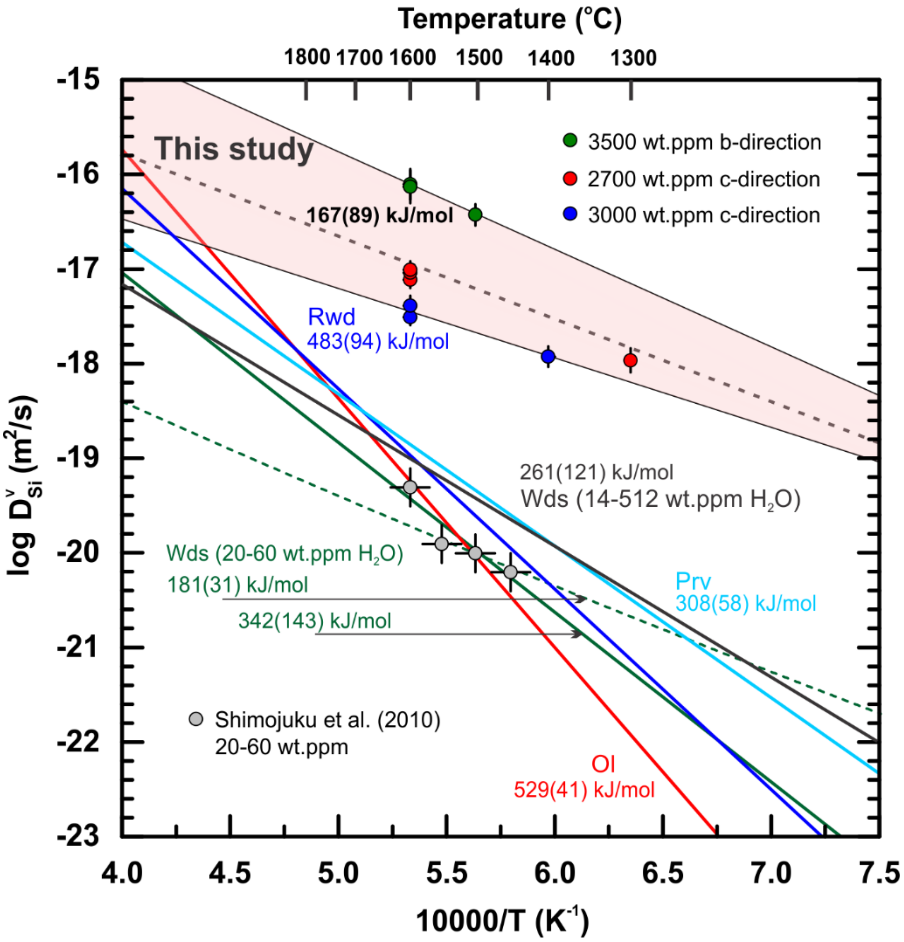

Fig. 9.2. Arrhenius plots of Si diffusivity of mantle minerals. Pink area bounded by thin black solid lines of fitting is wadsleyite with the lowest and highest water content from this study. Green solid line: wadsleyite with 20-60 wt. ppm H_2O content from (Shimojuku et al., 2010). Solid thick black line: wadsleyite with 14 – 507 wt. ppm water content from (Shimojuku et al., 2004). Blue line: $(Mg,Fe)_2SiO_4$ ringwoodite from (Shimojuku et al., 2009). Light blue line: bridgmanite from (Xu et al., 2011). Red solid line: olivine from (Dohmen, 2002). Green dashed line represent fitting of data from (Shimojuku et al., 2010) by removing the data point at 1600°C.

In this study, we did not obtain activation enthalpies of grain-boundary diffusion. Thus, in order to compare our results of the volume diffusion with grain-boundary diffusion in Mg_2SiO_4 wadsleyite, we used data from (Shimojuku et al., 2010, 2004). These studies suggested identical activation enthalpies for both volume and grain-boundary diffusion of wadsleyite with 14 – 510 wt. ppm water ($\Delta H_{\mathrm{gb}} = 260(120)$ kJ/mol and $\Delta H_{\mathrm{V}} = 260(120)$ kJ/mol). Wadsleyite with lower water contents of 20 – 60 wt. ppm shows higher activation enthalpy for volume diffusion ($\Delta H_{\mathrm{V}} = 340(140)$ kJ/mol) and lower for grain-boundary diffusion ($\Delta H_{\mathrm{gb}} = 160(120)$ kJ/mol) (Shimojuku et al., 2010). Accepting D_{gb} given by (Shimojuku et al., 2004, 2009, 2010) and our rates for volume diffusion D_{V}, values of the $D_{\mathrm{gb}}/D_{\mathrm{V}}$ ratio in this study are found to be $10^7 - 10^9$ which is similar to 10^9, which was reported for Si diffusion in forsterite (Farver & Yund, 2000) but lower than that of 10^5 found previously for wadsleyite by (Shimojuku et al., 2010, 2009, 2004).

9.1.2. O diffusion

Volume diffusion coefficients for O, $D_{\mathrm{O}}^{\mathrm{V}}$, as a function of temperature are illustrated in **Fig. 9.3**. The $D_{\mathrm{O}}^{\mathrm{V}}$ in the a- and b- directions showed almost no water dependence (see **Section 9.2, Fig. 9.8**). Therefore, all data obtained using samples with a different water content were simultaneously fitted by the Arrhenius equations (**Eq. 9.1**) in the a- and b- directions individually. The c-direction, in turn, showed significant water-content dependence, and therefore, data with the same water content were used for determination of the activation enthalpy. **Fig. 9.3** indicates that O diffuses along the b- direction by half an order of magnitude faster than along the a- direction. Additionally, the diffusion along the c-direction at a water content of 0.27 wt.% of H_2O is 1.5 orders of magnitude lower than those along the a- and c- directions at a water content of 0.3 wt.% of H_2O. The obtained activation enthalpy ranges from 160(60) kJ/mol (c-direction) to 180(40) kJ/mol (a- and b-directions). These values are much smaller than those obtained for Fe-bearing wadsleyite by (Shimojuku et al.,

2009) with $\Delta H_O^V = 290(80)$ kJ/mol and for other Earth's mantle phases like Fe-bearing ringwoodite ($\Delta H_O^V = 370(80)$ kJ/mol) by (Shimojuku et al., 2009), olivine ($\Delta H_O^V = 340(10)$ kJ/mol) by (Dohmen et al., 2002) and bridgmanite ($\Delta H_O^V = 501(80)$ kJ/mol) by (Dobson et al., 2008) (**Fig. 9.4**). Activation enthalpy ΔH_O^V is also higher in pure forsterite (370(60) kJ/mol) by (H. Fei et al., 2014).

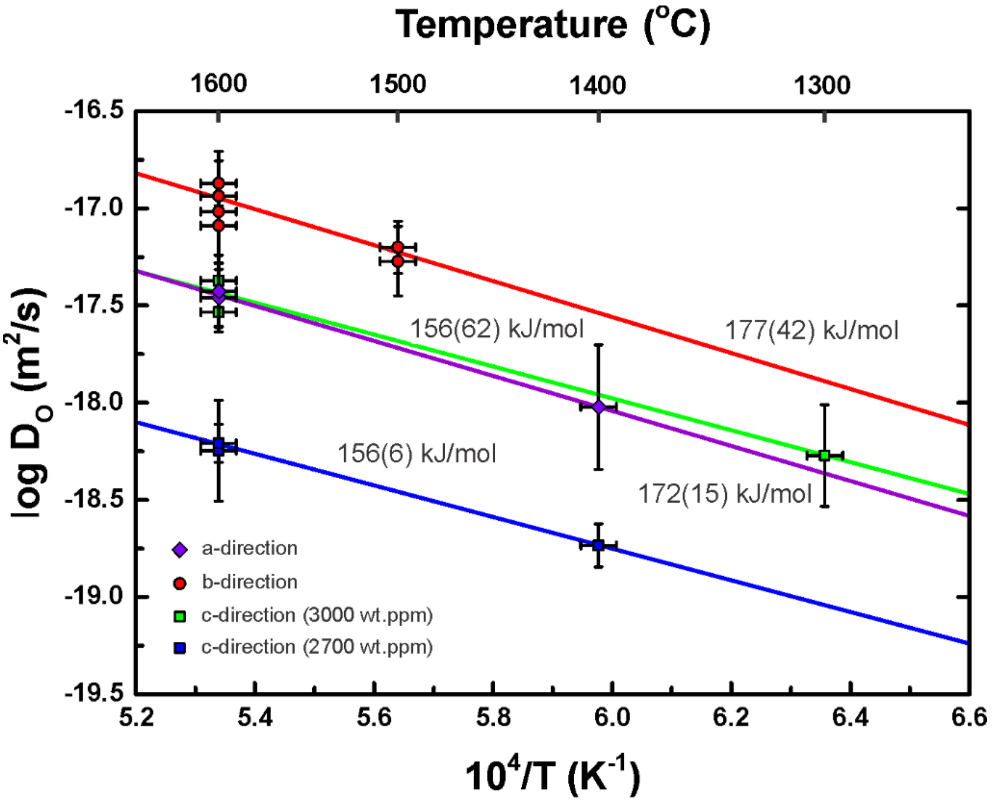

Fig. 9.3. O volume diffusion coefficients. Solid lines represent Arrhenius fitting at different crystallographic orientations and different water content, numbers are activation enthalpies.

Like the case of Si diffusion mentioned above, the data point for O diffusion obtained at 1600 °C by (Shimojuku et al., 2009) seems too high most likely due to inaccurate separation of volume and grain-boundary diffusion. Indeed, fitting only those three data points at 1400 – 1500 °C from (Shimojuku et al., 2009) leads to lower activation enthalpy $\Delta H_O^V = 200(30)$ kJ/mol, which is close to the average value in all directions obtained in our study ($\Delta H_O^V = 170(80)$ kJ/mol) within the error.

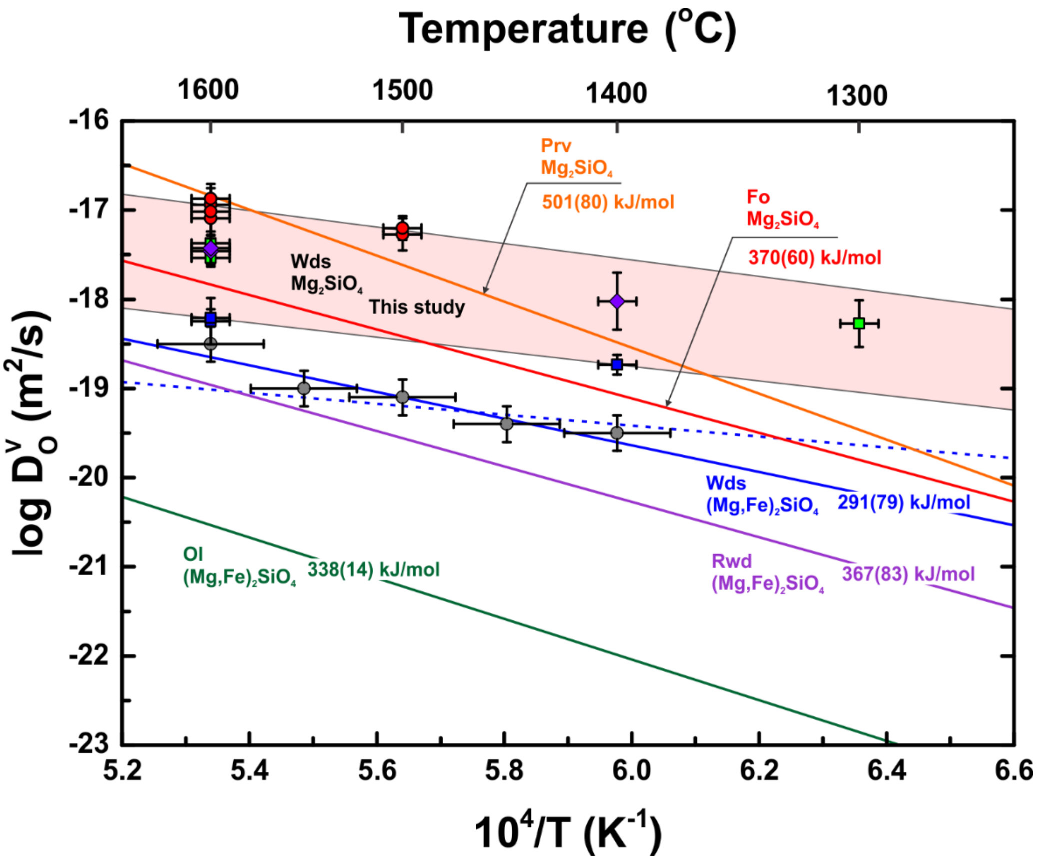

Fig. 9.4. Arrhenius plots of O diffusion in wadsleyite obtained in this study together with those in mantle minerals in other studies. Pink area bounded by fitting curves (black solid lines) with the lowest and the highest activation enthalpies values. Solid blue and violet lines: wadsleyite and ringwoodite, respectively, from (Shimojuku et al., 2009), orange solid line: perovskite from (Dobson et al., 2008), green line: olivine from (Dohmen et al., 2002) and red line: forsterite from (H. Fei et al., 2014). Dashed blue line represents fitting of data from (Shimojuku et al., 2009) without including the 1600 ℃ data point.

Difference in water content from previous study (Shimojuku et al, 2009), however, cannot be applied to explain higher O diffusivity obtained in this study (**Fig. 9.4**) since, as it will be shown in a section below (**Section 9.2**), data for a-direction shows no water content dependence. We suggest that difference in O_2 fugacity (f_{O_2}) where these experiments were performed could probably lead to higher O diffusivity. Increasing f_{O_2} would oxidize a small fraction of Mg, creating additional vacancies at Mg-sites:

$$4\mathrm{Mg}_{\mathrm{Mg}}^{\times} + \mathrm{O}_2(\mathrm{gas}) = 2\mathrm{Mg}_{\mathrm{Mg}}^{\bullet} + \mathrm{V}_{\mathrm{Mg}}'' + 2\mathrm{MgO} \tag{9.2}$$

A positive dependence on f_{O_2} was found for Fe-bearing olivine (Gérard & Jaoul, 1989; Ryerson et al., 1989). In experiments of (Shimojuku et al., 2009) Ni capsules were used (Ni-NiO buffer). Therefore, the oxygen fugacity of their experiments can be estimated to be about two log units higher than the iron-wüstite buffer (from IW+0.8 to IW+2 for 1400 °C and 1600 °C at 16 GPa). Usage of a gold capsule and a gold powder in the present study should produce much higer f_{O_2} at 1600 °C and 20 GPa.

Fig. 9.5 compares Si and O diffusivities in Mg_2SiO_4 wadsleyite obtained in this study with Mg-Fe diffusivity in $(Mg,Fe)_2SiO_4$ wadsleyite obtained in previous studies (Chakraborty et al., 1999; Holzapfel et al., 2009; Kubo et al., 2004). This figure indicates that the Mg-Fe diffusivity is higher that the Si and O self-diffusivity in wadsleyite with water contents up to 0.3 wt.% in the whole temperature range of the upper mantle. Even assuming that the Mg-Fe interdiffusivity has a large pressure dependence, it should be higher than the O and the Si self-diffusivity.

O and Si in Mg_2SiO_4 wadsleyite have very similar self-diffusivities and Si has even higher diffusivity than O at high water concentrations. The similarity in activation enthalpies ($\Delta\mathrm{H(Si)} = 167(89)\ \mathrm{kJ/mol}$ and $\Delta\mathrm{H(O)} = 165(77)\ \mathrm{kJ/mol}$) for volume diffusivity of O and Si may due to simultaneous diffusion of both ionic species. The activation enthalpies of Si and O diffusivity obtained in this study are close to the values obtained for Mg-Fe diffusion of 145-172 kJ/mol. This could be interpreted as Si and O diffusion perhaps occur through Mg-site vacancies. A more detailed explanation of a mechanisms of O and Si diffusion in wadsleyite is described in a **Section 9.2**.

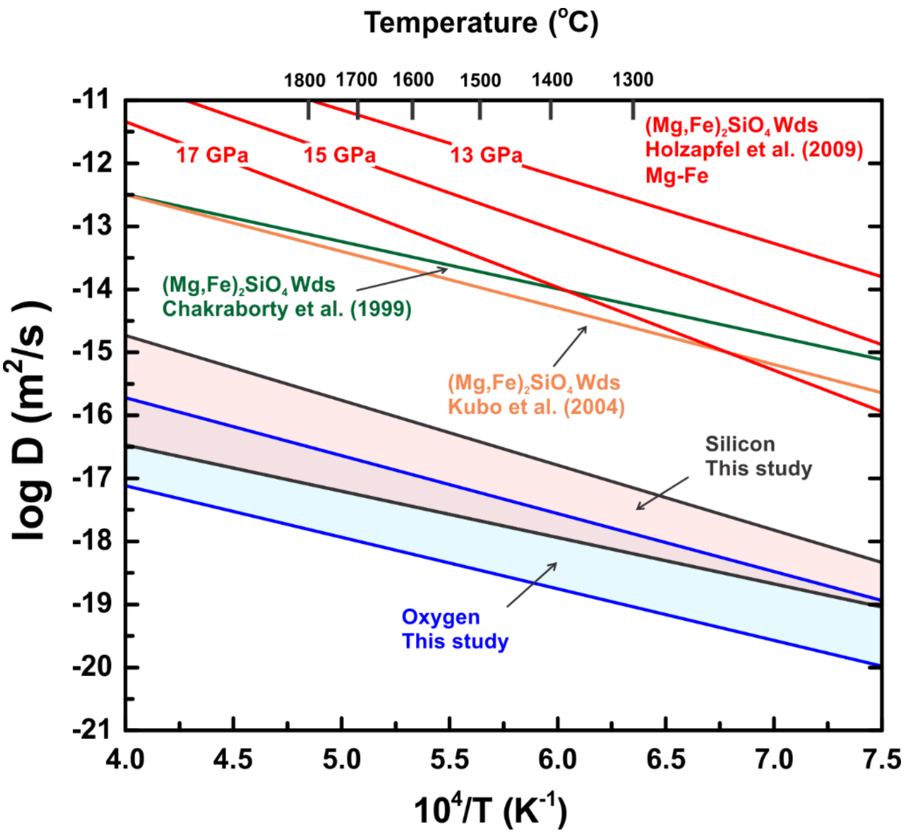

Fig. 9.5. Arrhenius plots of Mg, Si and O diffusivity of wadsleyite. The pink and blue areas bound by fittings with the lowest and highest activation enthalpies for the Si and O diffusivities from this study respectively. The Mg-Fe diffusivities taken from (Holzapfel et al., 2009), (Chakraborty et al., 1999) and (Kubo et al., 2004) are shown by the red, green and orange lines, respectively.

9.2. Water-content dependence

The volume diffusivity of Si, $D_{\mathrm{Si}}^{\mathrm{V}}$, obtained in this and (Shimojuku et al., 2004, 2010) studies is plotted against the water contents in **Fig. 9.6**. This figure indicates systematic increases in $D_{\mathrm{Si}}^{\mathrm{V}}$ with increasing $C_{\mathrm{H_2O}}$. It also indicates a strong axil anisotropy in $D_{\mathrm{Si}}^{\mathrm{V}}$. The *b*- and *c*- directions show stronger anisotropy, whereas the *a*-direction shows weaker anisotropy. The obtained diffusivity in each direction can be fitted to the Arrhenius equation including the effect of water as:

$$D_{Si} = D_0 \cdot C_{\mathrm{H_2O}}^{r} \cdot \exp\left(-\frac{\Delta H}{RT}\right) \tag{9.3}$$

where C_{H_2O} is the water content in wt. ppm, r is the water-content exponent, D_0 is the pre-exponential factor. The activation enthalpy, ΔH, used in this fitting is 167(89), which was obtained in **Section 9.1.1**. The fitting suggests $r = 0.57, 1.86(16)$ and $5.23(52)$ in the a-, b- and c- directions (**Fig. 9.6**).

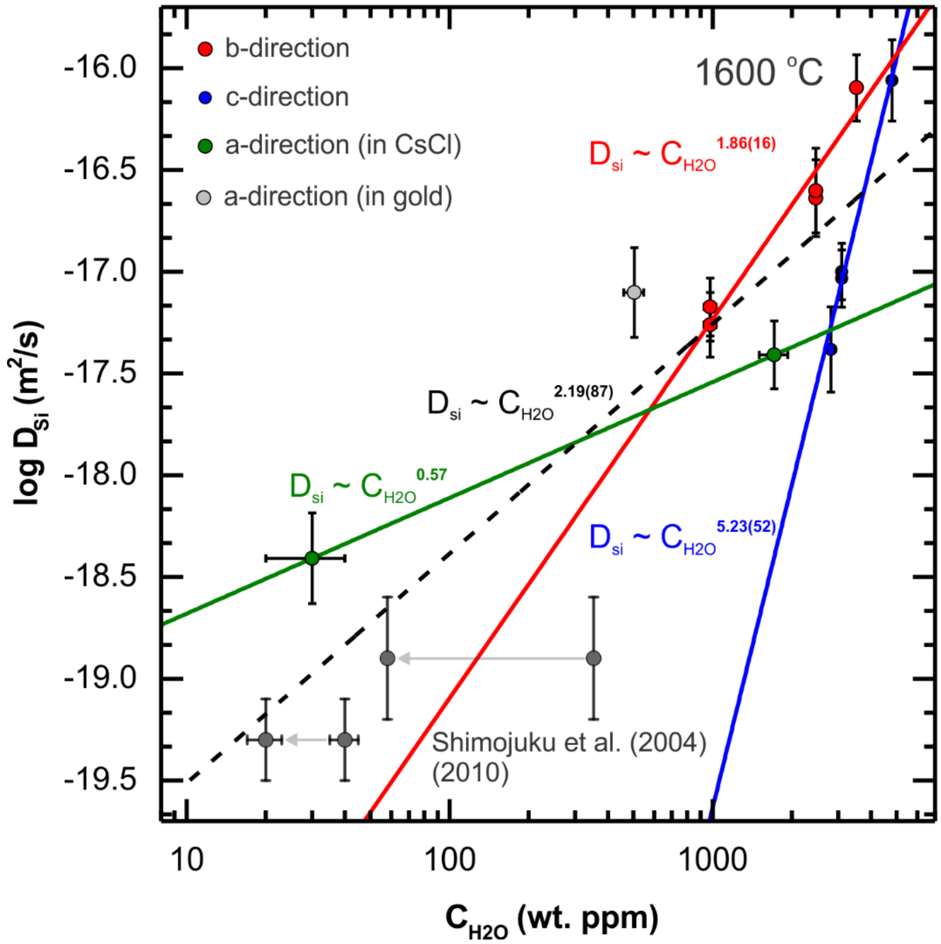

Fig. 9.6. Diffusion rate of Si in Mg_2SiO_4 wadsleyite in log units versus water content at 20 GPa and 1600 °C. Dark grey circles represent data for the Si volume diffusion coefficients from Shimojuku et al. (2004, 2010) obtained at 1630 °C (arrows indicate water change during experiments). Green, red and blue lines are Arrhenius fitting along the a-, b- and c- directions to the current data set. Dashed black line represents fitting of all obtained data simultaneously.

Thus the water-content dependence of volume diffusivity of Si in wadsleyite is found to be extremely large. Though the Mg/Si ratios of hydrous wadsleyite suggest that almost all protons should substitute the Mg sites (Smyth, 1987), the large water content dependence implies that the Si sites are also substituted by protons significantly.

The water-content exponents obtained in this study are significantly different from that at $r = 0.6$ reported by (Shimojuku et al., 2010). I emphasize however, that their water-content exponents contains significant errors. They obtained their water content exponents through 4 data points, whose variations of diffusion coefficients is only half an order of magnitude. In addition, their water contents were significantly changed by dehydration during diffusion annealing. For example the water content in run SID05 decreased from 350 – 14 wt. ppm (at 1430 °C). If the water-content dependence of $D_{\mathrm{Si}}^{\mathrm{V}}$ is large, the obtained diffusivity should describe that at higher initial water contents. In this point of view, the present results agree with those of (Shimojuku et al., 2010).

The water exponents obtained in this study are much larger than others obtained for a various kind of minerals by previous researchers. Therefore, it requires a convincing explanation in view of a defect chemistry. I have calculated water exponents of defect concentrations in wadsleyite under different charge-neutrality conditions, which are presented in **Table 9.1** (for calculation details see **Section 2.5**).

In the case of the a-direction, it can be assumed that the main Si-related defects whose concentration depends on the water content are one proton in the Si site, $\mathrm{H}_{\mathrm{Si}}'''$. Its concentration under the charge neutrality condition of $[(\mathrm{OH})_{\mathrm{O}}^{\bullet}] = [\mathrm{H}_{\mathrm{Mg}}']$ is proportional to the 1/2 power of the water content, $[\mathrm{H}_{\mathrm{Si}}'''] \propto \mathrm{C}_{\mathrm{H_2O}}^{1/2}$. This exponent is close to 0.6, the value obtained in this study. Although there is no water-content dependence of the concentration of Si vacancies without any proton under the same charge balance conditions ($[\mathrm{V}_{\mathrm{Si}}''''] \propto \mathrm{C}_{\mathrm{H_2O}}^{0}$), we can still assume their presence. Thus, we suggest that the main diffusion mechanism of Si in wadsleyite in the a-direction occurs through vacancies $\mathrm{V}_{\mathrm{Si}}''''$ in the Si site and additionally enhanced by a creation of additional defects of a proton in the Si site, $\mathrm{H}_{\mathrm{Si}}'''$, then $\mathrm{Si}_{\mathrm{Si}}^{\times} \leftrightarrow \mathrm{H}_{\mathrm{Si}}'''$ exchange could occur.

As silicon diffusion is comparable with oxygen diffusion in wadsleyite, and the activation enthalpies of Si and O diffusions are identical within the errors, we could postulate that presence of O vacancies may enhance Si diffusion. Indeed, (H. Fei et al., 2013) suggested that, O vacancies should produce corridors for Si migration to promote Si diffusion, because Si in olivine is tightly surrounded by O anions to form a tetrahedron. Thus, by considering similar SiO_4 tetrahedron for both wadsleyite and olivine, enhancement of Si jumps by O vacancies could occur also in wadsleyite.

The water-content exponent of Si diffusivity in the *b*-direction can be interpreted by assuming that Si diffusion is controlled by Si-, O- and Mg-related defects simultaneously. Given that the Si-related defects are the same as those for the *a*-direction, $[\mathrm{H}_{\mathrm{Si}}''']$ is proportional to $\mathrm{C}_{\mathrm{H_2O}}^{1/2}$ under charge neutrality conditions of $[(\mathrm{OH})_{\mathrm{O}}^{\bullet}] = [\mathrm{H}_{\mathrm{Mg}}']$. We can also consider a creation of O- and Mg-related defects such as $[(\mathrm{OH})_{\mathrm{O}}^{\bullet}]$ and $[2\mathrm{H}_{\mathrm{Mg}}^{\times}]$ respectively, during hydration of wadsleyite. Their concentrations are proportional to $\mathrm{C}_{\mathrm{H_2O}}^{1/2}$ and $\mathrm{C}_{\mathrm{H_2O}}^{1}$ respectively. If presence of $(\mathrm{OH})_{\mathrm{O}}^{\bullet}$ and $\mathrm{H}_{\mathrm{Mg}}'$ promote Si migration, the Si diffusivity should be proportional to these three concentrations as $[\mathrm{H}_{\mathrm{Si}}'''] \times [(\mathrm{OH})_{\mathrm{O}}^{\bullet}] \times [2\mathrm{H}_{\mathrm{Mg}}^{\times}] = \mathrm{C}_{\mathrm{H_2O}}^{1/2} \times \mathrm{C}_{\mathrm{H_2O}}^{1/2} \times \mathrm{C}_{\mathrm{H_2O}}^{1} = \mathrm{C}_{\mathrm{H_2O}}^{2}$. The obtained value 2, is identical to the water-content exponent obtained in this study, 1.9(9), within the error. Although the exact concentrations of these defects, and their correlations with each other are unknown, this exponent may demonstrate that Si diffusion is driven by $[\mathrm{H}_{\mathrm{Si}}''']$ associated with $[(\mathrm{OH})_{\mathrm{O}}^{\bullet}]$ and $[2\mathrm{H}_{\mathrm{Mg}}^{\times}]$ in wadsleyite. The structure of wadsleyite suggests that $\mathrm{V}_{\mathrm{Si}}''''$ are possible in all crystallographic directions. Moreover, concentrations of vacancies at Si sites under $[(\mathrm{OH})_{\mathrm{O}}^{\bullet}] = [\mathrm{H}_{\mathrm{Mg}}']$ charge neutrality conditions is water content independent $[\mathrm{V}_{\mathrm{Si}}''''] \propto \mathrm{C}_{\mathrm{H_2O}}^{0}$, thus, the water-content exponent would not change with the creation of vacancies at Si sites. Therefore, a certain amount of Si vacancies can be assumed along *b*- and *c*- directions, as for the *a*-direction.

Table 9.1. *The water-fugacity exponents (r) calculated by assuming the proportionality of the water-fugacity in the environment and the water content in wadsleyite. The numbers in the green boxes show the water-content exponents of a diffusivity in the a- and b- directions, the orange boxes are water-content exponents in the b-direction.*

Charge neutrality	**Defects in wadsleyite**						
	$\mathrm{Mg}_{\mathrm{Mg}}^{\bullet}$	$\mathrm{V}_{\mathrm{Mg}}^{\prime\prime}$	$\mathrm{H}_{\mathrm{Mg}}^{\prime}$	$2\mathrm{H}_{\mathrm{Mg}}^{\times}$	$(\mathrm{OH})_{\mathrm{O}}^{\bullet}$	$\mathrm{V}_{\mathrm{O}}^{\bullet\bullet}$	$\mathrm{O}_{\mathrm{i}}^{\prime\prime}$
$[(\mathrm{OH})_{\mathrm{O}}^{\bullet}] = [\mathrm{V}_{\mathrm{Mg}}^{\prime\prime}]$	-1/6	1/3	2/3	1	1/3	-1/3	1/3
$[(\mathrm{OH})_{\mathrm{O}}^{\bullet}] = [\mathrm{H}_{\mathrm{Mg}}^{\prime}]$	0	0	1/2	1	1/2	0	0
$[\mathrm{Mg}_{\mathrm{Mg}}^{\bullet}] = [\mathrm{V}_{\mathrm{Mg}}^{\prime\prime}]$	0	0	1/2	1	1/2	0	0
$[\mathrm{Mg}_{\mathrm{Mg}}^{\bullet}] = [\mathrm{H}_{\mathrm{Mg}}^{\prime}]$	1/4	-1/2	1/4	1	3/4	1/2	-1/2

	Defects in wadsleyite					
	$\mathrm{V}_{\mathrm{Si}}^{\prime\prime\prime\prime}$	$\mathrm{Si}_{\mathrm{i}}^{\bullet\bullet\bullet\bullet}$	$\mathrm{H}_{\mathrm{Si}}^{\prime\prime\prime}$	$2\mathrm{H}_{\mathrm{Si}}^{\prime\prime}$	$3\mathrm{H}_{\mathrm{Si}}^{\prime}$	$4\mathrm{H}_{\mathrm{Si}}^{\times}$
$[(\mathrm{OH})_{\mathrm{O}}^{\bullet}] = [\mathrm{V}_{\mathrm{Mg}}^{\prime\prime}]$	2/3	-2/3	1	4/3	5/3	2
$[(\mathrm{OH})_{\mathrm{O}}^{\bullet}] = [\mathrm{H}_{\mathrm{Mg}}^{\prime}]$	0	0	1/2	1	3/2	2
$[\mathrm{Mg}_{\mathrm{Mg}}^{\bullet}] = [\mathrm{V}_{\mathrm{Mg}}^{\prime\prime}]$	0	0	1/2	1	3/2	2
$[\mathrm{Mg}_{\mathrm{Mg}}^{\bullet}] = [\mathrm{H}_{\mathrm{Mg}}^{\prime}]$	-1	1/3	-1/4	1/2	5/4	2

In contrast to the *a*- and *b*- directions, the extremely large water-content exponent in the *c*-direction, namely $r = 5.2(5)$, cannot be explained in view of point defect chemistry (**Table 9.1**). This high exponent has a possible explanation when Si diffusion in wadsleyite is carried out by migration through Mg-sites. In order to move in the *c*- direction, Si should cross the Mg-site at M3 octahedra. Wadsleyite incorporates the majority of proton in the Mg sites. I suggest that Si migrates through these vacant Mg-sites in the *c*-direction. At low water contents, the amount of Mg vacancies is limited, and there is almost no diffusion path in the *c*- direction as observed in this study. In this case, all diffusion occurs along a- and b-directions through Mg-nonrelated defects. On the other hand, high water contents lead to high defect concentrations in the Mg sites, and open paths for silicon to migrate in the *c*-direction, significantly enhancing the diffusion in this direction. Olivine and forsterite have much smaller water dependence (H. Fei et al., 2013). Since it incorporates water only through Si-related defects, there is smaller numbers of Mg-site vacancies than wadsleyite. This leads to lower water-exponent and apparent diffusion isotropy. Schematic diffusion mechanisms are shown in **Fig. 9.7**.

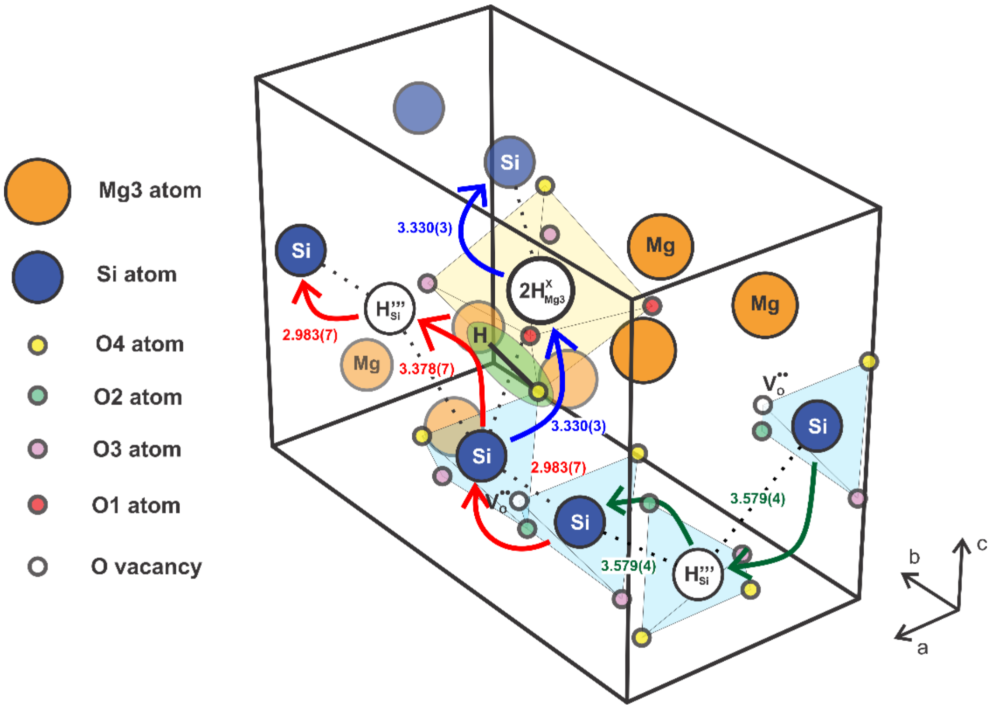

Fig. 9.7. Schematic representation of diffusion mechanism of Si in Mg_2SiO_4 wadsleyite along *a*-, *b*- and *c*- crystallographic orientations. Atoms and defects are presented by circles. Single unit cell is shown by solid black lines. Dashed black lines represent the pathway of hopping Si atom. Green, red and blue arrows and numbers show diffusion pathways and distance between nearest atoms for *a*-, *b*- and *c*- crystallographic directions correspondingly. SiO_4 tetrahedra are colored by light blue and M3 octahedron is colored yellowish. Green ellipse represents $(OH)^{\bullet}_{O}$.

Unlike olivine and forsterite (Dohmen, 2002; H. Fei et al., 2014; Gérard & Jaoul, 1989; Ryerson et al., 1989), where O diffusion anisotropy was found to be weak, O diffusion in Mg_2SiO_4 wadsleyite is strongly anisotropic (**Fig. 9.8**). Moreover, O diffusion in the b- and c-directions accelerates with increasing water content and an estimation by fitting these data with an Arrhenius equation (**Eq. 9.3**) gives an exponent of water-content dependence of $r = 0.5(2)$ and $r = 3.5(4)$ respectively. Diffusion in the a-direction has no water-content dependence.

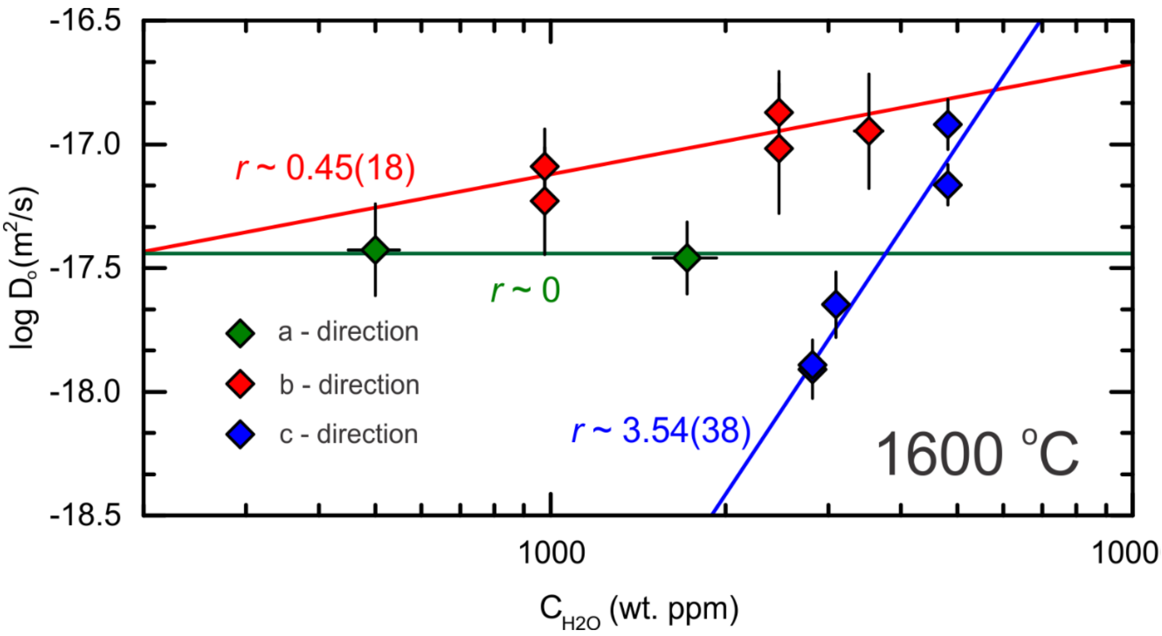

Fig. 9.8. O volume diffusion coefficients in Mg_2SiO_4 wadsleyite at different water content at 1600 °C.

Assuming the same charge neutrality conditions of $[(\mathrm{OH})_\mathrm{O}^{\bullet}] = [\mathrm{H}'_\mathrm{Mg}]$, i.e. the same as Si diffusivity, no water-content dependence in the a-direction can be interpreted by the fact that O self-diffusion in Fe-free wadsleyite occurs through O vacancies $D_\mathrm{O}(100) \propto [\mathrm{V}_\mathrm{O}^{\bullet\bullet}] = C_{\mathrm{H_2O}}^{0}$. As diffusion in the b-direction has $r = 0.5(2)$ water exponent, water incorporation should create additional $[(\mathrm{OH})_\mathrm{O}^{\bullet}]$ defects. Thus, one can write $D_\mathrm{O}(010) \propto [(\mathrm{OH})_\mathrm{O}^{\bullet}] \times [\mathrm{V}_\mathrm{O}^{\bullet\bullet}] = \mathrm{C}_{\mathrm{H_2O}}^{1/2} \times \mathrm{C}_{\mathrm{H_2O}}^{0} \approx C_{\mathrm{H_2O}}^{0.5(2)}$. The strong water-content dependence along the c-direction $D_\mathrm{O}(001) \propto \mathrm{C}_{\mathrm{H_2O}}^{3.5(4)}$ cannot be interpreted in view of point defect chemistry. Our hypothesis is cluster diffusion of O with Si in the *c*-direction through Mg-site vacancies in M3 octahedra.

By comparing O and Si volume diffusivities in Fe-free wadsleyite at 16 GPa and around 1800 K at different water content (**Fig. 9.9**), O is found to diffuse faster than Si ($D_\mathrm{O}^\mathrm{V} > D_\mathrm{Si}^\mathrm{V}$) in the respective directions at water contents of $C_{\mathrm{H_2O}} \leq$ 800 wt.ppm (blue area). This order changes to $D_\mathrm{Si}^\mathrm{V} > D_\mathrm{O}^\mathrm{V}$ in the respective directions at water contents of $\mathrm{C}_{\mathrm{H_2O}} \geq 1500$ wt.ppm.

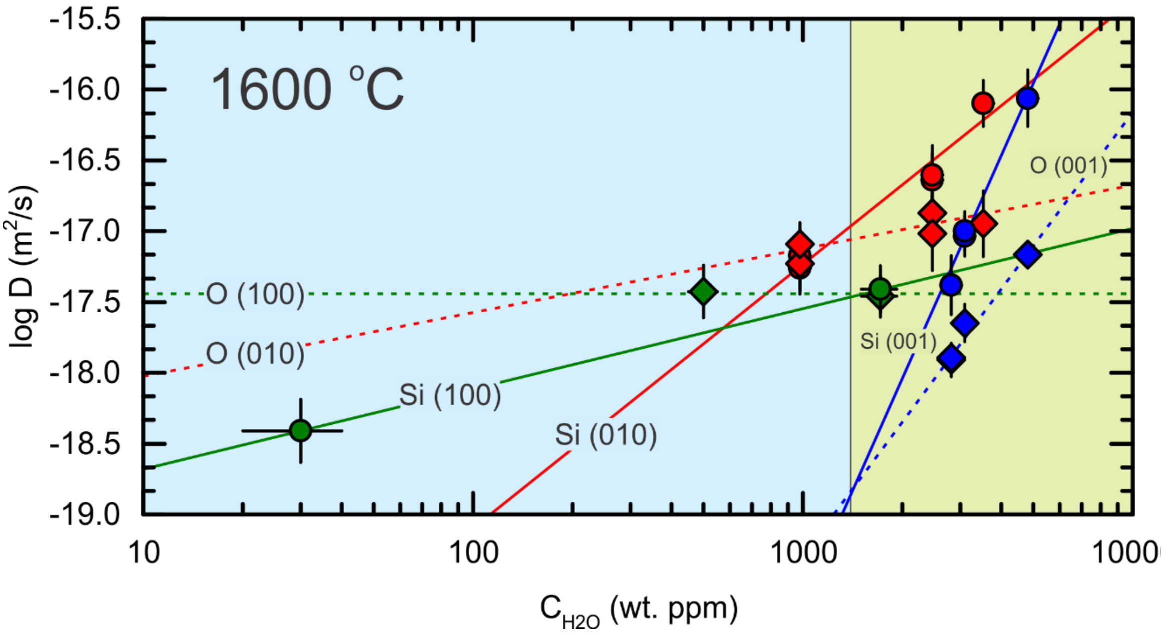

Fig. 9.9. O diffusivities (diamonds) and Si diffusivities (rounds) in Mg_2SiO_4 wadsleyite as a function of water content. The solid and broken lines denote fitting of Si and O diffusivity. The green, red and blue colors indicate the *a*-, *b*- and *c*-directions, respectively. The blue and green zones correspond to conditions where O and Si diffusion are faster respectively.

The deformation experiments reveal that all possible slip systems in wadsleyite are [100](010), [100](001), [100]{011}, [100]{021}, 1/2⟨111⟩{101}, [010](001), [010]{101} and ⟨101⟩(010) (Thurel, Cordier, et al., 2003; Thurel, Douin, et al., 2003). The easiest systems to be found are 1/2⟨111⟩{101}, [100](010) and [100]{011}. Another dominant system of [001](010) was found recently (Demouchy et al., 2011; Kawazoe et al., 2013). It was found by (Kawazoe et al.,

2013) that the [001] axis and (010) plane of wadsleyite tend to be subparallel to the shear direction and plane, respectively. The calculation of slip systems by (Metsue et al., 2010) leads to the easiest slip system of not the [001](010) but 1/2⟨111⟩{101}, and the second easiest one of [100](010).

Both Si and O data obtained in this study show the high water-content dependence the *c*-direction, and the highest diffusivity in the [100] *a*-direction at low water contents in wadsleyite. Thus, the easiest slip direction could be the *a*- and *c*-direction in dry and hydrous wadsleyite respectively. However, the easiest slip in the *c*-direction was found at low water contents (Kawazoe et al., 2013). Such discrepancy could be due to a high-density at dislocations produced by deformation experiments due to high stresses. The *b*-direction, in which diffusion becomes faster at H_2O contents of 1000 – 3000 wt. ppm, corresponds to the longest Burgers vector in the wadsleyite lattice. Therefore, glide is not preferred in this direction. On the other hand, the observed and calculated 1/2⟨111⟩{101} slip system would be the best candidate as the easiest one at this water conditions in wadsleyite (Metsue et al., 2010; Thurel, Cordier, et al., 2003; Thurel, Douin, et al., 2003).

9.3. Rheology application

Plastic deformation rates at high temperature in wadsleyite can be calculated from the slowest diffusing species. Diffusivity of both Si and O were used for further calculations because Si diffusivity exceeds that of O at water contents higher than 1000 wt. ppm (**Fig. 9.9**).

9.3.1. Strain rate in MTZ

Using **Eq. 3.21** (see **Section 3.3.3**), it is possible to estimate the strain rate in wadsleyite controlled by dislocation creep using the diffusivities obtained in this study. I have used the following parameters: the Burger vector b was taken to be one of the unit cell parameters, the shear modulus μ taken to be 116 GPa (Kiefer, Stixrude, Hafner, & Kresse, 2001), molar volume Ω was equal to 40.53 cm^3/mol, the ratio of the glide distance over the climb distance l_g/l_c was taken to be equal to 1 or 200. As the l_g/l_c is unclear for wadsleyite, I have taken the values used in previous studies for both wadsleyite and olivine (Costa & Chakraborty, 2008; Kohlstedt, 2018; Shimojuku et al., 2009).

Strain rates at 1600 ℃ as a function of water at different stresses are shown in **Fig. 9.10**. The estimated strain rates for Mg_2SiO_4 wadsleyite demonstrate three regions with different water exponents indicated by the superscript: (1) dry wadsleyite with less than 1000 wt. ppm H_2O has $\dot{\varepsilon} \propto C_{H_2O}^{0.7(2)}$ where a water exponent strongly effected by diffusion along a-direction of Si atom, (2) intermediate 1000 – 5000 wt. ppm with $\dot{\varepsilon} \propto C_{H_2O}^{0.5(2)}$ and (3) hydrous wadsleyite at more than 5000 wt.ppm H_2O where $\dot{\varepsilon} \propto C_{H_2O}^{3.5(4)}$ is mainly determined by O diffusion along c-direction.

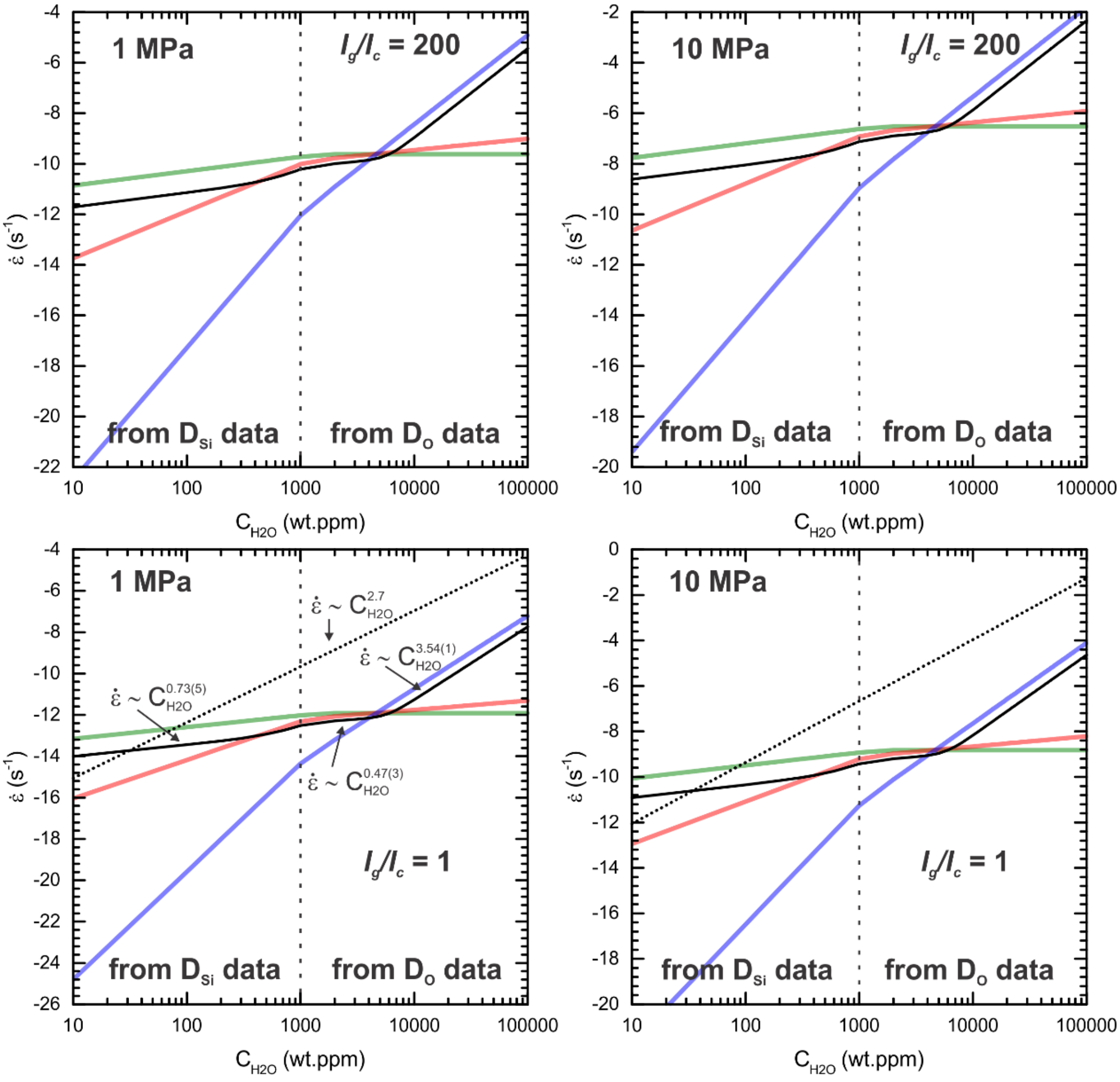

Fig. 9.10. Strain rates constructed for different stresses based on Si and O diffusion data at different water contents a temperature of 1600 ℃ ($\boldsymbol{l_g/l_c}$ = 1). The green, red and blue solid lines denote normal strain rates in the a-, b- and c-directions, respectively. The solid black line shows strain rates in the [111] direction. Strain rates in wadsleyite constructed based on the data of (Kawazoe et al., 2013) are shown by the dotted black lines. Dashed lines indicate the borders of water content separating regions of Si (left side) and O (right side) as the slowest atomic species.

Since diffusion and dislocation creep are believed to be controlled by diffusion of the slowest atomic species in wadsleyite as well as in olivine (Chakraborty, 2010; Weertman et al., 1999), the water-content exponents of creep are expected to be identical to the diffusivities of rate-controlling species.

Deformation experiments performed on polycrystalline wadsleyite with the San Carlos olivine composition gave a water exponent of 2.7 at a pressure of 15 GPa and temperatures of 1400 to 1700 K in the water range of 200 to 1000 wt. ppm (Kawazoe et al., 2013). In this range for relatively dry wadsleyite, Si diffusivity is the slowest, and therefore wadsleyite creep is controlled by Si diffusion. Water exponent of 0.7(2) obtained in this study at the same water content range is three times lower than water-content exponent of 2.7 by (Kawazoe et al., 2013).

This discrepancy could be due to many reasons. There are three most probable of them that are represented below. The stress conditions in (Kawazoe et al., 2013) experiments range from 100 to 540 MPa. This range exceeds estimated stress conditions of the mantle TZ by more than 2 orders of magnitude. Such high-stress conditions should have produced high-density dislocations. It is noted that the water-exponent and stress-exponents were not constrained independently by (Kawazoe et al., 2013) study. It is noted that the stresses and therefore dislocation densities are higher at high water-contents in this study, and therefore, the apparently high water-content dependence might be caused by the possible high stresses. Another reason could be selective water incorporation in dislocations. If this is the case, the high water-content dependence of wadsleyite creep cannot be applied to the mantle transition zone due to the low stresses and therefore low dislocation density. Thus, the large water-content exponent obtained by deformation experiments is totally unreasonable for TZ conditions. Additionally, (Farla, Amulele, Girard, Miyajima, & Karato, 2015) suggested that the grain size ranged from 5 to 40 μm in (Kawazoe et al., 2013), and this range lays in the diffusional-creep regime in the deformation mechanisms map constructed by (Shimojuku et al., 2009). Thus, the water-content dependence suggested by (Kawazoe et al., 2013) cannot be compared to those obtained in the present study.

9.3.2. Deformation maps

It is convenient to use deformation mechanism maps to illustrate the parameter space (like a grain size) where one mechanism dominates over others. Based on the formulas of **Eqs. (3.16)** and **(3.21)** for diffusion and dislocation creep, respectively, I have constructed stress-temperature deformation mechanism maps for Mg_2SiO_4 wadsleyite at a pressure of 20 GPa, water contents of 10 and 10000 wt. ppm and grain sizes from 0.01 to 100 mm (**Fig. 9.11**). The effective diffusion coefficient D^{eff} for diffusion creep has been calculated using **Eq. (3.15)** and the grain-boundary diffusivity reported by (Shimojuku et al, 2009, 2010). The molar volume Ω and constant α_{NH}, respectively, are set to be 40.53 cm3/mol and 13.3 (H. J. Frost & Ashby, 1982; Shimojuku et al., 2009). In the case of dislocation creep, I have adopted the same parameters and formulas as described in the beginning of this section. Construction was based on the sum of Si and O diffusivity vectors in the a-, b- and c-directions obtained by this study.

The temperature and stress ranges corresponded to the MTZ and subducted slabs are marked as hatched rectangles in **Fig. 9.11**. The temperature range in the MTZ is chosen from 1800 to 2000 K according to (Katsura et al., 2010). The lowest temperature in slabs is assumed to be 1100 K (“cold” slab), and the highest is 1500 K (“warm” slab). Stress range in the MTZ (purple rectangular) is assumed to be between 1 to 10 MPa based on estimations in the literature (Shimojuku et al., 2009; Vassiliou et al., 1984). A further stress range in the MTZ (green rectangular) is estimated from the assumption that strain rates are from 10^{-14} to 10^{-16} s^{-1} (Billen, 2008). Stresses are assumed by one – two orders of magnitude higher (10 – 100 MPa) in slabs than ambient mantle.

Fig. 9.11 shows that the increasing water content shifts strain rates to lower values at the same applied stresses. Thus, within the same grain size of 0.01 mm, if strain rates were for example 10^{-9} – 10^{-11} s^{-1} at 10 wt. ppm H_2O, they would increase to 10^{-6} – 10^{-8} s^{-1} at 10000 wt. ppm H_2O. On the other hand, the grain size mostly determines stress conditions of the creep mechanism transition from dislocation creep to diffusion creep. Namely, at a H_2O content of 10 wt. ppm, a grain size increase from 0.01 to 10 mm shifts boundary for the stress condition of the dislocation-diffusion creep from 10^2 to 10^{-1} MPa.

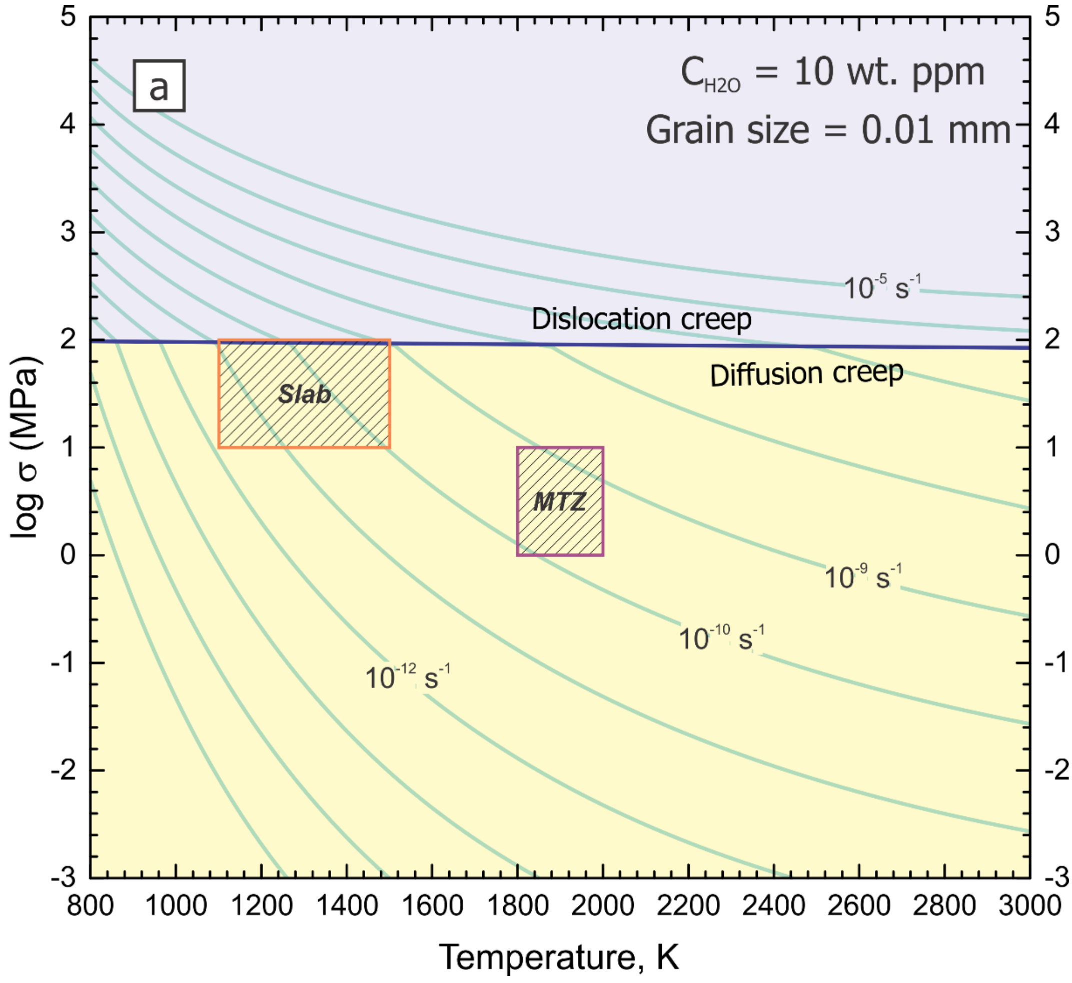

Fig. 9.11 a. A deformation map showing the boundaries between the various deformation mechanisms in stress-temperature space estimated at 20 GPa at *10 wt. ppm* H_2O and *0.01 mm* grain size. Solid blue line is boundary between dislocation and diffusion creep. Levels of some strain rates are noted with numbers. Stress-temperature ranges for slabs and MTZ are shown by hatched rectangular.

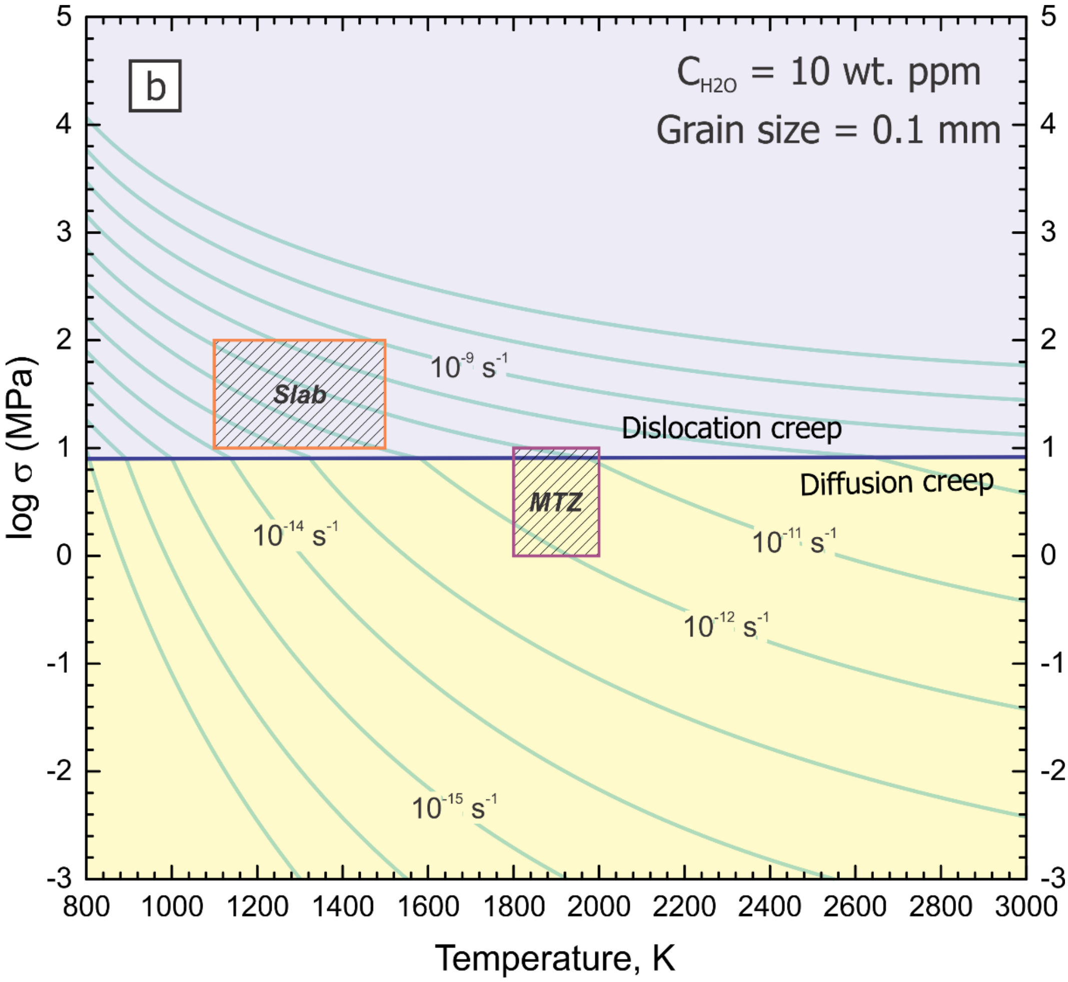

Fig. 9.11 b. A deformation map showing the boundaries between the various deformation mechanisms in stress-temperature space estimated at 20 GPa at *10 wt. ppm* H_2O and *0.1 mm* grain size. Solid blue line is boundary between dislocation and diffusion creep. Levels of some strain rates are noted with numbers. Stress-temperature ranges for slabs and MTZ are shown by hatched rectangular.

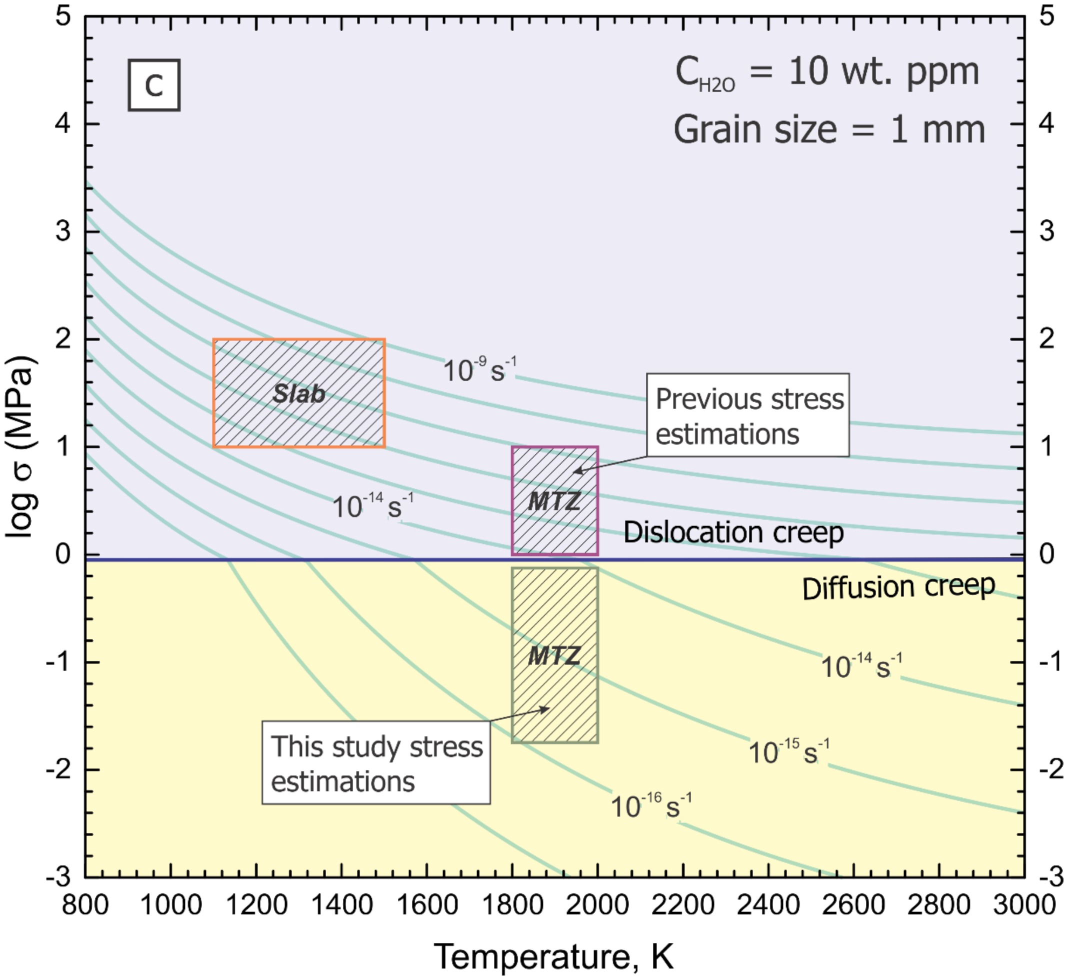

Fig. 9.11 c. A deformation map showing the boundaries between the various deformation mechanisms in stress-temperature space estimated at 20 GPa at *10 wt. ppm* H_2O and *1 mm* grain size. Solid blue line is boundary between dislocation and diffusion creep. Light green lines are strain rate with one order of magnitude step, levels of some strain rates are noted with numbers. Stress-temperature ranges for slabs and MTZ are shown by hatched rectangular.

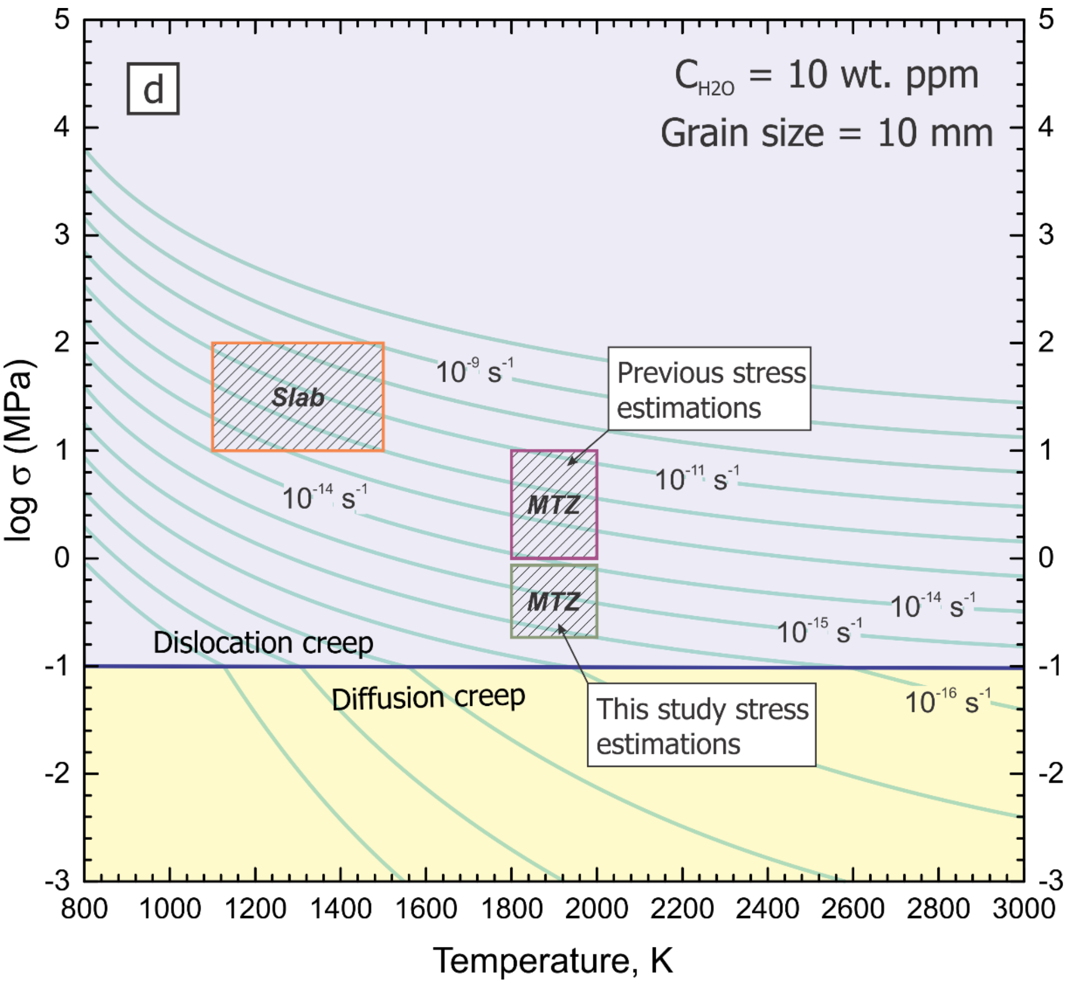

Fig. 9.11 d. A deformation map showing the boundaries between the various deformation mechanisms in stress-temperature space estimated at 20 GPa at *10 wt. ppm* H_2O and *10 mm* grain size. Solid blue line is boundary between dislocation and diffusion creep. Light green lines are strain rate with one order of magnitude step, levels of some strain rates are noted with numbers. Stress-temperature ranges for slabs and MTZ are shown by hatched rectangular.

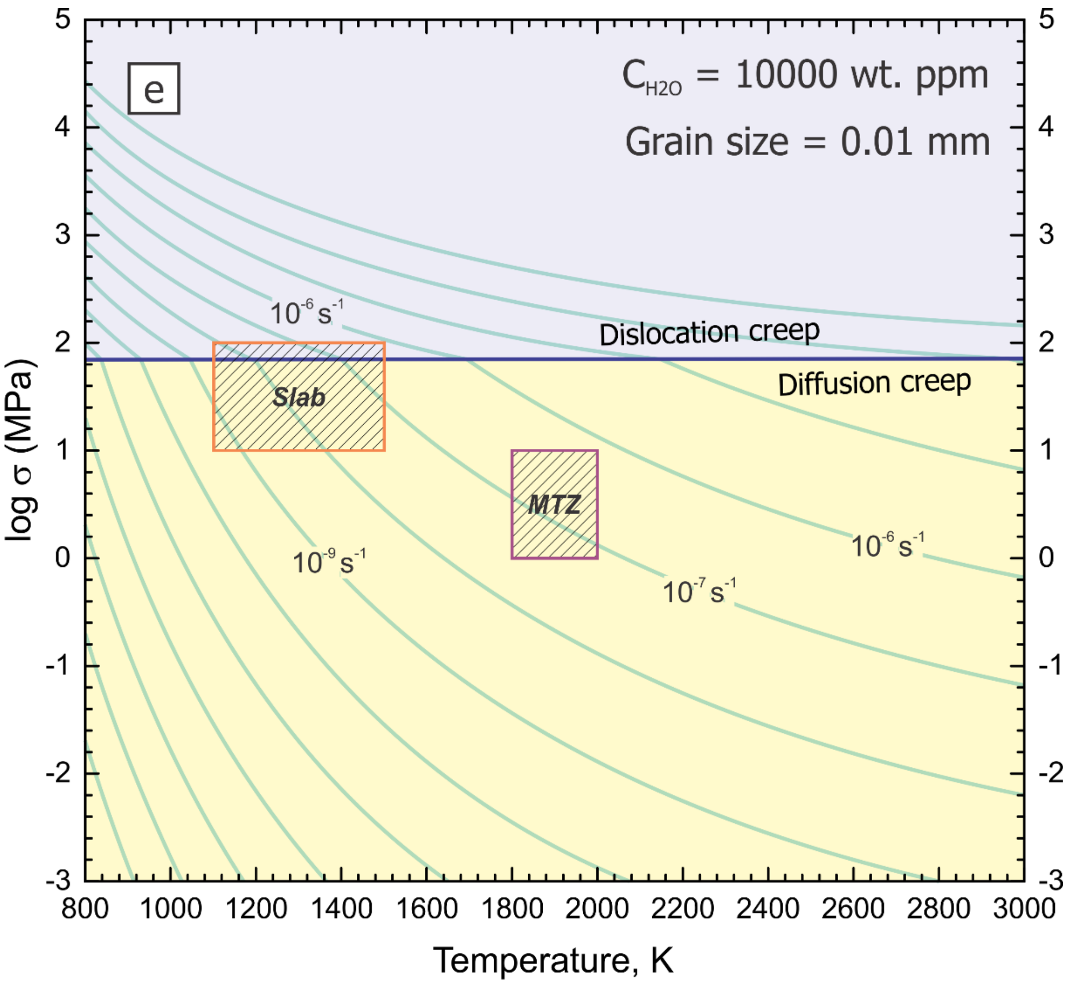

Fig. 9.11 e. A deformation map showing the boundaries between the various deformation mechanisms in stress-temperature space estimated at 20 GPa at *10000 wt. ppm* H_2O and *0.01 mm* grain size. Solid blue line is boundary between dislocation and diffusion creep. Levels of some strain rates are noted with numbers. Stress-temperature ranges for slabs and MTZ are shown by hatched rectangular.

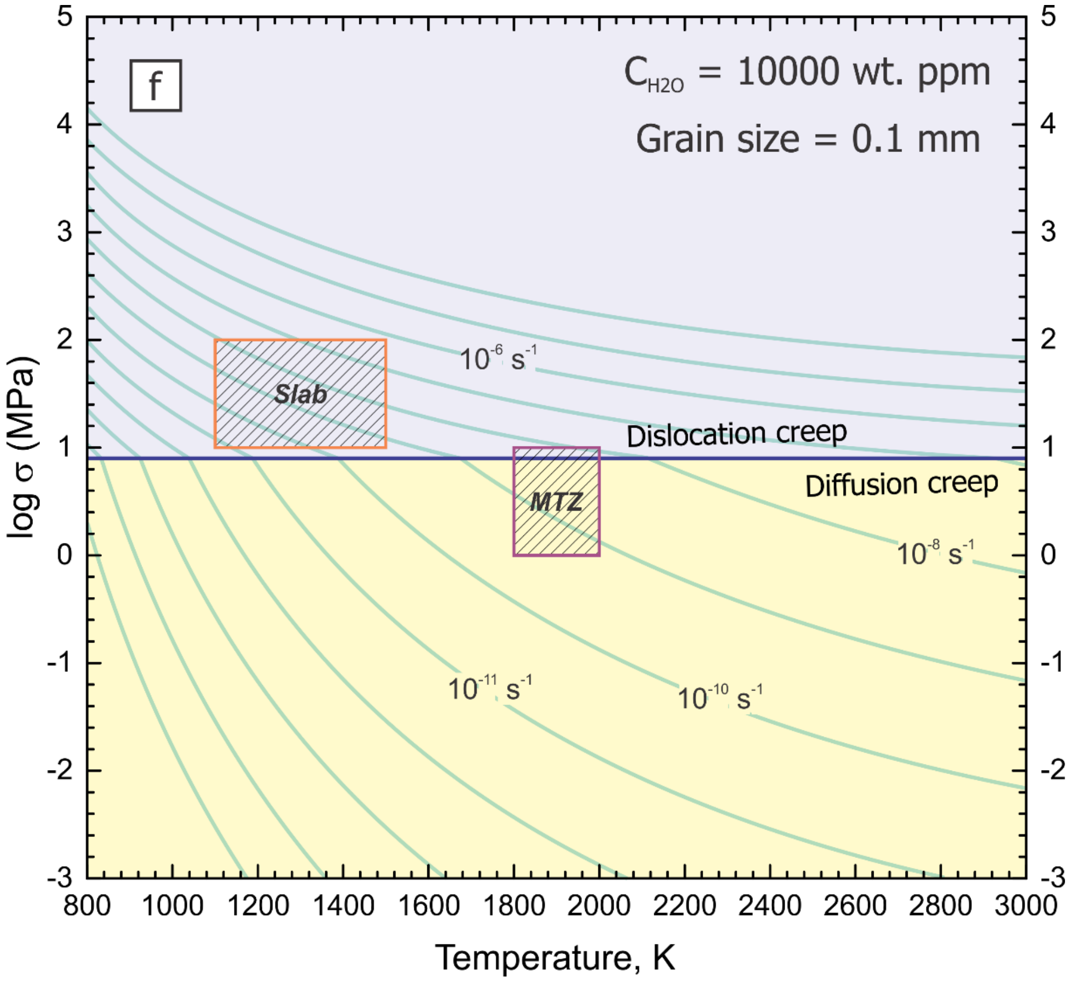

Fig. 9.11 f. A deformation map showing the boundaries between the various deformation mechanisms in stress-temperature space estimated at 20 GPa at *10000 wt. ppm* H_2O and *0.1 mm* grain size. Solid blue line is boundary between dislocation and diffusion creep. Levels of some strain rates are noted with numbers. Stress-temperature ranges for slabs and MTZ are shown by hatched rectangular.

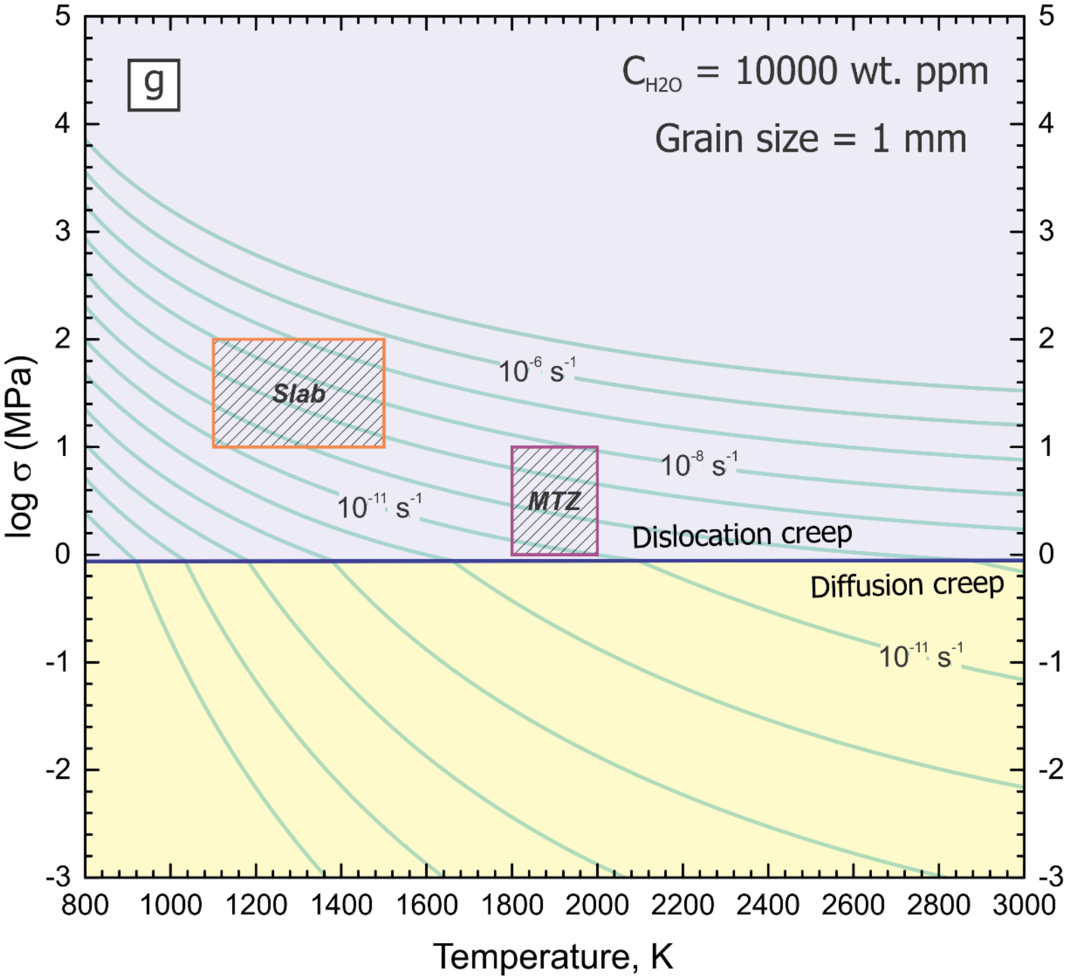

Fig. 9.11 g. A deformation map showing the boundaries between the various deformation mechanisms in stress-temperature space estimated at 20 GPa at *10000 wt. ppm* H_2O and *1 mm* grain size. Solid blue line is boundary between dislocation and diffusion creep. Levels of some strain rates are noted with numbers. Stress-temperature ranges for slabs and MTZ are shown by hatched rectangular.

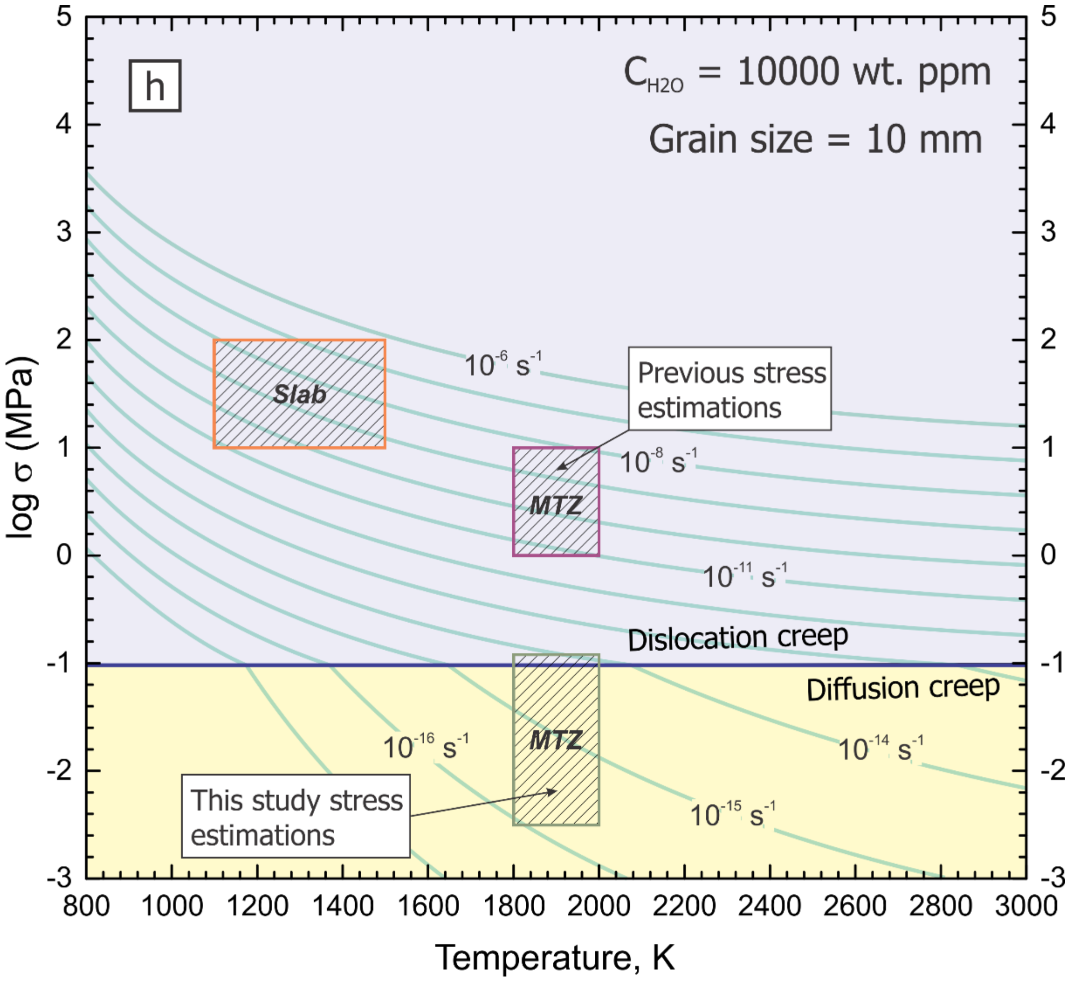

Fig. 9.11 h. A deformation map showing the boundaries between the various deformation mechanisms in stress-temperature space estimated at 20 GPa at *10000 wt. ppm* H_2O and *10 mm* grain size. Solid blue line is boundary between dislocation and diffusion creep. Light green lines are strain rate with one order of magnitude step, levels of some strain rates are noted with numbers. Stress-temperature ranges for slabs and MTZ are shown by hatched rectangular.

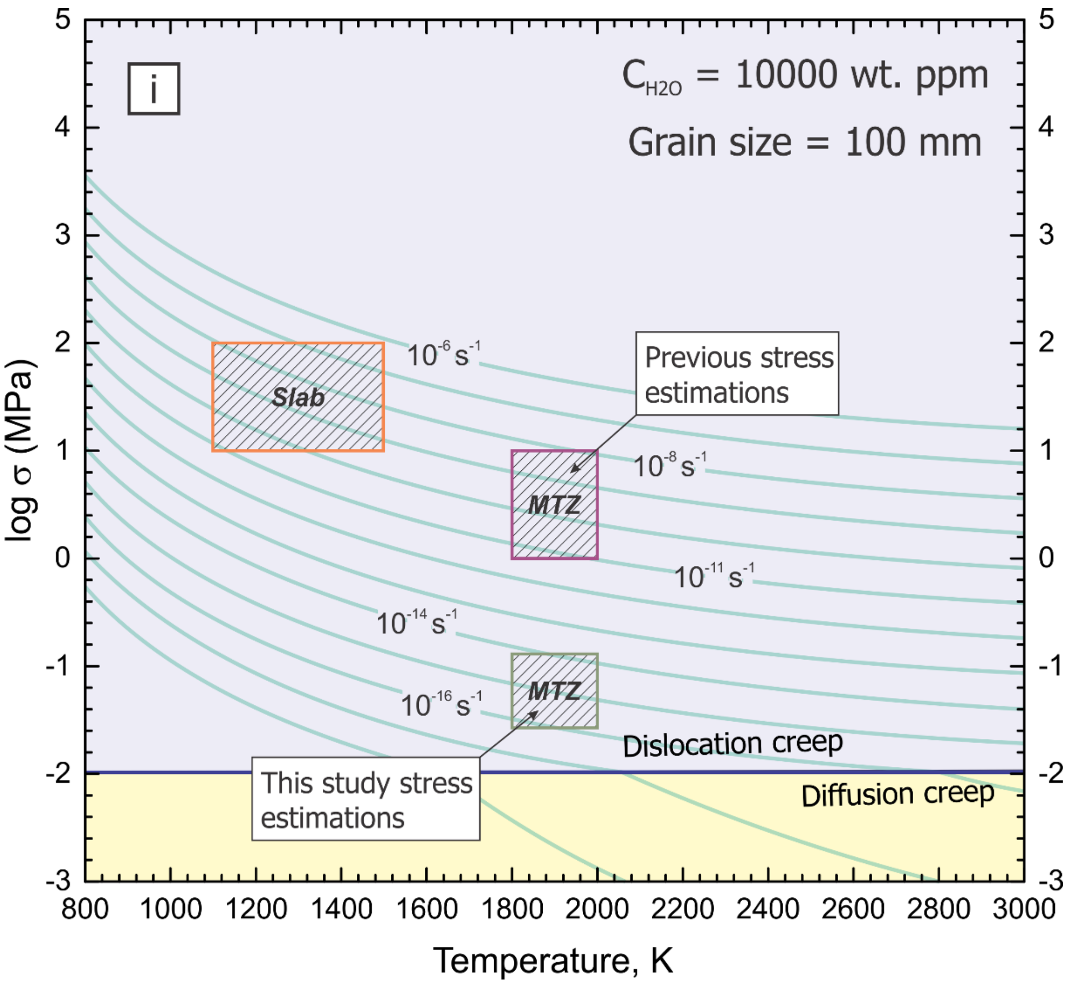

Fig. 9.11 i. A deformation map showing the boundaries between the various deformation mechanisms in stress-temperature space estimated at 20 GPa at *10000 wt. ppm* H_2O and *100 mm* grain size. Solid blue line is boundary between dislocation and diffusion creep. Light green lines are strain rate with one order of magnitude step, levels of some strain rates are noted with numbers. Stress-temperature ranges for slabs and MTZ are shown by hatched rectangular.

In the stress range from 1 to 10 MPa (purple rectangular) and at a H2O content of 10 wt. ppm, the MTZ condition leads to the dislocation creep regime as long as grain size is equal to or larger than 1 mm (**Fig. 9.11 a – d**). However, strain rates corresponding to these stresses range from 10^{-11} to 10^{-14} s^{-1}, which is higher than estimations in literature of 10^{-14} – 10^{-16} s^{-1}. Assuming previous strain rate estimations, one can conclude that dry MTZ with 10 wt. ppm of H_2O is under stresses from 0.01 to 1 MPa and 0.5 – 1 MPa at grain size of 1 and 10 mm, respectively. These ranges are by up to 2 orders of magnitude lower (green rectangular) than previously proposed for MTZ (1 – 10 MPa). Lower stresses enable dry MTZ to deform by diffusion mechanism at grain sizes smaller than 1 mm (**Fig. 9.11 c**) and by dislocation mechanism as long as grain size is equal or larger than 10 mm (**Fig. 9.11 d**). Dry slabs with 10 wt. ppm H_2O within the stress range from 10 to 100 MPa are in the dislocation creep regime as long as grain size is larger than 0.1 mm. They deform at strain rates of 10^{-9} to 10^{-14} s^{-1} (**Fig. 9.11 b – d**).

Fig. 9.11 e – i show deformation maps for hydrous wadsleyite of 1 wt.% H_2O in the stress–temperature spaces at a pressure of 20 GPa. According to these maps, MTZ in the stress range from 1 to 10 MPa deforms by dislocation-creep mechanism if grain size is equal or larger than 1 mm (**Fig. 9.11 g**). Strain rates under these stress-temperature conditions are from 10^{-8} to 10^{-11} s^{-1}. On the other hand, assuming that strain rates in hydrous MTZ are 10^{-14} – 10^{-16} s^{-1}, the stress range shifts to 0.005 – 0.1 MPa and 0.05 – 0.1 MPa with grain sizes of 10 and 100 mm, respectively. Under these stresses and at temperatures of 1800 to 2000 K, hydrous MTZ with 1 wt.% H_2O is in the dislocation-creep regime as long as the grain size is equal or larger than 50 mm. Assuming that the stress range is 10 – 100 MPa in slabs, they are in the diffusion-creep regime at a water content of 1 wt.% if the grain size is equal to or smaller than 100 μm at strain rates from 10^{-6} to 10^{-9} s^{-1}. Slabs are believed to be hydrous with grain sizes a few orders smaller than in MTZ, and with a strain rate that is higher than in MTZ. Under these assumptions slabs are always in the diffusion-creep regime (**Fig. 9.11 e**).

The result that the MTZ is in the dislocation-creep regime is consistent with observed seismic anisotropy in the MTZ (Trampert & Van Heistz, 2002; Visser, Trampert, Lebedev, & Kennett, 2008) suggested by the velocity contrast between horizontally-polarized and vertically-polarized S-waves. It is also consistent with the idea that the seismic anisotropy in MTZ is caused by lattice preferred orientation of wadsleyite. However, MTZ might be in the diffusion-creep regime, in which lattice preferred orientation of wadsleyite does not occur by creep. This argument implies that there must be regions in MTZ where anisotropy is very weak or completely absent.

9.3.3. Viscosity in MTZ and Subduction slabs

Below, I estimate the viscosity of wadsleyite as a function of temperature at a water contents of 10 wt. ppm and 1 wt.% based on Si an O diffusivity obtained in this study and stress/grain size parameters evaluated above. I estimate viscosity in the dislocation regime using the following equation:

$$\eta = \frac{\sigma}{2\dot{\varepsilon}} \tag{9.4}$$

where $\dot{\varepsilon}$ is the strain rates calculated as a function of temperature by **Eq. (3.21)** with $l_g/l_c = 1$,and σ is the stress. Resulted viscosity as a function of temperature and stress at water contents of 10 and 10000 wt. ppm is plotted in **Fig. 9.12**. The rectangle shows the stress-temperature ranges in the MTZ and slabs based on estimations described above.

In the stress range of 1 to 10 MPa, a dry MTZ with 10 wt. ppm H_2O has viscosity from $10^{17.5}$ to 10^{20} Pa·s (**Fig. 9.12 a**). This range covers partly overlap that of geologically estimated MTZ viscosity of $10^{19.5}$ to 10^{21} Pa·s (Peltier, 1998; Soldati et al., 2009) at a stress of 1 MPa. Lower stresses of 0.2 to 1 MPa based on strain rates from 10^{-14} to 10^{-16} s^{-1} lead to the conclusion that the MTZ viscosity ranges from $10^{19.5}$ to $10^{21.5}$ Pa·s, which also agree to the geological observations. Dry slabs at stresses from 10 to 100 MPa have viscosity from $10^{16.5}$ to $10^{20.5}$, which falls in the dislocation regime.

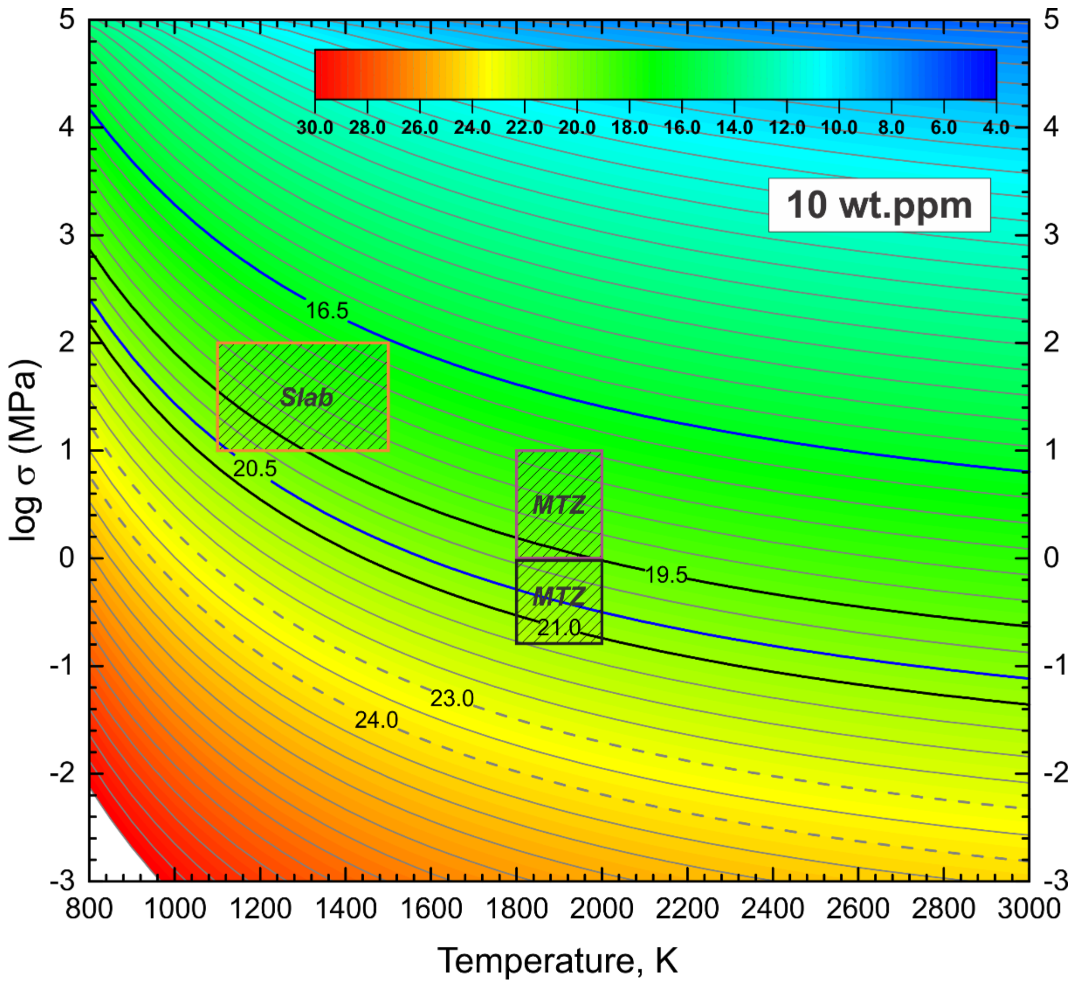

Fig. 9.12 a. A 2D contour map of viscosity (log units in Pa·s) for a dislocation regime at different stress and temperature constructed for *10 wt. ppm* H_2O in wadsleyite using diffusion data of Si and O from this study by Eq. (9.4). Each 0.5 log units Pa·s of viscosity are shown with gray lines. Blue lines represent viscosity in subducting slabs estimated in this study respectively Thick black lines show viscosity intervals for the MTZ according to geological observations. Dashed gray lines show viscosity in slabs based on literature data (Čížková, van Hunen, van den Berg, & Vlaar, 2002; Enns, Becker, & Schmeling, 2005). Orange and purple hatched tetragons are temperature and stress ranges of slabs and MTZ respectively based on stress intervals 1 – 10 MPa in MTZ and 10 – 100 MPa in slabs. Black rectangular shows stress and temperature range assuming strain rate in MTZ is 10^{-14} – 10^{-16} s^{-1}.

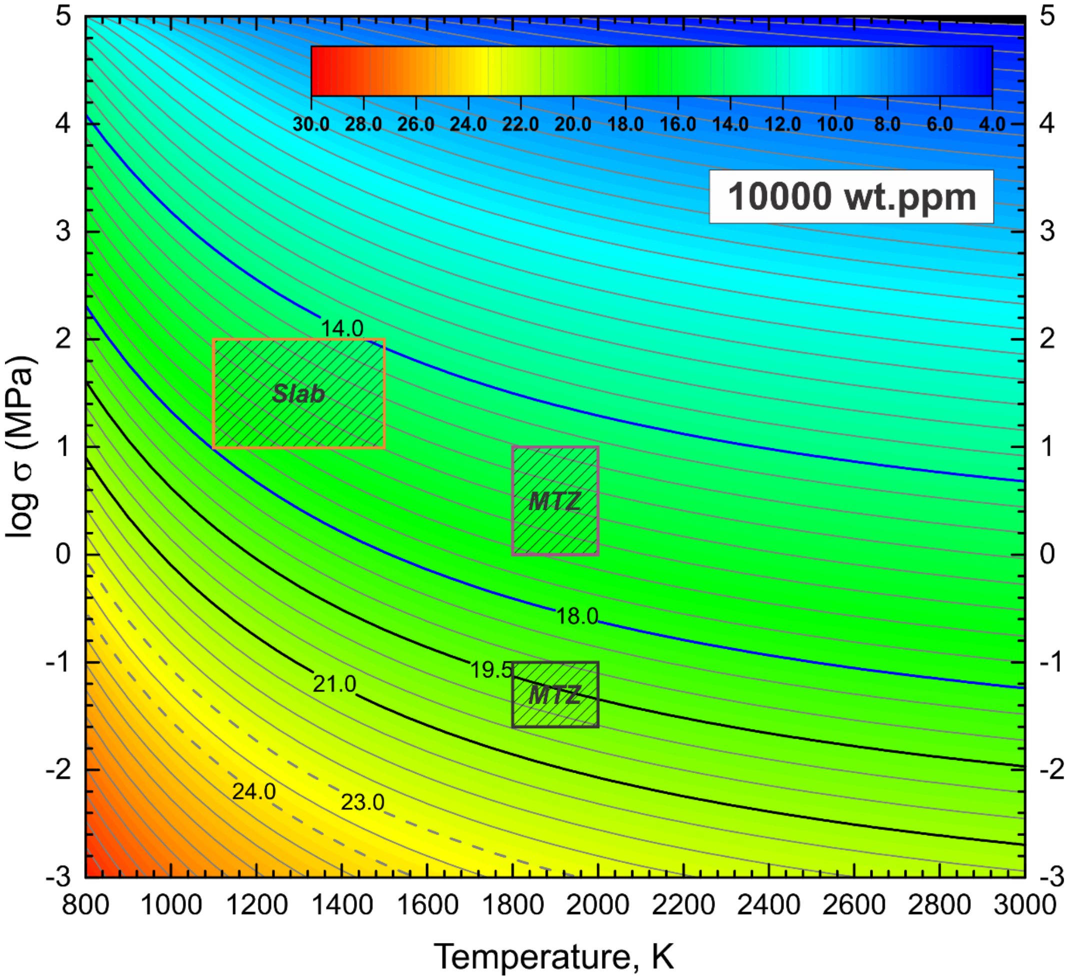

Fig. 9.12 b. A 2D contour map of viscosity (log units in Pa·s) for a dislocation regime at different stress and temperature constructed for *10000 wt. ppm* H_2O in wadsleyite using diffusion data of Si and O from this study by Eq. (9.4). Each 0.5 log units Pa·s of viscosity are shown with gray lines. Blue lines represent viscosity in subducting slabs estimated in this study respectively Thick black lines show viscosity intervals for the MTZ according to geological observations. Dashed gray lines show viscosity in slabs based on literature data (Čížková et al., 2002; Enns et al., 2005). Orange and purple hatched tetragons are temperature and stress ranges of slabs and MTZ respectively based on stress intervals 1 – 10 MPa in MTZ and 10 – 100 MPa in slabs. Black rectangular shows stress and temperature range assuming strain rate in MTZ is 10^{-14} – 10^{-16} s^{-1}.

Hydrous MTZ with 10000 wt. ppm H_2O has viscosity from $10^{14.5}$ to 10^{17} Pa·s at stresses from 1 to 10 MPa. These values show that the hydrous MTZ is 4 – 5 orders of magnitude less viscous than geologically observed. However, the assumption that the strain rates in the MTZ range from 10^{-14} to 10^{-16} s^{-1} gives lower stresses of 0.05 to 0.1 MPa. Viscosity in MTZ under these conditions is from 10^{19} to $10^{20.5}$ Pa·s and in agreement with geological observations of $10^{19.5}$ to $10^{21.5}$ Pa·s. Hydrous slabs with 1 wt.% H_2O have viscosity of 10^{14} – 10^{18} Pa·s at stresses from 10 to 100 MPa.

I have calculated contour maps of the viscosity η for diffusion creep (**Fig. 9.13**) at water contents of 10 and 10000 wt. ppm using the following equation:

$$\eta = \frac{10kTd^2}{D^{\mathrm{eff}}m} \tag{9.5}$$

where k is the Boltzmann constant, d is the grain size, and m is the molar weight of atomic species respectively (**Fig. 9.13**). D^{eff} was calculated using **Eq. (3.15)** based on the volume diffusivity of Si and O at water content smaller and larger than 1000 wt. ppm, respectively, obtained in this study and the grain-boundary diffusivity by (Shimojuku et al., 2009, 2010). Based on the **Fig. 9.11,** the largest grain size and temperature range at which diffusion creep is dominant in MTZ and slabs were marked as colored line segments. “Arrows” in **Fig.9.13** indicate the weakening of the slabs and MTZ with grain size reduction under diffusion creep regime. The blue line segment represents largest grain size of 0.1 mm and temperature range for MTZ at diffusion creep regime under stress of 1 – 10 MPa (**Fig. 9.13**). The viscosity of dry MTZ under these conditions is $10^{16.5}$ – 10^{17} Pa·s and hydrous MTZ has viscosity of $10^{14.5}$ – 10^{15} Pa·s. The red line segment shows temperature range and largest grain size of 1 mm and 10 mm for dry and hydrous MTZ at diffusion creep, respectively, under stresses below 1 MPa estimated based on a strain rate in MTZ of 10^{-14} to 10^{-16} s^{-1}. According to **Fig. 9.13,** MTZ should have viscosity of 10^{19} – $10^{19.5}$ at both 10 and 10000 wt. ppm of H_2O, in order to maintain strain rate of 10^{-14} to 10^{-16} s^{-1}. These viscosity estimations within a stress below 1 MPa at diffusion regime are in agreement with geological observations of viscosity in MTZ of $10^{19.5}$ – 10^{21} Pa·s (Peltier, 1998; Soldati et al., 2009).

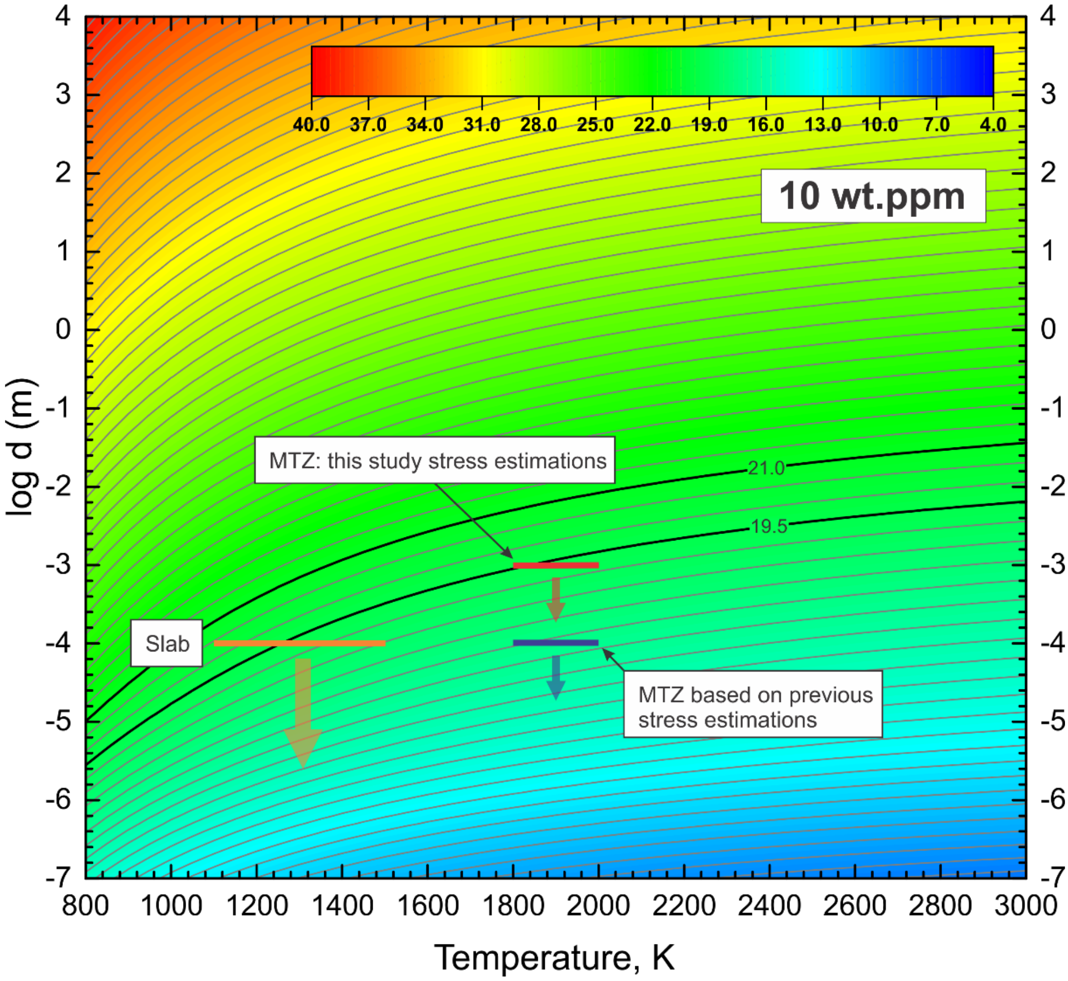

Fig. 9.13 a. A 2D contour map of viscosity (log units in Pa·s) for a diffusion creep regime at different stress and temperature constructed for *10 wt. ppm* H_2O in wadsleyite using the Si and O diffusivity obtained in this study with Eq. (9.5). Each 0.5 log units Pa·s of viscosity is shown with gray curves. Thick black lines show viscosity intervals for the MTZ according to geological observations. Thick red and blue line segments show the largest grain size and temperature range for a diffusion creep regime in the MTZ if stress is estimated based on 10^{-14} to 10^{-16} s^{-1} strain rate in MTZ and is in the range of 1 – 10 MPa respectively. Orange line segment represent the maxima of grain size and temperature of the dislocation regime in slabs.

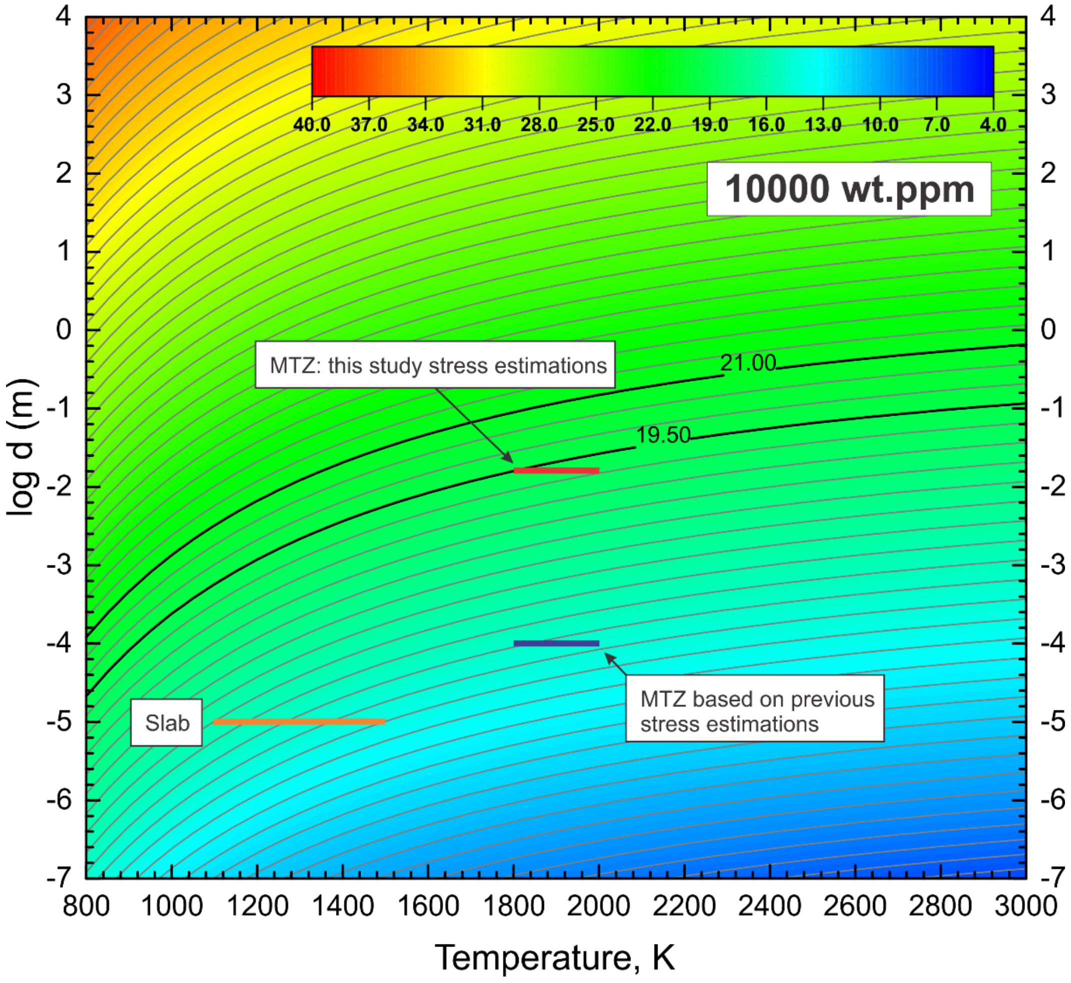

Fig. 9.13 b. A 2D contour maps of viscosity (log units in Pa·s) for a diffusion creep regime at different stress and temperature constructed for *10000 wt. ppm* H_2O in wadsleyite using the Si and O diffusivity obtained in this study with Eq. (11.2). Each 0.5 log units Pa·s of viscosity is shown with gray curves. Thick black lines show viscosity intervals for the MTZ according to geological observations. Thick red and blue line segments show the largest grain size and temperature range for a diffusion creep regime in the MTZ if stress is estimated based on 10^{-14} to 10^{-16} s^{-1} strain rate in MTZ and is in the range of 1 – 10 MPa respectively. Orange line segment represent the maxima of grain size and temperature of the dislocation regime in slabs.

A short summary of this section is shown below. Estimated strain rate in Mg_2SiO_4 wadsleyite indicates three regions with different water exponent: $\dot{\varepsilon} \propto C_{H_2O}^{0.7(2)}$ at less than 1000 wt. ppm H_2O, $\dot{\varepsilon} \propto C_{H_2O}^{0.5(2)}$ at 1000 – 5000 wt. ppm H_2O, $\dot{\varepsilon} \propto C_{H_2O}^{3.5(4)}$ at more than 5000 wt. ppm H_2O. Based on the deformation maps constructed from Si and O diffusivity in wadsleyite, possible deformation mechanism in very dry MTZ is found to be a dislocation creep as long as grain size is larger than 1 mm. Hydrous MTZ of 1 wt.% of H_2O is under dislocation regime if the grain size is larger than 5 cm. This study stress and viscosity estimations in MTZ indicate that, in order to correspond previously obtained stress values of 1 – 10 MPa (Shimojuku et al., 2009; Vassiliou et al., 1984) and viscosity values of $10^{19.5}$ to $10^{21.5}$ Pa·s (Peltier, 1998; Soldati et al., 2009), MTZ should be very dry of 10 wt. ppm H_2O. Hydrous MTZ of 1 wt. % of H_2O, in turn, should be at lower stresses of 0.05 – 0.1 MPa, in order to have viscosity similar to geophysical observations. In contrast to the surrounding MTZ, according to the deformation maps, slabs are in diffusion creep regime as long as grain size is less than 100 μm.

10. Conclusion

In this thesis the main constituent of the upper part of the MTZ was studied. In particular, rates of Si and O volume self-diffusion as a function of temperature and water content were determined within preliminary synthesized Mg_2SiO_4 wadsleyite single crystals. Diffusion sources of ^{29}Si and ^{18}O isotope enriched forsterite thin films were prepared by PLD. The diffusion profiles were measured after the annealing experiments by NanoSIMS. Diffusivities were estimated by fitting those profiles with depth to the Fick's second law solution for a thin-film, and by numerical simulation. The most important results of this work are:

- It was shown, in this study, that the activation enthalpies for Si and O diffusion are similar: $\Delta\mathrm{H}_\mathrm{O}^\mathrm{V} = \Delta\mathrm{H}_\mathrm{Si}^\mathrm{V} = 170(90)$ kJ/mol.
- The measurement shows that Si diffusivity is strongly water content dependent and anisotropic: $D_\mathrm{Si}^\mathrm{V}(100) \propto \mathrm{C}_{\mathrm{H_2O}}^{0.6}$, $D_\mathrm{Si}^\mathrm{V}(010) \propto \mathrm{C}_{\mathrm{H_2O}}^{1.9(2)}$, $D_\mathrm{Si}^\mathrm{V}(001) \propto \mathrm{C}_{\mathrm{H_2O}}^{5.2(5)}$.
- Diffusivity of O is also water content dependent and anisotropic: $D_\mathrm{O}^\mathrm{V}(100) \propto \mathrm{C}_{\mathrm{H_2O}}^{0}$, $D_\mathrm{O}^\mathrm{V}(010) \propto \mathrm{C}_{\mathrm{H_2O}}^{0.5(2)}$, $D_\mathrm{O}^\mathrm{V}(001) \propto \mathrm{C}_{\mathrm{H_2O}}^{3.5(4)}$.
- The water dependency exponents suggest that Si and O diffusion in wadsleyite occurs by a vacancy mechanism. Moreover, at water content of 5000 wt. ppm diffusion along c-direction prevails a- and b- directions, due to Si and O migration through Mg-site vacancies in M3 octahedra.
- It appears, from this study, that Si is the slowest atomic species in wadsleyite at water content lower 1500 wt. ppm. At higher water content, however, O is slower.
- The estimated strain rates for Mg_2SiO_4 wadsleyite demonstrate three regions with different water exponents indicated by the superscript: (1) dry wadsleyite with less than 1000 wt. ppm H_2O has $\dot{\varepsilon} \propto \mathrm{C}_{\mathrm{H_2O}}^{0.7(2)}$ where a water

exponent strongly qffected by diffusion along a-direction of the Si atom, (2) intermediate 1000 – 5000 wt. ppm with $\dot{\varepsilon} \propto \mathrm{C}_{\mathrm{H_2O}}^{0.5(2)}$ and (3) hydrous wadsleyite at more than 5000 wt.ppm H_2O where $\dot{\varepsilon} \propto \mathrm{C}_{\mathrm{H_2O}}^{3.5(4)}$ is mainly determined by O diffusion along c-direction.

- Based on the deformation mechanism maps constructed from Si and O diffusivities, plausible deformation mechanism in the upper mantle transition zone is found to be dislocation creep as long as grain size is larger than 1 mm at dry conditions and larger than 5 cm at 1 wt.% H_2O.
- In order to match previous stress estimations at 1 – 10 MPa and viscosity observations of $10^{19.5}$ to $10^{21.5}$ Pa·s upper MTZ should be dry. A hydrous MTZ of 1 wt.% H_2O, however, would be possible at stresses in the range 0.05 – 0.1 MPa.
- In contrast to the surrounding MTZ, according to the deformation maps, slabs are in diffusion creep regime as long as grain size is less than 100 μm.

Bibliography

Bali, E., Bolfan-Casanova, N., & Koga, K. T. (2008). Pressure and temperature dependence of H solubility in forsterite: An implication to water activity in the Earth interior. *Earth and Planetary Science Letters*, *268*(3–4), 354–363. https://doi.org/10.1016/j.epsl.2008.01.035

Batchelor, G. K. (2000). *An Introduction to Fluid Dynamics*. https://doi.org/10.1017/CBO9780511800955

Bell, D. R., Rossman, G. R., Maldener, J., Endisch, D., & Rauch, F. (2003). Hydroxide in olivine: A quantitative determination of the absolute amount and calibration of the IR spectrum. *Journal of Geophysical Research: Solid Earth*, *108*(B2). https://doi.org/10.1029/2001JB000679

Billen, M. I. (2008). Modeling the Dynamics of Subducting Slabs. *Annual Review of Earth and Planetary Sciences*, *36*(1), 325–356. https://doi.org/10.1146/annurev.earth.36.031207.124129

Bolfan-Casanova, N. (2000). *Distribution of water in the Earth's mantle*. Universität Bayreuth, Germany.

Bolfan-Casanova, N. (2005). Water in the Earth's mantle. *Mineralogical Magazine*, *69*(3), 229–258. https://doi.org/10.1180/0026461056930248

Bolfan-Casanova, N., Keppler, H., & Rubie, D. C. (2000). Water partitioning between nominally anhydrous minerals in the MgO-SiO_2-H_2O system up to 24 GPa: Implications for the distribution of water in the Earth's mantle. *Earth and Planetary Science Letters*, *182*(3–4), 209–221. https://doi.org/10.1016/S0012-821X(00)00244-2

Borch, R. S., & Green, H. W. (1987). Dependence of creep in olivine on homologous temperature and its implications for flow in the mantle. *Nature*, *330*(6146), 345–348. https://doi.org/10.1038/330345a0

Borch, R. S., & Green, H. W. (1989). Deformation of peridotite at high pressure in a new molten salt cell: comparison of traditional and homologous temperature treatments. *Physics of the Earth and Planetary Interiors*, *55*(3–4), 269–276. https://doi.org/10.1016/0031-9201(89)90075-7

Chakraborty, S. (1997). Rates and mechanisms of Fe-Mg interdiffusion in olivine at 980°-1300°C. *Journal of Geophysical Research: Solid Earth*, *102*(B6), 12317–12331. https://doi.org/10.1029/97JB00208

Chakraborty, S. (2010). Diffusion Coefficients in Olivine, Wadsleyite and Ringwoodite. *Reviews in Mineralogy and Geochemistry*, *72*(1), 603–639. https://doi.org/10.2138/rmg.2010.72.13

Chakraborty, S., Farver, J., Yund, R. A., & Rubie, D. C. (1994). Mg tracer diffusion in synthetic forsterite and San Carlos olivine as a function of P, T and *f*O2. *Physics and Chemistry of Minerals*, *21*(8). https://doi.org/10.1007/BF00203923

Chakraborty, S., Knoche, R., Schulze, H., Rubie, D. C., Dobson, D. P., Ross, N. L., & Angel, R. J. (1999). Enhancement of cation diffusion rates across the 410-kilometer discontinuity in Earth's mantle. *Science*, *283*(5400), 362–365. https://doi.org/10.1126/science.283.5400.362

Chang, S. J., & Ferreira, A. M. G. (2019). Inference on Water Content in the Mantle Transition Zone Near Subducted Slabs From Anisotropy Tomography. *Geochemistry, Geophysics, Geosystems*, *20*(2), 1189–1201. https://doi.org/10.1029/2018GC008090

Cherniak, D. J., Hervig, R., Koepke, J., Zhang, Y., & Zhao, D. (2010). Analytical Methods in Diffusion Studies. *Reviews in Mineralogy and Geochemistry*, *72*(1), 107–170. https://doi.org/10.2138/rmg.2010.72.4

Čížková, H., van Hunen, J., van den Berg, A. P., & Vlaar, N. J. (2002). The influence of rheological weakening and yield stress on the interaction of slabs with the 670 km discontinuity. *Earth and Planetary Science Letters*, *199*(3–4), 447–457. https://doi.org/10.1016/S0012-821X(02)00586-1

Coble, R. L. (1963). A Model for Boundary Diffusion Controlled Creep in Polycrystalline Materials. *Journal of Applied Physics*, *34*(6), 1679–1682. https://doi.org/10.1063/1.1702656

Costa, F., & Chakraborty, S. (2008). The effect of water on Si and O diffusion rates in olivine and implications for transport properties and processes in the upper mantle. *Physics of the Earth and Planetary Interiors*, *166*(1–2), 11–29. https://doi.org/10.1016/j.pepi.2007.10.006

Crank, J. (1975). *The Mathematics of Diffusion* (2nd ed.). Oxford University Press.

Demouchy, S., Deloule, E., Frost, D. J., & Keppler, H. (2005). Pressure and temperature-dependence of water solubility in Fe-free wadsleyite. *American Mineralogist*, *90*(7), 1084–1091. https://doi.org/10.2138/am.2005.1751

Demouchy, S., Mainprice, D., Tommasi, A., Couvy, H., Barou, F., Frost, D. J., & Cordier, P. (2011). Forsterite to wadsleyite phase transformation under shear stress and consequences for the Earth's mantle transition zone. *Physics of the Earth and Planetary Interiors*, *184*(1–2), 91–104. https://doi.org/10.1016/j.pepi.2010.11.001

Deon, F., Koch-Müller, M., Rhede, D., Gottschalk, M., Wirth, R., & Thomas, S. M. (2010). Location and quantification of hydroxyl in wadsleyite: New insights. *American Mineralogist*, *95*(2–3), 312–322. https://doi.org/10.2138/am.2010.3267

Dimanov, A., & Jaoul, O. (1998). Calcium self-diffusion in diopside at high temperature: implications for transport properties. *Physics and Chemistry of Minerals*, *26*(2), 116–127. https://doi.org/10.1007/s002690050168

Dobson, D. P., Dohmen, R., & Wiedenbeck, M. (2008). Self-diffusion of oxygen and silicon in $MgSiO_3$ perovskite. *Earth and Planetary Science Letters*, *270*(1–2), 125–129. https://doi.org/10.1016/j.epsl.2008.03.029

Dohmen, R. (2002). Si and O diffusion in olivine and implications for characterizing plastic flow in the mantle. *Geophysical Research Letters*, *29*(21), 2030. https://doi.org/10.1029/2002GL015480

Dohmen, R. (2008). A new experimental thin film approach to study mobility and partitioning of elements in grain boundaries: Fe-Mg exchange between olivines mediated by transport through an inert grain boundary. *American Mineralogist*, *93*(5–6), 863–874. https://doi.org/10.2138/am.2008.2671

Dohmen, R., Becker, H. W., & Chakraborty, S. (2007). Fe-Mg diffusion in olivine I: Experimental determination between 700 and 1,200°C as a function of composition, crystal orientation and oxygen fugacity. *Physics and Chemistry of Minerals*, *34*(6), 389–407. https://doi.org/10.1007/s00269-007-0157-7

Dohmen, R., Becker, H. W., Meißner, E., Etzel, T., & Chakraborty, S. (2002). Production of silicate thin films using pulsed laser deposition (PLD) and applications to studies in mineral kinetics. *European Journal of Mineralogy*, *14*(6), 1155–1168. https://doi.org/10.1127/0935-1221/2002/0014-1155

Dohmen, R., & Chakraborty, S. (2007). Fe–Mg diffusion in olivine II: point defect chemistry, change of diffusion mechanisms and a model for calculation of diffusion coefficients in natural olivine. *Phys Chem Minerals*. https://doi.org/10.1007/s00269-007-0158-6

Dohmen, R., Marschall, H., & Ludwig, T. (2009). Diffusive fractionation of Nb and Ta in rutile. *Geochim Cosmochim Acta 73*, *73*, A297.

Downs, J. W. (1989). Possible sites for protonation in beta -Mg_2SiO_4 from an experimentally derived electrostatic potential. *American Mineralogist*, *74*(9–10), 1124–1129.

Einstein, A. (1905). Über die von der molekularkinetischen Theorie der Wärme geforderte Bewegung von in ruhenden Flüssigkeiten suspendierten Teilchen. *Annalen Der Physik*, *322*(8), 549–560. https://doi.org/10.1002/andp.19053220806

Enns, A., Becker, T. W., & Schmeling, H. (2005). The dynamics of subduction and trench migration for viscosity stratification. *Geophysical Journal International*, *160*(2), 761–775. https://doi.org/10.1111/j.1365-246X.2005.02519.x

Farber, D. L., Williams, Q., & Ryerson, F. J. (2000). Divalent cation diffusion in Mg_2SiO_4 spinel (ringwoodite), betta phase (wadsleyite), and olivine: Implications for the electrical conductivity of the mantle. *Journal of Geophysical Research*, *105*(1), 513–529.

Farla, R., Amulele, G., Girard, J., Miyajima, N., & Karato, S. I. (2015). High-pressure and high-temperature deformation experiments on polycrystalline wadsleyite using the rotational Drickamer apparatus. *Physics and Chemistry of Minerals*, *42*(7), 541–558. https://doi.org/10.1007/s00269-015-0742-0

Farver, J., & Yund, R. (2000). Silicon diffusion in a natural quartz aggregate: constraints on solution-transfer diffusion creep. *Tectonophysics*, *325*(3–4), 193–205. https://doi.org/10.1016/S0040-1951(00)00121-9

Fei, H., Hegoda, C., Yamazaki, D., Wiedenbeck, M., Yurimoto, H., Shcheka, S., & Katsura, T. (2012). High silicon self-diffusion coefficient in dry forsterite. *Earth and Planetary Science Letters*, *345–348*, 95–103. https://doi.org/10.1016/j.epsl.2012.06.044

Fei, H., Wiedenbeck, M., Yamazaki, D., & Katsura, T. (2013). Small effect of water on upper-mantle rheology based on silicon self-diffusion coefficients. *Nature*, *498*(7453), 213–215. https://doi.org/10.1038/nature12193

Fei, H., Wiedenbeck, M., Yamazaki, D., & Katsura, T. (2014). No effect of water on oxygen self-diffusion rate in forsterite. *Journal of Geophysical Research: Solid Earth*, *119*(10), 7598–7606. https://doi.org/10.1002/2014JB011141

Fei, H., Yamazaki, D., Sakurai, M., Miyajima, N., Ohfuji, H., Katsura, T., & Yamamoto, T. (2017). A nearly water-saturated mantle transition zone inferred from mineral viscosity. *Science Advances*, *3*(6), e1603024. https://doi.org/10.1126/sciadv.1603024

Fei, Y., & Bertka, C. M. (1999). Phase transitions in Earth's mantle and mantle mineralogy. *Mantle Petrology: Field Observations and High Pressure Experimentation (a Tribute to Francis R. (Joe) Boyd)*, *6*(6), 189–207.

Fick, A. (1995). On liquid diffusion. *Journal of Membrane Science*, *100*(1), 33–38. https://doi.org/10.1016/0376-7388(94)00230-V

Forsyth, D. W. (1975). The Early Structural Evolution and Anisotropy of the Oceanic Upper Mantle. *Geophysical Journal International*, *43*(1), 103–162. https://doi.org/10.1111/j.1365-246X.1975.tb00630.x

Frost, D. J., & Dolejš, D. (2007). Experimental determination of the effect of H 2 O on the 410-km seismic discontinuity. *Earth and Planetary Science Letters*, *256*(1–2), 182–195. https://doi.org/10.1016/j.epsl.2007.01.023

Frost, H. J., & Ashby, M. F. (1982). *Deformation mechanism maps: the* *plasticity and creep of metals and ceramics.* Oxford, UK: Pergamon Press.

Fukao, Y., Obayashi, M., Inoue, H., & Nenbai, M. (1992). Subducting slabs stagnant in the mantle transition zone. *Journal of Geophysical Research*, *97*(B4), 4809. https://doi.org/10.1029/91JB02749

Fukao, Y., Obayashi, M., & Nakakuki, T. (2009). Stagnant Slab: A Review. *Annual Review of Earth and Planetary Sciences*, *37*(1), 19–46. https://doi.org/10.1146/annurev.earth.36.031207.124224

Fukao, Y., Widiyantoro, S., & Obayashi, M. (2001). Stagnant slabs in the upper and lower mantle transition region. *Reviews of Geophysics*, *39*(3), 291–323. https://doi.org/10.1029/1999RG000068

Gaherty, J. B., Kato, M., & Jordan, T. H. (1999). Seismological structure of the upper mantle: a regional comparison of seismic layering. *Physics of the Earth and Planetary Interiors*, *110*(1–2), 21–41. https://doi.org/10.1016/S0031-9201(98)00132-0

Ganguly, J., Cheng, W., & Chakraborty, S. (1998). Cation diffusion in aluminosilicate garnets: experimental determination in pyrope-almandine diffusion couples. *Contributions to Mineralogy and Petrology*, *131*(2–3), 171–180. https://doi.org/10.1007/s004100050386

Ganguly, J., Ito, M., & Zhang, X. (2007). Cr diffusion in orthopyroxene: Experimental determination, ^{53}Mn–^{53}Cr thermochronology, and planetary applications. *Geochimica et Cosmochimica Acta*, *71*(15), 3915–3925. https://doi.org/10.1016/j.gca.2007.05.023

Gardés, E., Jaoul, O., Montel, J.-M., Seydoux-Guillaume, A.-M., & Wirth, R. (2006). Pb diffusion in monazite: An experimental study of interdiffusion. *Geochimica et Cosmochimica Acta*, *70*(9), 2325–2336. https://doi.org/10.1016/j.gca.2006.01.018

Gérard, O., & Jaoul, O. (1989). Oxygen diffusion in San Carlos olivine. *Journal of Geophysical Research: Solid Earth*, *94*(B4), 4119–4128. https://doi.org/10.1029/JB094iB04p04119

Grand, S. P. (2002). Mantle shear–wave tomography and the fate of subducted slabs. *Philosophical Transactions of the Royal Society of London. Series A: Mathematical, Physical and Engineering Sciences*, *360*(1800), 2475–2491. https://doi.org/10.1098/rsta.2002.1077

Griffiths, P. R., De Haseth, J. A., & Winefordner, J. D. (2006). *Fourier Transform Infrared Spectrometry* (2nd ed.). New Jersey: A John Wiley & Sons, Inc.

Griggs, D. (1967). Hydrolytic Weakening of Quartz and Other Silicates. *Geophysical Journal of the Royal Astronomical Society*, *14*(1–4), 19–31. https://doi.org/10.1111/j.1365-246X.1967.tb06218.x

Gung, Y., Panning, M., & Romanowicz, B. (2003). Global anisotropy and the thickness of continents. *Nature*, *422*(6933), 707–711. https://doi.org/10.1038/nature01559

Hazen, R. M. (1976). Effects of temperature and pressure on the crystal structure of forsterite. *American Mineralogist*, *61*(11–12), 1280–1293.

Herring, C. (1950). Diffusional viscosity of a polycrystalline solid. *Journal of Applied Physics*, *21*(5), 437–445. https://doi.org/10.1063/1.1699681

Herring, C., & Bardeen, J. (1951). *Atom Movements*. Cleveland: A.S.M.

Hirschmann, M. M., Aubaud, C., & Withers, A. C. (2005). Storage capacity of H_2O in nominally anhydrous minerals in the upper mantle. *Earth and Planetary Science Letters*, *236*(1–2), 167–181. https://doi.org/10.1016/j.epsl.2005.04.022

Hirth, G., & Kohlstedt, D. L. (2003). *Rheology of the upper mantle and the mantle wedge: A view from the experimentalists*. https://doi.org/10.1029/138GM06

Hirth, J. P., & Lothe, J. (1982). *Theory of dislocations* (2nd ed.). New York: Wiley.

Hofmann, S. (1994). Atomic mixing, surface roughness and information depth in high-resolution AES depth profiling of a GaAs/AlAs superlattice structure. *Surface and Interface Analysis*, *21*(9), 673–678. https://doi.org/10.1002/sia.740210912

Holl, C. M., Smyth, J. R., Jacobsen, S. D., & Frost, D. J. (2008). Effects of hydration on the structure and compressibility of wadsleyite, ß-(Mg_2SiO_4). *American Mineralogist*, *93*(4), 598–607. https://doi.org/10.2138/am.2008.2620

Holzapfel, C., Chakraborty, S., Rubie, D. C., & Frost, D. J. (2009). Fe-Mg interdiffusion in wadsleyite: The role of pressure, temperature and composition and the magnitude of jump in diffusion rates at the 410 km discontinuity. *Physics of the Earth and Planetary Interiors*, *172*(1–2), 28–33. https://doi.org/10.1016/j.pepi.2008.09.005

Hoppe, P., Cohen, S., & Meibom, A. (2013). NanoSIMS: Technical Aspects and Applications in Cosmochemistry and Biological Geochemistry. *Geostandards and Geoanalytical Research*, *37*(2), 111–154. https://doi.org/10.1111/j.1751-908X.2013.00239.x

Houlier, B., Cheraghmakani, M., & Jaoul, O. (1990). Silicon Diffusion in San-Carlos Olivine. *Physics of the Earth and Planetary Interiors*, *62*(3–4), 329–340. https://doi.org/10.1016/0031-9201(90)90177-Y

Huang, X., Xu, Y., & Karato, S. I. (2005). Water content in the transition zone from electrical conductivity of wadsleyite and ringwoodite. *Nature*, *434*(7034), 746–749. https://doi.org/10.1038/nature03426

Inoue, T., Ueda, T., Tanimoto, Y., Yamada, A., & Irifune, T. (2010). The effect of water on the high-pressure phase boundaries in the system Mg_2SiO_4-Fe_2SiO_4. *Journal of Physics: Conference Series*, *215*, 012101. https://doi.org/10.1088/1742-6596/215/1/012101

Jacobsen, S. D., Demouchy, S., Frost, D. J., Ballaran, T. B., & Kung, J. (2005). A systematic study of OH in hydrous wadsleyite from polarized FTIR spectroscopy and single-crystal X-ray diffraction: Oxygen sites for hydrogen storage in Earth's interior. *American Mineralogist*, *90*(1), 61–70. https://doi.org/10.2138/am.2005.1624

Jaoul, O., Poumellec, M., Froidevaux, C., & Havette, A. (1981). Silicon diffusion in forsterite: A new constraint for understanding mantle deformation. In *Anelasticity in the Earth* (pp. 95–100). https://doi.org/10.1029/GD004p0095

Karato, S. I. (1998). A Dislocation Model of Seismic Wave Attenuation and Micro-creep in the Earth: Harold Jeffreys and the Rheology of the Solid Earth. *Pure and Applied Geophysics*, *153*(2–4), 239–256. https://doi.org/10.1007/s000240050195

Karato, S. I. (2008). *Deformation of Earth Materials*. https://doi.org/10.1017/CBO9780511804892

Karato, S. I. (2010). Rheology of the Earth's mantle: A historical review. *Gondwana Research*, *18*(1), 17–45. https://doi.org/10.1016/j.gr.2010.03.004

Karato, S. I., & Rubie, D. C. (1997). Toward an experimental study of deep mantle rheology: A new multianvil sample assembly for deformation studies under high pressures and temperatures. *Journal of Geophysical Research: Solid Earth*, *102*(B9), 20111–20122. https://doi.org/10.1029/97JB01732

Karato, S. I., & Wu, P. (1993). Rheology of the Upper Mantle: A Synthesis. *Science*, *260*(5109), 771–778. https://doi.org/10.1126/science.260.5109.771

Katsura, T., & Ito, E. (1989a). A temperature profile of the mantle transition zone. *Geophysical Research Letters*, *16*(5), 425–428.

Katsura, T., & Ito, E. (1989b). The system Mg_2SiO_4-Fe_2SiO_4 at high pressures and temperatures: Precise determination of stabilities of olivine, modified spinel, and spinel. *Journal of Geophysical Research: Solid Earth*, *94*(B11), 15663–15670. https://doi.org/10.1029/JB094iB11p15663

Katsura, T., Yamada, H., Nishikawa, O., Song, M., Kubo, A., Shinmei, T., … Funakoshi, K. (2004). Olivine-wadsleyite transition in the system $(Mg,Fe)_2SiO_4$. *Journal of Geophysical Research: Solid Earth*, *109*(B2), 1–12. https://doi.org/10.1029/2003jb002438

Katsura, T., Yamada, H., Shinmei, T., Kubo, A., Ono, S., Kanzaki, M., … Utsumi, W. (2003). Post-spinel transition in Mg_2SiO_4 determined by high P–T in situ X-ray diffractometry. *Physics of the Earth and Planetary Interiors*, *136*(1–2), 11–24. https://doi.org/10.1016/S0031-9201(03)00019-0

Katsura, T., Yoneda, A., Yamazaki, D., Yoshino, T., Ito, E., Suetsugu, D., … Jellinek, M. (2010). Adiabatic temperature profile in the mantle. *Physics of the Earth and Planetary Interiors*, *183*(1–2), 212–218. https://doi.org/10.1016/j.pepi.2010.07.001

Kawazoe, T., Buchen, J., & Marquardt, H. (2015). Synthesis of large wadsleyite single crystals by solid-state recrystallization. *American Mineralogist*, *100*(10), 2336–2339. https://doi.org/10.2138/am-2015-5400

Kawazoe, T., Karato, S. I., Ando, J. I., Jing, Z., Otsuka, K., & Hustoft, J. W. (2010). Shear deformation of polycrystalline wadsleyite up to 2100 K at 14-17 GPa using a rotational Drickamer apparatus (RDA). *Journal of Geophysical Research: Solid Earth*, *115*(8), 1–11. https://doi.org/10.1029/2009JB007096

Kawazoe, T., Nishihara, Y., Ohuchi, T., Nishiyama, N., Higo, Y., Funakoshi, K. I., & Irifune, T. (2011). In situ stress-strain measurements in a deformation-DIA apparatus at P-T conditions of the upper part of the mantle transition zone. *American Mineralogist*, *96*(11–12), 1665–1672. https://doi.org/10.2138/am.2011.3818

Kawazoe, T., Ohuchi, T., Nishihara, Y., Nishiyama, N., Fujino, K., & Irifune, T. (2013). Seismic anisotropy in the mantle transition zone induced by shear deformation of wadsleyite. *Physics of the Earth and Planetary Interiors*, *216*, 91–98. https://doi.org/10.1016/j.pepi.2012.12.005

Keppler, H., & Frost, D. J. (2005). Introduction to minerals under extreme conditions. *EMU Notes in Mineralogy*, *7*(2005), 1–30.

Kiefer, B., Stixrude, L., Hafner, J., & Kresse, G. (2001). Structure and elasticity of wadsleyite at high pressures. *American Mineralogist*, *86*(11–12), 1387–1395. https://doi.org/10.2138/am-2001-11-1207

Koch-Müller, M., & Rhede, D. (2010). IR absorption coefficients for water in nominally anhydrous high-pressure minerals. *American Mineralogist*, *95*(5–6), 770–775. https://doi.org/10.2138/am.2010.3358

Kohlstedt, D. L. (2006). The Role of Water in High-Temperature Rock Deformation. *Reviews in Mineralogy and Geochemistry*, *62*(1), 377–396. https://doi.org/10.2138/rmg.2006.62.16

Kohlstedt, D. L. (2018). The role of water in high-temperature rock deformation. *Water in Nominally Anhydrous Minerals*, *62*, 377–396. https://doi.org/10.2138/rmg.2006.62.16

Kohlstedt, D. L., & Goetze, C. (1974). Low-stress high-temperature creep in olivine single crystals. *Journal of Geophysical Research*, *79*(14), 2045–2051. https://doi.org/10.1029/JB079i014p02045

Kohlstedt, D. L., Keppler, H., & Rubie, D. C. (1996). Solubility of water in the α, β and γ phases of $(Mg,Fe)_2SiO_4$. *Contributions to Mineralogy and Petrology*, *123*(4), 345–357. https://doi.org/10.1007/s004100050161

Kohn, S. C., Brooker, R. A., Frost, D. J., Slesinger, A. E., & Wood, B. J. (2002). Ordering of hydroxyl defects in hydrous wadsleyite (β-Mg2SiO4). *American Mineralogist*, *87*(2–3), 293–301.

Kröger, F. A., & Vink, H. J. (1956). Relations between the Concentrations of Imperfections in Crystalline Solids. In *Volume 3: Solid State Physics* (pp. 307–435). https://doi.org/10.1016/S0081-1947(08)60135-6

Kubo, T., Shimojuku, A., & Ohtani, E. (2004). Mg-Fe interdiffusion rates in wadsleyite and the diffusivity jump at the 410-km discontinuity. *Physics and Chemistry of Minerals*, *31*(7), 456–464. https://doi.org/10.1007/s00269-004-0412-0

Kudoh, Y., & Inoue, T. (1999). Mg-vacant structural modules and dilution of the symmetry of hydrous wadsleyite, $\beta\text{-}Mg_{2-x}SiH_{2x}O_4$ with $0.00 \leq x \leq 0.25$. *Physics and Chemistry of Minerals*, *26*(5), 382–388. https://doi.org/10.1007/s002690050198

Le Claire, A. D. (1963). The analysis of grain boundary diffusion measurements. *British Journal of Applied Physics*, *14*(6), 351–356. https://doi.org/10.1088/0508-3443/14/6/317

Libowitzky, E., & Rossman, G. R. (1997). An IR absorption calibration for water in minerals. *American Mineralogist*, *82*(11–12), 1111–1115. https://doi.org/10.2138/am-1997-11-1208

Litasov, K. D., & Shatskiy, A. (2011). Systematic study of hydrogen incorporation into Fe-free wadsleyite. *Phys Chem Minerals*, 75–84. https://doi.org/10.1007/s00269-010-0382-3

Mainprice, D. (2007). Seismic Anisotropy of the Deep Earth from a Mineral and Rock Physics Perspective. In *Volume 2: Mineral Physics* (pp. 437–491). https://doi.org/10.1016/B978-044452748-6/00045-6

Mao, Z., Jacobsen, S. D., Jiang, F., Smyth, J. R., Holl, C. M., & Duffy, T. S. (2008). Elasticity of hydrous wadsleyite to 12 GPa: Implications for Earth's transition zone. *Geophysical Research Letters*, *35*(21), L21305. https://doi.org/10.1029/2008GL035618

Maxwell, J. C. (1867). On the dynamical theory of gases. *Proceedings of the Royal Society of London*, *15*, 167–171. https://doi.org/10.1098/rspl.1866.0039

McKenzie, D. P. (1967). The Viscosity of the Mantle. *Geophysical Journal of* *the Royal Astronomical Society*, *14*(1–4), 297–305. https://doi.org/10.1111/j.1365-246X.1967.tb06246.x

Mehrer, H. (2007). *Diffusion in Solids* (Vol. 155). https://doi.org/10.1007/978-3-540-71488-0

Metsue, A., Carrez, P., Denoual, C., Mainprice, D., & Cordier, P. (2010). Plastic deformation of wadsleyite: IV Dislocation core modelling based on the Peierls-Nabarro-Galerkin model. *Acta Materialia*, *58*(5), 1467–1478. https://doi.org/10.1016/j.actamat.2009.10.047

Michelson, A. A. (1891). XXVIII. Visibility of interference-fringes in the focus of a telescope. *The London, Edinburgh, and Dublin Philosophical Magazine and Journal of Science*, *31*(190), 256–259. https://doi.org/10.1080/14786449108620101

Milke, R., Dohmen, R., Becker, H. W., & Wirth, R. (2007). Growth kinetics of enstatite reaction rims studied on nano-scale, Part I: Methodology, microscopic observations and the role of water. *Contributions to Mineralogy and Petrology*, *154*(5), 519–533. https://doi.org/10.1007/s00410-007-0207-7

Montagner, J. (1998). Where Can Seismic Anisotropy Be Detected in the Earth's Mantle? In Boundary Layers... *Pure and Applied Geophysics*, *151*(4), 223. https://doi.org/10.1007/s000240050113

Morishima, H., Kato, T., Suto, M., Ohtani, E., Urakawa, S., Utsumi, W., … Kikegawa, T. (1994). The Phase Boundary Between agr- and beta-Mg2SiO4 Determined by in Situ X-ray Observation. *Science*, *265*(5176), 1202–1203. https://doi.org/10.1126/science.265.5176.1202

Nabarro, F. R. N. (1948). "Report of a Conference on the Strength of Solids." *The Physical Society*, (75).

Nishihara, Y., Shinmei, T., & Karato, S. I. (2008). Effect of chemical environment on the hydrogen-related defect chemistry in wadsleyite. *American Mineralogist*, *93*(5–6), 831–843. https://doi.org/10.2138/am.2008.2653

Paterson, M. S. (1970). A high-pressure, high-temperature apparatus for rock deformation. *International Journal of Rock Mechanics and Mining Sciences & Geomechanics Abstracts*, *7*(5), 517–526. https://doi.org/10.1016/0148-9062(70)90004-5

Paterson, M. S. (1982). The determination of hydroxyl by infrared absorption in quartz, silicate glasses and similar materials. *Bulletin de Mineralogi*, *105*, 20–29.

Pearson, D. G., Brenker, F. E., Nestola, F., McNeill, J., Nasdala, L., Hutchison, M. T., … Vincze, L. (2014). Hydrous mantle transition zone indicated by ringwoodite included within diamond. *Nature*, *507*(7491), 221–224.

https://doi.org/10.1038/nature13080

Peltier, W. R. (1998). Postglacial variations in the level of the sea: Implications for climate dynamics and solid-earth geophysics. *Rev. Geophys.*, *36*, 603–689. https://doi.org/10.1109/ICASIC.2007.4415573

Price, G. D. (1983). The nature and significance of stacking faults in wadsleyite, natural ß-$(Mg,Fe)_2SiO_4$ from the Peace River meteorite. *Physics of the Earth and Planetary Interiors*, *33*(2), 137–147. https://doi.org/10.1016/0031-9201(83)90146-2

Purevjav, N., Okuchi, T., Tomioka, N., Wang, X., & Hoffmann, C. (2016). Quantitative analysis of hydrogen sites and occupancy in deep mantle hydrous wadsleyite using single crystal neutron diffraction. *Scientific Reports*, *6*(June), 1–8. https://doi.org/10.1038/srep34988

Raj, R., & Ashby, M. F. (1971). On grain boundary sliding and diffusional creep. *Metallurgical Transactions*, *2*(4), 1113–1127. https://doi.org/10.1007/BF02664244

Ringwood, A. E. (1962). A model for the upper mantle. *Journal of Geophysical Research*, *67*(2), 857–867. https://doi.org/10.1029/JZ067i002p00857

Ringwood, A. E., & Major, A. (1966). Synthesis of Mg_2SiO_4-Fe_2SiO_4 spinel solid solutions. *Earth and Planetary Science Letters*, *1*(4), 241–245. https://doi.org/10.1016/0012-821X(66)90077-X

Ringwood, A. E., & Major, A. (1970). The system Mg_2SiO4-Fe_2SiO_4 at high pressures and temperatures. *Physics of the Earth and Planetary Interiors*, *3*, 89–108. https://doi.org/10.1016/0031-9201(70)90046-4

Ryerson, F. J., Durham, W. B., Cherniak, D. J., & Lanford, W. A. (1989). Oyxgen diffusion in olivine: effect of oxygen fugacity and implications for creep. *Journal of Geophysical Research*, *94*(B4), 4105–4118. https://doi.org/10.1029/JB094iB04p04105

Sano-Furukawa, A., Kuribayashi, T., Komatsu, K., Yagi, T., & Ohtani, E. (2011). Investigation of hydrogen sites of wadsleyite: A neutron diffraction study. *Physics of the Earth and Planetary Interiors*, *189*(1–2), 56–62. https://doi.org/10.1016/j.pepi.2011.07.003

Sawamoto, H. (1986). Single crystal growth of the modified spinel (ß) and spinel (γ) phases of $(Mg,Fe)_2SiO_4$ and some geophysical implications. *Physics and Chemistry of Minerals*, *13*(1), 1–10. https://doi.org/10.1007/BF00307307

Schmalzried, H. (1995). *Chemical Kinetics of Solids* (H. Schmalzried, Ed.). https://doi.org/10.1002/9783527615537

Shatskiy, A., Litasov, K. D., Matsuzaki, T., Shinoda, K., Yamazaki, D., Yoneda, A., … Katsura, T. (2009). Single crystal growth of wadsleyite. *American*

Mineralogist, *94*(8–9), 1130–1136. https://doi.org/10.2138/am.2009.3150

Shimojuku, A., Kubo, T., Ohtani, E., Nakamura, T., & Okazaki, R. (2010). Effects of hydrogen and iron on the silicon diffusivity of wadsleyite. *Physics of the Earth and Planetary Interiors*, *183*(1–2), 175–182. https://doi.org/10.1016/j.pepi.2010.09.011

Shimojuku, A., Kubo, T., Ohtani, E., Nakamura, T., Okazaki, R., Dohmen, R., & Chakraborty, S. (2009). Si and O diffusion in $(Mg,Fe)_2SiO_4$ wadsleyite and ringwoodite and its implications for the rheology of the mantle transition zone. *Earth and Planetary Science Letters*, *284*(1–2), 103–112. https://doi.org/10.1016/j.epsl.2009.04.014

Shimojuku, A., Kubo, T., Ohtani, E., & Yurimoto, H. (2004). Silicon self-diffusion in wadsleyite: Implications for rheology of the mantle transition zone and subducting plates. *Geophysical Research Letters*, *31*(13), 2–5. https://doi.org/10.1029/2004GL020002

Siesler, H., Ozaki, Y., Kawata, S., & Heise, H. (2008). *Near-Infrared Spectroscopy: Principles, Instruments, Applications*. Wiley-VCH.

Smith, D. (1995). *Thin Film Deposition: Principles and Practice.* New York: McGraw-Hill, Inc.

Smyth J. Kawamoto, T. (1997). Wadsleyite II: A new high pressure hydrous phase in the peridotite-H2O system. *Earth and Planetary Science Letters*, *146*(303). https://doi.org/10.1016/S0012-821X(96)00230-0

Smyth, J. R. (1987). The beta -Mg_2SiO_4: a potential host for water in the mantle? *American Mineralogist*, *72*(11–12), 1051–1055.

Smyth, J. R. (1994). A crystallographic model for hydrous wadsleyite (β-Mg_2SiO_4): An ocean in the Earth's interior? *American Mineralogist*, *79*(9–10), 1021–1024.

Smyth, J. R., & Jacobsen, S. D. (2006). Nominally Anhydrous Minerals and Earth's Deep Water Cycle. *Geophysical Monograph*, 1–24. https://doi.org/10.1029/168GM02

Soldati, G., Boschi, L., Deschamps, F., & Giardini, D. (2009). Inferring radial models of mantle viscosity from gravity (GRACE) data and an evolutionary algorithm. *Physics of the Earth and Planetary Interiors*, *176*(1–2), 19–32. https://doi.org/10.1016/j.pepi.2009.03.013

Thomas, S.-M., Koch-Müller, M., Reichart, P., Rhede, D., Thomas, R., Wirth, R., & Matsyuk, S. (2009). IR calibrations for water determination in olivine, r-GeO_2, and SiO_2 polymorphs. *Physics and Chemistry of Minerals*, *36*(9), 489–509. https://doi.org/10.1007/s00269-009-0295-1

Thurel, E., Cordier, P., Frost, D., & Karato, S. I. (2003). Plastic deformation of wadsleyite: II. High-pressure deformation in shear. *Physics and Chemistry* *of Minerals*, *30*(5), 267–270. https://doi.org/10.1007/s00269-003-0313-7

Thurel, E., Douin, J., & Cordier, P. (2003). Plastic deformation of wadsleyite: III. Interpretation of dislocations and slip systems. *Physics and Chemistry of Minerals*, *30*(5), 271–279. https://doi.org/10.1007/s00269-003-0314-6

Trampert, J., & Van Heistz, H. J. (2002). Global azimuthal anisotropy in the transition zone. *Science*, *296*(5571), 1297–1299. https://doi.org/10.1126/science.1070264

Van der Hilst, R. D., Widiyantoro, S., & Engdahl, E. R. (1997). Evidence for deep mantle circulation from global tomography. *Nature*, *386*(6625), 578–584. https://doi.org/10.1038/386578a0

Van der Hist, R., Engdahl, R., Spakman, W., & Nolet, G. (1991). Tomographic imaging of subducted lithosphere below northwest Pacific island arcs. *Nature*, *353*(6339), 37–43. https://doi.org/10.1038/353037a0

Van Der Pluijm, B. A., & Marshak, S. (2004). *Earth Structure: An Introduction to Structural Geology and Tectonics.* (2nd ed.). New York: WW Norton.

Vassiliou, M. S., Hager, B. H., & Raefsky, A. (1984). The distribution of earthquakes with depth and stress in subducting slabs. *Journal of Geodynamics*, *1*(1), 11–28. https://doi.org/10.1016/0264-3707(84)90004-8

Visser, K., Trampert, J., Lebedev, S., & Kennett, B. L. N. (2008). Probability of radial anisotropy in the deep mantle. *Earth and Planetary Science Letters*, *270*(3–4), 241–250. https://doi.org/10.1016/j.epsl.2008.03.041

Vogt, K. (2008). *Mg-Fe Diffusion in Spinellen.* Ruhr-Universität Bochum, Germany.

Wang, Y., Durham, W. B., Getting, I. C., & Weidner, D. J. (2003). The deformation-DIA: A new apparatus for high temperature triaxial deformation to pressures up to 15 GPa. *Review of Scientific Instruments*, *74*(6), 3002–3011. https://doi.org/10.1063/1.1570948

Watson, E. B., Cherniak, D. J., Thomas, J. B., Hanchar, J. M., & Wirth, R. (2016). Crystal surface integrity and diffusion measurements on Earth and planetary materials. *Earth and Planetary Science Letters*, *450*, 346–354. https://doi.org/10.1016/j.epsl.2016.06.043

Weertman, J. R. (1955). Theory of Steady-State Creep Based on Dislocation Climb. *Journal of Applied Physics*, *26*(10), 1213–1217. https://doi.org/10.1063/1.1721875

Weertman, J. R., Farkas, D., Hemker, K., Kung, H., Mayo, M., Mitra, R., & Swygenhoven, H. Van. (1999). Structure and Mechanical Behavior of Bulk Nanocrystalline Materials. *MRS Bulletin*, *24*(2), 44–53. https://doi.org/10.1557/S088376940005154X

Widiyantoro, S., Kennett, B. L. N., & van der Hilst, R. D. (1999). Seismic tomography with P and S data reveals lateral variations in the rigidity of deep slabs. *Earth and Planetary Science Letters*, *173*(1–2), 91–100. https://doi.org/10.1016/S0012-821X(99)00216-2

Xu, J., Yamazaki, D., Katsura, T., Wu, X., Remmert, P., Yurimoto, H., & Chakraborty, S. (2011). Silicon and magnesium diffusion in a single crystal of MgSiO3perovskite. *Journal of Geophysical Research: Solid Earth*, *116*(12). https://doi.org/10.1029/2011JB008444

Ye, Y., Smyth, J. R., & Frost, D. J. (2011). Structural study of the coherent dehydration of wadsleyite. *American Mineralogist*, *96*(11–12), 1760–1767. https://doi.org/10.2138/am.2011.3852

Yoshino, T., Manthilake, G., Matsuzaki, T., & Katsura, T. (2008). Dry mantle transition zone inferred from the conductivity of wadsleyite and ringwoodite. *Nature*, *451*(7176), 326–329. https://doi.org/10.1038/nature06427

Zhang, B., Yoshino, T., & Zhao, C. (2019). The Effect of Water on Fe-Mg Interdiffusion Rates in Ringwoodite and Implications for the Electrical Conductivity in the Mantle Transition Zone. *Journal of Geophysical Research: Solid Earth*, *124*(3), 2510–2524. https://doi.org/10.1029/2018JB016415

Zhang, Y. (2010). Diffusion in Minerals and Melts: Theoretical Background. In *Reviews in Mineralogy and Geochemistry* (Vol. 72). https://doi.org/10.2138/rmg.2010.72.2

Zhao, D. (2004). Global tomographic images of mantle plumes and subducting slabs: insight into deep Earth dynamics. *Physics of the Earth and Planetary Interiors*, *146*(1–2), 3–34. https://doi.org/10.1016/j.pepi.2003.07.032

11. Appendix

11.1. FTIR spectra

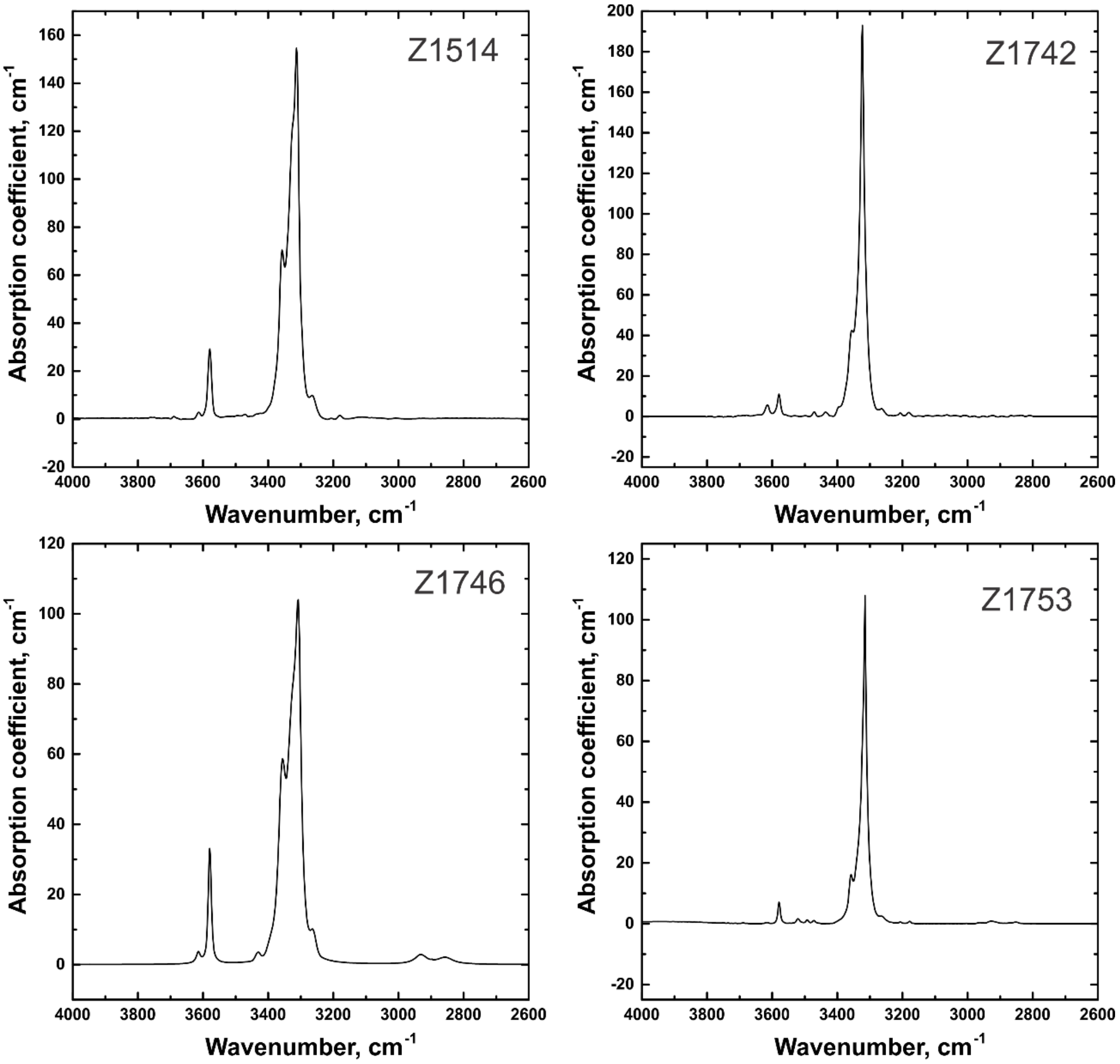

Fig. 11.1. FTIR spectra of samples after diffusion annealing.

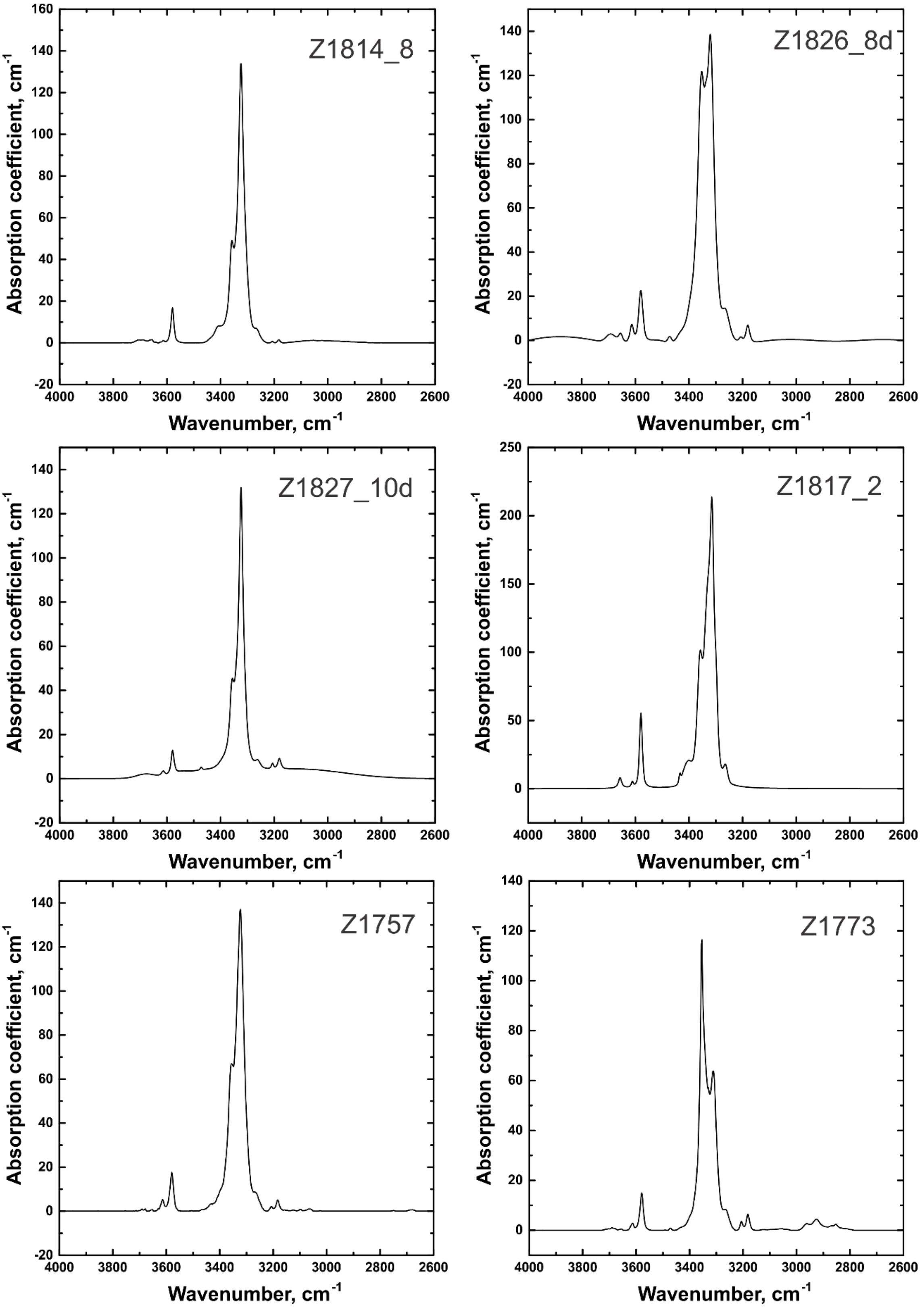

Fig. 11.1. (continued) FTIR spectra of samples after diffusion annealing.

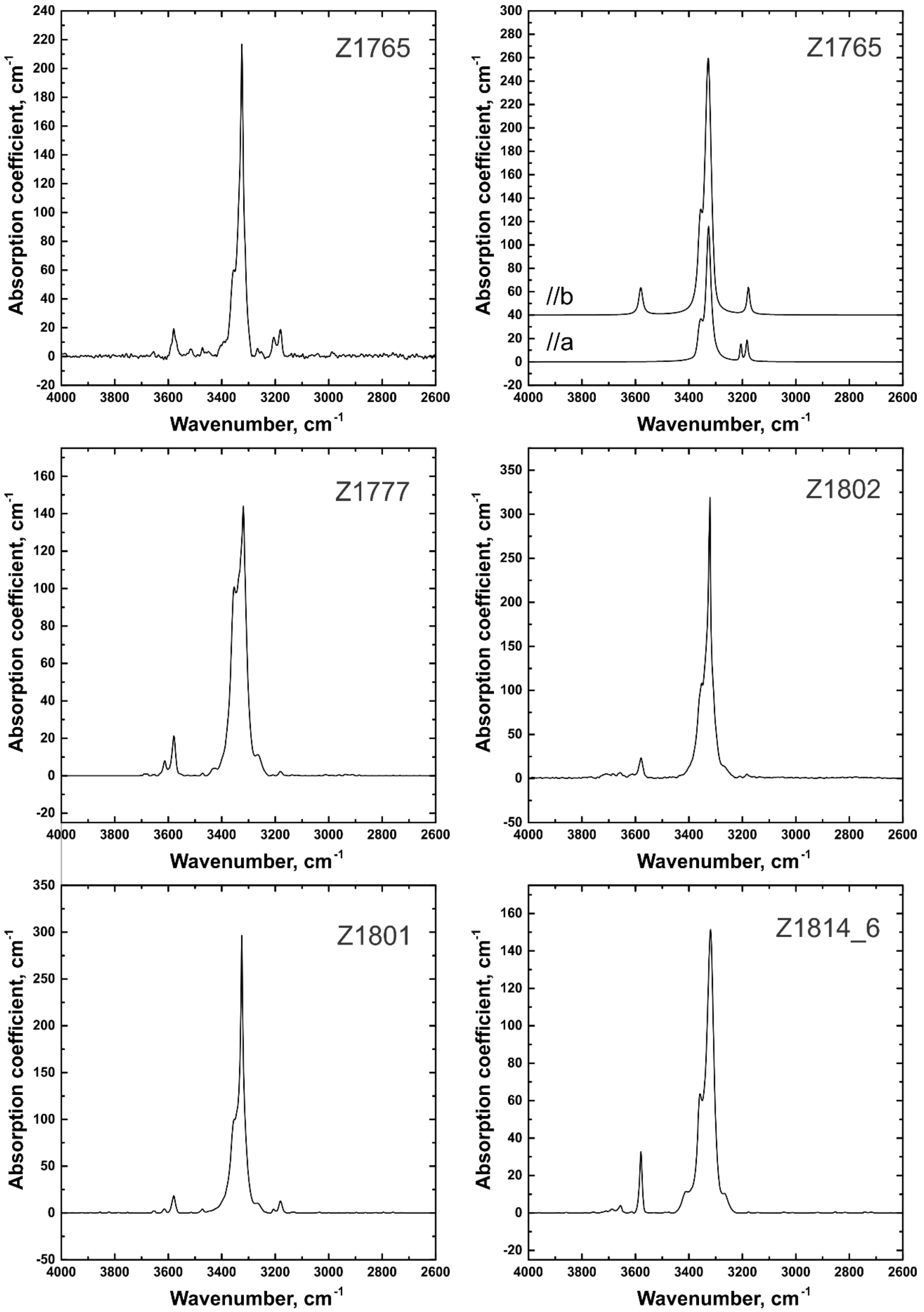

Fig. 11.1. (continue). FTIR spectra of samples after diffusion annealing.

11.2. FTIR peak positions

Table 11.1. *Positions of all identified peaks of all samples used in this study.*

Sample	Thickness (cm)	Absorbance Peaks
Z1309	0.0102	3613, 3579, 3359, 3323
Z1338	0.0102	3358, 3325, 3207
Z1449	0.0102	3357, 3325
Z1478	0.0102	3616, 3579, 3398, 3358, 3321, 3265
Z1534	0.0102	3356, 3325, 3207
Z1599	0.0102	3354, 3321
Z1603	0.0102	3614, 3579, 3386, 3359, 3320, 3265, 3207, 3178
Z1634	0.0102	3357, 3323, 3280
Z1639	0.0102	3353, 3323
Z1646	0.0071	3579, 3358, 3325, 3263, 3209, 3180
Z1649	0.0100	3579, 3358, 3400, 3319, 3265, 3180
Z1654	0.0102	3614, 3579, 3400, 3358, 3325, 3267, 3184
Z1800	0.0083	3689, 3614, 3579, 3358, 3317, 3265, 3178
Z1815	0.0162	3689, 3614, 3579, 3471, 3435, 3398, 3358, 3317, 3265, 3207, 3178
Z1856	0.0106	3358, 3325, 3207
Z1860	0.0106	3356, 3322, 3207
Z1863	0.0104	3358, 3322
Z1865	0.0105	3579, 3357, 3317
Z1867	0.0102	3579, 3359, 3319
Z1871	0.0101	3579, 3358, 3320
Z1875	0.0166	3689, 3614, 3579, 3435, 3396, 3357, 3313, 3265
Z1514	0.0203	3689, 3614, 3579, 3471, 3358, 3320, 3311, 3265, 3180
Z1695	0.0205	-
Z1742	0.0095	3614, 3579, 3471, 3437, 3395, 3356, 3323, 3265, 3207, 3180
Z1746	0.0153	3614, 3580, 3431, 3360, 3323, 3308, 3265
Z1753	0.0240	3614, 3579, 3521, 3493, 3471, 3358, 3315, 3265, 3207, 3178
Z1757	0.0100	3614, 3579, 3431, 3356, 3323, 3269, 3207, 3183
Z1765	0.0063	3579, 3517, 3471, 3395, 3356, 3325, 3267, 3253, 3205, 3180
Z1773	0.0246	3614, 3579, 3473, 3354, 3324, 3265, 3207, 3180
Z1777	0.0118	3614, 3579, 3471, 3430, 3354, 3319, 3265, 3180
Z1801	0.0102	3614, 3579, 3471, 3354, 3325, 3265, 3207, 3180
Z1802	0.0105	3614, 3579, 3354, 3321, 3265, 3210, 3180
Z1814_6	0.0097	3689, 3658, 3614, 3579, 3411, 3357, 3319, 3265, 3180
Z1814_8	0.0098	3689, 3658, 3614, 3579, 3410, 3358, 3323, 3263, 3207, 3184
Z1817	0.0099	3579, 3358, 3317
Z1826_8	0.0105	3691, 3656, 3614, 3579, 3471, 3354, 3321, 3265, 3207, 3180
Z1827_10	0.0100	3614, 3579, 3471, 3356, 3323, 3264, 3207, 3180
Z1886	0.0298	3314
Z1890	0.0296	-
Z1893_1	0.0203	3614, 3579, 3471, 3356, 3323, 3264, 3207, 3180
Z1895	0.0278	3691, 3656, 3614, 3579, 3471, 3354, 3321, 3265, 3207, 3180
Z1906_75	0.0203	3614, 3579, 3354, 3321, 3265, 3207, 3180

11.3. Craters topography

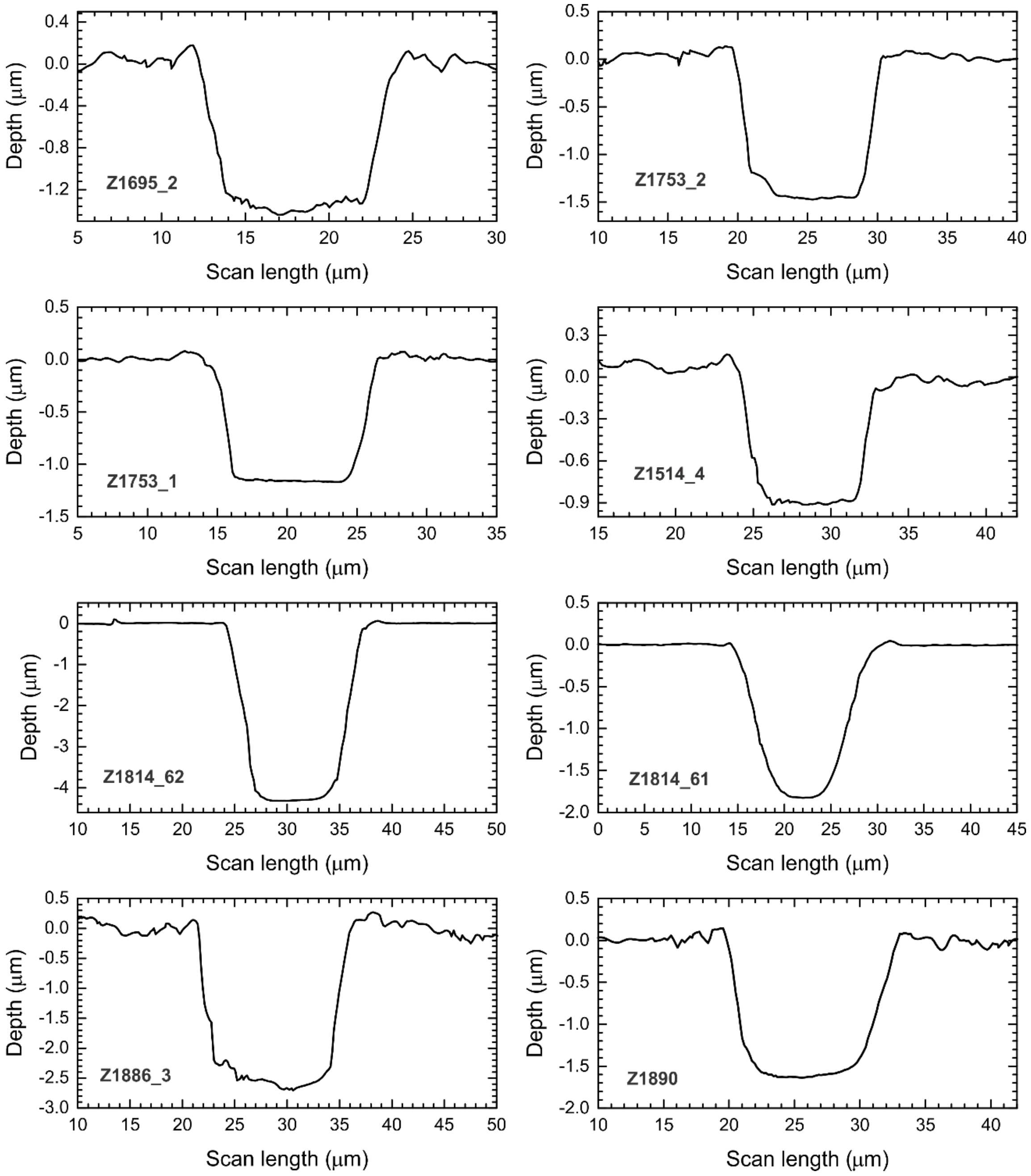

Fig. 11.2. Crater depth profiles, obtained by Confocal Microscope.

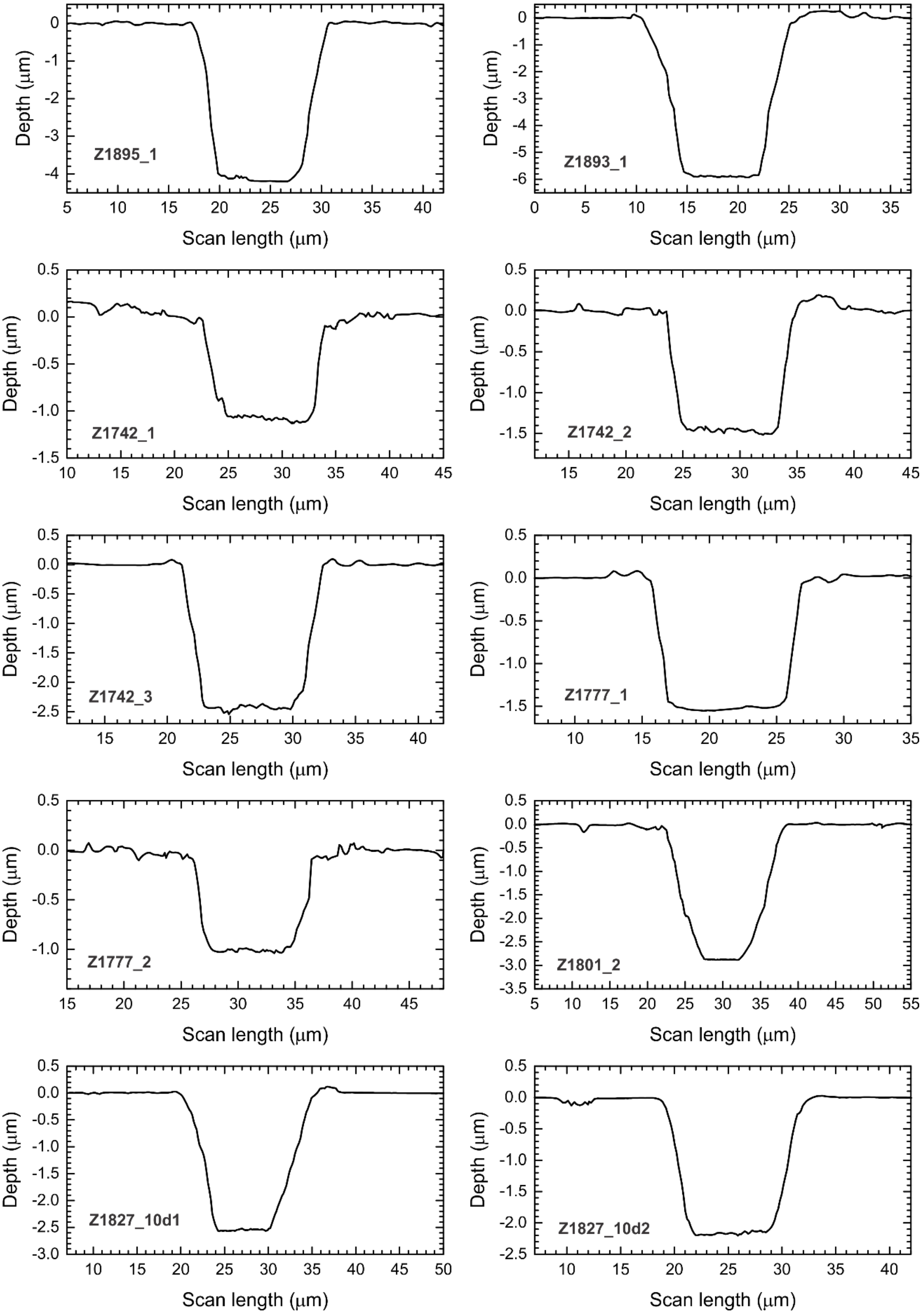

Fig. 11.2. (continued) Crater depth profiles, obtained by Confocal Microscope.

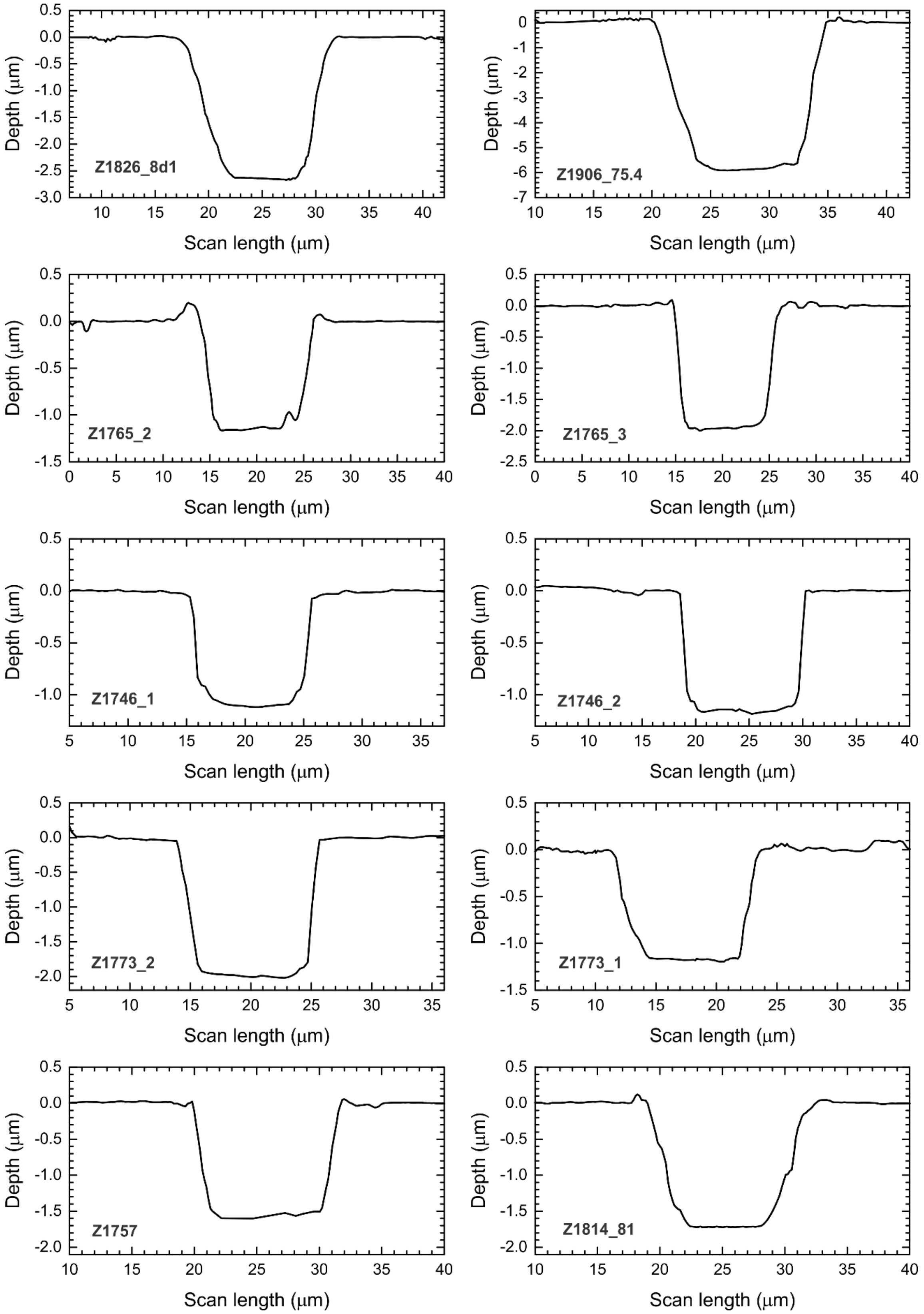

Fig. 11.2. (continued) Crater depth profiles, obtained by Confocal Microscope.

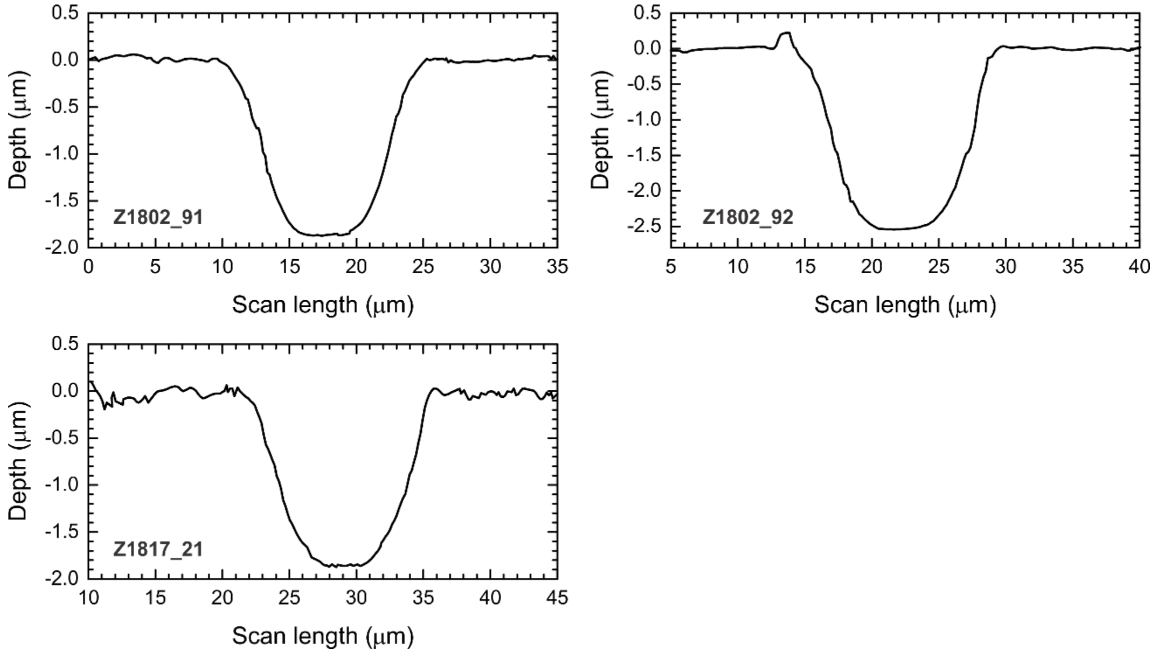

Fig. 11.2. (continued) Crater depth profiles, obtained by Confocal Microscope.

11.4. Examples of diffusion profiles

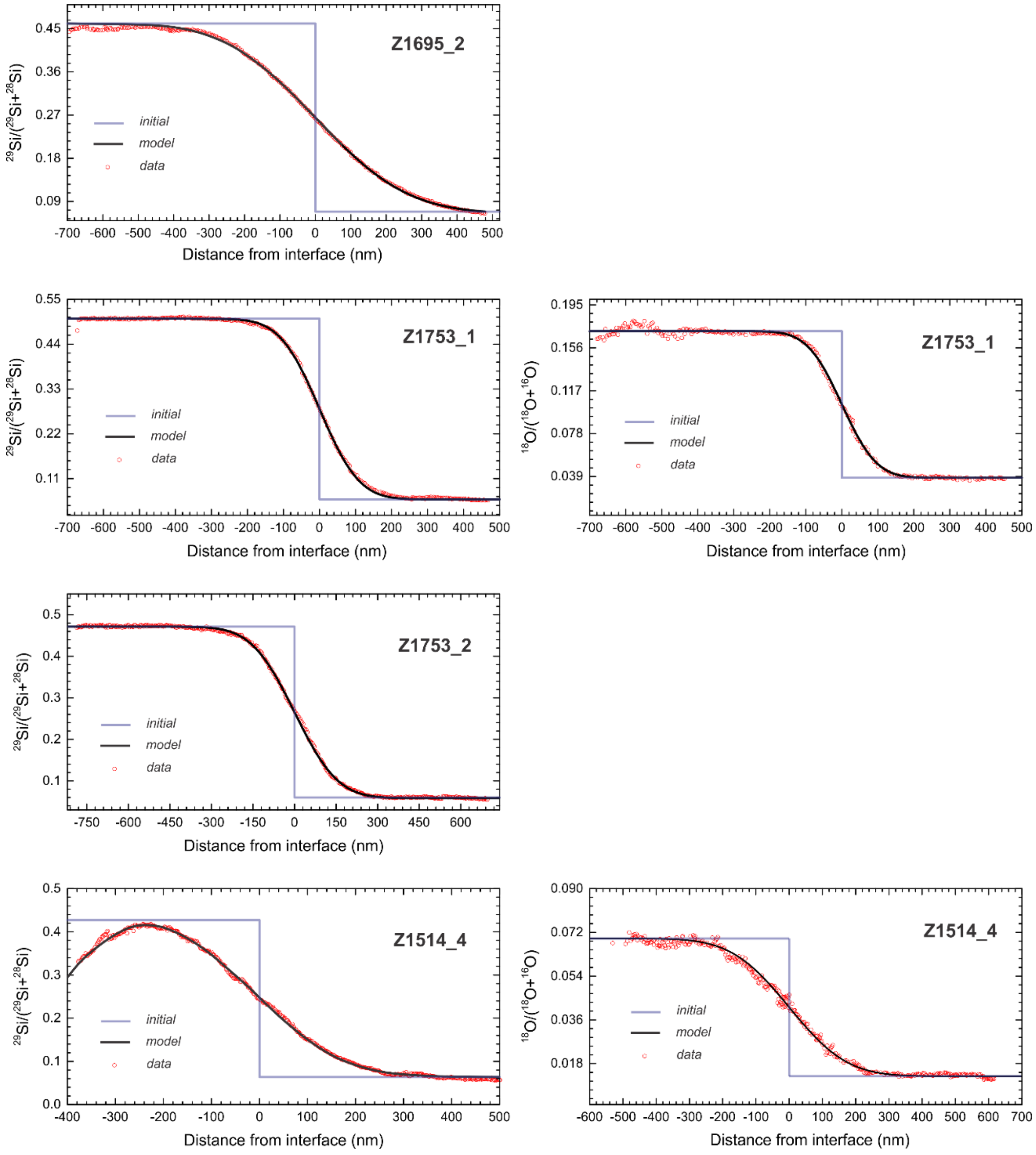

Fig. 11.3. Si (left figures) and O (right figures) depth diffusion profiles (rounds) and fits (black line). Initial profiles are shown with blue line.

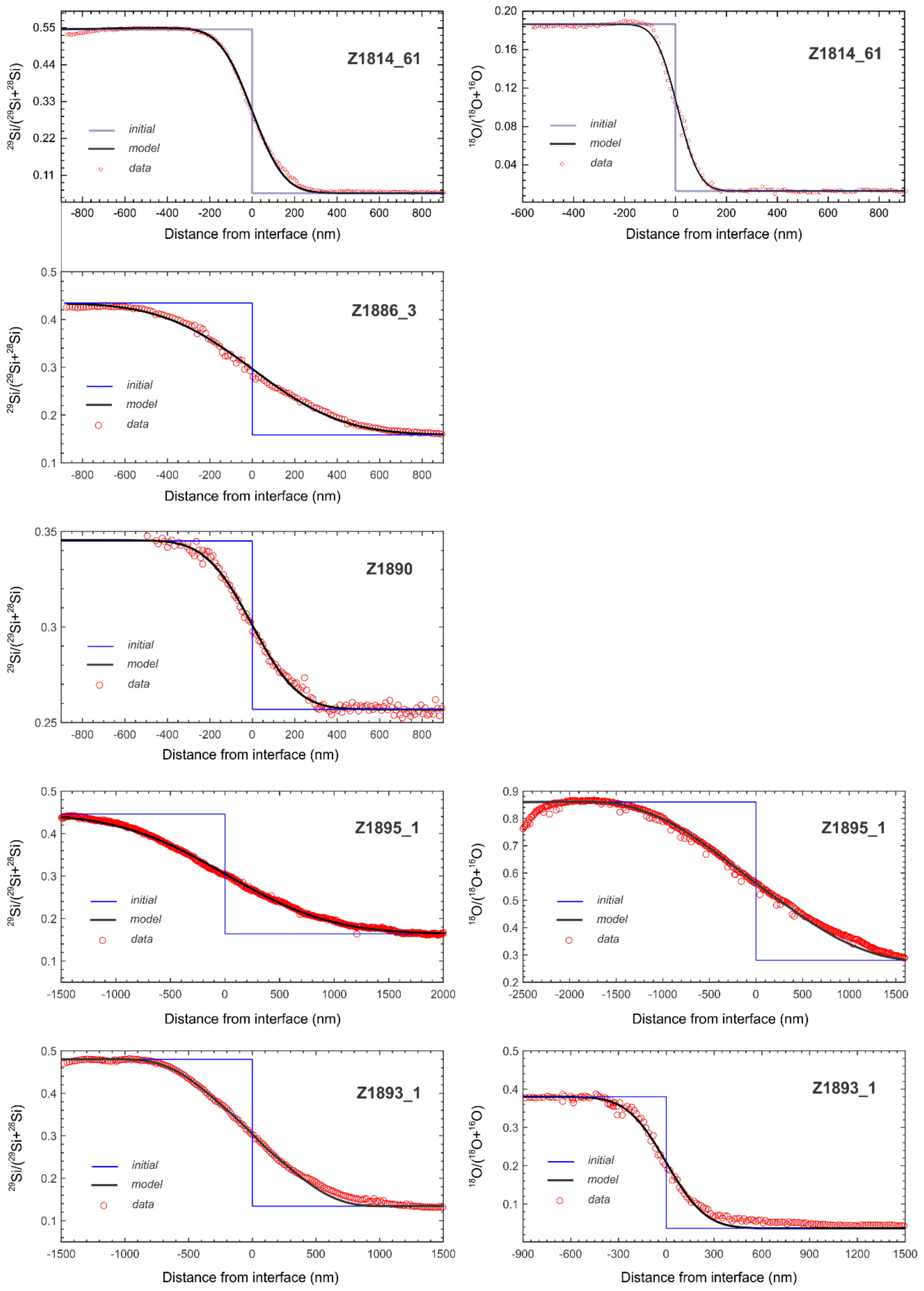

Fig. 11.3. (continued) Si (left figures) and O (right figures) depth diffusion profiles (rounds) and fits (black line). Initial profiles are shown with blue line.

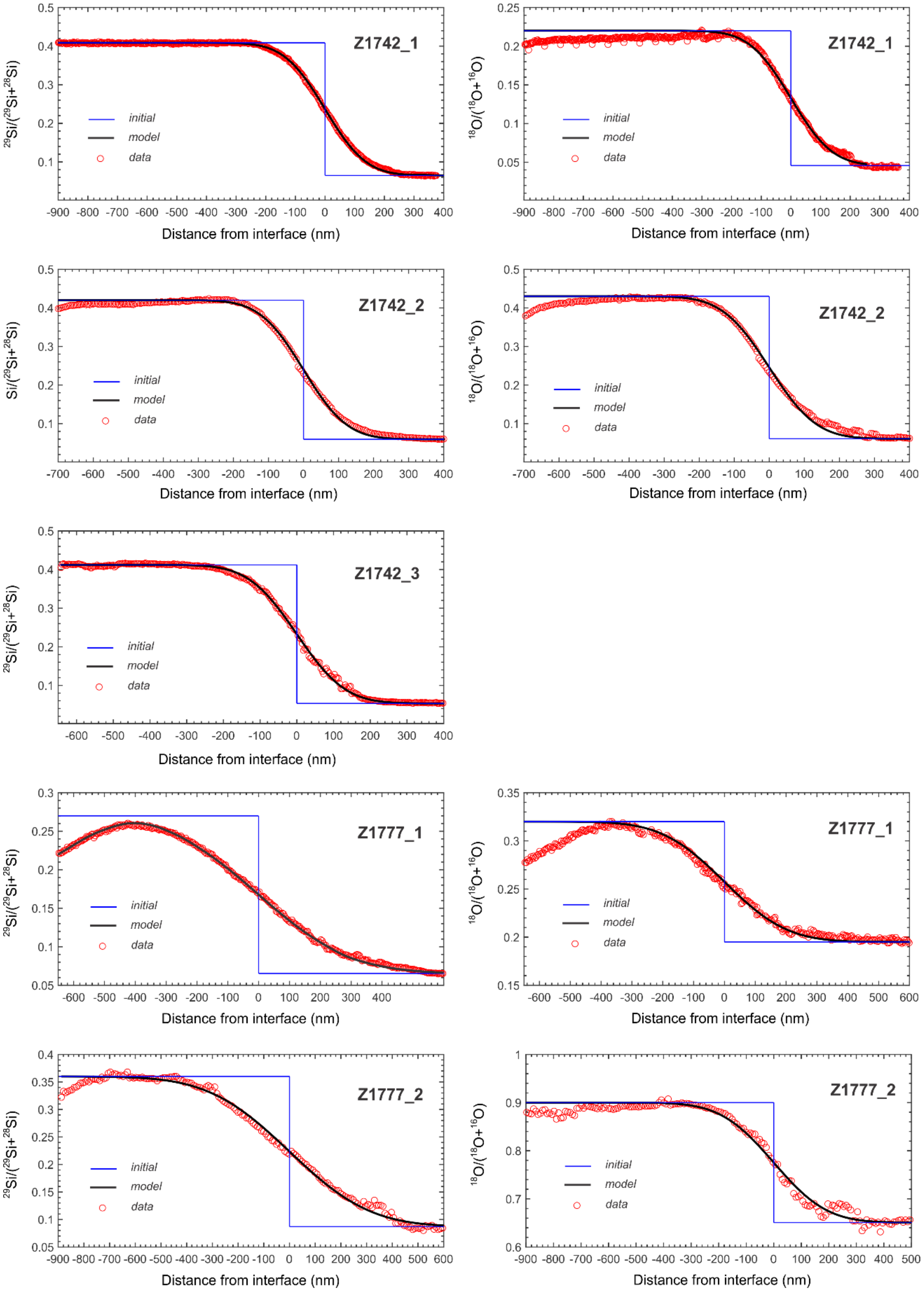

Fig. 11.3. (continued) Si (left figures) and O (right figures) depth diffusion profiles (rounds) and fits (black line). Initial profiles are shown with blue line.

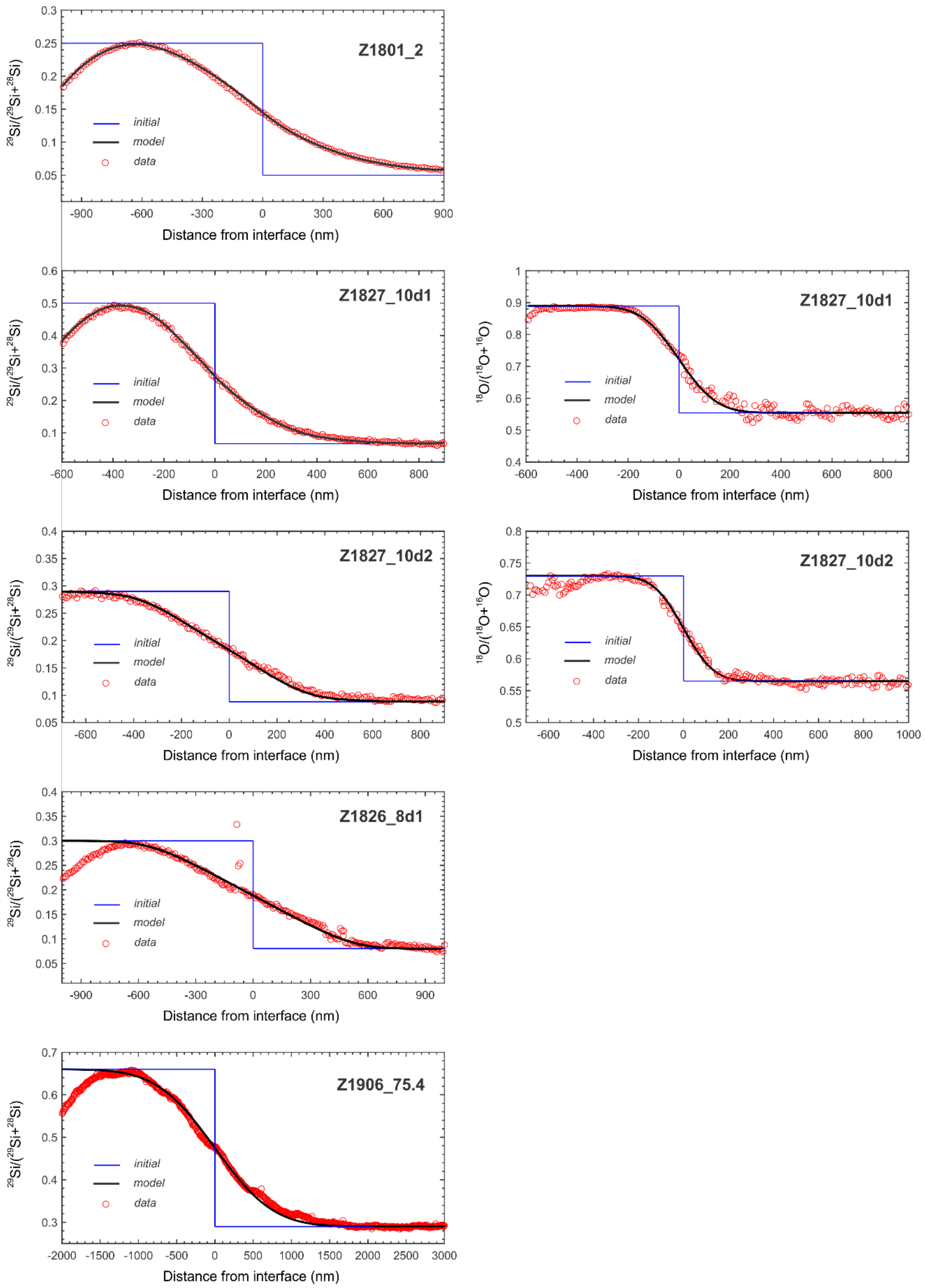

Fig. 11.3. (continued) Si (left figures) and O (right figures) depth diffusion profiles (rounds) and fits (black line). Initial profiles are shown with blue line.

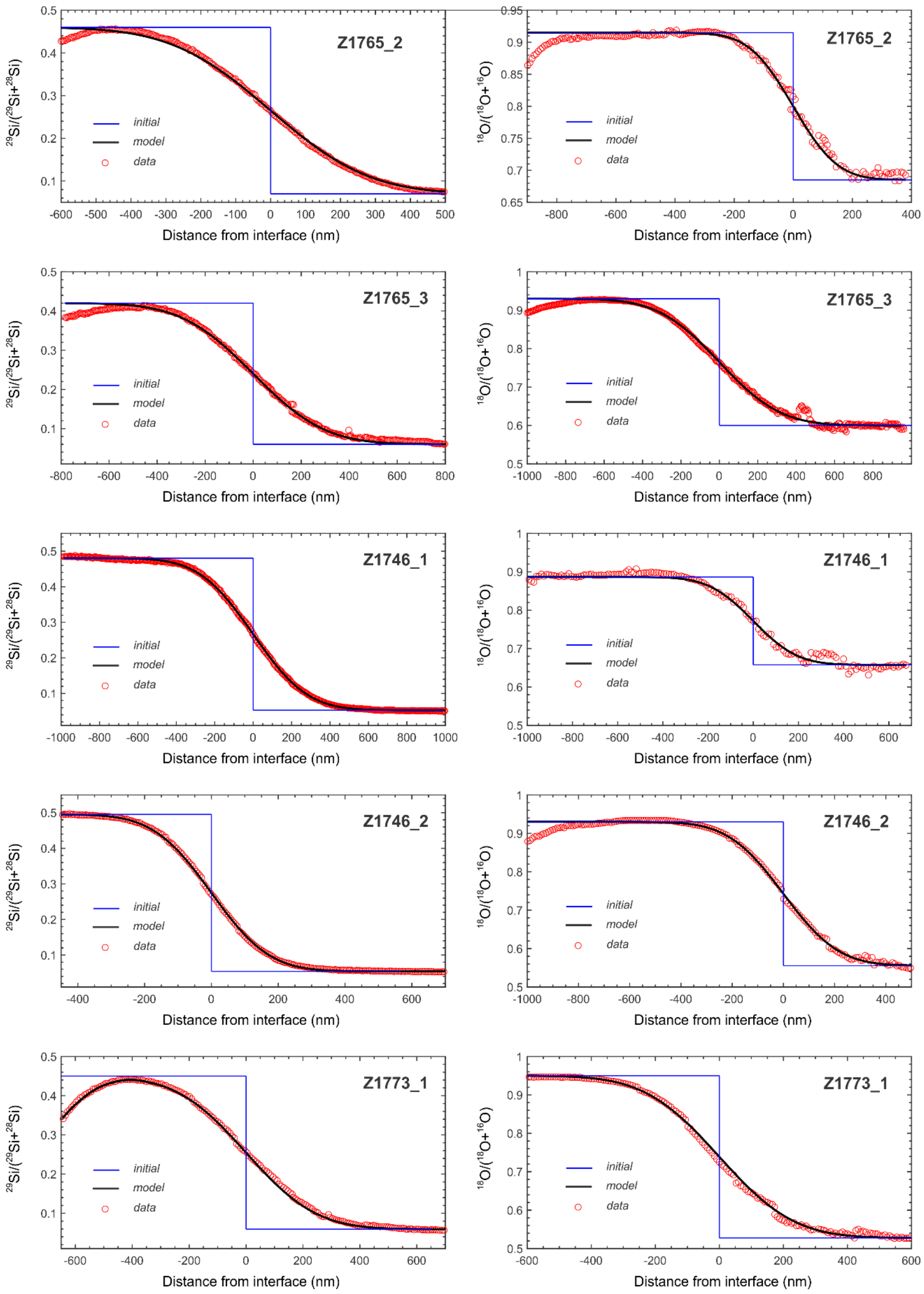

Fig. 11.3. (continued) Si (left figures) and O (right figures) depth diffusion profiles (rounds) and fits (black line). Initial profiles are shown with blue line.

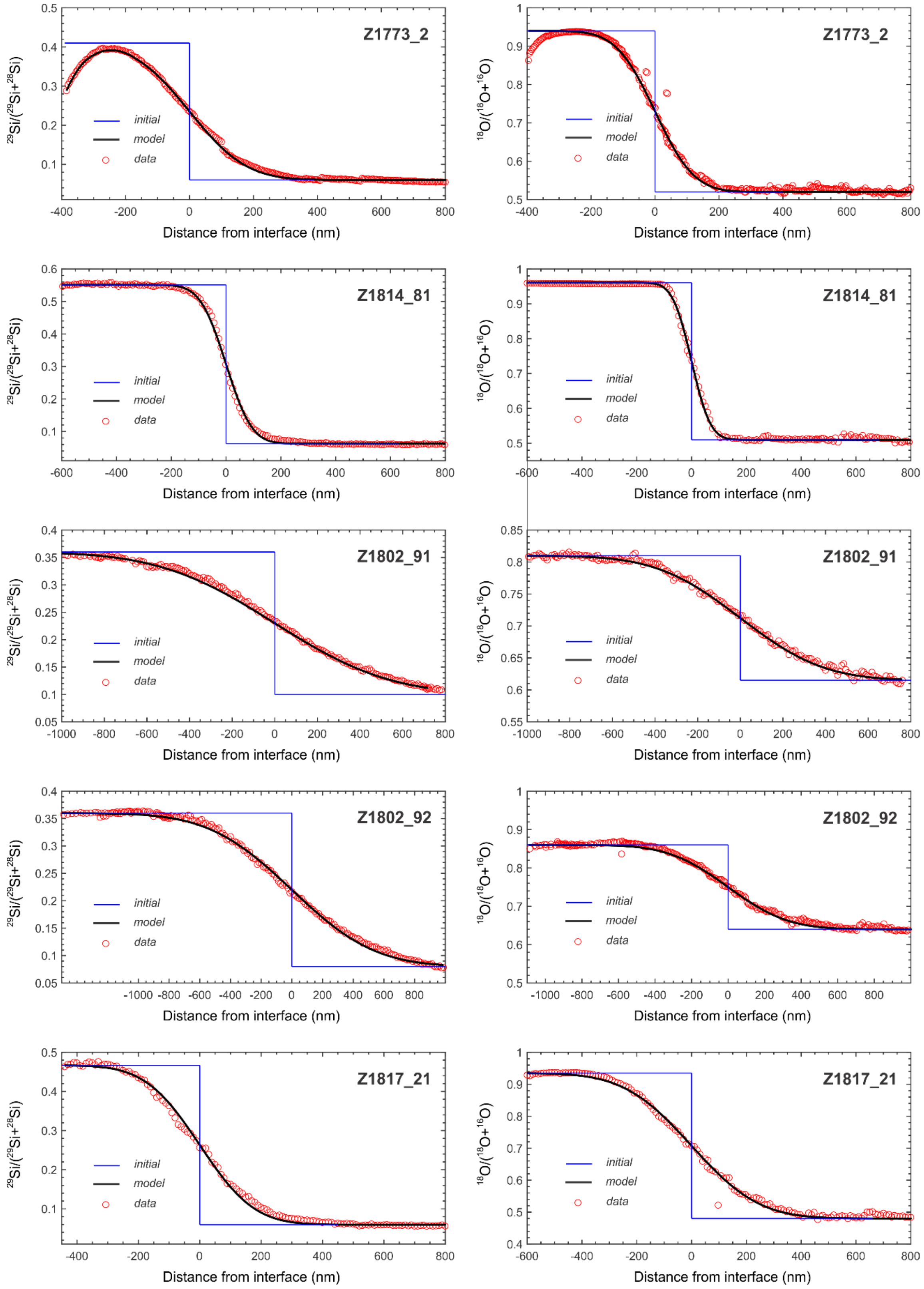

Fig. 11.3. (continued) Si (left figures) and O (right figures) depth diffusion profiles (rounds) and fits (black line). Initial profiles are shown with blue line.

11.5. Matlab code

Fitting with Fick's law solution

Matlab code presented below was used for D_{Si} and D_{O} determination by fitting of a loaded diffusion profile by Eq. 7.1 (Section 7.7). It creates an interface (**Fig. 11.4**) in which isotope depth distribution from loaded file is fitted by using inputted parameters and boundary conditions. Then result numbers and fitted profile can be output and saved in a .pdf file.

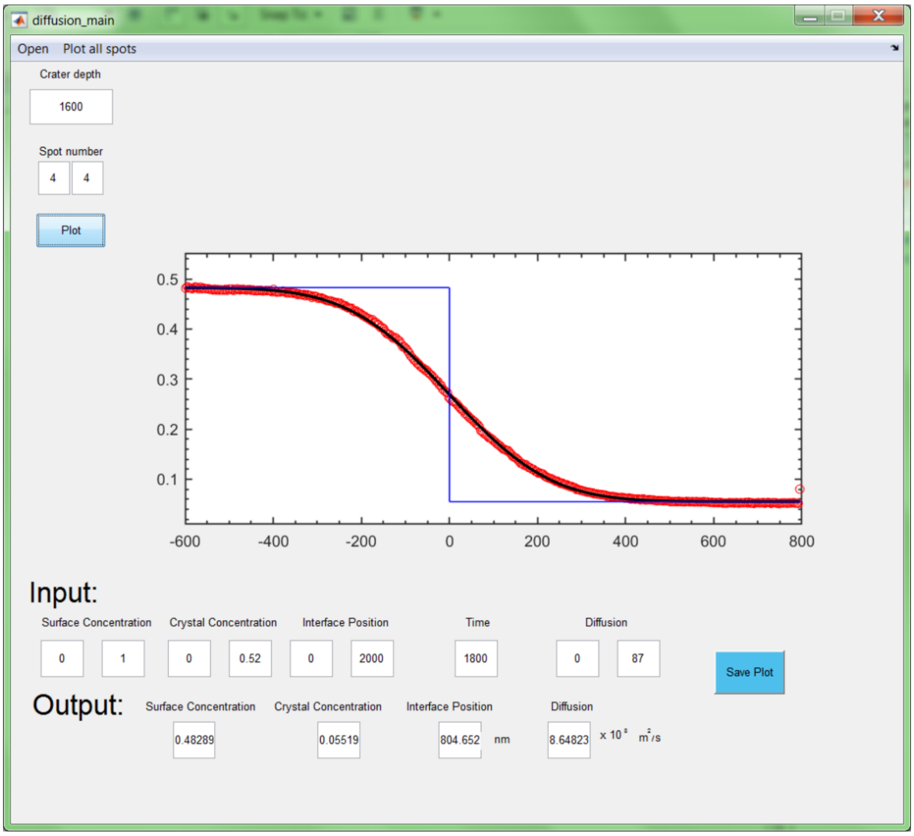

Crater depth: 1600

Spot number: 4 4

Input:

Surface Concentration: 0 1
Crystal Concentration: 0 0.52
Interface Position: 0 2000
Time: 1800
Diffusion: 0 87

Output:

Surface Concentration: 0.48289
Crystal Concentration: 0.05519
Interface Position: 804.652 nm
Diffusion: 8.64823 x 10^{8} m^2/s

Fig. 11.4. Interface window of Matlab script for D_{Si} and D_{O} determination by fitting of a loaded diffusion profile by Eq. 7.1 (Section 7.7).

Creation of a working interface:

```
function varargout = diffusion_main(varargin)
gui_Singleton = 1;
gui_State = struct('gui_Name',       mfilename, ...
                   'gui_Singleton',  gui_Singleton, ...
                   'gui_OpeningFcn', @diffusion_main_OpeningFcn, ...
                   'gui_OutputFcn',  @diffusion_main_OutputFcn, ...
                   'gui_LayoutFcn',  [] , ...
                   'gui_Callback',   []);
```

```
if nargin && ischar(varargin{1})
    gui_State.gui_Callback = str2func(varargin{1});
end
if nargout
    [varargout{1:nargout}] = gui_mainfcn(gui_State, varargin{:});
else
    gui_mainfcn(gui_State, varargin{:});
end

function diffusion_main_OpeningFcn(hObject, eventdata, handles, varargin)
handles.output = hObject;
guidata(hObject, handles);

function varargout = diffusion_main_OutputFcn(hObject, eventdata, handles)
varargout{1} = handles.output;
set(0,'DefaultAxesFontSize', 11);
```

Loading of .xlsx file with isotope depth distributions:

```
function open_file_menu_Callback(hObject, eventdata, handles)
openfile = uigetfile({'*.xlsx'});
if openfile==0
     return
end
data29 = xlsread(openfile,1);
data28 = xlsread(openfile,2);
handles.data29 = data29;
handles.data28 = data28;
guidata(hObject, handles);
```

Creation of fields, where depth of a crater and number of a studied spot can be input:

```
function crater_depth_Callback(hObject, eventdata, handles)
function crater_depth_CreateFcn(hObject, eventdata, handles)
if          ispc          &&          isequal(get(hObject,'BackgroundColor'),
get(0,'defaultUicontrolBackgroundColor'))
    set(hObject,'BackgroundColor','white');
end
function number_M_Callback(hObject, eventdata, handles)
function number_M_CreateFcn(hObject, eventdata, handles)
if          ispc          &&          isequal(get(hObject,'BackgroundColor'),
get(0,'defaultUicontrolBackgroundColor'))
    set(hObject,'BackgroundColor','white');
end
function Number_N_Callback(hObject, eventdata, handles)
function Number_N_CreateFcn(hObject, eventdata, handles)
if          ispc          &&          isequal(get(hObject,'BackgroundColor'),
get(0,'defaultUicontrolBackgroundColor'))
    set(hObject,'BackgroundColor','white');
end
```

Fitting, using input parameters and boundary conditions. Creation a plot with data, initial profile and resulted fit:

```
function Plot_button_Callback(hObject, eventdata, handles)
N = str2double(get(handles.Number_N,'string'));
M = str2double(get(handles.number_M,'string'));
d = str2double(get(handles.crater_depth,'string'));
c1 = str2double(get(handles.c1_input,'string'));
c1_low = str2double(get(handles.c1_lower,'string'));
c0 = str2double(get(handles.c0_input,'string'));
c0_low = str2double(get(handles.c0_lower,'string'));
```

```
h = str2double(get(handles.h_input,'string'));
h_low = str2double(get(handles.h_lower,'string'));
t = str2double(get(handles.t_input,'string'));
dif = str2double(get(handles.d_input,'string'));
dif_low = str2double(get(handles.d_lower,'string'));
L = 45;
if isempty(M)
    uiwait(msgbox('Input spot number','Spot','error'));
    return
else
        if isempty(N)
            uiwait(msgbox('Input spot number','Spot','error'));
            return
        else
            Num = 8*M - (8-N);
            data29 = handles.data29;
            data28 = handles.data28;
            setappdata(0,'data29',data29);
            setappdata(0,'data28',data28);
            [s1,r1] = size(data29);
            [s2,r2] = size(data28);
            dataX = data29(:,1)*(d/s1);
            dataY = ((data29(:,Num+1)./(data28(:,Num+1)+data29(:,Num+1))));
            outliers = excludedata(dataX,dataY,'domain',[0 6000])
            ft = fittype( '0.5*(c1-c0)*erf((x-h)/sqrt(4*d*t+45^2))+0.5*(c1+c0)',
'independent', 'x', 'dependent', 'y' , 'coefficients',{'c0','c1','d','t','h'});
            opts = fitoptions( 'Method', 'NonlinearLeastSquares' );
            opts.Exclude = outliers;
            opts.Display = 'off';
            opts.Lower = [c1_low c0_low dif_low t h_low];
            opts.Upper = [c1 c0 dif t h];
            [fitresult, gof] = fit( dataX, dataY, ft, opts );
            p = coeffvalues(fitresult);
            set(handles.c1_out, 'String', p(1));
            set(handles.c0_out, 'String', p(2));
            set(handles.h_out, 'String', p(5));
            set(handles.dif_out, 'String', p(3));
%             figure (1);
%             set(gca,'units','centimeters','position',[1,1,13.2,6.6]);
            p1 = plot(dataX-p(5),dataY,'ko', 'color', 'r');
            hold on;
            yPlot = 0.5*(p(2)-p(1))*erf((dataX -
p(5))/sqrt(4*p(3)*t+L^2))+0.5*(p(1)+p(2));
            p2 = plot(dataX-p(5), yPlot, 'k');
                        set(p2, 'LineWidth',2);
                        hold on;
                        x1 = -p(5):1:0;
                        zeroPlot1 = p(1)+x1*0;
                        x2 = 0:1:p(5);
                        zeroPlot2 = p(2)+x2*0;
            p3 = plot(x1, zeroPlot1, 'b');
            p4 = plot(x2, zeroPlot2, 'b');
            set(p3, 'linewidth',1);
            set(p4, 'linewidth',1);
            p5 = line([0 0], [p(1) p(2)]);
            set(p5,'color','b', 'linewidth', 1);
            set(gca,'linewidth',        1,'XLim',[-500        1000],'YLim',[0.01
0.3],'XTick',[-1000:200:800],'XMinorTick','on','YMinorTick','on');
            hold off;

        end
end
function plot_all_menu_Callback(hObject, eventdata, handles)
```

Creation of fields, where boundary conditions can be input:

```
function c1_input_Callback(hObject, eventdata, handles)
function c1_input_CreateFcn(hObject, eventdata, handles)
if          ispc          &&          isequal(get(hObject,'BackgroundColor'),
get(0,'defaultUicontrolBackgroundColor'))
    set(hObject,'BackgroundColor','white');
end
function c1_lower_Callback(hObject, eventdata, handles)
function c1_lower_CreateFcn(hObject, eventdata, handles)
if          ispc          &&          isequal(get(hObject,'BackgroundColor'),
get(0,'defaultUicontrolBackgroundColor'))
    set(hObject,'BackgroundColor','white');
end
function c0_input_Callback(hObject, eventdata, handles)
function c0_input_CreateFcn(hObject, eventdata, handles)
if          ispc          &&          isequal(get(hObject,'BackgroundColor'),
get(0,'defaultUicontrolBackgroundColor'))
    set(hObject,'BackgroundColor','white');
end
function c0_lower_Callback(hObject, eventdata, handles)
function c0_lower_CreateFcn(hObject, eventdata, handles)
if          ispc          &&          isequal(get(hObject,'BackgroundColor'),
get(0,'defaultUicontrolBackgroundColor'))
    set(hObject,'BackgroundColor','white');
end
function h_input_Callback(hObject, eventdata, handles)
function h_input_CreateFcn(hObject, eventdata, handles)
if          ispc          &&          isequal(get(hObject,'BackgroundColor'),
get(0,'defaultUicontrolBackgroundColor'))
    set(hObject,'BackgroundColor','white');
end
function h_lower_Callback(hObject, eventdata, handles)
function h_lower_CreateFcn(hObject, eventdata, handles)
if          ispc          &&          isequal(get(hObject,'BackgroundColor'),
get(0,'defaultUicontrolBackgroundColor'))
    set(hObject,'BackgroundColor','white');
end
function t_input_Callback(hObject, eventdata, handles)
function t_input_CreateFcn(hObject, eventdata, handles)
if          ispc          &&          isequal(get(hObject,'BackgroundColor'),
get(0,'defaultUicontrolBackgroundColor'))
    set(hObject,'BackgroundColor','white');
end
```

```
function d_input_Callback(hObject, eventdata, handles)
function d_input_CreateFcn(hObject, eventdata, handles)
if          ispc          &&          isequal(get(hObject,'BackgroundColor'),
get(0,'defaultUicontrolBackgroundColor'))
    set(hObject,'BackgroundColor','white');
end
function d_lower_Callback(hObject, eventdata, handles)
function d_lower_CreateFcn(hObject, eventdata, handles)
if          ispc          &&          isequal(get(hObject,'BackgroundColor'),
get(0,'defaultUicontrolBackgroundColor'))
    set(hObject,'BackgroundColor','white');
end
```

Output results:

```
function c1_out_Callback(hObject, eventdata, handles)
function c1_out_CreateFcn(hObject, eventdata, handles)
if          ispc          &&          isequal(get(hObject,'BackgroundColor'),
get(0,'defaultUicontrolBackgroundColor'))
```

```
    set(hObject,'BackgroundColor','white');
end
function c0_out_Callback(hObject, eventdata, handles)
function c0_out_CreateFcn(hObject, eventdata, handles)
if          ispc          &&          isequal(get(hObject,'BackgroundColor'),
get(0,'defaultUicontrolBackgroundColor'))
    set(hObject,'BackgroundColor','white');
end
function h_out_Callback(hObject, eventdata, handles)
function h_out_CreateFcn(hObject, eventdata, handles)
if          ispc          &&          isequal(get(hObject,'BackgroundColor'),
get(0,'defaultUicontrolBackgroundColor'))
    set(hObject,'BackgroundColor','white');
end
function dif_out_Callback(hObject, eventdata, handles)
function dif_out_CreateFcn(hObject, eventdata, handles)
if          ispc          &&          isequal(get(hObject,'BackgroundColor'),
get(0,'defaultUicontrolBackgroundColor'))
    set(hObject,'BackgroundColor','white');
end
```

Saves resulted plot to a .pdf file:

```
function Save_plot_Callback(hObject, eventdata, handles)
saveas(figure(1),'saved.pdf');



function Name_tag_Callback(hObject, eventdata, handles)
function Name_tag_CreateFcn(hObject, eventdata, handles)
if          ispc          &&          isequal(get(hObject,'BackgroundColor'),
get(0,'defaultUicontrolBackgroundColor'))
    set(hObject,'BackgroundColor','white');
end
```

Numerical simulations

Below is a matlab code that was used for D_{Si} and D_{O} determination with numerical simulations from a loaded diffusion depth profile (**Eq. 4.4, Section 4.4**).

```
clear();
%units micrometer and seconds
data = xlsread('test.xlsx') ;% Input file with data to compare with
X = 0 : 1 : 2000;
nx = length(X); deltax = 2; %grid size
h = 700; film_grid = floor(h/deltax); %film thickness
D1 = 60; %diffusion coefficient
runtime = 1200; %time of experiment in seconds
runtime2 = 600;
delta_t = 0.4*((deltax)^2)/D1;
timesteps = floor(runtime/delta_t);
Cfilm = 0.38; C0 = 0.085; %Initial concentration in the film, in the substrate
%Initialization of initial concentration profile
Initial=zeros(1,nx);
flux=zeros(1,nx);
fill=zeros(1,nx);
t(1)=1;
for i = 1 : film_grid
```

```
        Initial(i) = Cfilm;
end;
for i = film_grid+1 : nx
        Initial(i) = C0;
end;
Csurface=0.28;
Initial(1)=Csurface;
Conc=Initial;
for i = 1 : timesteps
       buff = Conc;
       for j= 2 : nx-1
           Conc(j) = buff(j) + delta_t/(deltax^2)*D1*(buff(j-1)-
   2*buff(j)+buff(j+1));
       end
   end;
               for n = 2 : film_grid
                   flux(n) = abs((((Cfilm - buff(n)) + (Cfilm - buff(n-
   1)))*deltax))/2;
                   flux(1) = flux(2);
               end
               for n = film_grid+1 : nx-1
                   flux(n) = abs(((buff(n) - C0) + (buff(n-1) - C0))*deltax)/2;
                   flux(nx) = flux(nx-1);
               end
   colflux = flux.';
   ConcColum=Conc.';
   xColum=X.';
   figure(1);
   plot(X*deltax,Conc,data(:,1),data(:,2))
   ylim([0 0.6])
   xlim([0 3000])
   grid on;
```

(Eidesstattliche) Versicherungen und Erklärungen

(§ 9 Satz 2 Nr. 3 PromO BayNAT)

Hiermit versichere ich eidesstattlich, dass ich die Arbeit selbstständig verfasst und keine anderen als die von mir angegebenen Quellen und Hilfsmittel benutzt habe (vgl. Art. 64 Abs. 1 Satz 6 BayHSchG).

(§ 9 Satz 2 Nr. 3 PromO BayNAT)

Hiermit erkläre ich, dass ich die Dissertation nicht bereits zur Erlangung eines akademischen Grades eingereicht habe und dass ich nicht bereits diese oder eine gleichartige Doktorprüfung endgültig nicht bestanden habe.

(§ 9 Satz 2 Nr. 4 PromO BayNAT)

Hiermit erkläre ich, dass ich Hilfe von gewerblichen Promotionsberatern bzw.-vermittlern oder ähnlichen Dienstleistern weder bisher in Anspruch genommen habe noch künftig in Anspruch nehmen werde.

(§ 9 Satz 2 Nr. 7 PromO BayNAT)

Hiermit erkläre ich mein Einverständnis, dass die elektronische Fassung meiner Dissertation unter Wahrung meiner Urheberrechte und des Datenschutzes einer gesonderten Überprüfung unterzogen werden kann.

(§ 9 Satz 2 Nr. 8 PromO BayNAT)

Hiermit erkläre ich mein Einverständnis, dass bei Verdacht wissenschaftlichen Fehlverhaltens Ermittlungen durch universitätsinterne Organe der wissenschaftlichen Selbstkontrolle stattfinden können.

____

Ort, Datum, Unterschrift